

RIKAGAKU KENKYUSHO

*the Institute of Physical and Chemical Research*

Wako-shi, Saitama Pref., JAPAN

'79

***IPCR cyclotron***  
**Progress Report 1979**

**Vol. 13**

***IPCR*** Cyclotron Progress Report

**Vol. 13**

The Institute of Physical and Chemical Research  
"RIKAGAKU KENKYUSHO" Wako-shi, Saitama, 351 JAPAN  
December, 1979

## Editors

F. Ambe	A. Hashizume
Y. Hattori	H. Kamitsubo
T. Nomura	M. Odera
M. Uda	T. Wada
S. Yamaji	

This volume contains recent information of the IPCR Cyclotron, informal reports and abstracts of papers which will be published at scientific meetings or in publications by staff members, guests, and visitors.

All rights reserved. This report or any part thereof may not be reproduced in any form (including photostatic or microfilm form) without written permission from the publisher.

# CONTENTS

	Page
1. INTRODUCTION .....	1
2. MACHINE OPERATION .....	2
3. MACHINE DEVELOPMENT AND ACCELERATOR PHYSICS	
3-1. Study of Field Correction by the Trim Coils for the SSC Magnet .....	4
3-2. Design of Injection System for Separated-Sector Cyclotron .....	7
3-3. Design of RF Resonator for Proposed Separated-Sector Cyclotron .....	10
3-4. Computer Code for the Accelerated Orbit in a Separated-Sector Cyclotron .....	12
3-5. Improvement of the Heavy Ion Source .....	15
3-6. Metal Ion Source for the Cyclotron and Acceleration of Metal Ions .....	17
3-7. Present States of the Baby Cyclotron .....	20
4. NUCLEAR PHYSICS	
Scattering and Reactions	
4-1. Adiabatic Treatment of Deuteron Breakup on a Nucleus .....	21
4-2. Fission Fragment Angular Distributions in 15 MeV Proton-Induced Fission of $^{232}\text{Th}$ .....	24
4-3. Spin-Flip Asymmetry in the Inelastic Scattering of Protons on $^{12}\text{C}$ at 24.1, 26.2, and 28.0 MeV .....	27
4-4. Vector Analyzing Power and Polarization Measurement for the $^{116}\text{Sn}(d, p)^{117}\text{Sn}(\text{g.s. } 1/2^+)$ and the Deuteron D-state Effects .....	30
4-5. Measurements of Particle- $\gamma$ Angular Correlations for the $^{58}\text{Ni}(p, d)^{57}\text{Ni}$ Reaction at $E_p = 30$ MeV .....	33
4-6. Coulomb Nuclear Interference in the Inelastic Scattering of $^{18}\text{O}$ .....	36
4-7. Semiclassical Treatment of the Direct Reactions Induced by Heavy Ions .....	39

	Page
4–8. Mass Exchange in an Analysis of the Heavy-Ion Reaction Based on the Linear Response Theory . . . . .	42
4–9. Study of the $^{27}\text{Al}(^{14}\text{N}, \text{HI } \alpha)$ Reaction . . . . .	45
4–10. Systematic Study of Reaction Cross Sections in the $^{14}\text{N} + ^{93}\text{Nb}$ Reaction . . . . .	48
4–11. Spin Polarization of $^{12}\text{B}$ in the $^{197}\text{Au}(^{19}\text{F}, ^{12}\text{B})$ Reaction at 186 MeV . . . . .	51
4–12. Isotopic Dependence of the Fission-Like Events in the 115 MeV Nitrogen-Induced Reactions on Nickel . . . . .	54
4–13. Preequilibrium Alpha Particle Emission Following Heavy-Ion Transfer Reactions . . . . .	56
4–14. $\gamma$ -Ray Multiplicity Measurement Following Preequilibrium $\alpha$ -Particle Emission in $^{14}\text{N}$ -Induced Reactions . . . . .	59
4–15. Relaxation of Angular Momentum Following Preequilibrium $\alpha$ Emission in Heavy-Ion Reactions . . . . .	62
 5. NUCLEAR PHYSICS Nuclear Spectroscopy and Instrumentation	
5–1. Recoil-Distance Lifetime Measurement of States in $^{118}\text{Xe}$ . . . . .	65
5–2. $\gamma$ -Ray Spectroscopy in the $^{144}\text{Nd} + ^{20}\text{Ne}$ Reaction . . . . .	67
5–3. In-Beam $\alpha$ -, $\gamma$ -Spectroscopic Study on $^{214}\text{Rn}$ . . . . .	70
 6. ATOMIC AND SOLID-STATE PHYSICS	
6–1. X-Rays Following Multiple Inner-Shell Ionization (4) . . . . .	73
6–2. Systematics in Multiple Ionization . . . . .	76
6–3. Contribution of Electron Transfer to K-Shell Ionizations by $\text{N}^{7+}$ -Ion Bombardment . . . . .	79
6–4. K X-Rays of Kr Measured with a Crystal Spectrometer . . . . .	82
6–5. K X-Rays of Kr Measured with a Si(Li) Detector . . . . .	84
6–6. Vacancy Rearrangement in the M Shell Prior to X-Ray Emission . . . . .	86

6-7.	Effects of Strain Rate on High Temperature Mechanical Properties of Helium-Injected Fe-Ni-Cr Austenitic Alloys .....	89
6-8.	Lattice Location of Sn Atoms Implanted into Al .....	92
6-9.	Secondary Electron Emission from Metals by High-Speed Proton Bombardments .....	94
6-10.	Angular Correlation of Positron Annihilation Radiation and Compton Profiles in Magnesium .....	97
6-11.	Mössbauer Study of $^{119}\text{Sn}$ in Chromium and Manganese Dioxides .....	100
7.	<b>RADIOCHEMISTRY AND NUCLEAR CHEMISTRY</b>	
7-1.	Charged-Particle Activation Analyses of Oxygen in $\text{GaAs}_{1-x}\text{P}_x$ .....	102
7-2.	Yield of Low-Z Radionuclides in Charged-Particle Reactions .....	104
7-3.	Recoil Range of $^{18}\text{F}$ Formed by Various Reactions .....	106
7-4.	$^{119}\text{Sn}$ -Mössbauer Emission Study on Se and SnSe Doped with $^{119\text{m}}\text{Te}$ .....	109
7-5.	Chemical States of Defect Tin Atoms in InSb and $\text{In}_2\text{Te}_3$ by Mössbauer Emission Spectroscopy .....	112
7-6.	Exchange Reaction of Seleno-Compound with Elemental Selenium .....	115
8.	<b>RADIATION CHEMISTRY AND RADIATION BIOLOGY</b>	
8-1.	Measurement of the Decay of the Emission from $\sigma$ -Excitons Produced in a KBr Crystal by Heavy-Ion Irradiation .....	117
8-2.	New Apparatus for Cyclotron-Beam Irradiation of Biological Samples .....	118
8-3.	Inactivation of Ribonuclease A in Solution by Cyclotron Beams .....	120
8-4.	Studies on Mutation Induction in Microorganisms by Cyclotron Beams .....	121
9.	<b>RADIATION MONITORING</b>	
9-1.	Routine Monitoring .....	124

9-2.	Leakage-Radiation Measurement at the Underground Passage . . . . .	126
10.	HEAVY ION LINEAR ACCELERATOR PROJECT	
10-1.	Status of the Constructional Work . . . . .	128
10-2.	Vacuum System . . . . .	131
10-3.	Control System . . . . .	134
10-4.	Installation of the Cooling System . . . . .	137
10-5.	Insulating Pipe and Column Structure for Supply of Coolant to the High Voltage Terminal . . . . .	140
10-6.	Plate Power Supplies for the Exciter Amplifiers of the IPCR Heavy-Ion Linear Accelerator . . . . .	141
10-7.	Initial Operation of the Proto-Type Power Amplifier Coupled with the First Cavity . . . . .	143
10-8.	Current Load of the Injector High-Voltage Generator without Beam Acceleration . . . . .	145
10-9.	Performance Test of Injector System . . . . .	147
10-10.	Beam Buncher Characteristics . . . . .	149
10-11.	Design of a Magnet for the Side-Extraction PIG-Type Ion Source . . . . .	151
10-12.	Performance of the Quadrupole Magnets of the Beam Transport System . . . . .	154
11.	LIST OF PUBLICATIONS . . . . .	156
12.	LIST OF PERSONNEL . . . . .	161
13.	LIST OF OUTSIDE USERS AND THEIR THEMES . . . . .	165
	AUTHOR INDEX . . . . .	167

## 1. INTRODUCTION

During the past one year the IPCR cyclotron was operated in good condition as before. Several improvements have been made in the machine itself and its accessory facilities which resulted in more stable and efficient operation.

In the fields of research using the cyclotron a majority of research works have been carried out with heavy ions. Extensive studies on preequilibrium emission of light particles and energy relaxation phenomena were performed in nuclear reactions induced by heavy ions. Nuclear structure studies were also continued. Multiple ionization phenomena in the collision of heavy ions on gaseous and solid materials were extensively studied to get information on the excitation mechanism as well as the effects of chemical state of surroundings on X-ray spectra. Positron annihilation and Mössbauer studies were made on several materials. Activation analysis by charged particles were applied for the study of semiconductor surfaces. Studies of radiation chemistry and radiation biology were continued using heavy ions as well as alpha particles.

The new heavy-ion linac has been completed and the first acceleration test was performed in the pre-injector and the first resonator. Design study of the separated sector cyclotron was continued.

*Hiromichi Kamitsubo*

---

Hiromichi Kamitsubo

Editor

## 2. MACHINE OPERATION

S. Kohara, T. Kageyama, K. Ikegami, K. Ogiwara,  
S. Fujita, H. Takebe, and I. Kohno

During the period from Oct. 23, 1978 to Oct. 22, 1979, the cyclotron was operated on the 24 h a day basis.

Table 1 shows the statistics of machine operation. The total beam time of 4516.0 h is nearly equal to that of last year.

Table 2 shows the beam time allotted to various activities in this period. The beam time allotted to nuclear physics groups was slightly, i.e. 196 h decreased and the time to groups of fields other than nuclear physics was increased by 168 h compared with that of last year.

Table 3 shows the distribution of the beam time among particles accelerated. In this period, deuteron was not accelerated. Most of the highly charged ions as  $N^{5+}$ ,  $O^{5+}$ , and  $Ne^{6+}$  ions were produced and accelerated using pulsed operation of the heavy ion source.

The sputtering ion source for production of metal ions was tested during the time of periodical inspection and overhaul, and  $Li^{2+}$ ,  $Be^{3+}$ , and  $B^{3+}$  ions were successfully accelerated in the cyclotron.

Table 1. Machine operation.

	Oscillator	Ion-source	Beam
Reading of time meter on Oct. 23, 1978	56752.7 (h)	60594.1 (h)	28357.1 (h)
Reading of time meter on Oct. 22, 1979	61899.6	65865.6	32873.1
Difference	5146.9	5271.5	4516.0
Percentage of 365 days	58.8 %	60.2 %	51.6 %
Schedule in this period			
Beam time		245 (day)	
Overhaul and installation work		53	
Periodical inspection and repair		29	
Vacation and holidays		38	

Table 2. Scheduled beam time and subjects of activity in the period XIV.

Subject		Heavy ion	Light particles	Total
Nucl. Phys.	Nuclear reaction	2778 (h)	30 (h)	2808 (h)
	In-beam spectroscopy	351	0	351
	RI production	0	72	72
Fields others than Nucl. Phys.	Nuclear chemistry	25	285	310
	Radiation chemistry	356	0	356
	Radiation biology	156	176	332
	Solid state physics	0	685	685
	Inner atomic shell excitation study	498	127	625
Outside users	Track measurement	24	0	24
	Nuclear fuel study	0	126	126
	RI production	0	31	31
Total		4188	1532	5720
Percent in total		73.2 %	26.8 %	100 %
-----				
Maintenance, operation and engineering				
	Exchange of ion source		97 (h)	
	Machine inspection and repair		696	
	Total		793	

Table 3. Distribution of beam time among particles accelerated.

Particle	(h)	(%)
P	725	12.7
d	0	0
$^3\text{He}^{++}$	161	2.8
$^4\text{He}^{++}$	646	11.3
$\text{C}^{4+}$	497	8.7
$\text{N}^{4+}$	2133	37.3
$\text{N}^{5+}$	1159	20.3
$\text{O}^{5+}$	117	2.0
$^{20}\text{Ne}^{6+}$	282	4.9
Total	5720	100.0

### 3. MACHINE DEVELOPMENT AND ACCELERATOR PHYSICS

#### 3-1. Study of Field Correction by the Trim Coils for the SSC Magnet

H. Takebe, S. Motonaga, T. Wada,  
J. Fujita, and K. Ogiwara

Studies on magnetic field have been made for IPCR separated-sector cyclotron using about 1/4 scale model of a single sector magnet. Some experiments by the model on the characteristics of the trim coils were made to get data useful for the design of feasible trim coils to produce an isochronous magnetic field for all accelerating particles.

Proposed separated-sector cyclotron accelerates all heavy ion up to uranium. The beam energy ranges from 120 MeV/A for fully stripped ions to 15 MeV/A for very heavy ions. Acceleration of proton is also possible up to 200 MeV. The large range in energy and particles requires that the radial profile of magnetic field is adjustable to match the accelerated particles. An increase of the field from injection to extraction radius of about 22 % is needed in case of proton of 200 MeV and for very heavy ions the field profile have to rise approximately 1.5 %. The sector magnet with angular width of  $50^\circ$  has been designed to operate at maximum field strength of 17.5 kG. It is estimated that in the sector magnet 30 pairs or more of trim coils will be mounted which are of varying width to achieve the isochronous field for all particles.

The design of the trim coils was started recollecting the calculation on the circular trim coils mounted on the magnet pole faces of the cyclotron.<sup>1)</sup>

First experiment was done with seven pairs of coils mounted at various radial positions. The measurement

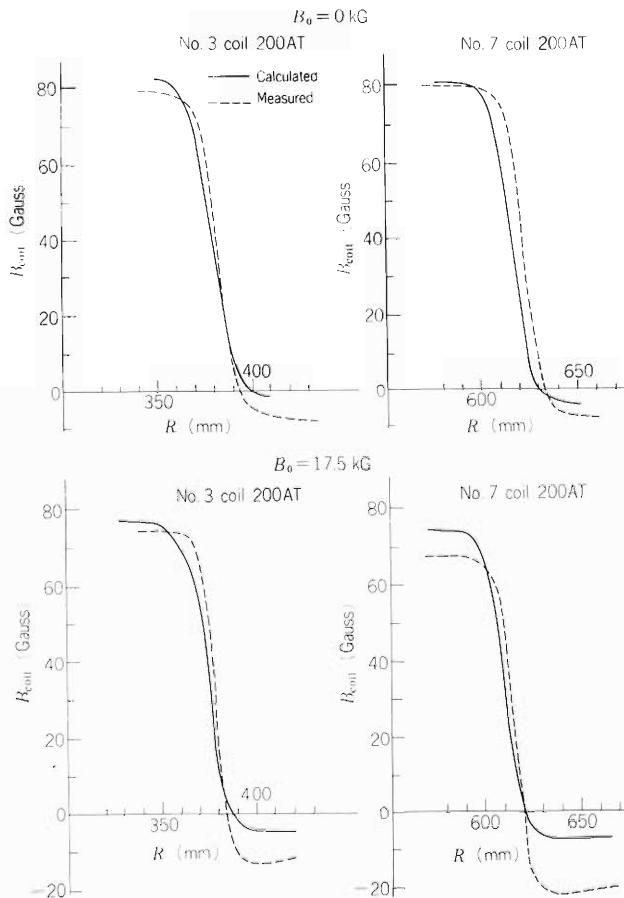


Fig. 1. Comparison between measured and calculated values of field induced by the test trim coil.

was made along the center line of the sector magnet using a Hall generator with precision of 0.05 %.

Some examples of the results for the radial field profiles are shown in Fig. 1. This figure shows comparison between the measured and calculated values. The measured value was 10 % lower than the calculated one when the main field is 17.5 kG, and decrease of field at outer radius of the coil was larger by about a factor of two than the result of the calculation. Profiles of radial distribution of the measured and calculated ones have identical slope. A desirable magnetic field gradient can be obtained by superposition of induced field which has been measured on the model.

On the basis of the procedure mentioned above, a system of the trim coils was designed and fabricated for the model magnet. A configuration of the trim coils is shown in Fig. 2. The trim coils consists of 14 pairs of copper bands which have an individual center of the curvature. There are two different coil widths, 30 mm and 15 mm. The coils #2 and #3 or #4 and #5 together may act as single trim coil each in case of field correction which require the same current in both conductors.

Then the effective width of coil in that combination is 60 mm (2 gap lengths) radially. The coils #6 – 10 have width of 30 mm (1 gap) and #11 – 14 have width of 15 mm (1/2 gap). The curved shape of every coil conforms to the equilibrium orbit shape of the hard edge calculation. Figure 3 shows the coils assembled. All of the trim coils are made to return their current around the side and outer periphery of the pole tip.

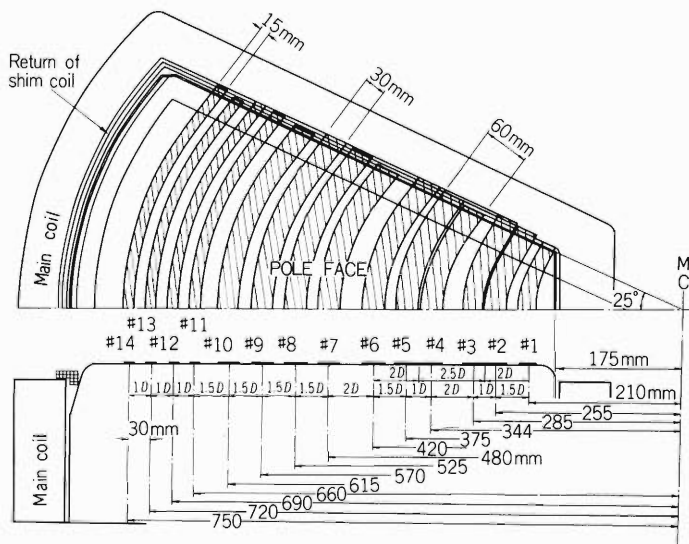


Fig. 2. Configuration of the trim coils for the model magnet.

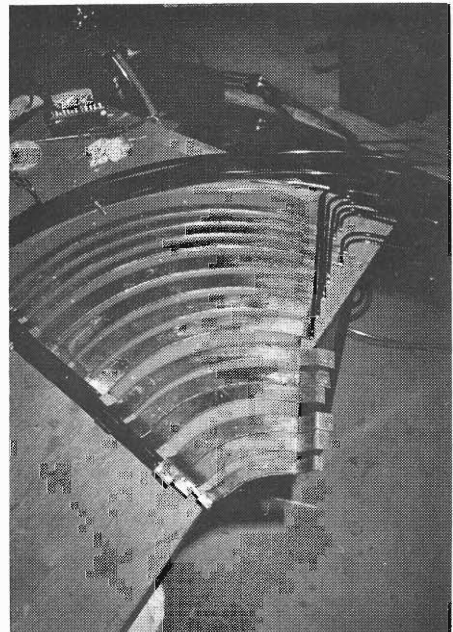


Fig. 3. A photograph of the trim coil system for 1/4 scale magnet.

Figure 4 shows an example of the radial profiles of the induced field by three trim coils at the main field of 15 kG. The increments or decrements of the induced field are proportional to exciting currents of the trim coils and smooth change of the field strength within the width of each coil is seen in this figure.

The induced field strength is affected by the strength of the main field.<sup>1), 2)</sup> Figure 5 shows the dependence on the main field of the induced field corresponding to coil current of 50 A and 100 A. The field change induced by the trim coil tends to decrease with increasing the main field. This effect is due to the change of permeability of the pole iron with field strength. If the permeability of the iron is known exactly, effect can be estimated numerically.

In order to form a desired isochronous field for the model magnet, the currents for every trim coil must be determined by iterative procedure of the superposition of those data. The measurement of the radial field distribution was made along the center line of the sector magnet.

Results of the measurement for the fields required for acceleration of  $C^{6+}$  to 45 MeV/A and  $U^{37+}$  to 8.5 MeV/A are shown in Fig. 6. Relative values were normalized to the magnetic field at injection radius. The

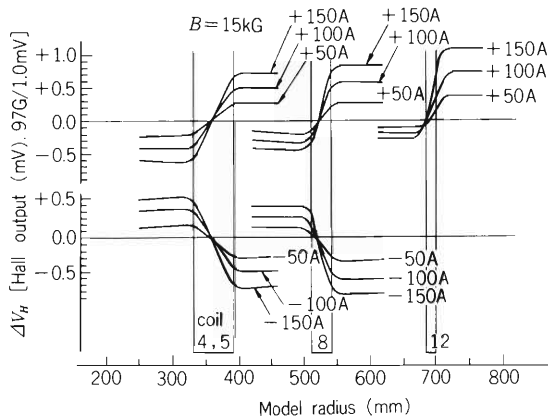


Fig. 4. Radial field profiles induced by excitation of trim coils #4 and #5 combined, #8 and #12 separately at the main field of 15 kG.

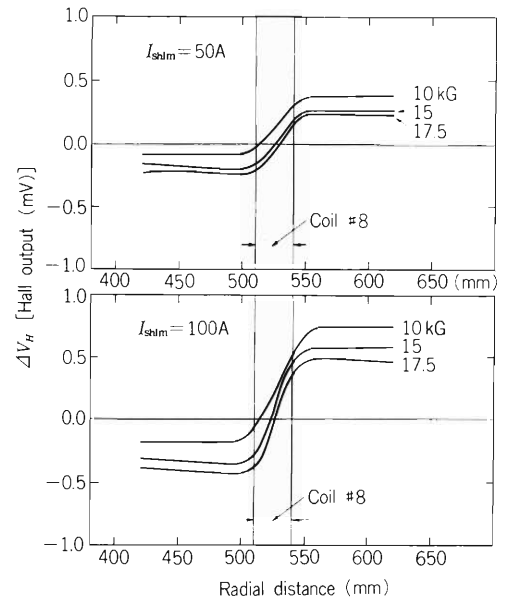


Fig. 5. Dependence on the main field of the induced field corresponding to coil currents of 50 A and 100 A.

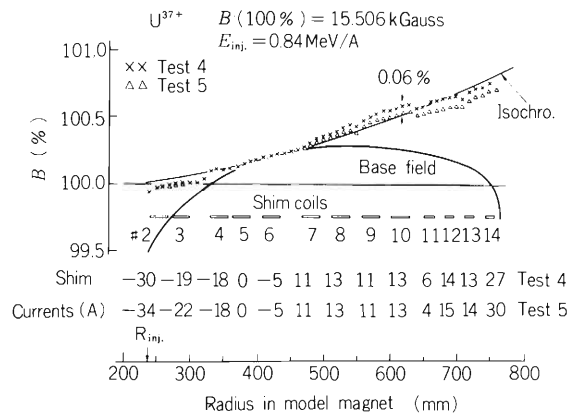
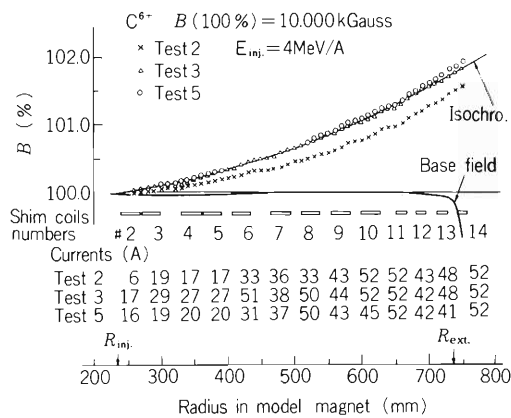


Fig. 6. Comparison of measured field distribution with the trim coils excited and isochronous field for acceleration of  $C^{6+}$  to 45 MeV/A and  $U^{37+}$  to 8.5 MeV/A.

figure shows comparison of measured field distribution with 14 trim coil pairs and calculated isochronous field (thin solid line). The distributions of the main fields of the sector magnet were also shown in the figures. Currents of the trim coils are indicated below each figure. It is observed that the maximum deviation from the isochronous field can be made as small as 0.06%. The radial distance between the coil #3 and #4 was found to be too wide for correction of the main field over 15.5 kG.

The isochronous field profiles were obtainable by this configuration of the trim coils as far as radial distributions. Measurement of azimuthal distribution is now in progress.

## References

- 1) N. Nakanishi, S. Motonaga, and T. Karasawa: Japan. J. appl. Phys., **8**, 1229 (1969).
- 2) D.L. Friesel and R.E. Pollock: IEEE Trans. Nucl. Sci., **NS-22**, 189 (1975).  
E.H. Hudson, J. A. Martin, M.L. Mallory, and F.E. McDaniel: Proc. 7th Int. Conf. on Cyclotron, p. 201 (1975).

### 3-2. Design of Injection System for Separated-Sector Cyclotron

Y. Yano, T. Wada, S. Motonaga, and H. Kamitsubo

The injection system for the separated sector cyclotron (SSC) planned<sup>1)</sup> at IPCR has been designed as shown in Fig. 1. A transported beam from a variable frequency linac<sup>2)</sup> and an AVF cyclotron, which is injected to the central region of the SSC through one of the valleys, is guided onto the first equilibrium orbit by means of three types of inflecting elements, i.e., bending magnets (BM1, BM2, BM3), magnetic inflection channel (MIC) and electrostatic inflection channel (EIC). The main characteristics of the injection elements are given in Table 1. A considerable effort is devoted to the feasible design of these elements since they must be capable of bending particles with large magnetic rigidity up to about 800 kG-cm and be located in the limited available space of the SSC central region.

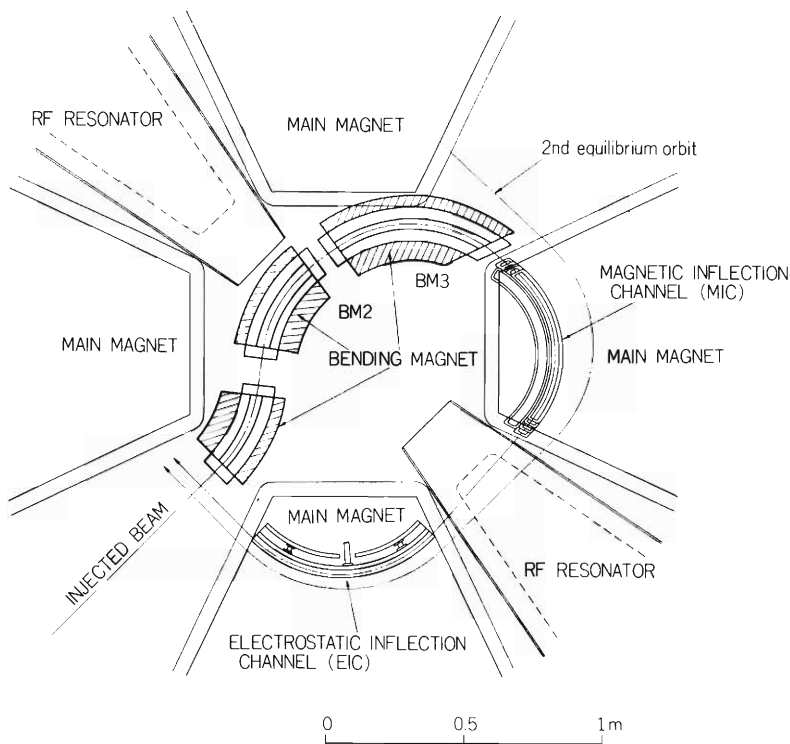


Fig. 1. Layout of injection elements in the central region of SSC.

The bending magnets, as illustrated in Fig. 2, are of a modified window frame design with a pure iron yoke. A magnet of this type is just like a hybrid between an H-shaped magnet and a window frame one. It can generate uniform magnetic field over a whole region of the aperture. The magnetic field distributions have been calculated by using a computer code TRIM<sup>3)</sup> and ascertained to have the homogeneity of more than 99.95 % over the beam range in the gap. The leakage flux outside the side yokes is evaluated to be less than 2 G. To produce a magnetic flux density of 18 kG in the air gap, current densities up to 53 A/mm<sup>2</sup> are required in 9 mm × 9 mm copper hollow conductors with a 6 mm $\phi$  cooling water duct. Cooling calculations show that the conductor temperature can be limited to 60 °C by adopting independent cooling for 6 pancakes with 4 electric turns, with maximum water velocities up to 5.53 m/sec and a pressure drop of

Table 1. Characteristics of injection elements.

## Bending magnets

Element	Angle of bend (deg)	Radius (cm)	Maximum magnetic field (kG)
BM1	37°	46	18
BM2	45.2°	46	18
BM3	75°	46	18

## Inflection channels

Element	Angle of bend (deg)	Length (cm)	Radius (cm)	Main magnetic field (kG)	Maximum added field dB (kG)	dE (kV/cm)
MIC	93.5°	65.3	40	16.8	+2.6 (in case of $^{238}\text{U}^{40+}$ , 0.81 MeV/u)	
EIC	93.3°	71.6	44	14.8		+22 (in case of $^{12}\text{C}^{6+}$ , 5.6 MeV/u)

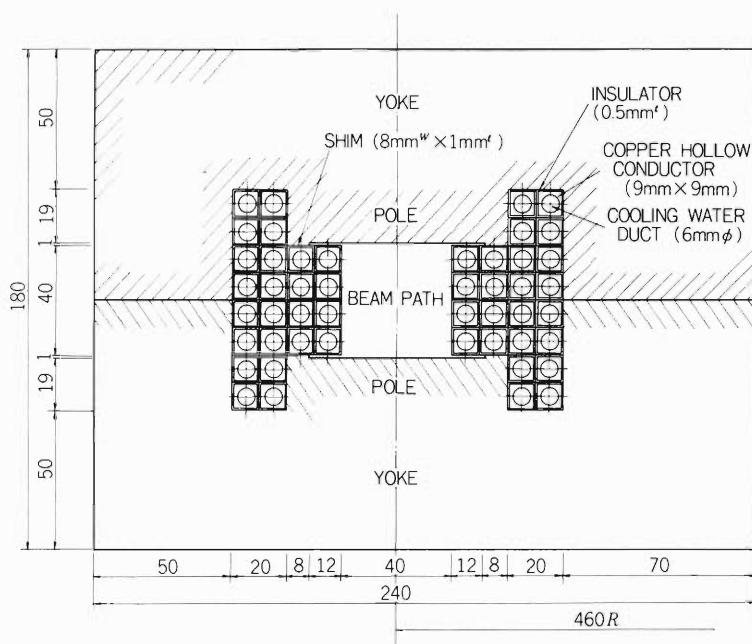


Fig. 2. Cross-Section of bending magnet.

4.4 kg/cm<sup>2</sup> for a cooling water temperature difference of 30 °C between at the inlet and outlet ends of the cooling circuits. A model of the magnet will be built at the end of 1979.

The magnetic inflection channel is composed of two coils as shown in Fig. 3. One is used to accomplish the adequate field rise (channel coil) and the other to compensate for an undershoot which is described below (compensation coil). The superposition of the sector field with the channel coil field gives rise to the undershoot of the sector field outside the coil. The field produced by the compensation coil whose current direction is opposite to that of the channel coil brings about the overshoot and is able to cancel the undershoot in the accelerating area. This

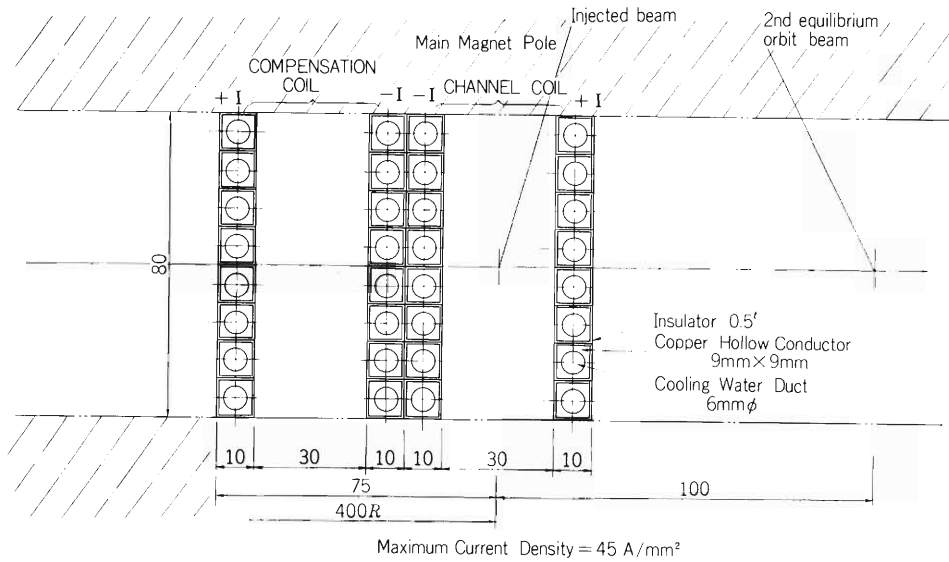


Fig. 3. Cross-Section of magnetic inflection channel.

fact has been verified in the calculations by TRIM.

The electrostatic inflection channel is illustrated in Fig. 4. Shapes of the anode and the cathode have been designed to produce sufficiently homogenous electric field ( $> 99.9\%$ ) in the volume occupied by the beam. This was done using a trial-error method with the aid of a computer program solving the Laplace equation (VEPO 2).<sup>4)</sup> The maximum E.V value is about  $7000 \text{ kV}^2/\text{cm}$ .

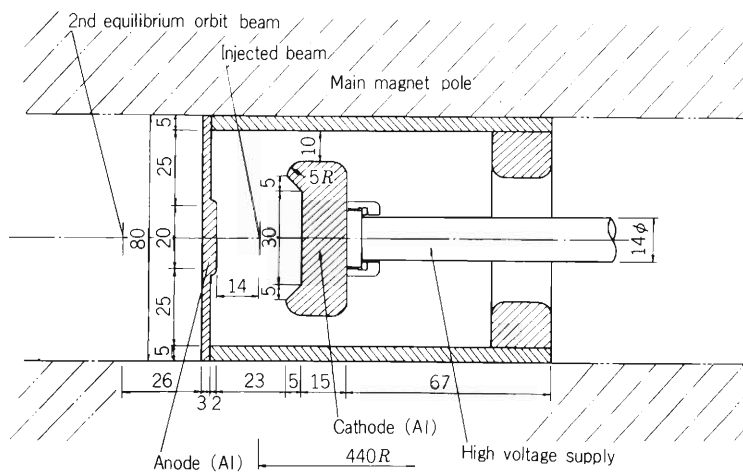


Fig. 4. Cross-Section of electrostatic inflection channel.

## References

- 1) H. Kamitsubo et al.: IPCR Internal Report SSC-1; Presented at the 2nd Symposium on Accelerator Science and Technology, at INS, Tokyo, March (1978).
- 2) M. Odera: Proc. of the 1976 Proton Linear Accelerator Conf.; M. Tonuma, F. Yoshida, and M. Odera: IEEE Trans. Nucl. Sci., NS-23, 1031 (1976).
- 3) J.S. Colonias and J. H. Porst: Magnet Design Applications of the Magnetostatic Program Called TRIM, UCRL-16382 (1965).
- 4) H. N. Jungwirth: Private communication.

### 3-3. Design of RF Resonator for Proposed Separated-Sector Cyclotron

K. Ogiwara, F. Yoshida, H. Takebe,  
and T. Fujisawa

Possibility of use of a quarter-wave structure in stead of the half-wave one of previous design<sup>1)</sup> was investigated this year. The new resonator is shown in Fig. 1. This system was designed to facilitate design and installation of the vacuum chamber and the magnetic inflection system of SSC. The length of this RF resonator is about 4 m. The delta shaped dee is attached to the triangle stem. The height of the dee is 20 cm and the aperture is 6 cm. The resonant frequency is changed by a travelling shorting plate as in the former design. The coaxial length, the Q value and the maximum current density at shorting end vs resonant frequency are calculated and shown in Fig. 2 (a). The distribution of RF voltage and current are calculated along the dee

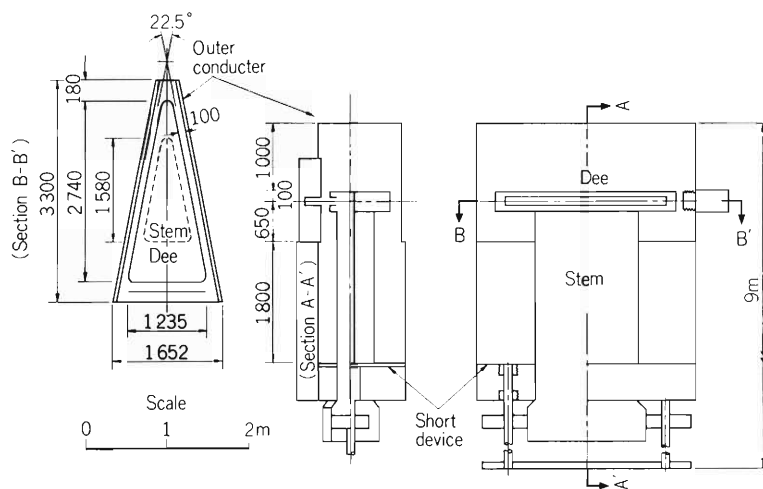


Fig. 1. Cross-sectional top and side view of the new resonator for proposed SSC.

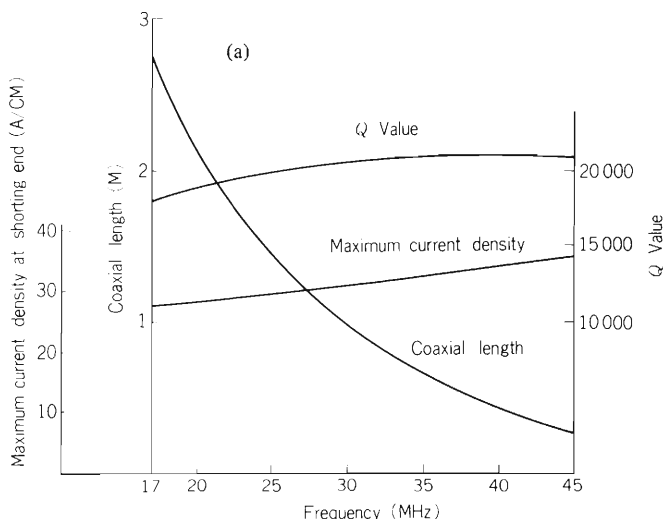


Fig. 2(a). The calculated RF-characteristics of the new resonator.

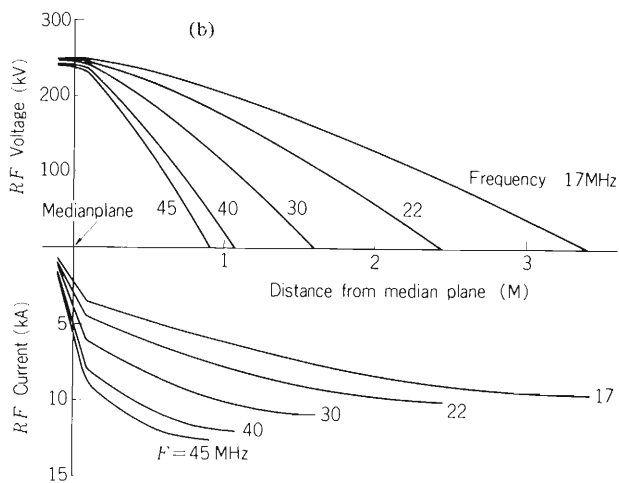


Fig. 2(b). The calculated distribution of RF voltage and current in the new resonator along the stem.

stem from the dee top to shorting end resulting in the curve shown Fig. 2 (b). A half-scale model cavity for this design was constructed to investigate these RF characteristics. Measurement of the RF characteristics of this model cavity is now in progress. Effect on the beam dynamics of possible asymmetry of the accelerating field with respect of the median plane of the dee of this structure is also being studied by calculation.

#### Reference

- 1) H. Nakajima, K. Ogiwara, F. Yoshida, and J. Fujita: IPCR Cyclotron Progr. Rep., 12, 16 (1978).

### 3-4. Computer Code for the Accelerated Orbit in a Separated-Sector Cyclotron

N. Nakanishi and S. Motonaga

A computer code EO for the equilibrium orbit in a separated sector cyclotron has been developed and calculations have been done on various particles at the different initial conditions using the magnetic field of a model magnet.<sup>1)</sup> The content of the code was described briefly elsewhere.<sup>2)</sup> Now, a code for the accelerated orbit has been developed extracting some subprograms from the code EO and adding new ones.

The program is composed of several parts which read input data, calculate some basic constants, set up differential equations to be solved, and execute the integration. For the purpose of obtaining the phase-plot information, the equilibrium orbits can also be calculated at various energies by this code.

Numerical integration is carried out on 14 equations which describe variation of positions and radial momenta of the reference beam and of the slightly radially and axially disturbed beams, giving variations of time, mass, azimuthal angle and so on. Some typical equations solved are as follows:

$$\begin{aligned}
 r' &= r \frac{P_r}{Q} \\
 P_r' &= Q - rB + \frac{mrE_r}{Q} \\
 m' &= r E_\theta + r \frac{P_r}{Q} E_r \\
 x' &= \frac{P_r}{Q} x + \frac{rP^2}{Q^3} P_x \\
 P_x' &= - \left( \frac{\partial(rB)}{\partial r} - \frac{mE_r}{Q} \right) x - \frac{P_r}{Q} \left( 1 - \frac{mrE_r}{Q^2} \right) P_x \\
 z' &= \frac{r}{Q} P_z \\
 P_z' &= \left( r \frac{\partial B}{\partial r} - \frac{P_r}{Q} \frac{\partial B}{\partial \theta} \right) z \\
 Q &= (P^2 - P_r^2)^{\frac{1}{2}}
 \end{aligned}$$

where prime means  $d/d\theta$ . Symbols  $r$ ,  $P_r$ ,  $m$ , and  $P$  represent radius and radial momentum of the reference beam, mass and momentum of the particle, respectively. Variables  $x(z)$  and  $P_x(P_z)$  are radial(axial) displacement and radial(axial) momentum deviation from the reference beam.  $E_r$  and  $E_\theta$  are radial and azimuthal components of the accelerating electric field, respectively. The axial component  $E_z$  of the field is neglected at present. In this code cyclotron units are adopted.

Informations have to be prepared on the isochronous field, geometrical shape of dee structure, and radial- and frequency- dependence of accelerating voltage in advance of use of the code. As the measured isochronous field is not available at present, the calculated ones are employed. As described in Ref. 3, the accelerating gap is designed to be constant, and the edge is straight in the radial direction. Parameters which specify the geometrical shape are shown in Fig. 1. Radial- and frequency- dependence of the accelerating voltage were measured using a model cavity.<sup>3)</sup> The radial distribution of voltage is expanded in a polynomial expression at each RF-frequency, and then the corresponding coefficients of each term are expressed by the polynomials of frequency.

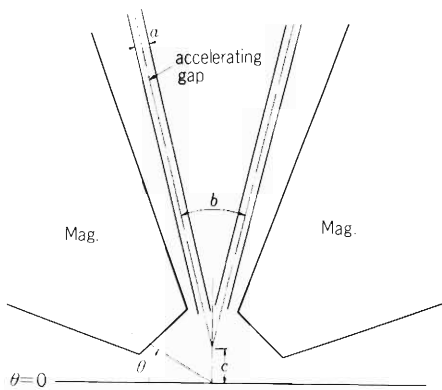


Fig. 1. Geometrical parameters  $a$ ,  $b$ , and  $c$  specifying the dee structure.

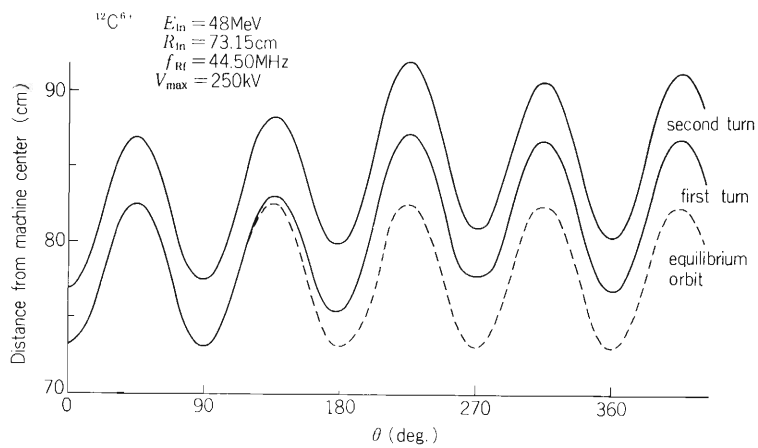


Fig. 2. Equilibrium (not-accelerated) and accelerated orbits in the first two turns.

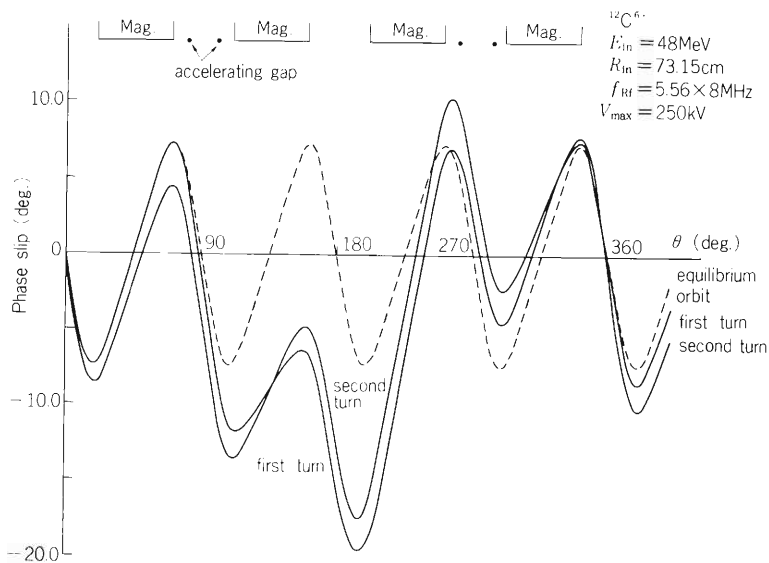


Fig. 3. Phase slip of a particle against the accelerating radio-frequency. Positions of sector magnets and accelerating gaps are also shown in the figure.

Some preliminary results are given below for  $^{12}\text{C}^{6+}$  injected at the radius of 73.15 cm at the energy of 4 MeV/A. Figure 2 shows the equilibrium orbit and the accelerated trajectories in the first few turns. Phase slip of a rotating particle against radio-frequency is shown for the first few turns in Fig. 3. Peak of the accelerating voltage is set coincident at the starting angle ( $\theta = 0$ ) of the particle. Behavior of the particle displaced from the reference orbit in phase space is shown in Fig. 4 for the first few turns in both of the cases with and without acceleration. The phase plot is often used to investigate the limits of radial stability of a particle. For a particle specified by some initial conditions for energy, radius and radial momentum, its motion is described over many revolutions by plotting the radius and radial momentum at a certain azimuthal angle. Figure 5 shows the phase plot for the 211 MeV  $^{12}\text{C}^{6+}$  ion.

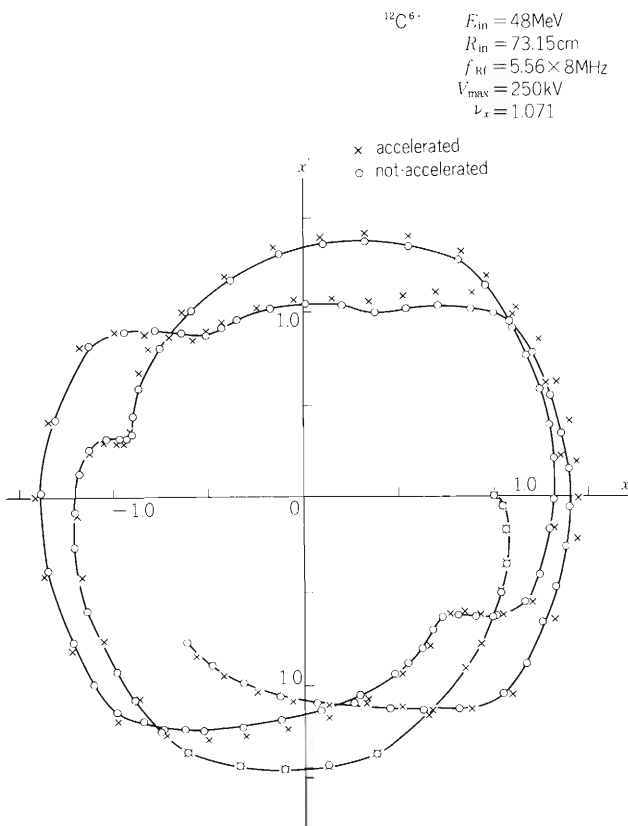


Fig. 4. Behavior of a disturbed particle in phase space. Closed circles show the starting points of each revolution.

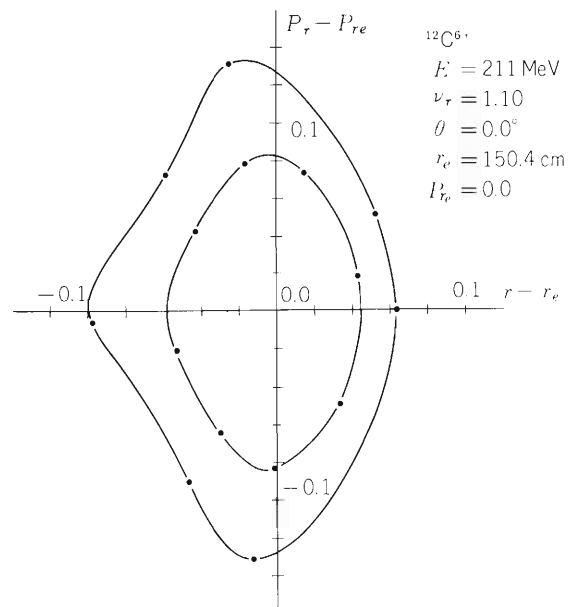


Fig. 5. Radial phase plot for  $^{12}\text{C}^{6+}$  at  $\theta = 0$  and  $E = 211\text{MeV}$ . Symbols  $r_e$  and  $P_{r_e}$  are the radius and radial momentum of the equilibrium orbit, respectively at  $\theta = 0$ . Two curves are different in the initial conditions. The outer one represents the limit of radial stability.

## References

- 1) M.M. Gordon, T.A. Welton, T.I. Arnette, and H.C. Owens: ORNL 59-11-2.
- 2) N. Nakanishi and S. Motonaga: IPCR Cyclotron Progr. Rep., 12, 18 (1978).
- 3) H. Nakajima, K. Ogiwara, F. Yoshida, and J. Fujita: *ibid.*, p. 16.

## 3-5. Improvement of the Heavy Ion Source

K. Ikegami and I. Kohno

At present, the heavy ion source used for the cyclotron is of the electron bombarded hot cathode PIG type and is operated in both DC mode<sup>1)</sup> and pulsed mode.<sup>2)</sup>

It is known that performance of a heavy ion source is generally evaluated by the capacity to produce higher charged ions, high intensity current of these ions and life time of the source under such working conditions. In order to obtain large quantities of multiply charged ions with this type of PIG source, following two conditions are prerequisite:

- an arc power as high as possible,
- a gas flow as small as possible.

The life time of the PIG source is limited by erosion of the upper cathode of the source. Erosion of the cathode is caused by the sputtering of the cathode material with bombardment by the ions. Therefore, the life time of the source decreases when the high arc power is applied to the source.

We have tried to lengthen the life time and increase the intensity of multiply charged ions by selecting material of the cathode and changing the geometries around the cathode, i.e., its heat shield and its holder. Until now tungsten (W) has been used for the upper cathode. In this report, test of the cathodes made of Hf and Ta is described. In the case of Hf cathode, it melted when the arc power of 1.5 kW was applied to the source, and this value of the arc power is insufficient to produce large quantity of the multiply charged ions such as  $N^{4+}$ ,  $C^{4+}$ , and  $O^{5+}$ . The Ta cathode was better for production of the multiply charged ions and permitted to lengthen the life time than the W cathode. However, in the case of Ta, arc discharge became unstable frequently at the beginning when the arc discharge is ignited. In order to avoid such an instability, we changed the geometries of the cathode as shown in Fig. 1. Using the improved Ta cathode we could obtain the life time of about 35 h with the intensity of  $N^{5+}$  ions sufficient to do experiments. Such efforts to improve the heavy ion source will be continued to carry out the experiments more effectively by the cyclotron.

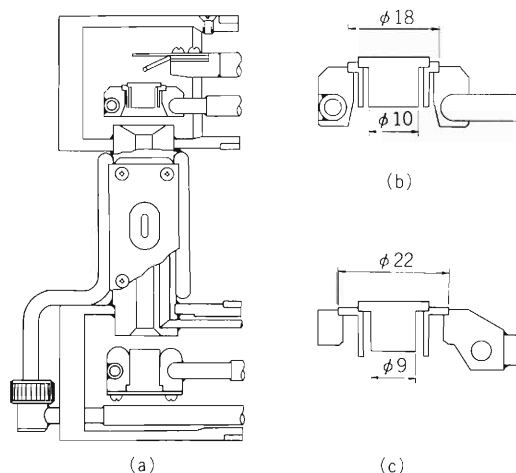


Fig. 1. (a): A cross sectional view of the heavy ion source, (b) and (c): old and new upper cathode, heat shield and cathode mount.

## References

- 1) Y. Miyazawa, I. Kohno, T. Inoue, T. Tonuma, A. Shimamura, and S. Nakajima: IEEE Trans. Nucl. Sci., NS-19, 105 (1972).
- 2) H. Nakajima, S. Kohara, T. Kageyama, and I. Kohno: Reports IPCR (in Japanese), 53, 132 (1977).

### 3-6. Metal Ion Source for the Cyclotron and Acceleration of Metal Ions

K. Ikegami, T. Kageyama, and I. Kohno

A metal ion source for the cyclotron has been developed to accelerate metal ions in the cyclotron. The structure and function of this source were already described before.<sup>1)</sup> In this report we describe production and acceleration of several metal ions ( $\text{Li}^{2+}$ ,  $\text{Be}^{3+}$ , and  $\text{B}^{3+}$ ) in the cyclotron.

As the materials to charge, single crystal of  $\text{LiF}$ , single crystal of  $\text{B}_2\text{O}_3$ , boron nitride and metallic  $\text{Be}$  were used for  $\text{Li}$ ,  $\text{B}$ , and  $\text{Be}$  ions, respectively. In the case of insulator such as  $\text{LiF}$ ,  $\text{B}_2\text{O}_3$  and boron nitride a copper rod 1.2 mm in diameter was buried in the insulator which made contact with the water-cooled supporting metal of the sputtering electrode.

The ion source is burnt with  $\text{Ar}$  gas at first. When a negative voltage with respect to the anode is applied to the sputtering electrode, the electrode material is sputtered by bombardment with  $\text{Ar}$  ions in the arc plasma and the sputtered atoms are ionized in the plasma.

Figure 1 shows variations of the sputtering current and the current intensity of  ${}^7\text{Li}^{2+}$  extracted from the cyclotron versus the sputtering voltage under a constant arc power. At the same sputtering voltage the sputtering current increases with the increase of the arc power applied to the ion source. It is clearly observed that the current intensity of  ${}^7\text{Li}^{2+}$  extracted from the cyclotron increases linearly with the increase of the applied sputtering voltage. Figures 2 and 3 show current intensities of  ${}^6\text{Li}^{2+}$  and  ${}^7\text{Li}^{2+}$ , and  $\text{Be}^{3+}$  extracted from the cyclotron versus the arc power applied to the source, respectively. The intensities of multiply-charged metal ions such as  $\text{Li}^{2+}$  and  $\text{Be}^{3+}$  increase greatly with the increase of the arc power. In the case of  $\text{Li}^{2+}$  ions, sufficient current was extracted from the cyclotron when the source was operated at the arc power of about 1.2 kW and the sputtering voltage of 200 V. The life time of the source was about 12 h under such condition.

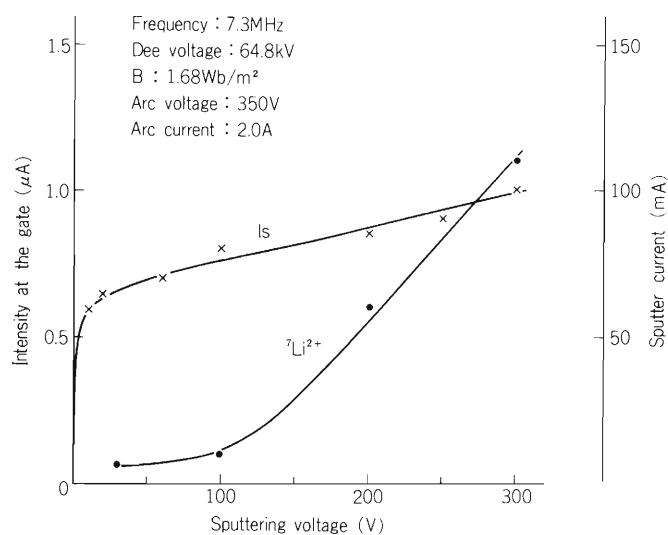


Fig. 1. The variations of sputtering current ( $I_s$ ) and the current intensity of  ${}^7\text{Li}^{2+}$  extracted from the cyclotron vs. the sputtering voltage under a constant arc power.

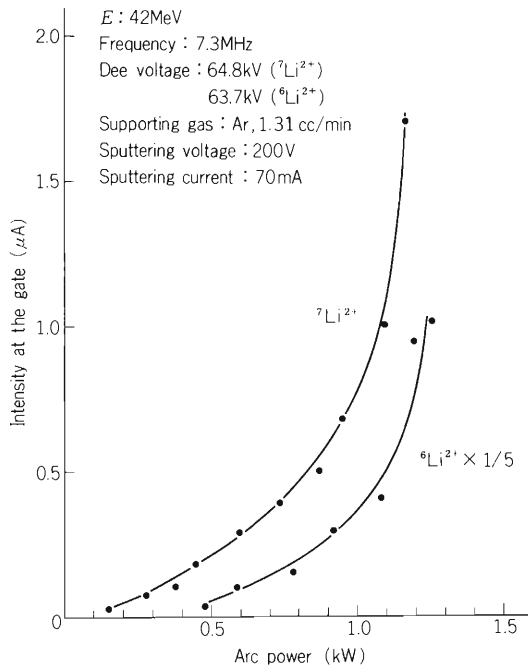


Fig. 2. The current intensities of  ${}^6\text{Li}^{2+}$  and  ${}^7\text{Li}^{2+}$  extracted from the cyclotron vs. the arc power under a constant sputtering voltage.

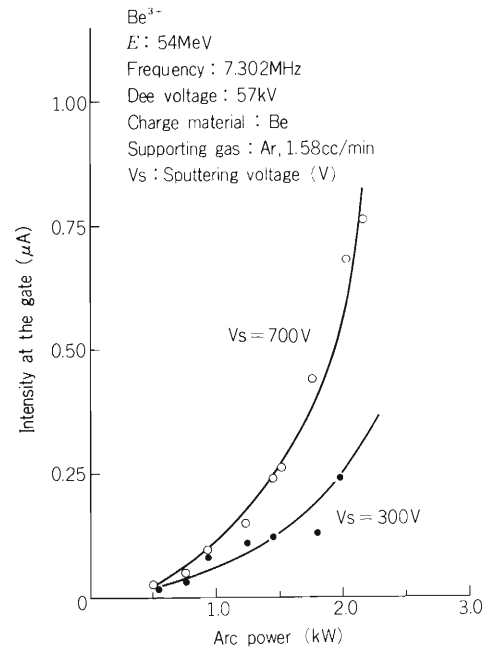


Fig. 3. The current intensities of  $\text{Be}^{3+}$  extracted from the cyclotron vs. the arc power at the sputtering voltage of 300 V and 700 V.

Table 1. Current intensities of several ions extracted from the cyclotron with the metal source.

Particle	Energy (MeV)	Arc power voltage (V)	Current (A)	Sputtering voltage (V)	Charge material	Intensity at the gate ( $\mu\text{A}$ )
${}^7\text{Li}^{2+}$	29 – 48	320	3.7	200	Lif	1.5 – 2.0
${}^7\text{Li}^{3+}$	29 – 75	340	5.5	50	Lif	30 – 50 nA
${}^6\text{Li}^{2+}$	25 – 48	280	4.5	200	LiF	100 – 200 nA
$\text{Be}^{3+}$	45	470	4.6	700	Be	0.7 – 0.8
${}^{11}\text{B}^{3+}$	66	400	4.5	0	$\text{B}_2\text{O}_3$	1.2 – 1.3
${}^{10}\text{B}^{3+}$	60	400	4.5	0	$\text{B}_2\text{O}_3$	250 – 300 nA
${}^{11}\text{B}^{4+}$	66	400	4.5	0	$\text{B}_2\text{O}_3$	3 nA
$\text{O}^{5+}$	96	400	4.5	0	$\text{B}_2\text{O}_3$	6 nA
${}^{11}\text{B}^{3+}$	66	400	5.0	900	BN	100 nA

Supporting gas: Ar, gas flow: 1.31 – 1.60 cc/min

Table 1 shows the results obtained from the test of this ion source to produce multiply charged metal ions and acceleration of metal ions in the cyclotron. In the case of  $B^{3+}$  ions it was more effective to use an ion source employing gaseous  $BCl_3$ <sup>2)</sup> in producing ions compared with the sputtering method described here.

#### References

- 1) K. Ikegami and I. Kohno: IPCR Cyclotron Progr. Rep., 12, 24 (1978).
- 2) A. Shimamura and I. Kohno: *ibid.*, 8, 4 (1974).

## 3-7. Present States of the Baby Cyclotron

T. Karasawa and T. Nozaki

## 1) Prototype

A prototype of the Baby Cyclotron was installed at the National Nakano Chest Hospital. A cyclotron building was completed in April 1979. It has a floor space of 150 m<sup>2</sup> in all and the cyclotron room is of a cubic shape with 4.5 m dimension. The thickness of shielding wall of the cyclotron room is 1 m or 0.6 m.

Since May, the cyclotron has been routinely operated and beam diagnosis has been studied using half of the machine time to improve beam extraction efficiency and to increase bombarding current.

A small magnetic channel was inserted between the deflector and the beam extraction window. It was composed of three ferrocobalt octagonal bars of 80 mm length and 10 mm diameter.

At present, internal beam current is about 50  $\mu$ A and extraction efficiency is from 10 to 30 %.

The other half of the machine time has been devoted to isotope production. The generation kits for <sup>11</sup>CO<sub>2</sub> and <sup>11</sup>CO,<sup>1)</sup> which work satisfactorily, were already attached to the cyclotron at the time of its installation. An aqueous solution of <sup>13</sup>NH<sub>3</sub> was found to be obtained easily and efficiently by the microwave heating of the proton-bombarded water added with TiCl<sub>3</sub> and NaOH. H<sub>2</sub><sup>15</sup>O was produced by the usual method.<sup>1)</sup> Some <sup>11</sup>C-labelled organic compounds such as glucose, fructose (by photosynthesis) and palmitic acid have been prepared. Also, <sup>13</sup>N-labelled glutamic acid has been obtained.

In near future, the production systems for the following radioisotopes will be completed: <sup>13</sup>N<sub>2</sub> (both gas and aqueous solution), <sup>15</sup>O<sub>2</sub>(in N<sub>2</sub>), <sup>18</sup>F(carrier-free aqueous solution), <sup>79</sup>Kr(by the <sup>79</sup>Br(p, n) <sup>79</sup>Kr reaction) and radio-bromines. In the <sup>18</sup>F production, enriched H<sub>2</sub><sup>18</sup>O will be bombarded by protons. Also, the following labelled compounds will be synthesized: some <sup>11</sup>C amino acids, <sup>11</sup>C-deoxyglucose, <sup>11</sup>C-mannose, <sup>18</sup>F- or radiobromine-steroids and some other <sup>18</sup>F-compounds.

## 2) The second baby cyclotron

In 1977, the second baby cyclotron, by which 6 MeV deuteron and 10 MeV proton can be accelerated, has been designed and manufactured. In mid course of magnetic field mapping, the design was modified to increase the energy of deuteron up to 7 MeV for higher yield of <sup>18</sup>F by <sup>20</sup>Ne(d,  $\alpha$ )<sup>18</sup>F reaction. We improved the shape of the pole tip sector pieces which generate the hill magnetic field of 2.3 Tesla and mounted a pair of circular trimming coil on the pole surface. Then, we have achieved the isochronous field for 7 MeV deuteron and 10 MeV proton at mean magnetic field 1.8 Tesla and 1.5 Tesla, respectively.

At the Muroran Plant of the Japan Steel Works, beam test have been continued and the cyclotron will be exported to Canada early 1980.

## Reference

- 1) J.C. Clark and P.D. Buckingham: Short-lived Radioactive Gases For Clinical Use, Butterworths & Co, Ltd. London and Boston (1975).

## 4. NUCLEAR PHYSICS

### Scattering and Reactions

#### 4-1. Adiabatic Treatment of Deuteron Breakup on a Nucleus

H. Amakawa and K. Yazaki\*

The breakup process of the high energy deuteron is investigated within the framework of a three-body model. In the three-body model, a deuteron-nucleus scattering system is assumed to consist of a proton, a neutron and an inert target nucleus. We use the adiabatic approximation which consists of neglecting the excitation energy of the p-n relative motion. This approximation has been used to include the breakup effect in the elastic deuteron scattering.<sup>1)</sup> If the adiabatic approximation is used, the Schrödinger equation for this scattering system is reduced to

$$(T_R + V(\vec{r}, \vec{R}) + \epsilon_d - E) \Psi(\vec{r}, \vec{R}) = 0, \quad (1)$$

where  $\vec{r}$  and  $\vec{R}$  are the relative and the center of mass coordinates of the p-n pair with respect to the target,  $\epsilon_d$  is the deuteron binding energy,  $T_R$  is the kinetic energy operator of the center of mass motion and  $V(\vec{r}, \vec{R})$  is given by the sum of the p-target and the n-target potentials. The three-body wave function  $\Psi(\vec{r}, \vec{R})$  is expressed as

$$\Psi(\vec{r}, \vec{R}) = \sum_{\ell, L, J} \chi_{\ell L J}(\vec{r}, \vec{R}) [Y_\ell(\hat{r}), Y_L(\hat{R})]_J. \quad (2)$$

We solve the coupled equation for  $\chi_{\ell L J}(r, R)$  with fixed  $r$  and  $J$ , and obtain the  $r$ -dependent t-matrix  $T_{\ell' L'; \ell L}^J(r)$ . The elastic cross section is given by<sup>1)-3)</sup>

$$\sigma_{e\ell} = \sum_L \sigma_{e\ell}(L) \quad \text{and}$$

$$\sigma_{e\ell}(L) = \frac{4\pi}{k^2} (2L+1) |\langle \phi_d | T_{\ell L; \ell L}^L(r) | \phi_d \rangle|^2, \quad (3)$$

where  $\phi_d$  is the deuteron wave function and  $k$  is the wave number of the center of mass motion. The breakup cross section is defined by

$$\sigma_b = \sum_L \sigma_b(L) \quad \text{and}$$

$$\sigma_b(L) = \frac{4\pi}{k^2} \sum_{\ell'} \sum_{\epsilon} (2L+1) |\langle \phi_{e, \epsilon} | T_{\ell' L; \ell L}^L(r) | \phi_d \rangle|^2, \quad (4)$$

\* Department of Physics, University of Tokyo.

where  $\phi_{\ell,\varepsilon}$  is the wave function of the p-n relative motion with angular momentum  $\ell$  and energy  $\varepsilon$ . The integration over  $\varepsilon$  can be performed to give.

$$\sigma_b(L) = \frac{4\pi}{k^2} \sum_{\ell'} (2L+1) \langle \phi_d | |T_{\ell'L':\ell L}^L(r)|^2 | \phi_d \rangle - \sigma_{e\ell}(L). \quad (5)$$

We can easily calculate the breakup cross section  $\sigma_b$ .

The breakup cross sections of the deuteron scattered from a  $^{58}\text{Ni}$  target are calculated at  $E_{\text{lab}} = 80$  MeV. The parameters of the nucleon- $^{58}\text{Ni}$  optical potential are taken from Ref. 4 and evaluated at half the incident energy of the deuteron. The coupled equation is solved with the s-wave ( $\ell = 0$ ) and d-wave ( $\ell = 2$ ) breakup channels. The coupled-channel program CCSEARCH<sup>5</sup> is used with a minor modification. The t-matrix  $T_{\ell'L':\ell L}^J(r)$  is a rather smooth function of the p-n relative distance  $r$ . The integrations over  $r$  in Eqns. (3) and (5) are carried out with a 0.4 fm interval up to  $r = 24$  fm.

The various cross sections are listed in Table 1. The Watanabe potential<sup>6</sup> (folding potential) which does not contain the breakup effect gives the largest elastic cross section. Adding the breakup channels reduces the elastic cross section, bringing it towards the value obtained by the phenomenological optical potential (série 1 of Ref. 7) which reproduces the experimental elastic cross section very nicely. The d-wave breakup cross section is about two times larger than the s-wave breakup cross section. The importance of the d-wave breakup is also seen by comparing the results with and without its effect. The breakup cross section is about 9 % of the reaction cross section.

Table 1. Various cross sections of d- $^{58}\text{Ni}$  scattering at  $E_{\text{lab}} = 80$  MeV in units of mb.  $\sigma_{e\ell}$ ,  $\sigma_r$ ,  $\sigma_{\text{tot}}$ , and  $\sigma_b$  represent the elastic, reaction, total and breakup cross sections, respectively.  $\sigma_{b,s}$  and  $\sigma_{b,d}$  are, respectively, the s-wave and d-wave breakup cross sections.

	$\sigma_{e\ell}$	$\sigma_r$	$\sigma_{\text{tot}}$	$\sigma_{b,s}$	$\sigma_{b,d}$	$\sigma_b$
Watanabe	1573.5	1437.3	3010.8	—	—	—
Adiabatic s	1510.8	1515.8	3026.6	93.0	—	93.0
Adiabatic s+d	1351.6	1533.0	2884.6	45.9	97.5	143.4
Phenom. Pot. <sup>a)</sup>	1313.8	1601.7	2915.5	—	—	—

a) série 1 of Ref. 7.

Figure 1 shows the various partial-wave cross sections of the deuteron- $^{58}\text{Ni}$  scattering as a function of the angular momentum  $L$ . The reaction cross section  $\sigma_r(L)$  is a smooth function of  $L$ , while the elastic cross section  $\sigma_{e\ell}(L)$  has some fluctuations reflecting the effect of the real potential. The breakup cross section is small for the internal partial waves ( $L \lesssim 12$ ) but becomes appreciable in the surface region ( $L \sim 16$ ), giving about one third of the reaction cross section for  $L \sim 20$ . The s-wave breakup cross section  $\sigma_{b,s}(L)$  has a dip at  $L = 12$ , which seems to be correlated with the variation of  $\sigma_{e\ell}(L)$  and is therefore ascribed to the effect of the real potential. A similar behaviour of  $\sigma_{b,s}(L)$  appeared in the coupled-channel calculation for deuteron- $^{40}\text{Ca}$  scattering at  $E_{\text{cm}} = 22.9$  MeV.<sup>3)</sup>

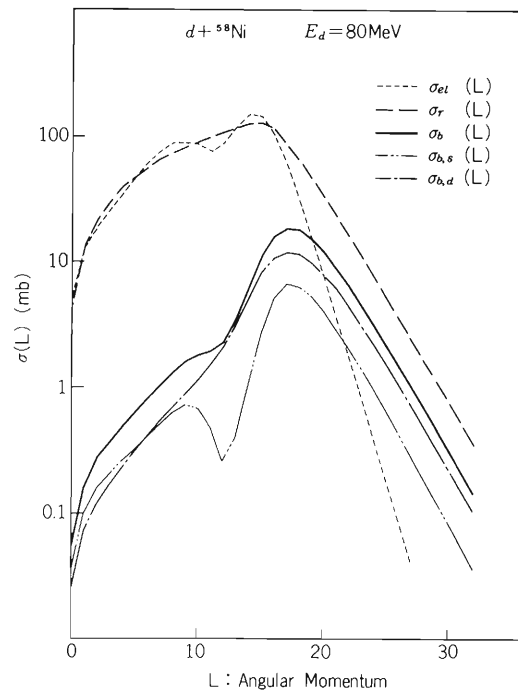


Fig. 1. Partial-wave cross sections of  $d\text{-}^{58}\text{Ni}$  scattering at  $E_{\text{lab}} = 80$  MeV as a function of the angular momentum  $L$ . Conventions used are the same as in Table 1.

## References

- 1) H. Amakawa, S. Yamaji, A. Mori, and K. Yazaki: *Phys. Lett.*, **82B**, 13 (1979).
- 2) Yu. A. Bereznoi and E. V. Inopin: *Yad. Fiz.*, **6**, 1197 (1967); [English transl. *Sov. J. Nucl. Phys.*, **6**, 872 (1968)].
- 3) N. Austern, C. M. Vincent, and J. P. Farrell Jr.: *Ann. Phys.*, (N. Y.), **114**, 93 (1978).
- 4) F. D. Becchetti, Jr. and G. W. Greenless: *Phys. Rev.*, **182**, 1190 (1969).
- 5) T. Wada and S. Yamaji: *Sci. Papers I. P. C. R.*, **68**, 65 (1974). This program is a version of JUPITOR-I written by T. Tamura modified to make an automatic parameter search.
- 6) S. Watanabe: *Nucl. Phys.*, **8**, 484 (1958).
- 7) G. Duhamel, L. Marcus, H. Langevin-Joliot, J. P. Didelez, P. Narboni, and C. Stephan: *Nucl. Phys.*, **A174**, 485 (1971).

## 4-2. Fission Fragment Angular Distributions in 15 MeV Proton-Induced Fission of $^{232}\text{Th}$

H. Kudo,\* H. Muramatsu,\* H. Nakahara,\* K. Miyano,\*\*  
I. Kohno, and M. Yanokura

Angular distributions of fission fragments were observed as a function of fragment masses in order to clarify the role of fission configurations on the mass division in fission process. It has been established that the angular distributions of the fission fragments produced from the fission of nuclei at the medium excitation energy are determined by the total angular momentum  $J$  of the compound nucleus and the  $K$  quantum number at the saddle point configuration.<sup>1)</sup> In general, a Gaussian  $K$  distribution is assumed for the fissioning compound nucleus and the average value  $K_0$  is given by the relation,  $K_0^2 = tI_{eff}/h^2$ , where  $t$  is the nuclear temperature and  $I_{eff}$  is the effective moment of inertia for the saddle point configuration. If we know the angular distributions for various specific fragment masses, we can deduce the values of  $tI_{eff}$  corresponding to each mass splitting.

According to Flynn et al.,<sup>2)</sup> who measured the 42 MeV alpha particle induced fission of  $^{209}\text{Bi}$ , the mass dependence of fission fragment anisotropy could not be observed for most of the fragment masses, although they found that the anisotropy of  $^{83}\text{Br}$  was 10 % smaller than those of other masses. This was explained by the  $N = 50$  shell effect on the saddle point configuration and by the higher excitation energy required to form the precursor of  $^{83}\text{Br}$ . Vandenbosch et al.<sup>3)</sup> reported that in the  $^{234}\text{U}(d, pf)$  reaction the mass dependence of the angular anisotropy was not observed within the experimental accuracy. Recently, Vorob'eva et al.<sup>4)</sup> reported on the 3 MeV neutron-induced fission of  $^{232}\text{Th}$ , in which they concluded that the saddle point configurations were the same for symmetric and asymmetric modes of separation. In the Flynn's system, however, the symmetric mass division might have been predominant, whereas in the Vandenbosch and Vorob'eva systems, they observed only a few symmetric events. Cohen et al.<sup>5)</sup> reported in 1955 that the angular distributions of the 22 MeV proton induced fission of  $^{232}\text{Th}$  is dependent on the fragment masses. In this system the yields of the symmetric and asymmetric mass divisions are comparable. In the so-called medium energy fission, however, there are possibilities of multiple chance fissions, and, therefore, the analysis of the data becomes more complicated.

In this work, we chose the Cohen's system, namely, the ( $^{232}\text{Th} + p$ ) reaction with the incident proton energy of 7 MeV lower than that they used. In order to better understand the degree of the contributions of multiple chance fissions, we examined in detail the excitation functions of ( $p, xn$ ) reactions and those of fission fragments. We attempted to interpret the observed data in terms of the two-mode hypothesis, and for this purpose, we modified the Alice code<sup>6)</sup> to include the symmetric and asymmetric fission barriers and the sub-barrier penetration terms.

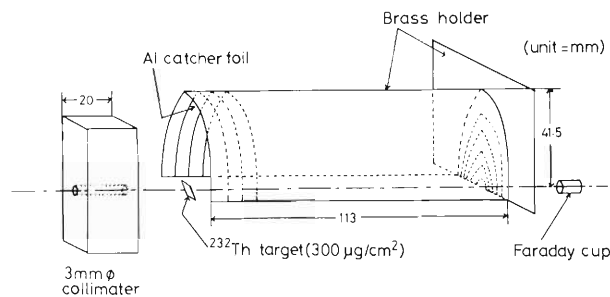


Fig. 1. Target assembly, schematically drawn.

\* Tokyo Metropolitan University.

\*\* Niigata University.

The target assembly for the measurement of the fragment angular distribution is schematically drawn in Fig. 1. The  $^{232}\text{Th}$  target was prepared by electroplating  $^{232}\text{Th}$  onto the nickel foil of  $10\ \mu\text{m}$  thickness. The thickness of  $^{232}\text{Th}$  itself was about  $300\ \mu\text{g}/\text{cm}^2$ . The bombardment was performed at the cyclotron with the proton energy of 15 MeV and the beam current of  $0.5 - 1\ \mu\text{A}$  for 5 to 12 h, and after the bombardment the Al catcher foil was taken out and sliced to strips of an appropriate width. The solid angle of each Al slice was about 1 % of  $4\pi$ . Some product nuclides were directly measured with Ge (Li) detector equipped with a 2048 channel pulse height analyser, and, for some low-yield species, the  $\gamma$ -ray spectrometry was performed after chemical separations.

From the analysis of the  $(p, xn)$  and fission excitation functions and the peak-to-trough ratios of the mass yield curves, the not-well-established parameters involved in the calculation of the competition between the neutron evaporation and fission were determined. When the two-mode hypothesis is assumed and those parameters are used, the average nuclear temperature of the fissioning nuclides at the saddle point configurations for the symmetric mass divisions is expected to be higher than that for the asymmetric mass divisions because of the different contributions of multiple chance fissions according to the two-mode hypothesis. Therefore, if the moment of inertias are about the same for the symmetric and asymmetric saddle configurations, the angular anisotropy for the symmetric mass division is expected to be larger than that for the asymmetric mass division.

In Fig. 2 is shown, as an example, the observed angular distribution for the fission fragment,  $^{143}\text{Ce}$ . The anisotropy of the angular distribution was evaluated by a least squares fitting of the experimental results with the form of  $W(\theta) = a + b \cdot \cos^2 \theta$ . Experiments were carried out several times to obtain these results. The angular anisotropies of some fragments thus evaluated are summarized in Fig. 3. In the figure the Cohen's data are also

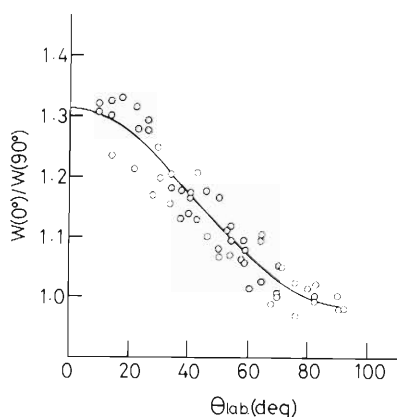


Fig. 2. Angular distribution of  $^{143}\text{Ce}$   
 — : the curve fitted by the least squares analysis with  $W(\theta) = a + b \cdot \cos^2 \theta$ ;  
 o: Experimental results.

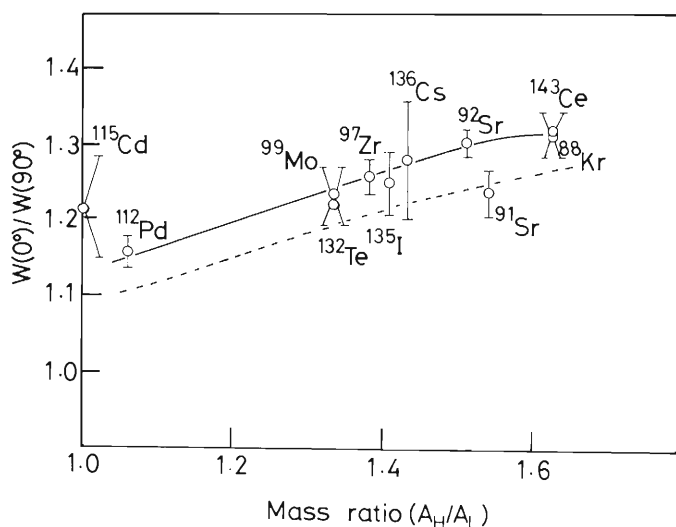


Fig. 3. Angular anisotropies of various fragment masses  
 -----: Cohen's data (Ref. 5).

shown by the dashed curve. Since the data of  $^{112}\text{Pd}$  is quite reliable, although that of  $^{115}\text{Cd}$  is still preliminary, the anisotropy for symmetric mass division is definitely smaller than that for asymmetric mass division, which is in agreement with the results expected from the nuclear temperature analysis. As the Cohen's data were obtained at the proton energy of 22 MeV, the effective temperature is expected to be higher than ours, and thus, our results of the anisotropy should be higher than the Cohen's. This expectation is also in agreement with the experimental results.

As a conclusion, the mass dependence of the angular anisotropies seems to be qualitatively explicable by the two-mode hypothesis, namely, the final mass division being governed by the saddle point configuration. However, in order to draw more definitive conclusion we have to improve the  $^{115}\text{Cd}$  data and also add some more data in the mass-ratio regions of about 1.2 to 1.3 and beyond 1.6.

#### References

- 1) A. Bohr: Proc. U. N. Int. Conf. Peaceful Uses at. Energy, New York, 2, 151 (1956).
- 2) K. F. Flynn, G. E. Glendenin, and J. R. Huizenga: Nucl. Phys., 58, 321 (1964).
- 3) R. Vandenbosch, J. P. Unik, and J. R. Huizenga: Proc. IAEA Symp. Phys. Chem. Fission, Salzburg, IAEA, Vienna, 1, 547 (1965).
- 4) V. G. Vorob'eva, N. P. D'yachenko, V. S. Mitrosanov, B. D. Kuz'minov, A. I. Sergachev, and D. Poenaru: Sov. J. Nucl. Phys., 26, 508 (1977).
- 5) B. L. Cohen, B. L. Ferrell-Bryan, D. J. Coombe, and M. K. Hullings: Phys. Rev., 98, 685 (1955).
- 6) F. Plasil: ORNL Report, TM-6054 (1977).

### 4-3. Spin-Flip Asymmetry in the Inelastic Scattering of Protons on $^{12}\text{C}$ at 24.1, 26.2, and 28.0 MeV

T. Fujisawa, T. Wada, M. Nakamura,\* K. Hatanaka,\*  
M. Yasue,\*\* N. Ueda,\*\* T. Hasegawa,\*\* M. Sekiguchi,\*\*  
F. Soga,\*\* H. Kamitsubo, T. Tanaka,\*\*\* and Y. Toba\*\*\*\*

The spin flip asymmetry (SFA) and the difference between the analyzing power and the polarization (A-P) in the inelastic scattering of protons on  $^{12}\text{C}$ (4.43 MeV state) were determined by measuring the spin flip probability of polarized protons.<sup>1)</sup> The large values of (A-P) were found at 24.1 and 26.2 MeV. Macro- and micro-scopic DWBA calculations were carried out for the 28 MeV data. Such calculations however failed to account for the spin-dependent data.

A polarized proton beam was extracted from an atomic beam type polarized ion source which was constructed at IPCR, and accelerated by the SF Cyclotron at Institute for Nuclear Study of University of Tokyo. The beam current on the target was about 1 – 3 nA and the beam polarization was 50% on the average. The details of the experimental procedure have already been reported.<sup>1)</sup>

The results obtained are shown in Figs. 1 – 4. The drastic changes of the shape and magnitude of (A-P) with the change of energy suggest an effect of some resonance on the direct reaction.<sup>2)</sup>

To explain these changes, the analysis is in progress by the method of coupled-channel calculation with Breit-Wigner terms using Jupiter-1 code developed by T. Tamura.

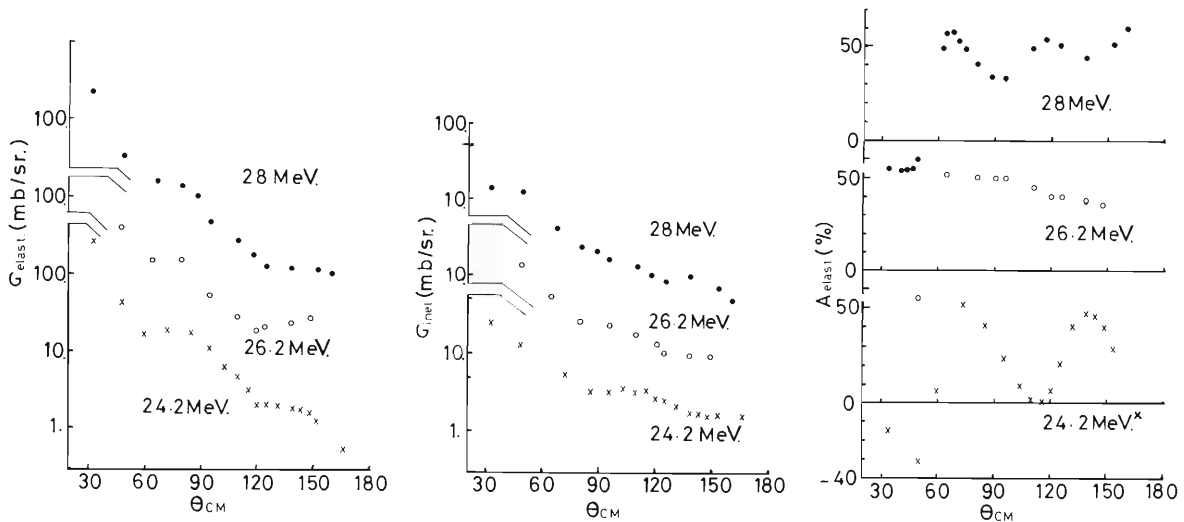


Fig. 1. Differential cross sections in the elastic and inelastic scattering (4.43 MeV  $2+$ ) and the asymmetry in the elastic scattering of protons on  $^{12}\text{C}$  at 24.1, 26.2, and 28.0 MeV.

\* Department of Physics, Kyoto University.

\*\* Institute for Nuclear Study, University of Tokyo.

\*\*\* Department of Engineering, Kyushu University.

\*\*\*\* Department of Physics, Tsukuba University.

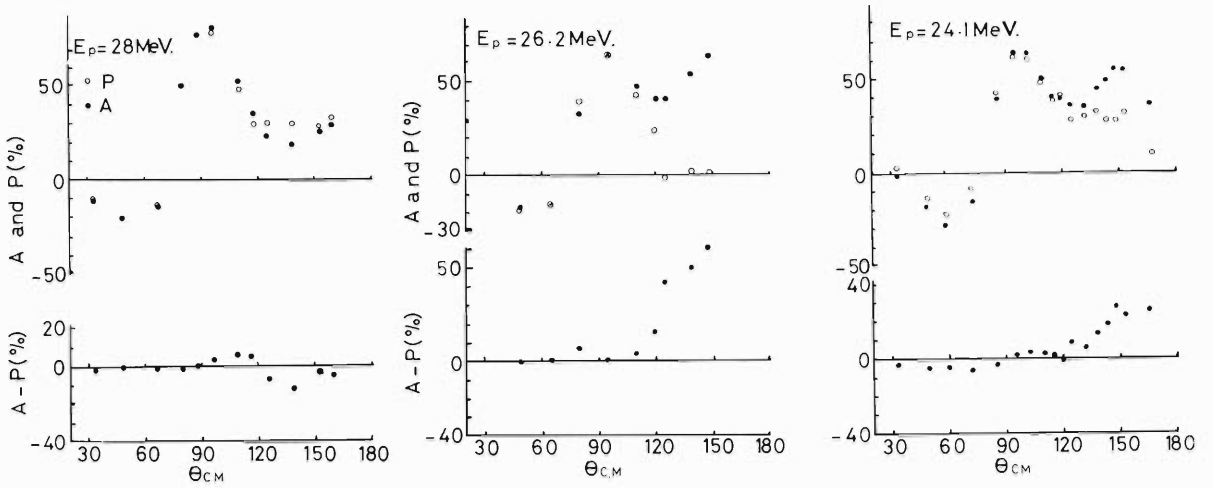


Fig. 2. Analyzing power (A), Polarization (P) and A-P in the inelastic scattering of protons on  $^{12}\text{C}(4.43 \text{ MeV } 2^+)$ .

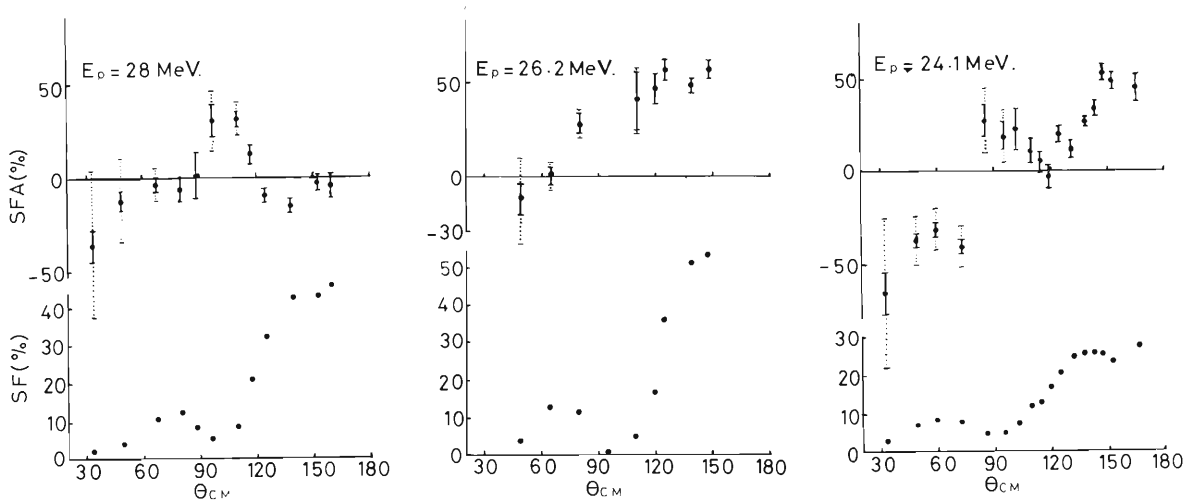


Fig. 3. Spin flip asymmetry (SFA) and spin flip probability in the inelastic scatterings of protons on  $^{12}\text{C}(4.43 \text{ MeV } 2^+)$ .

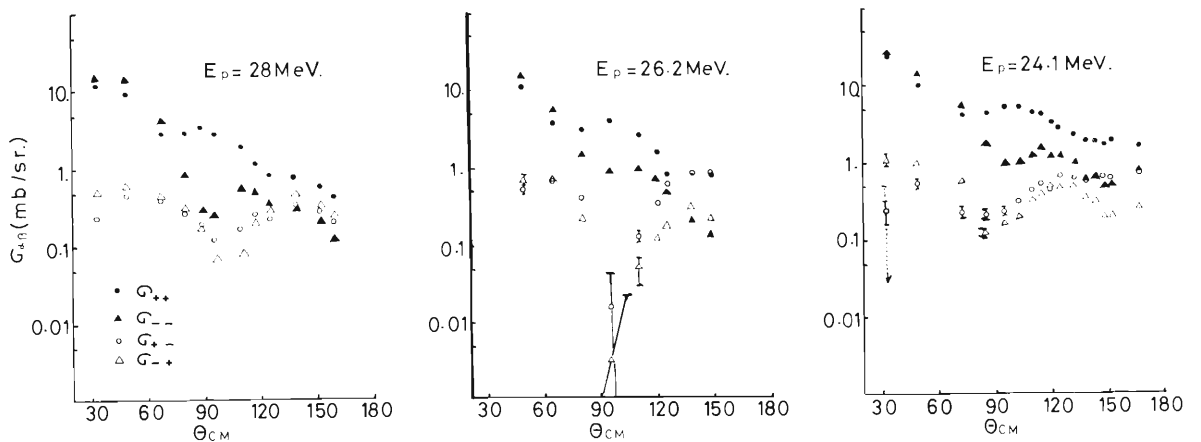


Fig. 4. Partial differential cross sections in the inelastic scatterings of protons on  $^{12}\text{C}(4.43 \text{ MeV } 2^+)$ .

## References

- 1) T. Fujisawa, M. Nakamura, M. Yasue, N. Ueda, T. Hasegawa, H. Kamitsubo, K. Hatanaka, T. Tanaka, M. Sekiguchi, T. Wada, Y. Toba, and F. Soga: *IPCR Cyclotron Progr. Rep.*, 12, 29 (1978); *Proc. INS Intern. Symp. on Nucl. Direct. Reac. Mech.*, p. 71 (Fukuoka Japan 1978).
- 2) T. Tamura and T. Terasawa: *Phys. Lett.*, 8, 41 (1964); H.V. Geramb, K. Amos, R. Sprickman, K.T. Knöpfle, M. Rogge, D. Ingham, and C. Mayer-Böricke: *Phys. Rev. C*, 12, 1697 (1975).

#### 4-4. Vector Analyzing Power and Polarization Measurement for the $^{116}\text{Sn}(d,p)^{117}\text{Sn}(\text{g.s. } 1/2^+)$ and the Deuteron D-state Effects

T. Kubo, N. Kishida, H. Ohnuma, T. Hasegawa,  
N. Ueda, T. Fujisawa, T. Wada,  
K. Iwatani, and T. Suehiro

It has been pointed out<sup>1)</sup> that the separation of proton and deuteron spin-orbit distortion can be approximately achieved through the quantities  $S_p = 2(P_y - A_y)$  and  $S_d = 3A_y - 2P_y$ . Here  $P_y$  is proton polarization, and  $A_y$  vector analyzing power, in an  $\ell_n = 0$  (d, p) reaction. Especially we are interested in the effects of the deuteron D-state on  $S_d$ . There is only one report<sup>2)</sup> of the  $S_p$  and  $S_d$  measurements at 8.22 MeV.

We have measured the cross section and vector analyzing power for the  $^{116}\text{Sn}(d, p)^{117}\text{Sn}$  (g.s.  $1/2^+$ ) reaction at  $E_d = 22$  MeV. Instead of measuring polarization of outgoing protons, we have measured the analyzing power for the  $^{117}\text{Sn}(p, d)^{116}\text{Sn}(\text{g.s. } 0^+)$  reaction at  $E_p = 27$  MeV.

Polarized beams were provided by an atomic-beam type polarized ion source, and injected into INS SF cyclotron. The average beam intensity was about 10 nA at the target. The beam polarization was continuously monitored by using a carbon-foil polarimeter, and was 40 % for deuterons and 50 % for protons. Self-supporting targets of enriched isotopes were used. Particles were detected with  $\Delta E$ -E counter telescopes. Experimental results are shown in Figs. 1-4 along with calculations.

Exact-finite-range DWBA(EFR-DWBA) calculations have been performed using the code TWOFNR<sup>3)</sup> modified so as to include the deuteron D-state effects.<sup>4)</sup> Distorting potential parameters are given in Table 1. The deuteron parameters are those searched for by using the code ELAST2<sup>5)</sup> to fit the cross section and polarization data for the elastic scattering measured simultaneously with (d, p). The proton parameters are obtained from the global fits of Becchetti and Greenlees.<sup>6)</sup>

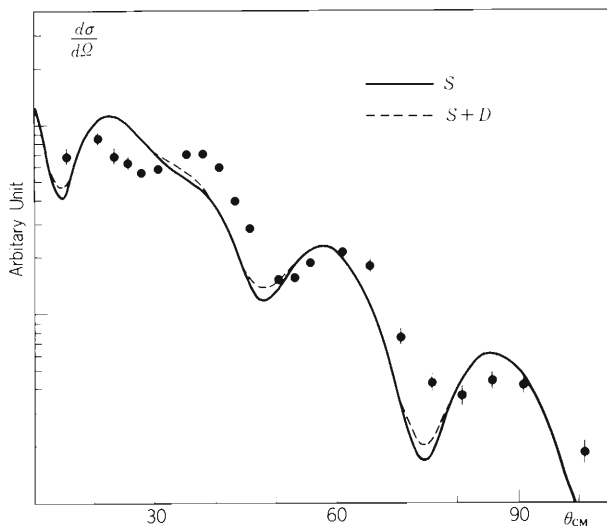


Fig. 1. Cross section for the  $^{116}\text{Sn}(d, p)^{117}\text{Sn}(\text{g.s. } 1/2^+)$  at 22 MeV. The curves are the results of EFR-DWBA calculations with and without the deuteron D-state contributions.

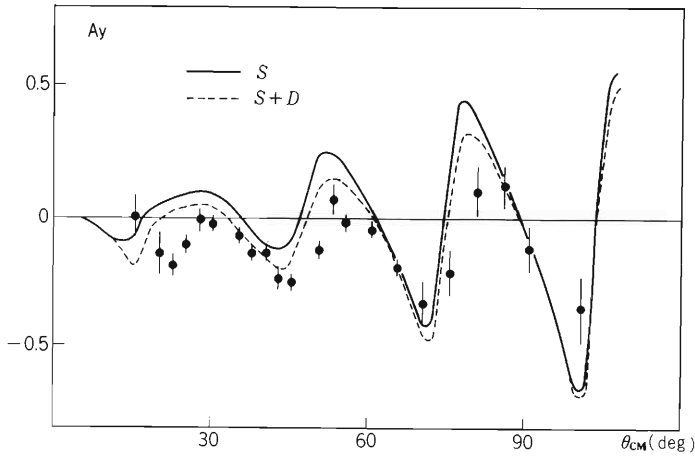


Fig. 2. Vector analyzing power for the  $^{116}\text{Sn}(d, p)^{117}\text{Sn}(\text{g.s. } 1/2^+)$ . See caption for Fig. 1.

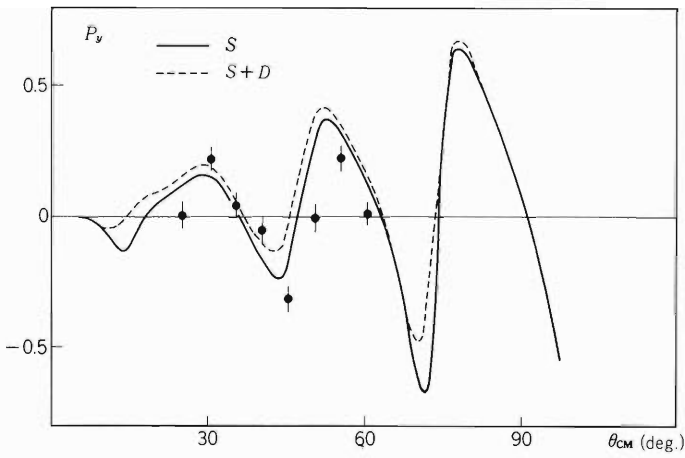


Fig. 3. Vector analyzing power for the  $^{117}\text{Sn}(p, d)^{116}\text{Sn}(\text{g.s. } 0^+)$  at 27 MeV. See caption for Fig. 1.

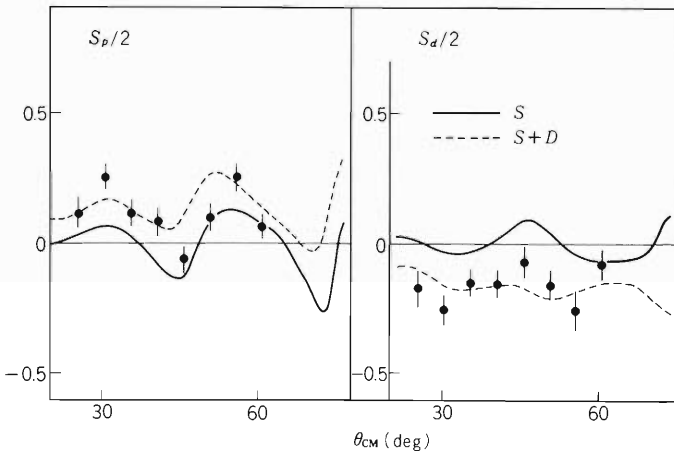


Fig. 4. Angular distributions of  $S_p$  and  $S_d$  obtained from  $A_y$  and  $P_y$ . See caption for Fig. 1.

Table 1. Distorting potential parameters.

Particle	$V_0$	$r_0$	$a_0$	$W$	$W_D$	$r_w$	$a_w$	$V_{so}$	$r_{so}$	$a_{so}$	$r_c$
p	53.0	1.17	0.75	3.17	6.87	1.32	0.61	6.20	1.01	0.75	1.25
d	99.64	1.10	0.887	—	16.3	1.33	0.72	4.16	0.81	0.113	1.3

Following the results of EFR-DWBA calculations, the effects of the deuteron D-state are not very large for the cross section, vector analyzing power and proton polarization. However, very remarkable D-state effects are found in  $S_p$  and  $S_d$ . Especially the fit to  $S_d$  is very poor without D-state effects. Thus it is found that the D-state effects can play an important role even in the first-rank polarization quantities.

Measurement of  $P_y$  at larger angles and further analyses are in progress.

#### References

- 1) R. C. Johnson: Nucl. Phys., 35, 654 (1962); A90, 289 (1967).
- 2) R. R. Cadmus, Jr. and W. Haeberli: *ibid.*, A327, 419 (1979).
- 3) M. Igarashi: unpublished.
- 4) N. Kishida and H. Ohnuma: J. Phys. Soc. Japan., 46, 1375 (1979).
- 5) M. Igarashi: INS-PT-26 (1970).
- 6) F. D. Becchetti and G. W. Greenlees: Phys. Rev., 182, 1190 (1969).

#### 4-5. Measurement of Particle- $\gamma$ Angular Correlations for the $^{58}\text{Ni}(p,d)^{57}\text{Ni}$ Reaction at $E_p = 30$ MeV

N. Kishida, J. Kasagi, T. Kubo, Y. Kamatani,  
 T. Murakami, H. Ohnuma, and M. Yasue\*

The mechanism of the (p, d) reaction has been mainly investigated by measuring differential cross sections, analyzing powers, and occasionally polarizations of outgoing particles. In general, residual nuclei are also left polarized, and this polarization gives information independent of the above quantities. An assembly of polarized nuclei is described by a density matrix or statistical tensors. We measured correlation functions between ejected deuterons and de-exciting  $\gamma$ -rays for the  $^{58}\text{Ni}(p, d)^{57}\text{Ni}$  reaction at 30 MeV in order to obtain experimental information on the statistical tensors of residual nuclei. There have already been differential cross section and analyzing power measurements<sup>1)</sup> for this reaction at the same incident energy.

The experiment was done with a 30 MeV proton beam from the INS SF cyclotron. Four  $2'' \times 2''$  NaI(Tl) detectors and four  $\Delta E$ -E counter telescopes were used to detect  $\gamma$ -rays and deuterons, respectively. Correlation functions were obtained by taking coincidences between  $\gamma$ -ray detectors and particle detectors. The target was  $2.4 \text{ mg/cm}^2$  thick metallic foil of enriched  $^{58}\text{Ni}$ .

Differential cross sections, analyzing powers, and correlation functions of the transition to the 2.58 MeV ( $7/2^-$ ) state in  $^{57}\text{Ni}$  are analyzed by DWBA and adiabatic deuteron breakup theory (ADB) including the D state of the deuteron ground state. The method of calculations are described in Ref. 2. Proton distorting potential parameters are taken from Ref. 3 and deuteron parameters for DWBA calculations from Ref. 4. The deuteron adiabatic potential is constructed from the proton and neutron parameters of Ref. 5 following Ref. 6. Non-locality corrections are included in local-energy approximation. The form factor is generated by usual separation energy method.

Results of the calculations are shown in Figs. 1-4 together with experimental data. The same normalization is used for S + D and S calculations. The DWBA calculations including the D-state reproduced differential cross sections, analyzing powers and correlation function at  $\theta_d = 25^\circ$  well. They also reproduce the correlation function at  $\theta_d = 45^\circ$ , but the fit is worse for large  $\theta \gamma$

Johnson and Santos stated<sup>7)</sup> that the D-state effects gave a partial account of  $\ell = 3$  J-dependence raising  $j = 7/2$  cross sections at minima. The D-state effects in fact increase the calculated cross sections around  $45^\circ$ , but the effects are barely noticeable at this energy (Fig. 1). On the other hand, the D-state effects are appreciable on the correlation functions at  $\theta_d = 45^\circ$  and considerably improves the fit to the data. At maxima of cross sections, e.g. at  $\theta_d = 25^\circ$ , the D-state effects are small even on the correlation functions.

The S + D DWBA calculations consistently reproduce the experimental data, but the fit to the correlation function at  $\theta_d = 45^\circ$  is not as excellent as the fits to cross sections and analyzing powers. This fact shows the advantage and importance of particle- $\gamma$  angular correlation data in testing reaction models.

All the calculations here are made by using the computer FACOM 230-75 at IPCR.

\* Institute for Nuclear Study, University of Tokyo.

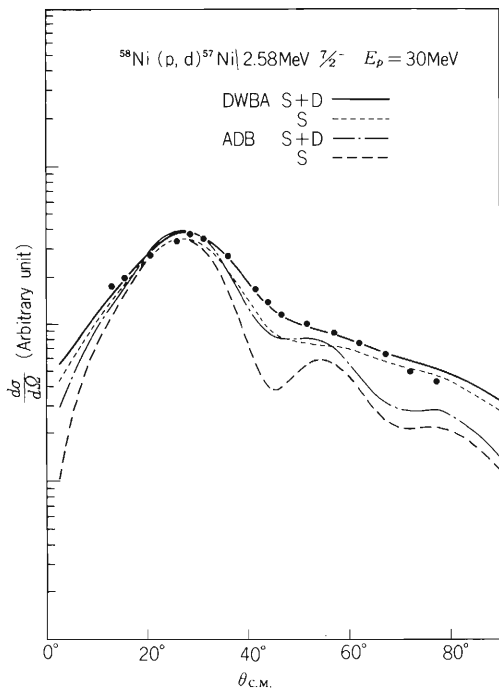


Fig. 1. DWBA and ADB calculations with (S + D) and without (S) the D-state compared with the differential cross sections.

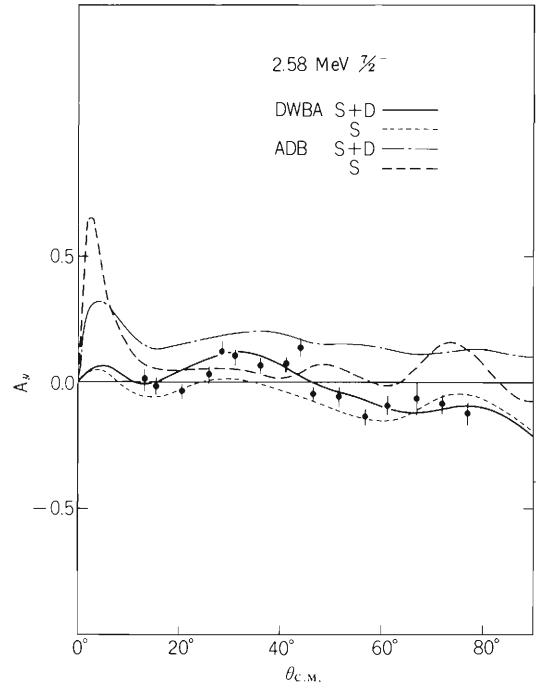


Fig. 2. DWBA and ADB calculations with (S + D) and without (S) the D-state compared with the analyzing powers.

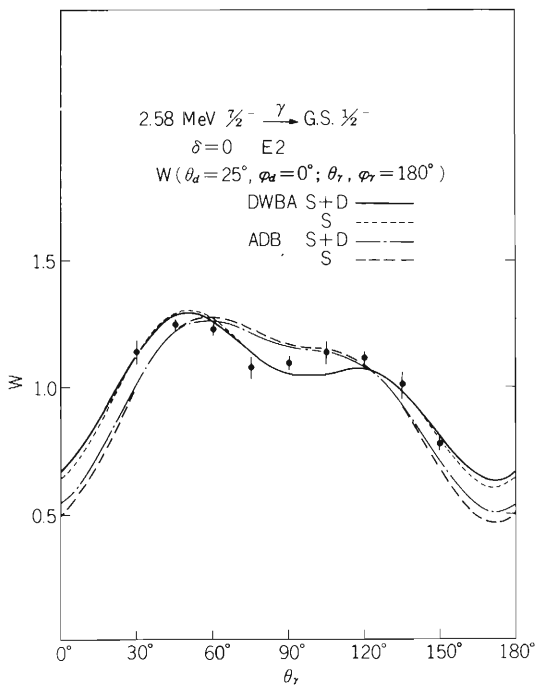


Fig. 3. DWBA and ADB calculations with (S + D) and without (S) the D-state compared with the correlation function at  $\theta_d = 25^\circ$ .

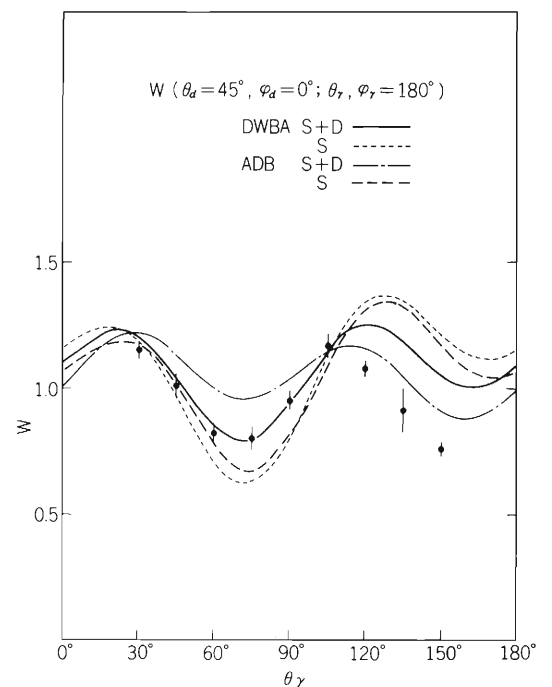


Fig. 4. DWBA and ADB calculations with (S + D) and without (S) the D-state compared with the correlation function at  $\theta_d = 45^\circ$ .

## References

- 1) T. Hasegawa, N. Ueda, N. Kishida, H. Ohnuma, T. Fujisawa, T. Wada, K. Iwatani, T. Tanaka, and Y. Wakuta: Proc. of "1978 INS Intern. Symp. on Nuclear Direct Reaction Mechanism", unpublished.
- 2) N. Kishida and H. Ohnuma: J. Phys. Soc. Japan, 46, 1375 (1979).
- 3) G. W. Greenlees and G. J. Pyle: Phys. Rev., 149, 836 (1966).
- 4) F. T. Baker, S. Davis, C. Glashauser, and A. B. Robbins: Nucl. Phys., A233, 409 (1974).
- 5) C. M. Perey, F. G. Perey, J. K. Dickens, and R. J. Silver: Phys. Rev., 175, 1460 (1968);  
F. D. Becchetti, Jr. and G. W. Greenlees: *ibid.*, 182, 1190 (1969).
- 6) G. L. Wales and R. C. Johnson: Nucl. Phys., A274, 168 (1976).
- 7) R. C. Johnson and F. D. Santos: Phys. Rev. Lett., 19, 364 (1967).

#### 4-6. Coulomb Nuclear Interference in the Inelastic Scattering of $^{18}\text{O}$

M. Ichimura and A. Ichimura\*

It is well known that in the inelastic scattering between heavy ions with incident energy slightly above the Coulomb barrier, the angular distribution and the excitation function show a typical interference pattern between the Coulomb excitation and the nuclear excitation. Most of such phenomena are well explained by the conventional DWBA with collective form factors and for some cases the importance of the channel coupling (CC) effects is reported.

However, it was reported<sup>1), 2)</sup> that the inelastic scattering induced by  $^{18}\text{O}$  which results in the projectile excitation of the  $^{18}\text{O}$  first  $2+$  excited state ( $E_x = 1.98$  MeV) shows anomalous pattern in the angular distribution, which cannot be explained by DWBA or CC analysis with the conventional collective form factors. In Fig. 1 the experimental angular distribution of the reaction  $^{58}\text{Ni}(^{18}\text{O}, ^{18}\text{O}^*)^{58}\text{Ni}$  at  $E = 63$  MeV is compared with the DWBA results where the vibrational

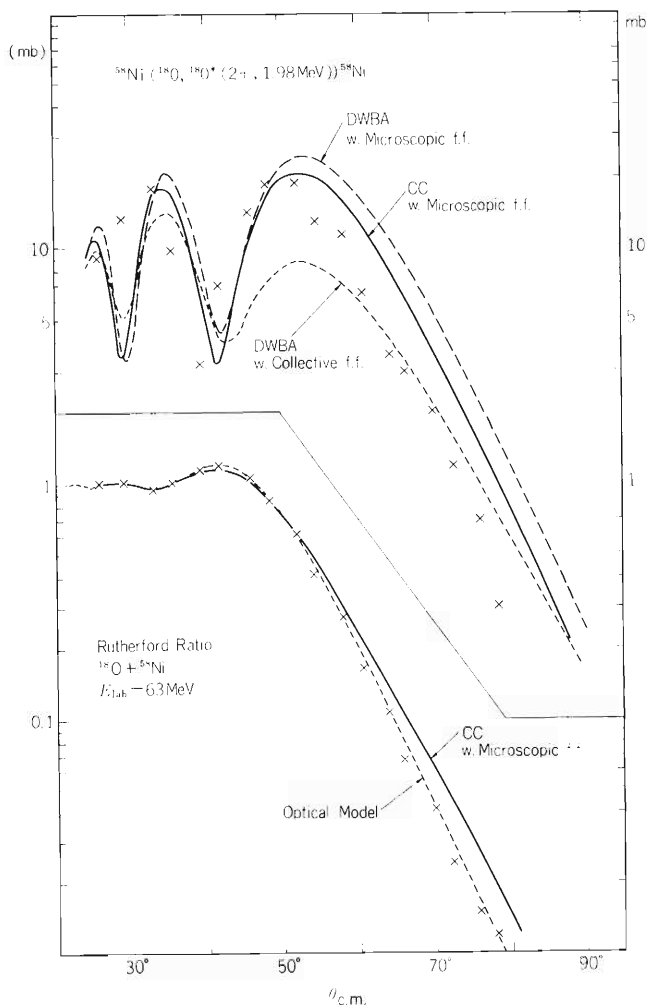


Fig. 1. Experimental and theoretical cross sections of the inelastic scattering  $^{58}\text{Ni}(^{18}\text{O}, ^{18}\text{O}^*(2+, 1.98\text{ MeV}))^{58}\text{Ni}$ . The dotted line denotes the result of DWBA with the vibrational form factor, while the broken line represents the result of DWBA with the microscopic form factor. The full line shows the result of the coupled channel (CC) calculation with the reorientation effects in terms of the microscopic form factors. The experimental data are shown by the crosses.

The elastic scatterings are also shown where the results of the optical potential are denoted by the dotted line while the CC results are denoted by the full line.

\* Institute of Physics, University of Tokyo.

form factor is used with the assumption that the nuclear deformation parameter is equal to the Coulomb deformation parameter. Marked differences are seen in the height of the peak at about  $\theta = 50^\circ$  and the position of the peaks and dips.

Several attempts have hitherto been made to explain this discrepancy: (i) Assume anomalously large nuclear deformation parameters and carry out the CC calculation where the reorientation effect is found to be very significant.<sup>1)</sup> However, this assumption of large deformation contradicts with recent improved measurement<sup>3)</sup> of the quadrupole moment of the 2+ state of  $^{18}\text{O}$ ; (ii) Adjust the phase of the nuclear collective form factor to reproduce the experimental data by DWBA,<sup>2)</sup> but this procedure has no physical justification; (iii) Adjust the geometrical parameters of the form factor as a simulation of a microscopic form factor<sup>4)</sup> but the values of the chosen parameters have poor theoretical justification; (iv) Take into account the two step process<sup>5)</sup>  $^{18}\text{O} \rightarrow ^{17}\text{O} \rightarrow ^{18}\text{O}^*$ , which somewhat improves the position of the dip at about  $\theta \approx 40^\circ$  but the fit for the large angle cross section is very poor.

Here we build up microscopic form factors for the transition from the ground state to the first 2+ state of  $^{18}\text{O}$  and for the reorientation within the first 2+ state. For the calculation of the microscopic form factors, we folded the nucleon-target ( $^{58}\text{Ni}$ ) optical potential by the shell model wave functions<sup>6)</sup> of the ground and the first excited states of  $^{18}\text{O}$ . The single particle wave functions of the bound state are calculated by the half-of-the-separation-energy method. In Fig. 2 we show the collective and the microscopic form factors for the transition from the ground state to the first excited state at the tail region, considering the fact that analysis shows that the contribution comes from the region from 8 fm to 13 fm. One sees much longer tail of the microscopic form factors which is due to the loosely bound valence nucleon in  $^{18}\text{O}$ .

DWBA and CC calculations with the reorientation in terms of the microscopic form factors are performed, and the results are compared with the experimental data and the DWBA results of the collective model in Fig. 1. As far as the magnitude of the peak at about  $\theta \approx 50^\circ$  is

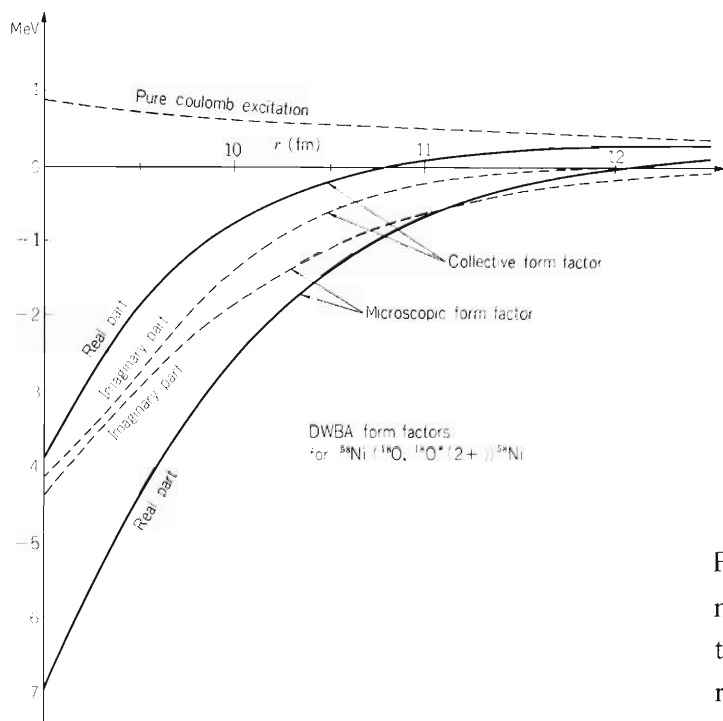


Fig. 2. Comparison between the microscopic transition form factor and that of the collective model at the tail region.

concerned, much improvement has been obtained by using the microscopic form factors, but the DWBA calculations with the microscopic form factor gave much too large cross sections at large angles. If we take into account the reorientation effect in the CC calculation, the cross sections at large angles are considerably reduced and the fit is improved though not yet satisfactory.

We used the optical potentials as the distorting potential in the present CC calculation and have not yet readjusted them to reproduce elastic scattering data. Therefore, the predicted elastic cross section is larger than the experimental one at large angles. By performing this readjustment, we may obtain more improved results.

As to the position of the dip at about  $\theta \approx 40^\circ$ , half of the difference between the experimental data and the result of the collective model DWBA calculation is remedied by the CC calculation with the reorientation effect by using the microscopic form factors.

Further investigations are in progress.

## References

- 1) F. Videbaek, P. R. Christensen, Ole Hansen, and K. Ulbak: Nucl. Phys., A256, 301 (1976).
- 2) K. E. Rehm, H. J. Körner, M. Richter, H. P. Rother, J. P. Schiffer, and H. Spieler: Phys. Rev., C12, 1945 (1975); H. Essel, K. E. Rehm, H. Bohn, H. J. Körner, and H. Spieler: *ibid.*, C19, 2224 (1979).
- 3) M. P. Fewell, A. M. Baxter, D. C. Kean, R. H. Spear, and T. H. Zabel: Nucl. Phys., A232, 457 (1979).
- 4) A. J. Baltz and S. Kahana: Phys. Rev., C17, 555 (1978).
- 5) K. S. Low: Proc. Intern. Conf. Nuclear Structure, Tokyo, p. 267 (1977).
- 6) T. Inoue, T. Sebe, H. Hagiwara, and A. Arima: Nucl. Phys., 59, 1 (1964).

#### 4-7. Semiclassical Treatment of the Direct Reactions Induced by Heavy Ions

T. Kammuri, K. Matsuoka,\* and M. Sano\*

Gross features of one-particle transfer reactions induced by heavy ions can be understood in a simple way by considering the conservation of the linear and angular momenta.<sup>1)</sup> We have derived an expression for the transition probability of the one-particle transfer, which agrees with the one originally given by Brink.<sup>1)</sup> We have extended the treatment to the inelastic scattering and sequential transfer.

We start from the semiclassical theory of Broglia and Winther.<sup>2)</sup> The differential cross section is given by the product of the elastic scattering cross section and the transition probability  $P = |c_{if}^{(1)}|^2$ . The amplitude  $c_{if}^{(1)}$  of the one-step process is given by

$$c_{if}^{(1)} = \frac{1}{i\hbar} \int_{-\infty}^{\infty} f_{if}^{(1)}(t) dt, \quad (1)$$

where  $f_{if}^{(1)}(t)$  is the form factor multiplied by the energy-dependent exponential function. We assume that the reaction is a peripheral one and that the main contributions come from the region between two nuclei. For one-particle transfer reaction,  $f_{if}^{(1)}(t)$  is given by

$$f_{if}^{(1)}(t) = N_{if}^{(1)} \exp \left\{ -\frac{1}{2} \left( \frac{R\Delta k}{\sigma_1} \right)^2 \right\} \exp \left( -\eta^2 t^2 - i\omega t \right). \quad (2)$$

Here

$$\left. \begin{aligned} \eta &= \frac{\sigma_2}{\sqrt{2}} \left( \frac{v}{R} \right), & \omega &= \Delta L \frac{v}{R}, \\ \sigma_1^2 &\simeq r_1 R^2 / R_1, & \sigma_2^2 &\simeq r_1 R, \\ \Delta k &= k_0 - \lambda_1 / R_1 - \lambda_2 / R_2, \\ \Delta L &= \lambda_2 - \lambda_1 + \frac{1}{2} k_0 (R_1 - R_2) + Q_{\text{eff}} R / \hbar v, \end{aligned} \right\} \quad (3)$$

\* Department of Physics, Osaka University.

and  $N_{if}^{(1)}$  lumps together c.f.p.'s, Clebsch-Gordan coefficients, reduced widths etc. We follow Ref. 1 for the definitions and notations on  $\Delta k$ ,  $\Delta L$  etc. Integration of Eqn. (2) over  $t$  gives

$$c_{if}^{(1)} \approx \frac{1}{\eta} \exp \left\{ -\frac{1}{2} \left( \frac{R \Delta k}{\sigma_1} \right)^2 - \frac{1}{2} \left( \frac{\Delta L}{\sigma_2} \right)^2 \right\}. \quad (4)$$

In the macroscopic approach of the collective excitation of the target nucleus, the form factor is proportional to the derivative of the Woods-Saxon potential. The amplitude is then given by

$$c_{if}^{(1)} \approx \frac{1}{\eta} \exp \left\{ -\frac{1}{2} \left( \frac{\Delta L}{\sigma_2} \right)^2 \right\}. \quad (5)$$

Here  $\sigma_2^2$  is given by  $R/a$ , with the surface diffuseness  $a$ , and

$$\Delta L = \lambda_2 + QR / \hbar v. \quad (6)$$

For the transition to a decaying collective level with the energy  $\omega_0$  and width  $\Gamma$ , we have to multiply a Lorentzian factor,<sup>3)</sup>

$$\tilde{c}_{if}^{(1)} = c_{if}^{(1)} (E^*) \frac{(\Gamma/2\pi)^{1/2}}{E^* - \omega_0 + i\Gamma/2}. \quad (7)$$

where  $E^*$  is the excitation energy of the corresponding nucleus.

The two-step amplitude is given by

$$c_{if}^{(2)} = \frac{1}{(i\hbar)^2} \int_{-\infty}^{\infty} f_{mf}^{(1)}(t) dt \int_{-\infty}^t f_{im}^{(1)}(t') dt'. \quad (8)$$

For the sequential transfer of two particles, it becomes

$$c_{if}^{(2)} \approx \frac{1}{\eta_1 \eta_2} \left\{ 1 - \operatorname{erf}(ix) \right\} \exp \left[ -\frac{1}{2} \sum_{i=1}^2 \left\{ \left( \frac{R \Delta k_i}{\sigma_i} \right)^2 + \left( \frac{\Delta L_i}{\sigma_2} \right)^2 \right\} \right], \quad (9)$$

in which  $\operatorname{erf}(z)$  is the error function and

$$x = \frac{\eta_1 \eta_2}{\sqrt{\eta_1^2 + \eta_2^2}} \left( \frac{w_1}{2\eta_1} - \frac{w_2}{2\eta_2} \right). \quad (10)$$

Quantities with suffices  $i = 1, 2$  refer to the first or second step of the two-step process respectively. In the calculation on the  $^{100}\text{Mo} (^{14}\text{N}, ^{12}\text{B}) ^{102}\text{Ru}$  reaction at  $E = 90$  MeV, both the simultaneous and sequential transfer processes give practically the same energy spectra and polarization distributions.

The energy spectrum can be approximated by

$$\exp \left[ - \left\{ (Q_{\text{eff}} - Q_{\text{eff}}^m) / W \right\}^2 \right]. \quad (11)$$

For one-particle transfer, the optimum value of the effective  $Q$  and the width  $W$  are given by

$$Q_{\text{eff}}^m \approx -\frac{1}{2}mv^2, \quad W \approx \left(\frac{\ell_1}{2} + 1\right) \frac{\hbar v}{R} \sigma_2. \quad (12)$$

In the case of sequential transfer, we have

$$Q_{\text{eff}}^m \approx -\frac{1}{2} \sum_{i=1}^2 m_i v_i^2, \quad W \approx \left(\frac{\ell_1}{2} + 1\right) \left\{ \sum_i \left( \frac{\hbar v_i}{R} \sigma_{2i} \right)^2 \right\}^{1/2}. \quad (13)$$

Increase of the widths with incident energy can be seen in the experimental results<sup>4)</sup> on  $^{52}\text{Cr} + ^{14}\text{N}$  for the incident  $^{14}\text{N}$  energies between 64 MeV and 95 MeV. Experimental widths increase with the numbers of transferred nucleons up to about 4.

#### References

- 1) D. M. Brink: Phys. Lett., 40B, 37 (1972).
- 2) R. A. Broglia and A. Winther: Nucl. Phys., A182, 112 (1972).
- 3) D. Drechsel and H. Überall: Phys. Rev., 181, 1383 (1969).
- 4) T. Mikumo, I. Kohno, K. Katori, T. Motobayashi, S. Nakajima, M. Yoshie, and H. Kamitsubo: *ibid.*, C14, 1458 (1976).

## 4-8. Mass Exchange in an Analysis of the Heavy-Ion Reaction Based on the Linear Response Theory

S. Yamaji

In our previous works,<sup>1),2)</sup> realistic calculations of friction tensors for the  $^{20}\text{Ne} + ^{28}\text{Si}$  system were performed using the two-center shell model on the basis of the linear response theory and the coupled dynamical equations of motion with friction were solved, taking the relative distance  $R$  and the deformation  $\delta$  of each nucleus as the collective variables. It was found<sup>2)</sup> that the calculated angular distribution reproduces the nearly exponentially decreasing feature of the experimental data of 120 MeV  $^{20}\text{Ne}$  with  $^{27}\text{Al}$  and that the calculated total kinetic energy loss reproduces nicely the experimentally observed most probable kinetic energy loss due to the inclusion of the deformation degree of freedom involved in the exit channel.<sup>3),4)</sup>

However, our calculated cross section<sup>2)</sup> had to be compared with the sum of the cross sections of the various reaction products in the experiment, because the effect of mass exchange<sup>5),6)</sup> was neglected. In Ref. 5, only the relative distance  $R$  and the mass asymmetry  $\eta = (A_1 - A_2)/(A_1 + A_2)$  were treated as the collective variables within the cranking formalism, neglecting the deformation degree of freedom. Although, in Ref. 6, the dynamical coupled equations of motion derived from the linear response theory<sup>7)</sup> were solved treating  $R$  and  $\eta$  as collective variables, friction tensors  $\gamma_{RR}$ ,  $\gamma_{\eta\eta}$ , and  $\gamma_{R\eta}$  were approximated with a phenomenological one, constant value and zero, respectively. The energy density potential written in a simple analytic form was taken as the nuclear interaction potential.<sup>6)</sup>

Table 1. Order of magnitude of friction and mass tensors for  $\delta = 0.0$  and  $0.4$ . The values of tensors relating to the mass asymmetry such as  $\gamma_{R\eta}$ ,  $\gamma_{\delta\eta}$ ,  $\gamma_{\eta\eta}$ ,  $m_{R\eta}$ ,  $m_{\delta\eta}$ , and  $m_{\eta\eta}$  are taken just inside the touching distance  $R_t(\eta)$ , i.e. at  $R = R_t(\eta) - 0.5$  fm for  $\eta = 0.0 \sim 0.6$ . The values of other tensors are those in the surface region with  $R = R_t(\eta) - 0.5 \sim R_t(\eta) + 0.5$  fm for  $\eta = 0.0 \sim 0.6$ . The nuclear temperature and the smearing width necessary for the calculation of friction tensors are taken to be 3 MeV and  $0.2 \hbar\omega_0$  ( $\hbar\omega_0 = 11.3$  MeV), respectively.

	Unit	$\delta = 0.0$	$\delta = 0.4$
$\gamma_{RR}$	$\text{MeV} \cdot 10^{-23} \text{ sec}/\text{fm}^2$	55 ~ 80	30 ~ 60
$\gamma_{R\delta}$	$\text{MeV} \cdot 10^{-23} \text{ sec}/\text{fm}$	-260 ~ -80	-140 ~ -20
$\gamma_{R\eta}$	$\text{MeV} \cdot 10^{-23} \text{ sec}/\text{fm}$	20 ~ 200	0 ~ 120
$\gamma_{\delta\delta}$	$\text{MeV} \cdot 10^{-23} \text{ sec}$	1000 ~ 2000	2000 ~ 3000
$\gamma_{\delta\eta}$	$\text{MeV} \cdot 10^{-23} \text{ sec}$	-500 ~ 500	-200 ~ 1500
$\gamma_{\eta\eta}$	$\text{MeV} \cdot 10^{-23} \text{ sec}$	3000 ~ 7000	3000 ~ 7000
$m_{RR}$	pmu (proton mass unit)	6 ~ 12	6 ~ 12
$m_{R\delta}$	pmu·fm	0.5 ~ 1.0	0.5 ~ 3
$m_{R\eta}$	pmu·fm	-35 ~ 0	-40 ~ 0
$m_{\delta\delta}$	pmu·fm <sup>2</sup>	65 ~ 85	250 ~ 400
$m_{\delta\eta}$	pmu·fm <sup>2</sup>	-20 ~ 0	-200 ~ 0
$m_{\eta\eta}$	pmu·fm <sup>2</sup>	1000 ~ 5000	1000 ~ 2000

In the present work, friction tensors  $\gamma_{\mu\nu}(\mu, \nu = R, \delta, \eta)$  were calculated microscopically using formulas given in Ref. 1, the mass tensors  $m_{\mu\nu}$  were approximately replaced with hydrodynamical ones obtained by the use of the Werner-Wheeler method<sup>8)</sup> and the Yukawa-plus-exponential folding potential<sup>9)</sup> was taken as the nuclear potential.

The calculation was performed over following ranges of parameters:  $\delta = -0.4 \sim 0.5$  at intervals of  $\Delta\delta = 0.1$ ,  $R = 2 \sim 20$  fm at intervals of  $\Delta R = 2$  fm and  $\eta = 0.0 \sim 0.7$  at intervals of  $\Delta\eta = 0.05$ . The order of magnitude of these tensors is given in Table 1. Now the numerical calculation of mass and friction tensors and potentials to be used in the dynamical equations of motion have been finished, it is possible to evaluate the time evolution of the expectation value  $R^{C\ell}(t)$ ,  $\delta^{C\ell}(t)$  and  $\eta^{C\ell}(t)$  and moments  $\chi_{\mu\nu}(t)$  ( $\mu, \nu = R, \delta, \eta$ ) of the distribution using the formulas in Ref. 7.

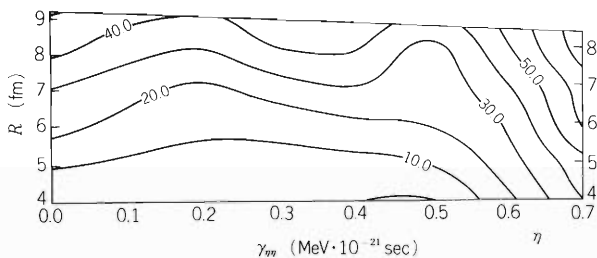


Fig. 1. Contour map of the friction tensor  $\gamma_{\eta\eta}(R, \delta, \eta, T)$  as functions of  $R$  and  $\eta$  for  $\delta = 0.4$  and  $T = 3$  MeV. The smearing width of  $0.2 \hbar\omega_0$  ( $\hbar\omega_0 = 11.3$  MeV) is used. The friction tensor is drawn only within the restricted region where two nuclei overlap.

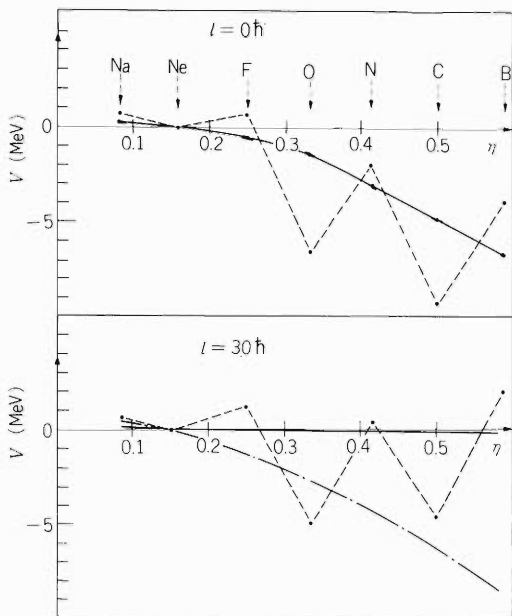


Fig. 2. The potential  $V(R, \delta, \eta)$  as a function of  $\eta$  for  $\delta = 0.0$  and  $R = 9$  fm. The solid curves show the Yukawa-plus-exponential folding potential and the dashed curves show the sum of the mutual Coulomb energy and the shell correction energy. The curves in the lower part include the contribution due to the centrifugal potential which is approximately equal to  $(2\hbar^2 \ell^2 / AR^2) \eta^2 \approx 19\eta^2$  for the angular momentum  $\ell = 30$ . The dot-dashed curve corresponds to  $c = -50$  MeV. The energy at  $\eta = 0.16$  corresponding to the entrance channel (Ne) is set equal to zero.

However, it is important to perform the qualitative estimation of mass exchange, before doing such an elaborate calculation. For that, we assume that the motions of mass asymmetry and of other degrees of freedom are statistically uncorrelated and that the acceleration term for the  $\eta$ -degree can be neglected. If we use constant values  $\gamma$  and  $T$  for the friction  $\gamma_{\eta\eta}$  and the temperature and assuming  $V = 1/2c\eta^2$ ,  $\eta^{C\ell}(t)$  and  $\chi_{\eta\eta}(t)$  are written as

$$\eta^{C\ell}(t) = \eta_0 e^{-\frac{c}{\gamma} t},$$

$$\chi_{\eta\eta}(t) = \frac{T}{2c} \left\{ 1 - e^{-\frac{2c}{\gamma} t} \right\},$$

where  $\eta_0$  denotes the initial mass asymmetry and the cross section  $\sigma(\eta, t)$  is proportional to

$$\exp \left\{ -\left( \eta - \eta^{C\ell}(t) \right)^2 / 4 \chi_{\eta\eta}(t) \right\},$$

The value of  $\gamma$  can be taken as  $5000 \text{ MeV} \cdot 10^{-23} \text{ sec}$  from Fig. 1. In order to obtain the constant value  $c$  in the potential  $V = 1/2c\eta^2$ , the  $\eta$ -dependence of the potential at 9 fm is shown in Fig. 2. The value of  $c$  for the sum of the Yukawa-plus-exponential potential and the centrifugal potential with the angular momentum  $30 \hbar$  is nearly equal to zero due to the cancellation between both potentials. Using this small value of  $c$ , we cannot reproduce the experimental results shown by the points  $\bullet$  in Fig. 3. The fact that the cross sections for the odd reaction products are smaller than those for the even ones implies the importance of the shell effect in the mass transfer. Therefore, we show the sum of the mutual Coulomb energy at 9 fm and the shell correction energy obtained from the experimental values of mass excesses in Fig. 2. Even if we include the contribution of the centrifugal term, we still have about  $-5 \text{ MeV}$  at  $\eta = 0.33$  and  $0.5$  corresponding to O and C channels, respectively. For simplicity, we restrict ourselves to the mass fragmentation induced by  $\alpha$ -particle transfers. Then, we can take  $V = -25\eta^2$  shown by the dot-dashed curve as the fragmentation potential. The temperature is taken to be  $1.5 \text{ MeV}$ , which is half of the temperature at the final stage of the reaction. Then, in order to reproduce the experimental values of  $\eta^{C\ell}(t) = 0.36, 0.42, \text{ and } 0.5$  for the c.m. angles of  $\theta_{\text{cm}} = 40^\circ, 60^\circ, \text{ and } 80^\circ$ , the collision time obtained are  $75, 90, \text{ and } 108 \times 10^{-23} \text{ sec}$ , respectively, whose order of magnitude is consistent with the collision time estimated in Ref. 2. The corresponding second moments  $\chi_{\eta\eta}(t)$  are evaluated to be  $0.05, 0.07, \text{ and } 0.12$  which are roughly by factor 3 larger than the values reproducing experimental mass distributions. The qualitative agreement between the calculated and experimental cross sections is seen in Fig. 3.

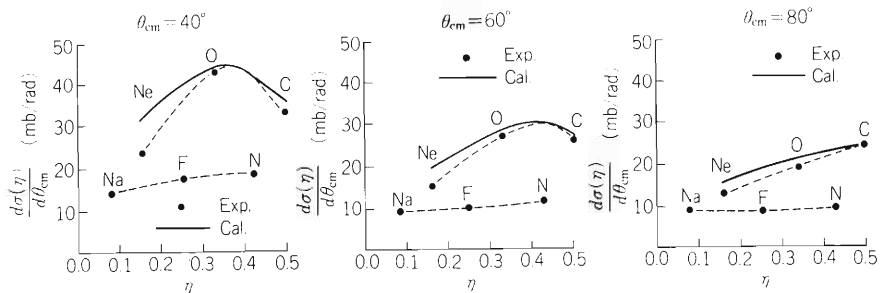


Fig. 3. Differential cross sections  $d\sigma(\eta)/d\theta_{\text{cm}}$  at three different c.m. angles of  $40^\circ, 60^\circ, \text{ and } 80^\circ$  as a function of mass asymmetry  $\eta$ .

Experimental cross sections are obtained by integrating the cross section  $d^2\sigma/d\theta_{\text{cm}}dE$  in Fig. 8 of Ref. 10 over the energy. They are plotted in units of mb/rad. Calculated cross sections are normalized to the experimental ones at the peaks.

## References

- 1) K. Sato, A. Iwamoto, K. Harada, S. Yamaji, and S. Yoshida: *Z. Physik*, **A288**, 383 (1978).
- 2) K. Sato, S. Yamaji, K. Harada, and S. Yoshida: *ibid.*, **A290**, 149 (1979).
- 3) J.P. Bondorf, J.R. Huizenga, M.I. Sobel, and D. Sperber: *Phys. Rev.*, **C11**, 1265 (1975).
- 4) H.H. Deubler and K. Dietrich: *Nucl. Phys.*, **A277**, 493 (1977).
- 5) S. Yamaji, W. Scheid, H.J. Fink, and W. Greiner: *Z. Physik*, **A278**, 69 (1976).
- 6) C. Ngo and H. Hofmann: *ibid.*, **A282**, 83 (1977).
- 7) H. Hofmann and P.J. Siemens: *Nucl. Phys.*, **A275**, 464 (1977).
- 8) K.T.R. Davies, A.J. Sierk, and J.R. Nix: *Phys. Rev.*, **C13**, 2385 (1976).
- 9) H.J. Krappe, J.R. Nix, and A.J. Sierk: *ibid.*, **C20**, 992 (1979).
- 10) J.B. Natowitz, M.N. Namboodiri, R. Eggers, P. Gonthier, K. Geoffroy, R. Hanus, C. Towsley, and K. Das: *Nucl. Phys.*, **A277**, 477 (1977).

4-9. Study of the  $^{27}\text{Al}(^{14}\text{N}, \text{HI}\alpha)$  Reaction

T. Sugitate, T. Nomura, M. Ishihara, T. Inamura,  
H. Utsunomiya, Y. Gono, and K. Ieki

In-plane angular correlations between ejected heavy ions (HI) and alpha particles( $\alpha$ ) have been studied in the  $^{27}\text{Al} + ^{14}\text{N}$  reaction. A self-supporting  $^{27}\text{Al}$  target of  $2.2 \text{ mg/cm}^2$  thickness was bombarded with  $95 \text{ MeV}$   $^{14}\text{N}$ -beam from the cyclotron. HI ( $2 \leq Z \leq 8$ ) and  $\alpha$ -particles were detected by counter telescopes consisting of  $20\text{--}2000 \mu\text{m}$  and  $30\text{--}2000 \mu\text{m}$   $\Delta\text{E}\text{--}\text{E}$  Si detectors, respectively. The HI counter was fixed at  $\theta_{\text{HI}}^{\text{lab}} = -25^\circ$  and  $-40^\circ$  (the negative sign denotes angles on the HI counter side with respect to the beam axis), while coincident  $\alpha$ -particles were detected at several angles in the reaction plane. An aluminium absorber ( $100 \mu\text{m}$ ) was placed in front of the  $\alpha$ -counter in the case of forward angles (i.e.,  $\theta_{\alpha}^{\text{lab}} = \pm 7^\circ$  and  $-10^\circ$ ) in order to remove elastic particles.

Figure 1 shows energy integrated cross sections of  $\alpha$ -particles coincident with various heavy ions. The yields have maxima near the beam axis and fall slowly with exponential slope on the side of positive angles, while they decrease rapidly at negative angles, where small dips are seen near the angles of the HI emission in the case of B, C, N, and O channels.

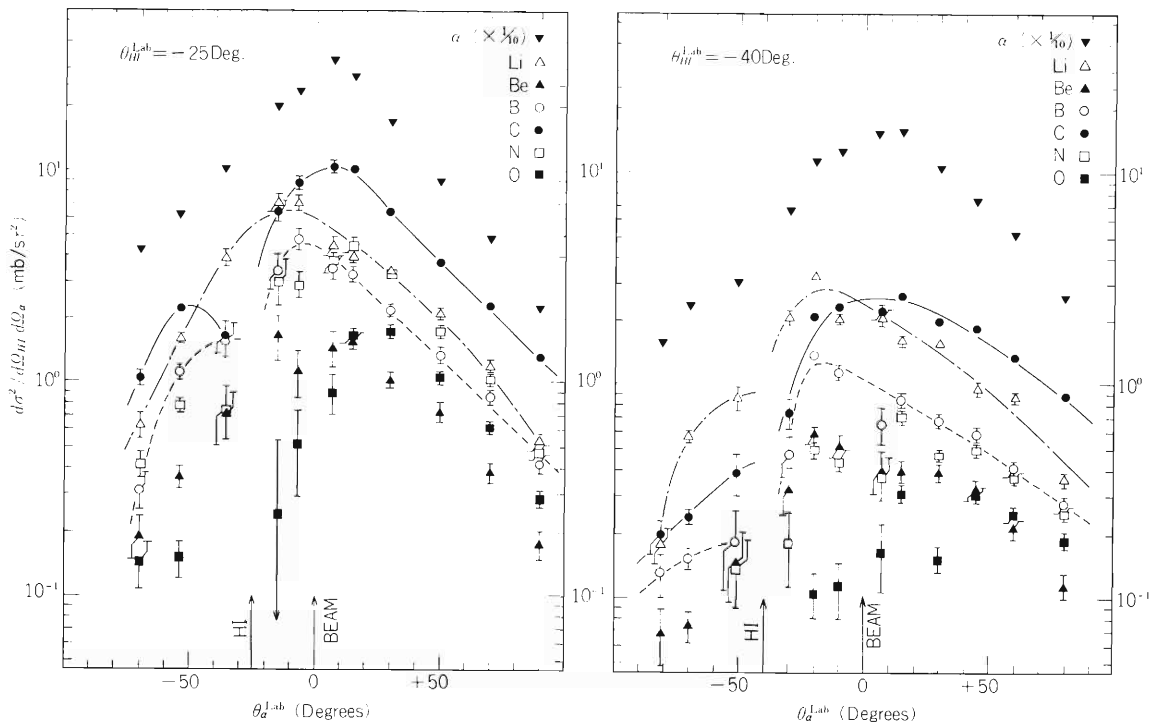


Fig. 1. Energy integrated cross sections of  $\alpha$ -particles coincident with various heavy ions in the  $^{27}\text{Al} + ^{14}\text{N}$  reaction at  $95 \text{ MeV}$  at  $\theta_{\text{HI}}^{\text{lab}} = -25^\circ$  and  $-40^\circ$ . The lines are drawn for the Li, B, and C channels to guide the eye. The arrows indicate the beam axis and the HI detection angle.

Figure 2 shows contour plots of the differential cross sections of  $\alpha$ -velocity in the case of Li, B, and C channels, which are obtained from the following transformation<sup>1)</sup>:

$$\frac{d^3 \sigma}{d\Omega_{\text{HI}} d\Omega_{\alpha} dE_{\alpha}} \longrightarrow \frac{d^3 \sigma}{d\Omega_{\text{HI}} d\Omega_{\alpha} dV_{\alpha}^3}.$$

The three-fold differential cross sections thus obtained are invariant with respect to the Galilei transformation, neglecting relativistic effects. From these figures, we obtained energy spectra of  $\alpha$ -particles at various angles

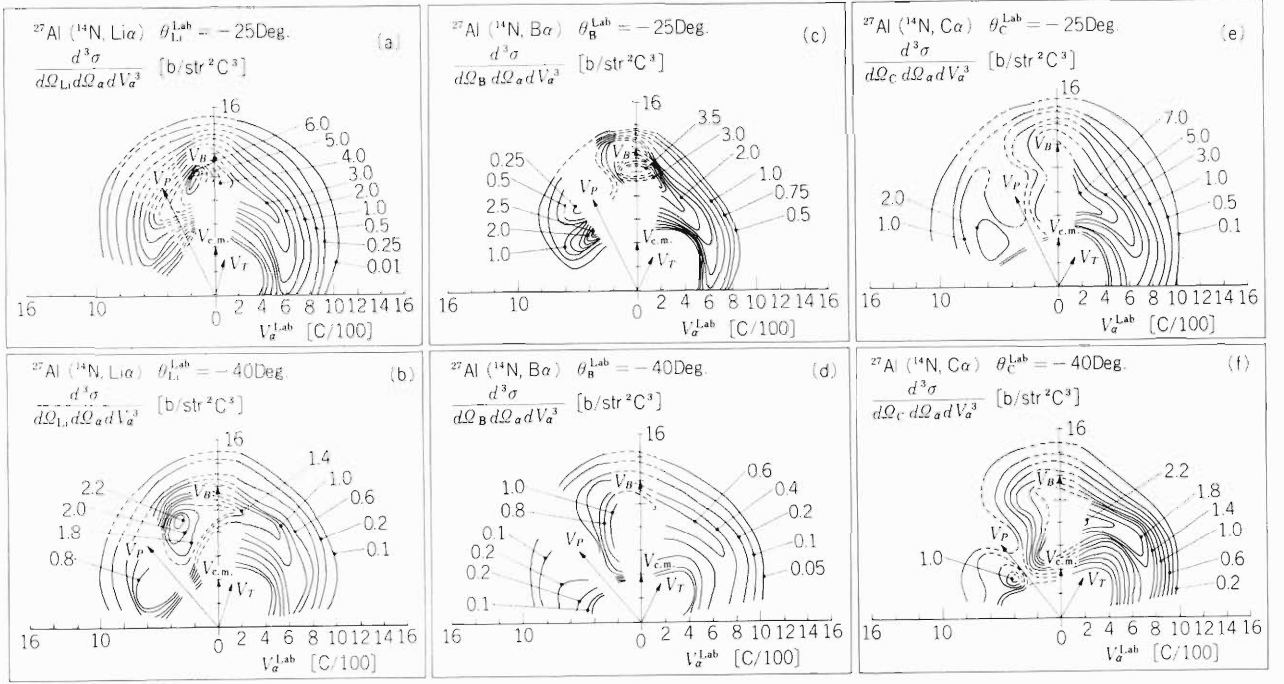


Fig. 2. Contour plots of differential cross sections  $d^3\sigma/d\Omega_{\text{HI}}d\Omega_{\alpha}dV_{\alpha}^3$  for  $\alpha$ -particles coincident with Li, B, and C ions. The vectors  $V_B$ ,  $V_{\text{cm}}$ ,  $V_P$ , and  $V_T$  correspond to the velocities and directions of the incident beam, the centre-of-mass, the ejected heavy ion, and the target-like nucleus, respectively. Cross sections and velocities are represented in the units of  $[\text{b}/\text{sr}^2\text{C}^3]$  and  $[\text{c}/100]$ , respectively, where  $c$  is the velocity of light.

in the c.m. system (Fig. 3(a)) and in the rest frame of the target-like nucleus (Fig. 3(b)), of which the average direction and energy were calculated by assuming a binary reaction process.

The following points should be noted.

- (1) The yields of  $\alpha$ -particles are not symmetric with respect to the beam axis nor the HI direction (Fig. 1).
- (2) The yields and average velocities of  $\alpha$ -particles on the positive-angle side decrease smoothly with increasing angles, and the values of most probable energy of  $\alpha$ -particles are nearly constant in the rest frame of the target-like nucleus (Fig. 3(b)). On the other hand, those in the c.m. system, for instance, show a sudden change between  $60^\circ$  and  $80^\circ$ , and thereafter result in an unnatural increase with increasing angles as seen in Fig. 3(a). We therefore conclude that the results obtained at positive angles mainly originate from the pre-equilibrium decay of the target-like nucleus.
- (3) The situation is very complex on the negative-angle side as well as at forward angles. The energy spectra of  $\alpha$ -particles for the Be – N channels show two peaks in the laboratory system; one corresponds roughly to the beam velocity especially for the data at  $\theta_{\text{HI}}^{\text{lab}} = -25^\circ$ . This indicates that the observed correlations originate from a fast process like projectile fragmentation. Another is situated at much lower energies. The detailed analysis is now in progress.

The observed energy spectra of pre-equilibrium decay of the target-like nucleus always show the Maxwell-Boltzmann distribution with high nuclear temperature( $T$ ). Figure 4 shows the values of  $T$  deduced from the fit as described in Ref. 2 at various angles, which is 4-5 MeV at small angles and decreases smoothly with increasing angles, reaching an equilibrium value at about  $80^\circ$ . The pre-equilibrium decay mentioned above is consistent with that expected in the hot-spot model;<sup>3)</sup> when the observed projectile-like fragment (HI) comes from transfer reactions, the excited target-like nucleus starts to rotate due to the transferred angular momenta. The direction of the above rotation is positive or negative according to the positive or negative deflection of HI. The present data therefore suggest the positive deflection of HI and the negative deflection of coincident  $\alpha$ -particles on the side of positive angles.

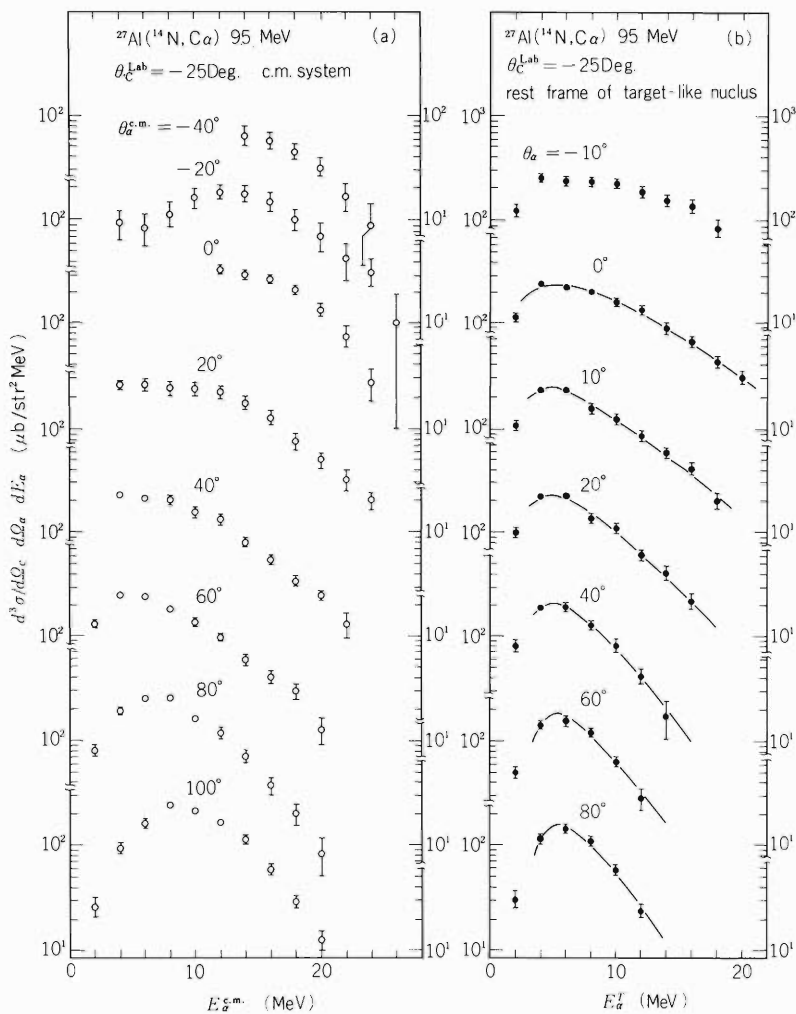


Fig. 3. Differential cross sections of  $\alpha$ -particles at various angles coincident with carbon at  $\theta_C^{\text{lab}} = -25^\circ$  in the different frame obtained from Fig. 2(e).

- Energy spectra in the c.m. system.
- Energy spectra in the rest frame of the target-like nucleus. Angles ( $\theta_\alpha^T$ ) are measured from the direction of the target-like nucleus. Solid curves show the fitted spectra as described in Ref. 2.

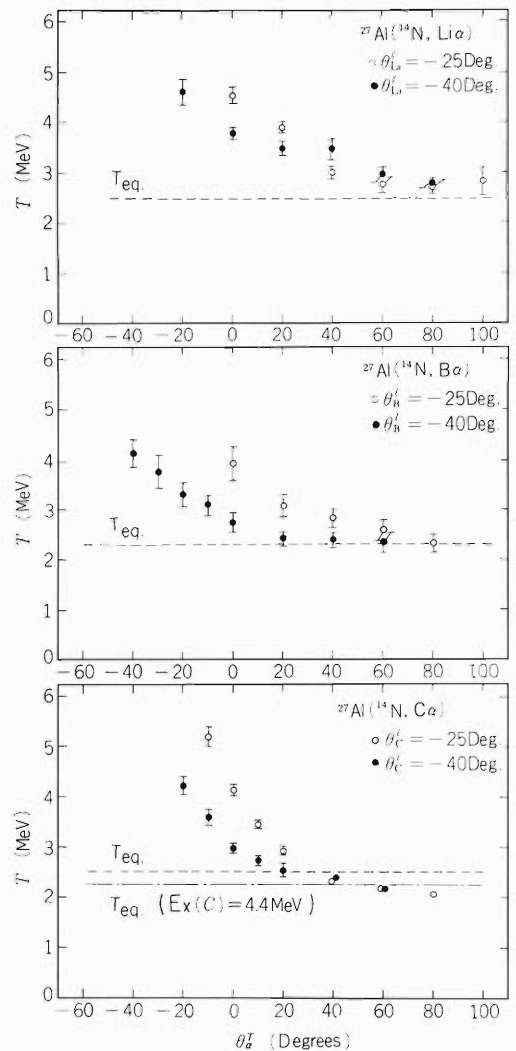


Fig. 4. Nuclear temperature plots at  $\theta_{\text{HI}}^{\text{lab}} = -25^\circ$  (open circles) and  $-40^\circ$  (solid circles) versus emission angle ( $\theta_\alpha^T$ ). Dashed lines show the equilibrium nuclear temperature of residual nuclei, and dashed-dot line shows the value when the ejected carbon is excited at 4.4 MeV.

## References

- P. Gonthier, H. Ho, M.N. Namboodiri, J.B. Natowitz, L. Adler, O. Hartin, P. Kasiraj, A. Khodai, S. Simon, and K. Hagel: Progr. in Research 1978-1979, Cyclotron Institute, Texas A & M University, p. 7.
- T. Nomura, H. Utsunomiya, T. Motobayashi, T. Inamura, and M. Yanokura: Phys. Rev. Lett., 40, 694 (1978).
- R. Weiner and M. Weström: Nucl. Phys., A286, 282 (1977).

4-10. Systematic Study of Reaction Cross Sections  
in the  $^{14}\text{N} + ^{93}\text{Nb}$  Reaction

M. Ishihara, H. Kamitsubo, T. Fukuda,\*  
M. Tanaka,\*\* H. Ogata,\*\*\* and I. Miura\*\*\*

Since the classical work<sup>1)</sup> of Wilczynski, the behaviour of the differential cross section  $\frac{d^2\sigma}{dE d\theta}$  as a function of kinetic energy  $E$  and scattering angle  $\theta$  has been used to argue the deflection function of the heavy ion reaction. So far two categories of deflection functions corresponding to orbiting<sup>1)</sup> and focusing<sup>2)</sup> have been recognized. It was further argued<sup>3)</sup> that a single parameter,

$$\eta' = Z_1 Z_2 e^2 / h v',$$

where  $v'$  is the relative velocity of two ions at the interaction barrier, may well serve as a criterion to determine the type of the deflection function. Systems with  $\eta' \lesssim 150-200$  are supposed to give rise to orbiting; the ridge of  $\frac{d^2\sigma}{dE d\theta}$  gradually moves from positive to negative angles with decreasing  $E$ .

In this work we measured  $\frac{d^2\sigma}{dE d\theta}$  for the  $^{14}\text{N} + ^{93}\text{Nb}$  reaction at 110, 159, and 209 MeV. The reaction system studied has extremely small  $\eta'$  of 10–22 in favour of orbiting. The experiment was performed at RCNP at Osaka University. The cross sections for various final channels were measured with Si-detector telescopes over an angular range from  $1.5^\circ$  to  $60^\circ$ . The measurement at very forward angles was carried out by incorporating a quadruple magnet lens and a deflection magnet to eliminate the disturbing contributions from the incident beam and the elastically scattered particles.

Some examples of Wilczynski plots are shown in Fig. 1. Contrary to the expectation, the focusing feature of the deflection functions is eminent. Namely the ridge of  $\frac{d^2\sigma}{dE d\theta}$  almost stays at a constant angle over the wide  $E$  range, and it moves to larger angles for the lowest  $E$ . No appreciable indication for crossover of the deflection angle from positive to negative is observed. This feature may be more clearly illustrated in Fig. 2, where  $\frac{d^2\sigma}{dE d\theta}$  for given  $E$  bins are plotted vs.  $\theta$ . Similar features of Wilczynski plots were observed for the other final channels. This was the case for all the incident energies used, though the favoured angle varied from  $\sim 10^\circ$  for 209 MeV to  $\sim 20^\circ$  for 110 MeV.

According to Strutinski, the angular distribution of the heavy ion reaction cross section may be approximated<sup>4)</sup> as

$$\frac{d\sigma}{d\theta} = N \left[ \exp \left\{ -\frac{(\theta - \psi)^2}{\Gamma^2} \right\} + \exp \left\{ -\frac{(\theta + \psi)^2}{\Gamma^2} \right\} \right].$$

\* Department of Physics, Osaka University.

\*\* Kobe Tokiwa Junior College.

\*\*\* Research Center for Nuclear Physics, Osaka University.

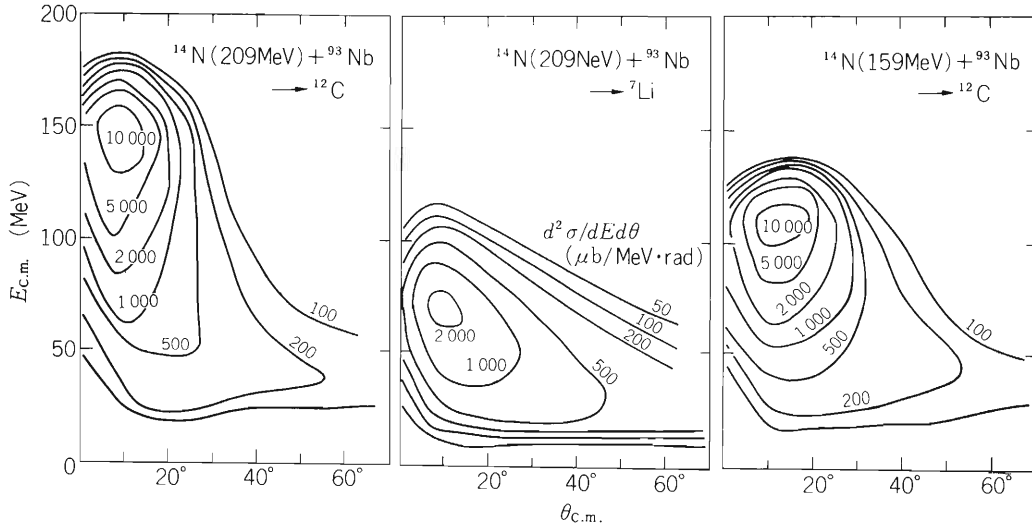


Fig. 1. The differential cross sections  $\frac{d^2\sigma}{dE d\theta}$  measured for the  $^{93}\text{Nb}(^{14}\text{N}, ^{12}\text{C})$  and  $(^{14}\text{N}, ^7\text{Li})$  reactions with incident energies of 209 and 159 MeV are shown in contour plots in the plane of the energy  $E$  vs. the scattering angle of the outgoing particle. The relative magnitude of the cross section is indicated by the number labelled to the contour line.

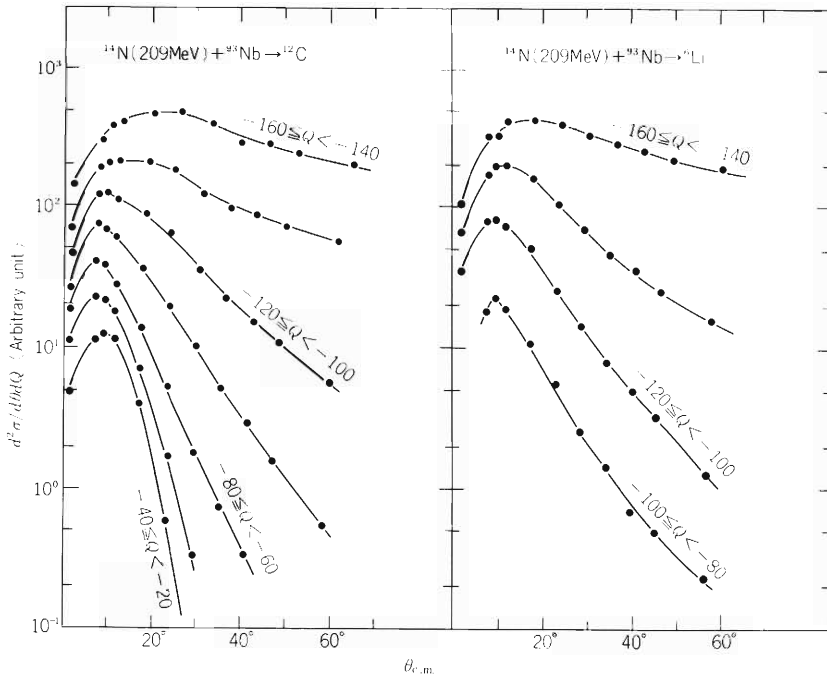


Fig. 2. The angular distributions of  $\frac{d^2\sigma}{dQ d\theta}$  obtained for given  $Q$ -values are shown for the  $^{93}\text{Nb}(^{14}\text{N}, ^{12}\text{C})$  and  $(^{14}\text{N}, ^6\text{Li})$  reactions with the 209 MeV incident energy. The angular distributions are drawn in the order of  $(-Q)$  value from the bottom to the top. The  $Q$ -value bins are taken in 20 MeV step.

Then the ridge of the cross section should nearly correspond to the deflection angle  $\psi$ . However it is to be remembered that this approximation fails at very forward angles  $\theta \lesssim 1/\ell$ , where  $\ell$  is the angular momentum of the outgoing channel. The rough evaluation of  $\ell$  values may be made using the relation,

$$\ell = R\sqrt{2\mu(E - B)} ,$$

where  $R$  is the reaction radius,  $B$  is the interaction barrier and  $\mu$  is the reduced mass. The critical angle thus deduced was at most  $3^\circ$  for the most part of the spectra, assuring the correspondence between  $\psi$  and the ridge angle observed.

The anomalous behaviour of deflection functions discussed above casts some doubt on the simple classification of reactions in terms of  $\eta'$ . Within the framework of the classical model with friction forces, the observed results may indicate that two isolated bins of initial angular momenta contribute to the reaction so that the deflection angle jumps from positive to negative sides without intersecting zero (forward) angle. To test such a hypothesis, the measurement of gamma-ray multiplicities is in progress.

#### References

- 1) J. Wilczynski: Phys. Lett., B47, 484 (1973).
- 2) J.R. Huizenga, J.R. Birkelund, W.U. Schröder, K.L. Wolf, and V.E. Viola: Phys. Rev. Lett., 37, 885 (1976).
- 3) J. Galin: Colloque du Journal de Physique, 37, C5-83 (1976).
- 4) V.M. Strutinski: Phys. Lett., 44B, 245 (1973).

4-11. Spin Polarization of  $^{12}\text{B}$  in the  $^{197}\text{Au}(^{19}\text{F}, ^{12}\text{B})$   
Reaction at 186 MeV

M. Ishihara, T. Shimoda, H. Kamitsubo, H. Fröhlich,\*  
K. Nagatani, T. Udagawa,\*\* and T. Tamura\*\*

In a series of previous reports, we reported on the measurements of spin polarization  $P$  of  $^{12}\text{B}$  for several heavy ion reactions. The reactions so far studied were limited to a few nucleon transfer reactions such as ( $^{14}\text{N}, ^{12}\text{B}$ ), ( $^{10}\text{B}, ^{12}\text{B}$ ), ( $^{12}\text{C}, ^{12}\text{B}$ ), and ( $^{13}\text{C}, ^{12}\text{B}$ ). These reactions all exhibited a common feature of  $P$ : By defining polarization axis as parallel to  $\vec{k}_i \times \vec{k}_f$ ,  $P$  is positive for high energies  $E$  of  $^{12}\text{B}$  and goes to negative as  $E$  is decreased. Obviously this behaviour is opposite to the prediction of the classical model in terms of friction forces. The theoretical analyses<sup>1),2)</sup> which followed revealed that such a feature of  $P$  is actually a signature of a direct reaction process in which a cluster is transferred in a single step reaction.

Provided that this conclusion is established, one may use the spin polarization as a probe to explore the degree of influence of the direct reaction process in various reactions. In this respect it would be most interesting to study some exotic reactions with large energy and mass transfers, since such reactions are usually regarded as typical deep inelastic reactions due to multiple scatterings.

Here we report on the result<sup>3)</sup> of such an investigation performed for the  $^{197}\text{Au}(^{19}\text{F}, ^{12}\text{B})$  reaction at 186 MeV. The measurement was made using the cyclotron at Texas A & M University. Experimental techniques used were similar to those of the previous experiments. However special cares were exerted to reduce background  $\beta$  rays from and outside of the target by improving the beam optics and by employing a long duty cycle of the pulsed beam. The latter helped to sufficiently reduce the contamination of long-life  $\beta$  rays which strongly appeared in this reaction.

The Wilczynski plot for this reaction is shown in Fig. 1. The distribution of  $\frac{d^2\sigma}{dE d\theta}$  exhibits a feature of a strongly damped reaction with cross sections concentrated in the low energy region in the vicinity of the Coulomb barrier. Moreover the pattern of the contour plot is suggestive of negative angle deflections in accord with the expectation from the friction model. Figure 2 shows the energy spectrum and the spin polarization measured at  $25^\circ$ . The feature of a damped reaction is again eminent in the energy spectrum with  $Q$ -values involved of typically ( $-100$ ) MeV. In spite of such appearance of the energy spectrum, the spin polarization shows the characteristic feature of  $Q$ -value dependence, which should be attributed to the direct reaction mechanism. In fact calculated results (shown by solid lines) using the DWBA theory<sup>2)</sup> reproduce the experimental data fairly well over a wide region of  $^{12}\text{B}$  energy. However it is also to be remarked that the theory deviates from the data at very low energies. This indicates the presence of more complicated reaction processes for those most damped components.

\* Physikalisches Institut, Universität Erlangen-Nürnberg, Erlangen, West Germany.

\*\* Department of Physics, University of Texas, Austin, Texas.

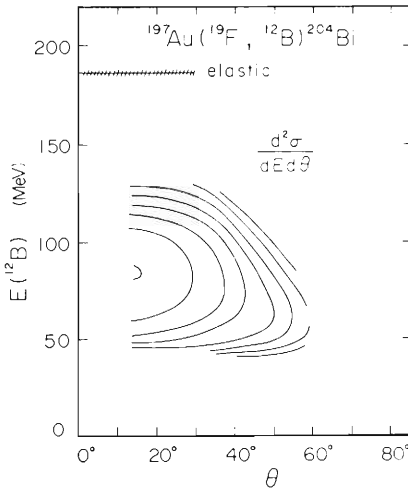


Fig. 1. The Wilczynski plot of  $\frac{d^2\sigma}{dE d\theta}$  obtained for the  $^{197}\text{Au}(^{19}\text{F}, ^{12}\text{B})$  reaction at 186 MeV. The contour lines of  $\frac{d^2\sigma}{dE d\theta}$  are drawn in steps of a factor of 2.

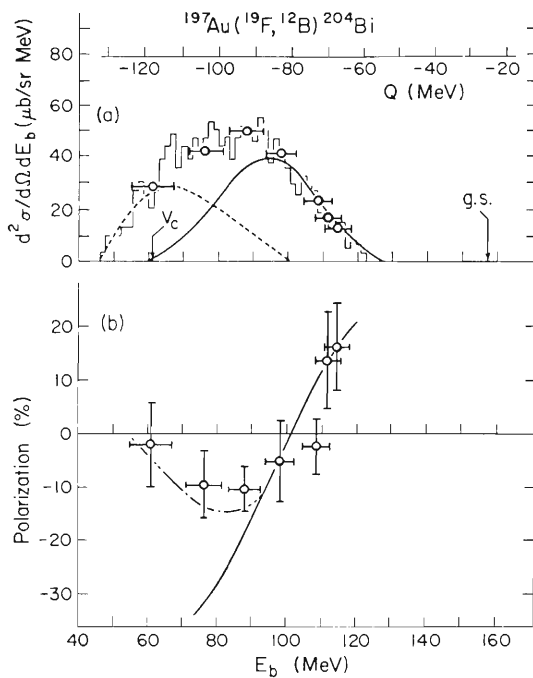


Fig. 2. The cross section  $\frac{d^2\sigma}{d\Omega dE}$  (a) and the spin polarization  $P$ (b) of the reaction  $^{197}\text{Au}(^{19}\text{F}, ^{12}\text{B})$  measured at  $25^\circ$  with the incident energy 186 MeV are shown as a function of the energy  $E_b$  of  $^{12}\text{B}$  and  $Q$ -value. The experimental points are shown by open circles. The histogram in (a) shows the energy spectrum obtained in a separate measurement using Si detectors. Solid lines represent the results of the DWBA calculation. The dot line in (a) corresponds to cross sections in excess of the calculation. The dot-dash line for  $P$  was obtained by attributing the zero polarization to the extra component in excess of the calculated cross section.

In the past years, heavy ion reactions have been customarily described<sup>4)</sup> in an unified way using the classical model in terms of the composite dinuclear system. In such descriptions the reactions are presumed to occur via multiple nucleon scatterings (or exchanges), regardless of the magnitudes of energy and mass transfers. However the present result exhibits the presence of a regime of reactions where the above unified picture is certainly inappropriate. Combined with the related studies<sup>5)</sup> on energy spectra, the dominant role of the simple direct reaction appears to be general in those heavy ion reactions induced by relatively light ( $A \lesssim 20$ ) ions.

Two of the authors (M.I and H.K) are indebted to Cyclotron Institute, Texas A & M University, for the support during this experiment.

## References

- 1) M. Ishihara, K. Tanaka, T. Kammuri, K. Matsuoka, and M. Sano: *Phys. Lett.*, 73B, 281 (1978).
- 2) T. Udagawa and T. Tamura: *Phys. Rev. Lett.*, 41, 1770 (1978).
- 3) M. Ishihara, T. Shimoda, H. Fröhlich, H. Kamitsubo, K. Nagatani, T. Udagawa, and T. Tamura: *ibid.*, 43, 111 (1979).
- 4) For a review see for instance: W. Schröder and J.R. Huizenga: *Ann. Rev. Nucl. Sci.*, 27, 465 (1977).
- 5) H. Fröhlich, T. Shimoda, M. Ishihara, K. Nagatani, T. Udagawa, and T. Tamura: *Phys. Rev. Lett.*, 42, 1518 (1979).

## 4-12. Isotopic Dependence of the Fission-Like Events in the 115 MeV Nitrogen-Induced Reactions on Nickel

M. Yanokura, I. Kohno, Y. Nagame, and H. Nakahara

The aim of the present work is to investigate the isotopic dependence of the heavy ion reactions in a relatively light system, with emphasis on the behavior of the fission-like events. Fissionability depends on a nuclear mass in the same charge systems. Reaction systems investigated are  $^{14}\text{N} + ^{58}\text{Ni}$  and  $^{14}\text{N} + ^{64}\text{Ni}$ . The neutron to proton ratios varied from 1.07 in  $^{58}\text{Ni}$  to 1.29 in  $^{64}\text{Ni}$ .

The experiment was performed with the 115 MeV  $^{14}\text{N}$  for the cyclotron. Self-supporting foils of  $^{58}\text{Ni}$  and  $^{64}\text{Ni}$  of about  $600 \mu\text{g}/\text{cm}^2$  thickness were used. A single counter telescope consisting of a gas  $\Delta E$  counter and a  $300 \mu\text{m}$  thick SSD was used. Product charges from  $Z = 6$  to 16 were well resolved. The quarter-point angles  $\theta_{1/4}$  were observed to be the same within the experimental error for the two reaction systems, i.e.,  $23.5^\circ$ . The maximum angular momentum  $\ell_{\text{max}}$ , and the interaction radius evaluated from the  $\theta_{1/4}$  were  $51 \hbar$  and  $8.83 \pm 0.05 \text{ fm}$ , respectively. The measurement was performed from  $\theta_{\text{lab}} = 12^\circ$  to  $45^\circ$ . In the energy spectra of the reaction products, the characteristic single bell-shaped kinetic energy peaks for the strongly damped events could be observed for  $Z > 11$ . Shape of energy spectra was no meaningful difference between the two reaction systems. The centroid energies of the products with  $Z > 11$  were found to be independent of the angles for  $\theta_{\text{c.m.}} > 25^\circ$ , and close to the values expected from the Coulomb repulsion energies of the two touching spheres ( $r_0 = 1.44 \text{ fm}$ ).

Figure 1 shows the energy-integrated differential cross sections for various reaction products in the  $^{14}\text{N} + ^{58}\text{Ni}$  system. It is to be noted that Al which is six charges away from the projectile

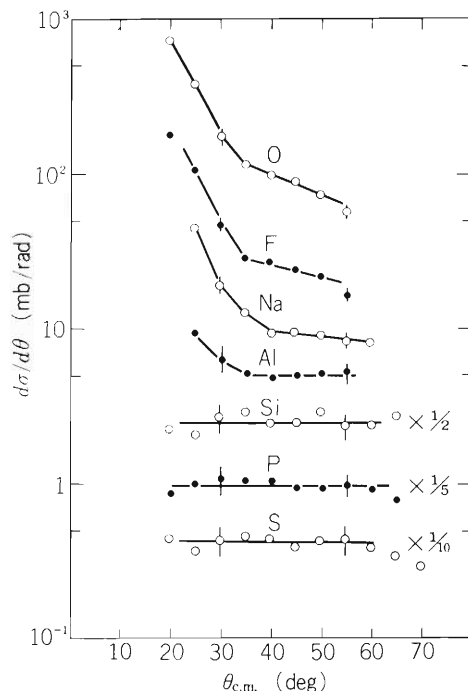


Fig. 1. The energy integrated differential cross sections for various products from  $^{14}\text{N} + ^{58}\text{Ni}$  reaction.

still shows a slightly forward peaking, whereas Si, P and S show uniform distributions from  $20^\circ$  to  $70^\circ$  (in the unit of  $d\sigma/d\theta$ ). The charge distributions of the two reaction systems at  $\theta_{\text{c.m.}} = 40^\circ$  are shown in Fig. 2. At this angle the events are mostly those due to strongly damped events. There is an obvious difference in cross section for  $Z > 12$  between two reaction systems. However they are nearly the same for  $Z < 11$ . The difference is 5 mb when the cross sections for  $Z = 14, 15,$  and  $16$  are summed. If the reaction products of large atomic numbers originate from deeply-inelastic collisions, it is difficult to explain this difference. On the other hand, if we assume the distributions to originate from fission events, the difference in question can be explained by the difference in the fission barrier height of the composite nuclei. By liquid-drop model calculation,<sup>1)</sup> the symmetric fission barrier heights for  $^{78}\text{Br}$  and  $^{72}\text{Br}$  were deduced to be 14 MeV and 6.5 MeV, respectively, for  $\ell_{\text{max}}$ . When the fission cross section is estimated by using the Alice code<sup>2)</sup> considering the single-particle effects<sup>3)</sup> and using the barrier heights predicted in Ref. 1, it is found to be 4 mb for  $^{14}\text{N} + ^{58}\text{Ni}$  system and 0.04 mb for  $^{14}\text{N} + ^{64}\text{Ni}$  system.

We found the isotopic difference in the cross sections of  $^{14}\text{N} + \text{Nickel}$  isotope systems. Thus, the result for the difference between the two reactions, 5 mb, is in good agreement with the liquid-drop model prediction.

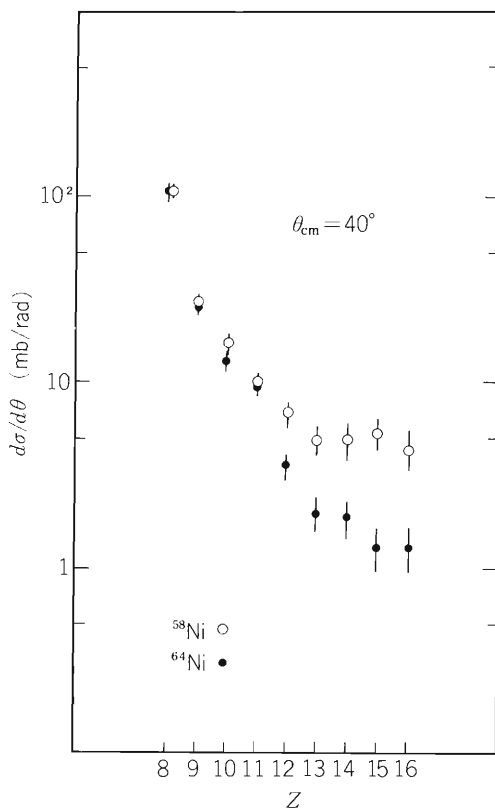


Fig. 2. The charge distribution of  $^{14}\text{N} + ^{58}\text{Ni}$  and  $^{14}\text{N} + ^{64}\text{Ni}$  systems at 40 degrees in c.m. system.

## References

- 1) S. Cohen, F. Plasil, and W. J. Swiatecki: *Ann. Phys.*, **82**, 557 (1974).
- 2) M. Blann: U.S. Energy Research and Development Administration Rep, No. COO-3493-29(1976), unpublished; F. Plasil: ORNL/TM-6054(1977), unpublished.
- 3) W. D. Myers and W. J. Swiatecki: *Ann. Phys.*, **55**, 395 (1969).

### 4-13. Preequilibrium Alpha Particle Emission Following Heavy-Ion Transfer Reactions

M. Ishihara, H. Kamitsubo, T. Fukuda,\*  
M. Tanaka,\*\* H. Ogata,\*\*\* and I. Miura\*\*\*

In an earlier experiment,<sup>1)</sup> we studied the alpha particle emission accompanying deep inelastic (or quasi elastic) reactions by bombarding  $^{93}\text{Nb}$  with 90 and 110 MeV  $^{14}\text{N}$  ions. At these energies we found that the main source of the alpha particles can be attributed to the sequential breakup of excited light fragments produced in the primary deep inelastic reactions. In the present report, we discuss an extended study of such alpha particle emission at a higher bombarding energy. The same  $^{14}\text{N} + ^{93}\text{Nb}$  system was studied using 210 MeV  $^{14}\text{N}$  ions from the RCNP cyclotron at Osaka University. The light (projectile-like) fragments were detected at  $22^\circ$ , while the coincident alpha particles were detected at several angles in and out of the scattering plane.

The results at 210 MeV showed some distinctive differences as compared to those at lower bombarding energies: 1) The energy integrated angular correlations (Fig. 1) show forward peaked distributions similar to those for lower energies. However the coincident cross sections are dramatically increased by a factor of 10 – 30. The multiplicity  $M_\alpha$  is 0.3 – 0.7 as compared to  $M_\alpha$  of typically 0.05 at lower energies. 2) The contribution from the light fragment breakup is minor, while several indications are in favour of sequential alpha emission from heavy fragments.

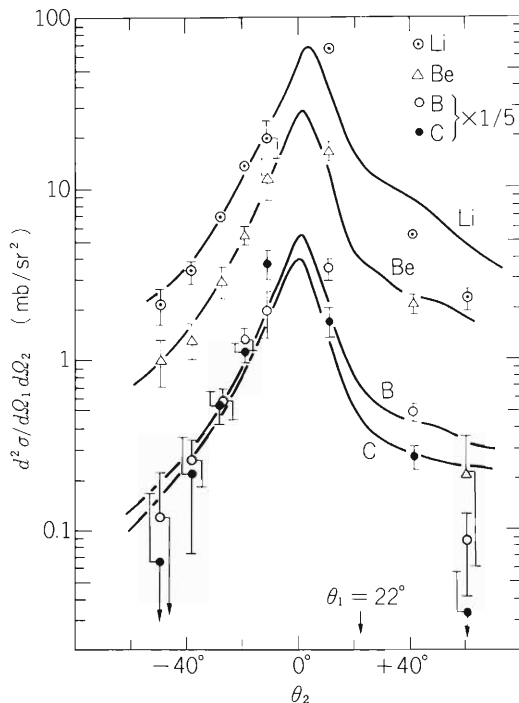


Fig. 1. The in-plane angular correlations between alpha particles and different light reaction products (Li, Be, B, and C) obtained in the  $^{14}\text{N} + ^{93}\text{Nb}$  reaction with 210 MeV incident energy. The energy integrated coincidence cross sections are plotted as a function of the alpha detection angle  $\theta_2$ . The light reaction products were detected at  $\theta_1 = 22^\circ$ . The solid curves correspond to the theoretical fits in terms of a “hot spot” model.

\* Department of Physics, Osaka University.

\*\* Kobe Tokiwa Junior College.

\*\*\* Research Center for Nuclear Physics, Osaka University.

These arguments are based on the analysis in terms of three-body kinematics and the systematic inspection of the energy correlations.

In the past years, a variety of possible mechanisms <sup>2),3)</sup> have been conjectured to account for the coincident alpha particle emission. So far none of them have been able to reproduce the data quantitatively. In the following we present a comparison of the experimental data with calculated results essentially based on the "hot spot" model of Ref. 2. The basic assumptions used for the calculation are as follows. In the course of the transfer reaction, the hot spot left in the surface region of the host nucleus rotates about the center of the nucleus by carrying the whole angular momentum transferred. At the same time the hot spot decays by emitting alpha particles as well as by relaxing towards the equilibration of the total nucleus. The relaxation property may be represented by the time variations of effective temperature  $T$  and volume  $V$  of the hot spot, the latter of which is related to the moment of inertia of the hot spot. In the calculation the three-body Coulomb trajectory and the shadow effect were treated in a similar way as in Ref. 2. The assumption of the isolated rotation of the hot spot from the rest of nucleus differs from the assumption of the original model<sup>2)</sup> that the hot spot and the rest of nucleus are stuck and rotate together. This assumption produced significant effects in the calculated results, enhancing the focusing of the alpha particle emission towards the direction of the moving hot spot and eliminating the influence of shadowing.

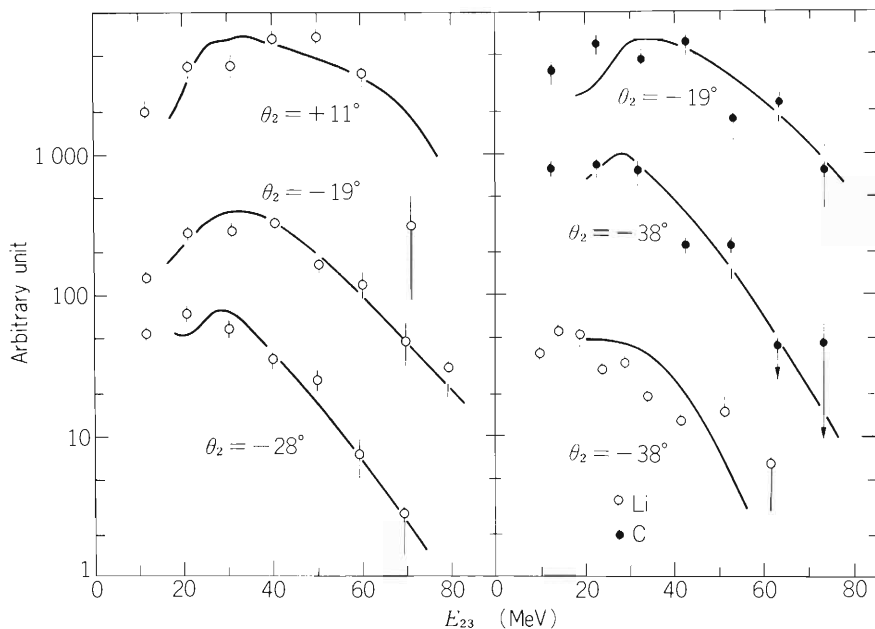


Fig. 2. The energy spectra of alpha particles obtained at different angles  $\theta_2$  in coincidence with Li and C. The abscissa  $E_{23}$  represents the relative kinetic energy of alpha particles in the rest frame of the  $(\alpha + \text{heavy fragment})$  system. The solid lines are due to the theoretical calculation.

Figures 1 and 2, respectively, depict the comparison between experiment and calculation for the energy integrated angular correlations and for the energy spectra of coincident alpha particles. In the calculation the relaxation time of  $2.5 \times 10^{-22}$  sec for both  $T$  and  $V$  and the initial temperature  $T = 7.0$  MeV were used. The overall agreement is fair, suggesting that the model used can reasonably simulate the undergoing reaction process. The relaxation time deduced is a

couple of times larger than the mean free time of the nucleon in the nucleus and may comply with the typical reaction time of the preequilibrium process observed in the reactions induced by light ions such as nucleons and alpha particles.

#### References

- 1) T. Shimoda, M. Ishihara, H. Kamitsubo, T. Motobayashi, and T. Fukuda: IPCR Cyclotron Report, 46, (1978).
- 2) P.A. Gottshalk and M. Weström: Phys. Rev. Lett., 39, 1250 (1977).
- 3) for instance, D.H.E. Gross and J. Wilczynski: Phys. Lett., 40, 1074 (1978).

#### 4-14. $\gamma$ -Ray Multiplicity Measurement Following Preequilibrium $\alpha$ -Particle Emission in $^{14}\text{N}$ -Induced Reactions

H. Utsunomiya, T. Nomura, M. Ishihara,  
T. Sugitate, K. Ieki, and Y. Gono

We reported in our previous papers<sup>1)</sup> that energy spectra of fast  $\alpha$ -particles emitted in low-energy heavy-ion reactions are well understood as the preequilibrium (PE) decay occurring before projectile- and target-nuclei fuse completely into the compound nucleus reaching thermal equilibrium. Using the hot-spot model of PE phenomena,<sup>2)</sup> the relaxation time of energy was deduced from the PE  $\alpha$ -particle spectra which were strongly dependent on the emission angles. We here report  $\gamma$ -ray multiplicities following the PE  $\alpha$ -particle emission in  $^{14}\text{N}$ -induced reactions in order to study relaxation of angular momenta.

Self-supporting  $^{93}\text{Nb}$ ,  $^{116}\text{Sn}$ , and  $^{159}\text{Tb}$  targets of 3-4 mg/cm<sup>2</sup> thickness were bombarded with  $^{14}\text{N}$  beam at 95 and 115 MeV from the cyclotron.  $\alpha$ -particles were detected with Si  $\Delta E$ -E(50 – 2000  $\mu\text{m}$ ) counter telescopes placed at various angles. A 7.5 cm  $\times$  7.5 cm NaI(Tl) detector usually mounted at 10 cm from the target and at 90° to the beam in the reaction plane was used to measure  $\gamma$ -rays. The measurement of angular correlation between  $\alpha$ -particles and  $\gamma$ -rays was also made in the  $^{93}\text{Nb} + ^{14}\text{N}$  reaction at  $E_{\text{lab}} = 95$  MeV using a 5 cm  $\times$  5 cm NaI(Tl) detector placed at 30 cm from the target. An absorber composed of 0.5 mm-Pb, 0.6 mm-Cd, and 1.0 mm-Cu was placed in front of the above two detectors. The overall efficiency  $\Omega_{\gamma}$  averaged over the observed  $\gamma$ -ray spectrum was 2.1 % for the former detector and 0.11 % for the latter.

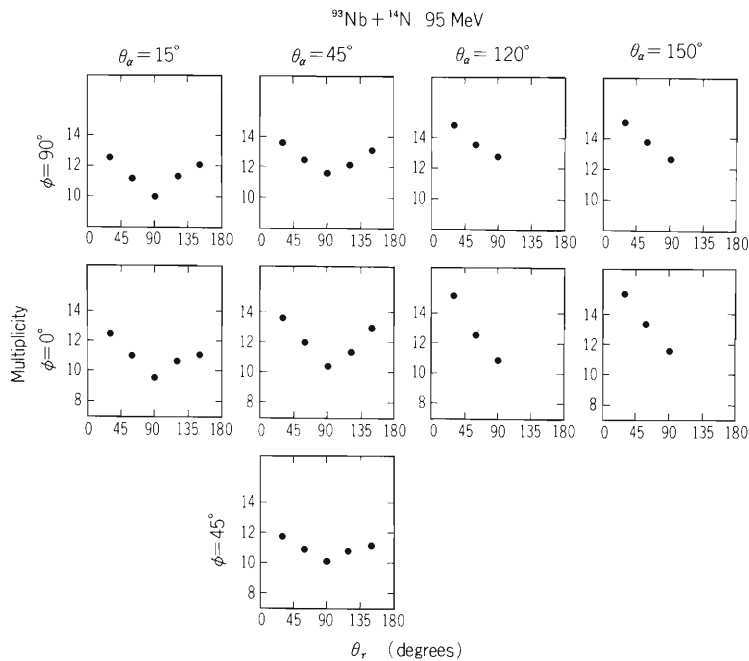


Fig. 1.  $\alpha$ - $\gamma$  angular correlations measured in the  $^{93}\text{Nb} + ^{14}\text{N}$  reaction at  $E_{\text{lab}} = 95$  MeV.  $\theta$  denotes the angle of  $\alpha$  counter with respect to the beam and  $\phi$  is the angle of the  $\gamma$ -ray counter measured from the normal direction of the reaction plane.

The threshold energy was 100 keV and 80 keV respectively.

The  $\gamma$ -ray multiplicity was determined by the following relation,  $M_\gamma(\theta_\alpha, E_\alpha) = N_{\text{coin}}(\theta_\alpha, E_\alpha) / \Omega_\gamma N_{\text{sing}}(\theta_\alpha, E_\alpha)$ , where  $N_{\text{sing}}$  and  $N_{\text{coin}}$  represent singles and coincident events, respectively, for  $\alpha$ -particles as a function of the emission angle  $\theta_\alpha$  and the kinetic energy  $E_\alpha$ . Figure 1 shows in-plane and out-of-plane  $\alpha$ - $\gamma$  angular correlations, where the z-axis was chosen along the beam direction and x-axis along the normal to the scattering plane. It should be noted that the distribution of  $\gamma$ -rays is almost independent of the emission angle of  $\alpha$ -particles and its intensity for out-of-plane ( $\phi = 0^\circ$  and  $45^\circ$ ) is roughly equal to that for in-plane ( $\phi = 90^\circ$ ). Therefore, in order to discuss relative values of  $M_\gamma$ , it is enough to measure  $M_\gamma$  at one angle. Hereafter, as the value of  $M_\gamma$ , we use the value obtained by the above mentioned 7.5 cm  $\times$  7.5 cm NaI(Tl) detector. Figures 2 – 3 show the dependence of  $M_\gamma$  on the kinetic energies ( $E_\alpha$ ) and the emission angles ( $\theta_\alpha$ ) of  $\alpha$ -particles in various  $^{14}\text{N}$ -induced reactions. It is remarkable that  $M_\gamma$  is practically independent of  $E_\alpha$  when measured at the same angle, although it slightly decreases with increasing  $E_\alpha$  especially in the case of the  $^{159}\text{Tb}$  target. On the other hand,  $M_\gamma$  rapidly decreases with decreasing emission angles  $\theta_\alpha$  of PE  $\alpha$ -particles.

The fact that  $M_\gamma$  is almost independent of  $E_\alpha$  disagrees apparently with the result of the previous  $\gamma$ -ray multiplicity measurement<sup>3)</sup> in  $^{159}\text{Tb}(^{14}\text{N}, \alpha xn\gamma)^{169-x}\text{Yb}$  reactions, in which  $M_\gamma$  of a particular residual nucleus decreases remarkably with the increase of  $E_\alpha$ . However, this difference can be understood in the following way. In the previous experiment we specified the final nuclei  $^{169-x}\text{Yb}$  by measuring their discrete  $\gamma$ -rays with a Ge(Li) counter. Then, the values of  $M_\gamma$  are strongly affected by an entry line of a particular residual nucleus, which is really expected to cause the observed  $E_\alpha$  dependence. In fact, the strong  $E_\alpha$  dependence on  $M_\gamma$  is appreciably weakened if we average  $M_\gamma$  values over three dominant reaction channels, i.e.,  $\alpha 3n$ ,  $\alpha 4n$ , and  $\alpha 5n$ . Moreover, the solid angle of the  $\alpha$  counter in the previous measurement subtended 0.52 sr, corresponding  $\theta_\alpha = 15.2^\circ - 28.1^\circ$ . Since  $M_\gamma$  decreases rapidly (as noted in the present results)

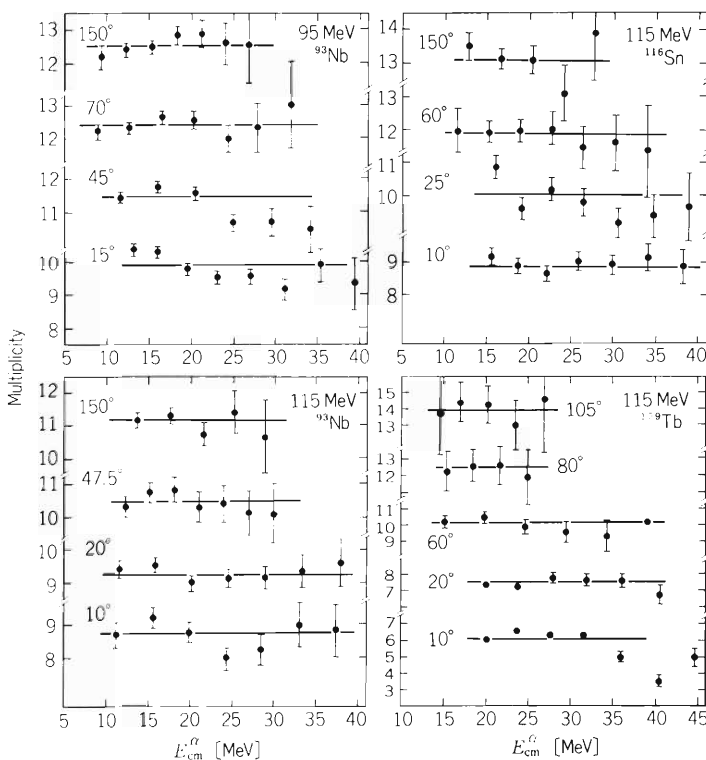


Fig. 2. Dependence of the average  $\gamma$ -multiplicity on kinetic energies of emitted  $\alpha$ -particles in various  $^{14}\text{N}$ -induced reactions. Solid lines show the energy-integrated average  $\gamma$ -multiplicity.

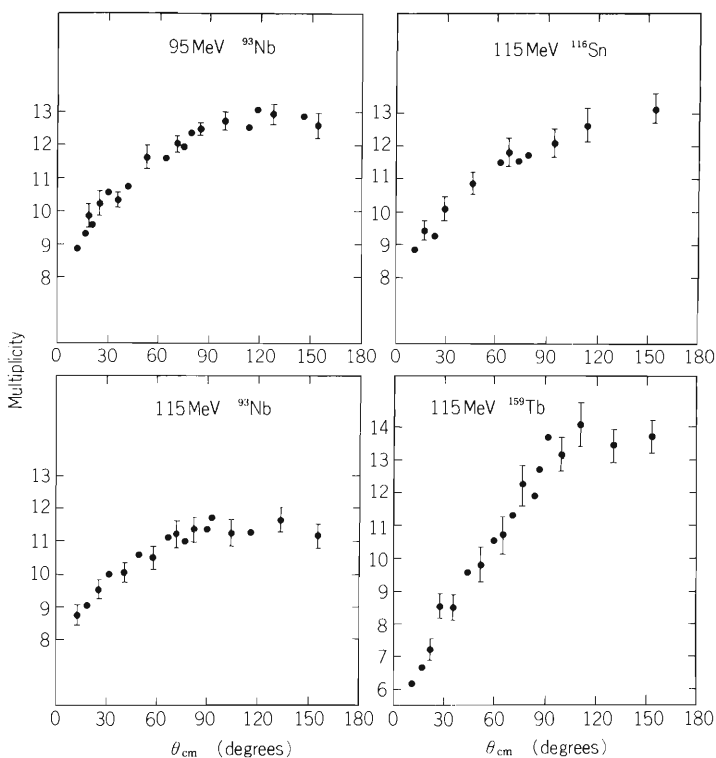


Fig. 3. Dependence of the energy-integrated average  $\gamma$ -multiplicity on the emission angles of  $\alpha$ -particles in various  $^{14}\text{N}$ -induced reactions.

and  $E_\alpha$  increases appreciably with the decrease of  $\theta_\alpha$ , the above large solid angle can also be considered to yield the apparent  $E_\alpha$  dependence on  $M_\gamma$ .

The present results (weak  $E_\alpha$  but strong  $\theta_\alpha$  dependence on  $M_\gamma$ ) are consistent with the hot-spot interpretation of PE  $\alpha$  particles. Since the small emission angle  $\theta_\alpha$  is considered to correspond to the short reaction time as mentioned in the previous papers,<sup>1)</sup> the relative angular momenta brought in are not transferred into the internal degree of freedom of the whole nucleus but are carried by the hot-spot. When the PE  $\alpha$  particles are emitted from this hot spot, they carry away large angular momenta, the values of which are roughly determined by the ratio of moment of inertia of the hot-spot to that of  $\alpha$  particles, which is independent of  $E_\alpha$  but strongly dependent on  $\theta_\alpha$  through the size of the hot-spot.

## References

- 1) T. Nomura, H. Utsunomiya, T. Motobayashi, T. Inamura, and M. Yanokura: Phys. Rev. Lett., 40, 694 (1978); T. Nomura, H. Utsunomiya, T. Inamura, T. Motobayashi, and T. Sugitate: J. Phys. Soc. Japan, 46, 335 (1979); H. Utsunomiya, T. Nomura, T. Inamura, T. Sugitate, and T. Motobayashi: Nucl. Phys., A 334, 127 (1980).
- 2) R. Weiner and M. Wesröm: *ibid.*, A286, 282 (1977).
- 3) T. Inamura, T. Kojima, T. Nomura, T. Sugitate, and H. Utsunomiya: Phys. Lett., 84B, 71 (1979).

#### 4-15. Relaxation of Angular Momentum Following Preequilibrium $\alpha$ Emission in Heavy-Ion Reactions

H. Utsunomiya, T. Nomura, M. Ishihara,  
T. Sugitate, K. Ieki, and Y. Gono

Two prominent features of the average  $\gamma$ -ray multiplicity ( $M_\gamma(\theta)$ ) measured in coincidence with the preequilibrium (PE)  $\alpha$  particles at angle  $\theta$  are summarized as follows<sup>1)</sup>:

- i)  $M_\gamma(\theta)$  is small when  $\theta$  is small and increases rapidly with the increase of  $\theta$ , almost reaching a constant value at backward angles.
- ii)  $M_\gamma(\theta)$  is almost independent of the kinetic energy of  $\alpha$  particles ( $E_\alpha$ ) measured at the same angle  $\theta$ .

In this report we try to explain the above features of  $M_\gamma(\theta)$  from the hot-spot model for PE  $\alpha$  emission.

Based on the diffusion model presented by Wolschin and Nörenberg,<sup>2)</sup> the relaxation of angular momentum is described by the following formula:

$$M_\gamma(t) = M_\gamma^{\text{eq}} (1 - e^{-t/\tau_\ell}) . \quad (1)$$

Here,  $M_\gamma(t)$  is the average  $\gamma$ -multiplicity which is associated with a certain reaction time  $t$ ,  $M_\gamma^{\text{eq}}$  the multiplicity after compound nucleus (CN) formation and  $\tau_\ell$  the relaxation time of angular momentum. From Eqn. (1), we obtain

$$M_\gamma^{\text{eq}} - M_\gamma(t) \propto e^{-t/\tau_\ell} , \quad (2)$$

which is very similar to the expression for the relaxation of energy discussed in our previous papers,<sup>3)</sup> i.e.,

$$T(t) - T_{\text{eq}} \propto e^{-t/\tau_\epsilon} , \quad (3)$$

with equilibrium nuclear temperature  $T_{\text{eq}}$  and the relaxation time of energy  $\tau_\epsilon$ . We plotted  $M_\gamma^{\text{eq}} - M_\gamma(\theta)$  and  $T(\theta) - T_{\text{eq}}$  versus  $\theta$  in Fig. 1, where  $T(\theta)$  is deduced from an energy spectrum of  $\alpha$  particles at  $\theta$  in the same way as in Ref. 3. A remarkable feature is that both  $M_\gamma^{\text{eq}} - M_\gamma(\theta)$  and  $T(\theta) - T_{\text{eq}}$  decay roughly exponentially with the same decay constant  $\mu$  in each reaction.

Inamura et al. have reported that in the  $^{14}\text{N} + ^{159}\text{Tb}$  reaction at 95 MeV angular momenta in the entrance channel leading to the PE (fast)  $\alpha$  emission are localized just above the critical angular momentum for complete fusion.<sup>4)</sup> For simplicity, if we assume a definite value  $L_0$  for the transferred angular momentum,  $L_0$  is expressed by

$$L_0 = I_R + \ell_\alpha + \ell_0 , \quad (4)$$

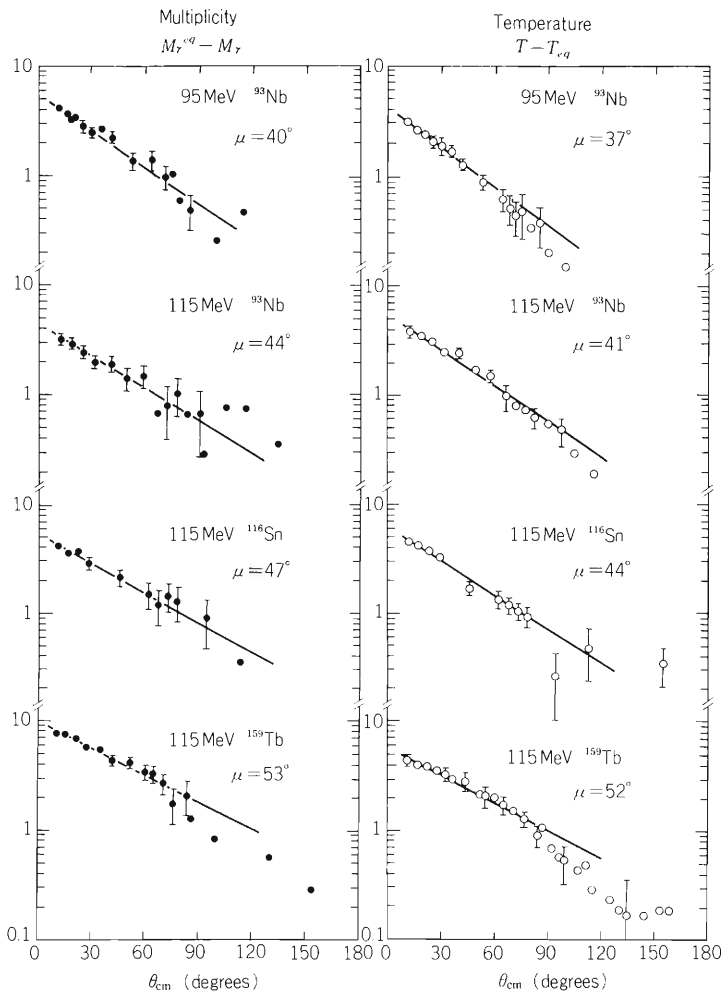


Fig. 1.  $M_{\gamma}^{\text{eq}} - M_{\gamma}(\theta)$  and  $T(\theta) - T_{\text{eq}}$  versus the emission angle in various  $^{14}\text{N}$ -induced reactions. The decay constant derived from the straight line is given for each reaction.

where  $I_{\text{R}}$  is the averaged angular momentum of residual nuclei which is usually related to the measured  $M_{\gamma}$  by

$$I_{\text{R}} = f \cdot M_{\gamma} \quad , \quad (5)$$

with constant value of  $f$ .  $\ell_{\alpha}$  and  $\ell_{\text{O}}$  are the angular momenta carried off by  $\alpha$ -particle and other nucleons like neutron and proton. If we ignore the dependence of  $\ell_{\text{O}}$  on  $\theta$ , we obtain

$$M_{\gamma}^{\text{eq}} - M_{\gamma}(\theta) = \frac{1}{f} \left( \ell_{\alpha}(\theta) - \ell_{\alpha}^{\text{eq}} \right) \quad , \quad (6)$$

where  $\ell_{\alpha}^{\text{eq}}$  is the angular momentum carried off by evaporation of  $\alpha$ -particle after the compound nucleus (CN) formation. The present results indicate, therefore, that  $\ell_{\alpha}$  is large at forward angles and decreases with increasing  $\theta$  with the decay constant  $\mu$ .

The above feature can be explained by the hot-spot model in the following way. Consider that the hot-spot sitting in the surface region of the composite system and at distance  $R$  from its center has angular momentum  $L_0$  and nuclear temperature  $T$ . Then, the angular momentum  $\ell_{\alpha}$  of  $\alpha$ -particle emitted from the hot-spot is roughly given by

$$\ell_{\alpha}(\theta) \approx 4R^2 \cdot L_0 / I(\theta) \quad , \quad (7)$$

where  $I(\theta)$  is the moment of inertia of the hot spot emitting  $\alpha$  particles at  $\theta$ . In the same way,

$l_{\alpha}^{\text{eq}}$  is given by

$$l_{\alpha}^{\text{eq}} \approx 4 \cdot L_0 / \frac{2}{5} A, \quad (8)$$

with mass  $A$  of CN. On the other hand, the hot spot has the angular velocity  $\omega(\theta)$  given by

$$\omega(\theta) = L_0 \hbar / I(\theta). \quad (9)$$

Combining Eqns. (6) – (9), we can deduce  $\omega(\theta)$  from the measured values of  $M_{\gamma}(\theta)$  on the assumption that values of  $M_{\gamma}$  at backward angles are equal to  $M_{\gamma}^{\text{eq}}$ .

Assuming that the reaction time  $t$  is related to  $\omega(\theta)$  by  $\Delta t = \Delta\theta/\omega(\theta)$ ,  $\tau_{\ell}$  and  $\tau_{\epsilon}$  can be estimated from

$$\tau_{\ell} \approx \tau_{\epsilon} = \int_0^{\mu} \frac{d\theta}{\omega(\theta)}. \quad (10)$$

Resultant relaxation time and parameters used in the present analysis are listed in Table 1. The relaxation time estimated is  $(4 - 5) \times 10^{-22}$  sec.

Table 1 Relaxation time of angular momentum and parameters used in the present analysis in various  $^{14}\text{N}$ -induced reactions.

Target	$E_{\text{in}}^{\text{lab}}$ (MeV)	$E_{\text{cm}}$ (MeV)	$V_{\text{c}}^{\text{a)}$ (MeV)	$R_{\text{cr}}^{\text{b)}$ (fm)	$L_{\text{cr}}$ ( $\hbar$ )	$L_{\text{O}}^{\text{c)}$ ( $\hbar$ )	$L_{\alpha}^{\text{eqd)}$ ( $\hbar$ )	$\mu$ (degree)	$\tau_{\text{R}}$ ( $10^{-22}$ sec)
$^{93}\text{Nb}$	95	80.8	38.4	6.94	34.5	36.5	3.41	40	3.7
$^{93}\text{Nb}$	115	98.2	38.4	6.94	41.0	43.0	4.02	44	4.4
$^{116}\text{Sn}$	115	100.8	44.6	7.29	42.3	44.3	3.41	47	5.2
$^{159}\text{Tb}$	115	103.9	54.0	7.83	43.5	45.5	2.63	53	5.3

$$\text{a) } V_{\text{c}} = \frac{z_1 z_2 e^2}{R} \quad R = 1.55 (A_1^{1/3} + A_2^{1/3})$$

$$\text{b) } R_{\text{cr}} = r_{\text{cr}} (A_1^{1/3} + A_2^{1/3}) \quad r_{\text{cr}} = 1.0 \pm 0.07$$

J. Galin et al.: Phys. Rev. C, 9, 1018 (1974).

$$\text{c) } L_0 = L_{\text{cr}} + 2$$

$$\text{d) } L_{\text{eq}} = \frac{4}{5} L_0$$

## References

- 1) H. Utsunomiya, T. Nomura, M. Ishihara, T. Sugitate, K. Ieki, and Y. Gono: A preceding report.
- 2) G. Wolschin and W. Nörenberg: Phys. Rev. Lett., 41, 691 (1978).
- 3) T. Nomura, H. Utsunomiya, T. Motobayashi, T. Inamura, and M. Yanokura: *ibid.*, 40, 694 (1978).
- 4) T. Inamura, M. Ishihara, T. Fukuda, T. Shimoda, and K. Hiruta: Phys. Lett., 68B, 51 (1977).

## 5. NUCLEAR PHYSICS

### Nuclear Spectroscopy and Instrumentation

#### 5-1. Recoil-Distance Lifetime Measurement of States in $^{118}\text{Xe}$

T. Katou, H. Kumagai, Y. Tendow,  
Y. Gono, and A. Hashizume

Lifetimes of several levels in the ground band of  $^{118}\text{Xe}$  were measured with a plunger apparatus reported before.<sup>1)</sup>

The levels of interest were populated by means of the reaction  $^{107}\text{Ag}(^{14}\text{N}, 3n)^{118}\text{Xe}$  at an incident energy of 62 MeV. The target consisted of a layer of  $400\ \mu\text{g}/\text{cm}^2$   $^{107}\text{Ag}$  metal evaporated onto a  $0.9\ \text{mg}/\text{cm}^2$  gold foil and the stopper for recoil nuclei was a gold foil  $20\ \text{mg}/\text{cm}^2$  in thickness. The experimental conditions were similar to those described in Ref. 2.

Some of the  $\gamma$ -ray spectra obtained at different distance ( $D$ ) between the target and the stopper are given in Fig. 1. From such spectra a quantity  $R$  which was defined by  $R = I_0 / (I_0 + I_s)$  was determined, where  $I_0$  is the intensity of  $\gamma$ -rays emitted after the recoil nuclei have been stopped in the stopper and  $I_s$  is the intensity emitted in flight. Values of  $I_0$  and  $I_s$  were estimated from least squares computer fits of appropriate parts of the  $\gamma$ -ray spectra. Some decay curves giving  $R$  versus  $D$ , obtained from the analysis, are shown in Fig. 2. The mean velocity of the recoil nuclei was determined to be  $0.0087c$  from the difference in centroid energies of shifted and unshifted  $\gamma$ -rays.

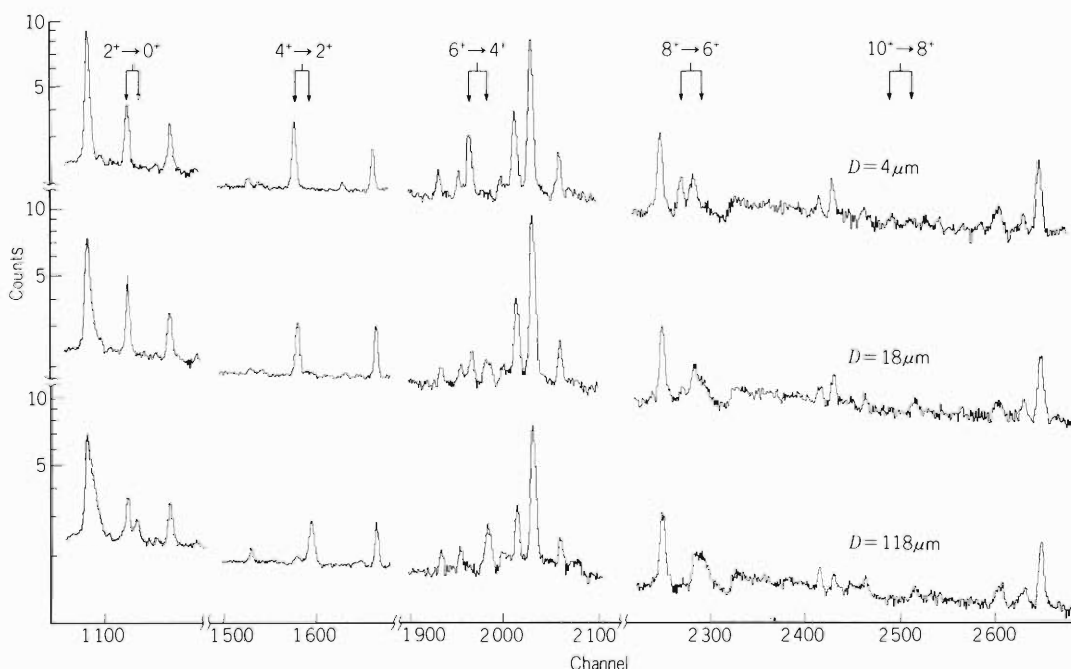


Fig. 1. Spectra for the  $^{107}\text{Ag}(^{14}\text{N}, 3n)^{118}\text{Xe}$  reaction, taken at several target-stopper separations.

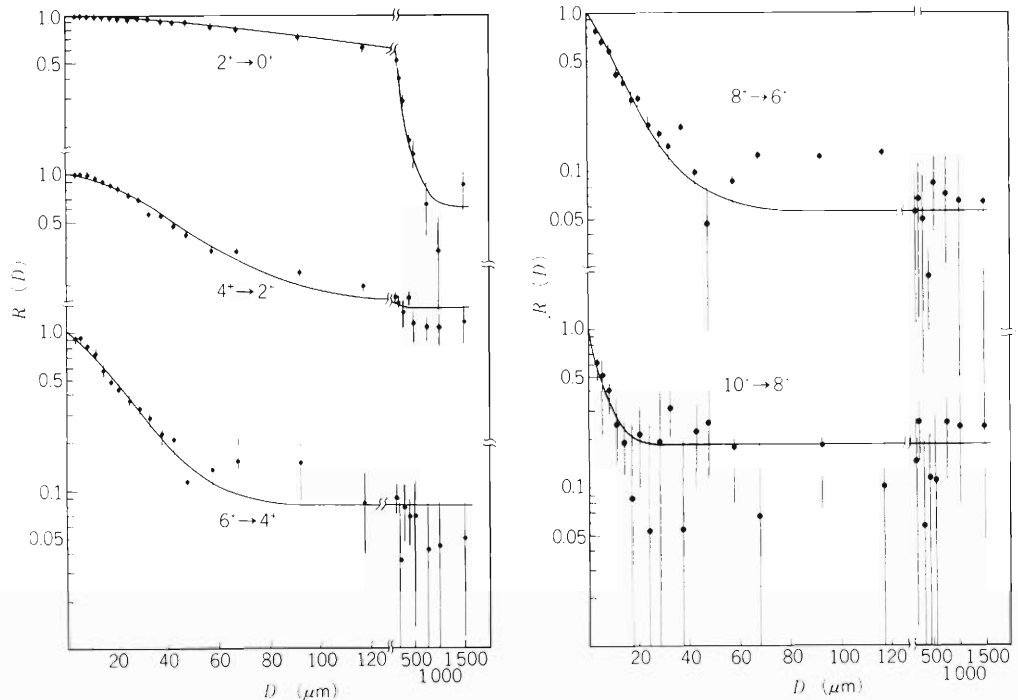


Fig. 2. Measured and calculated decay curves for several transitions in  $^{118}\text{Xe}$ . The solid lines are the results of the fitting procedure.

In order to extract the lifetimes from the function  $R(D)$ , we have used the nearly same method of correction and the error analysis proposed by Strum et al.<sup>3)</sup> Corrections for side-feeding transitions were not included in the present analysis.

The lifetimes obtained in the present experiment are shown in Table 1. The value for  $2^+$  state is in agreement with the value reported in Ref. 4, while that for  $4^+$  is not.

Table 1. Lifetimes of levels in  $^{118}\text{Xe}$ .

Transition	Energy	Lifetimes (ps) present exp.	Ref. 4
$2^+ - 0^+$	337.3	66.6 (3.9)	69 (5)
$4^+ - 2^+$	472.8	9.48 (1.77)	17 (4)
$6^+ - 4^+$	586.4	4.77 (0.25)	<5
$8^+ - 6^+$	676.7	4.42 (0.16)	
$10^+ - 8^+$	741.5	<2.3	

## References

- 1) T. Katou, H. Kumagai, Y. Tendow, Y. Awaya, and A. Hashizume: IPCR Cyclotron Progr. Rep., 11, 85 (1977).
- 2) T. Katou, H. Kumagai, Y. Tendow, Y. Awaya, and A. Hashizume: *ibid*, 12, 68 (1978).
- 3) R.J. Strum and M.W. Guidry: Nucl. Instr. Meth., 138, 345 (1976).
- 4) A.M. Bergdolt, J. Chevallier, J.C. Merdinger: Proc. Intern. Conf. on Nuclear Structure, Tokyo, p.359 (1977).

5-2.  $\gamma$ -Ray Spectroscopy in the  $^{144}\text{Nd} + ^{20}\text{Ne}$  Reaction

A. Hashizume, T. Katou, Y. Tendow, and H. Kumagai

When medium weight nucleus  $^{144}\text{Nd}$  is bombarded with  $^{20}\text{Ne}$ -ions in the energy range between 100 and 150 MeV, the dominant types of reactions are complete and incomplete fusions, and many reaction residues are produced in the mass range from 159 to 160. Though this experiment was initially designed to study high spin states of  $^{160}\text{Yb}$  excited by the  $(^{20}\text{Ne}, 4n)$  reaction,<sup>1)</sup> the origins of many  $\gamma$ -rays emitted from other reaction products were determined.

A 97.8 % enriched  $^{144}\text{Nd}$  target of self-supporting metallic foil of 26 mg/cm<sup>2</sup> in thickness was bombarded by 100 to 150 MeV  $^{20}\text{Ne}$ -ions. The prompt  $\gamma$ -rays and those from short-life radioactivities have been measured by Ge(Li) detectors. The  $\gamma$ -ray spectra from short-life activities were observed about 3 ms after the activation of 1 ms for each modulation cycle of the ion source.

When  $^{144}\text{Nd}$  was bombarded by 100 MeV  $^{20}\text{Ne}$ -ions, the  $\gamma$ -rays from radioactive nuclei of  $^{160}\text{Yb}$ ,  $^{161}\text{Yb}$ ,  $^{160}\text{Tm}$ ,  $^{161}\text{Tm}$ ,  $^{161}\text{Er}$ , and  $^{160}\text{Ho}$  were observed.  $^{160}\text{Er}$  is also expected to be produced by the  $(^{20}\text{Ne}, \alpha)$  reaction or as decay product of  $^{160}\text{Tm}$ (9.2m), but there is no means to detect it by  $\gamma$ -rays because no  $\gamma$ -ray is emitted in electron capture decay of  $^{160}\text{Er}$ .

The decay scheme of  $^{161}\text{Yb}$  has not yet been established. Only 599.8 and 631.5 keV and other three  $\gamma$ -rays have been reported.<sup>2)</sup> The observed  $\gamma$ -ray energies and intensity ratio are in good agreement with the above reported values. The half-life (4.2m) was also in agreement within the experimental error. Figure 1 shows the yield of the above two  $\gamma$ -rays as a function of incident energy. Because of thick target, the activity was saturated after it reached a maximum at about 125 MeV of  $^{20}\text{Ne}$ -ions. The existence of  $^{161}\text{Yb}$  activities in reaction residues confirms the first observation of  $(^{20}\text{Ne}, 3n)$  reaction in this mass region, though this type of reaction has been recognized in  $^{116}\text{Sn} + ^{20}\text{Ne}$ .<sup>3)</sup> The excited states in  $^{161}\text{Yb}$  are not well known though there has been reported 232 keV de-exciting  $\gamma$ -ray from  $17/2^+$  state to  $13/2^+$  state.<sup>4)</sup> The 232 keV  $\gamma$ -ray in prompt spectrum does not show the excitation feature of  $(^{20}\text{Ne}, 3n)$  reaction as expected, indicating that this  $\gamma$ -ray is probably contaminated by that from  $(^{20}\text{Ne}, 4n)$  reaction residues.

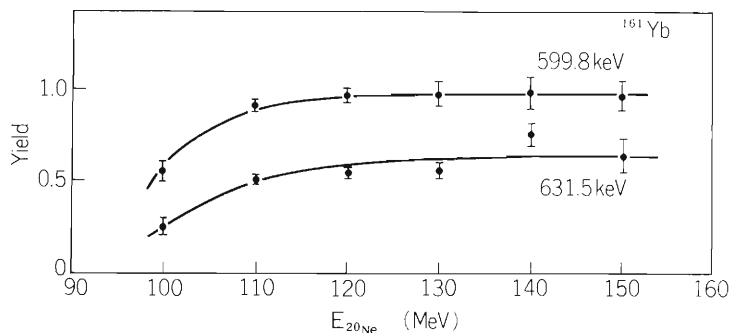


Fig. 1. Relative yield curves of  $^{161}\text{Yb}$  taken with 599.8 and 631.5 keV  $\gamma$ -rays.

Figure 2 shows the yield curves of  $^{160}\text{Yb}$  (4.8 m) produced by  $^{144}\text{Nd}(^{20}\text{Ne}, 4n)$  reaction obtained by measuring with 173.7 and 215.5 keV  $\gamma$ -rays and the dashed line shows the excitation function taken by prompt 636.3 keV ( $10^+ - 8^+$ )  $\gamma$ -ray in  $^{160}\text{Yb}$ , normalized to the same value as that for 215.5 keV  $\gamma$ -ray at 110 MeV of incident beam. If the half-life of  $\beta^-$  or electron capture decay is short compared to the time for taking in-beam prompt  $\gamma$ -ray spectrum, the excitation function taken with the prompt  $\gamma$ -rays and the yield curve of radioactivity as a function of incident beam energies should have the same character. The curves in Fig. 2 show this feature.

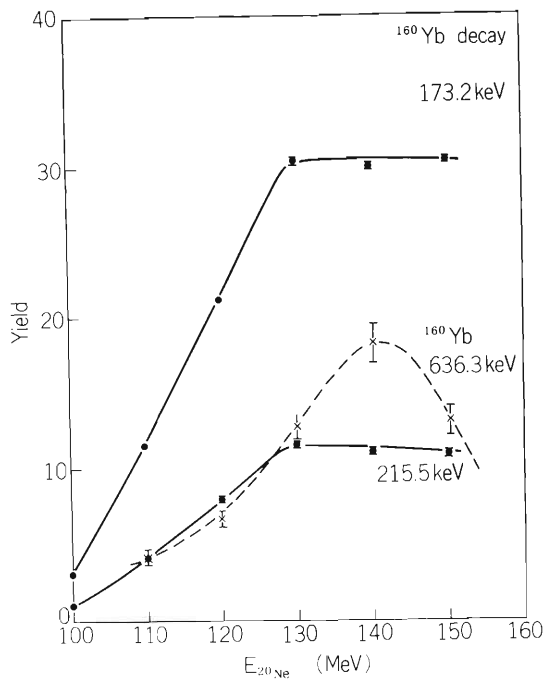


Fig. 2. Relative yield curve of  $^{160}\text{Yb}$ . The dotted line shows the excitation function taken with 636.3 keV ( $10^+ - 8^+$ )  $\gamma$ -ray in  $^{160}\text{Yb}$ .

Two  $\gamma$ -rays 166.1 and 177.0 keV are reported for the decay of  $^{159}\text{Yb}$  (1.7 m).<sup>5)</sup> Figure 3 shows the yield curves of  $^{159}\text{Yb}$  taken with these  $\gamma$ -rays. These curves keep nearly the same character as the excitation function taken by 447.4 keV de-exciting  $\gamma$ -ray in  $^{159}\text{Yb}$  (Fig. 4). These results confirm the results of Gromov et al.<sup>5)</sup> De Boer has reported 173.9 and 215.7 keV  $\gamma$ -rays from  $^{158}\text{Yb}$  or possibly  $^{159}\text{Yb}$ .<sup>6)</sup> Our results exclude the possibility that these  $\gamma$ -rays are emitted from  $^{160}\text{Yb}$  decay.

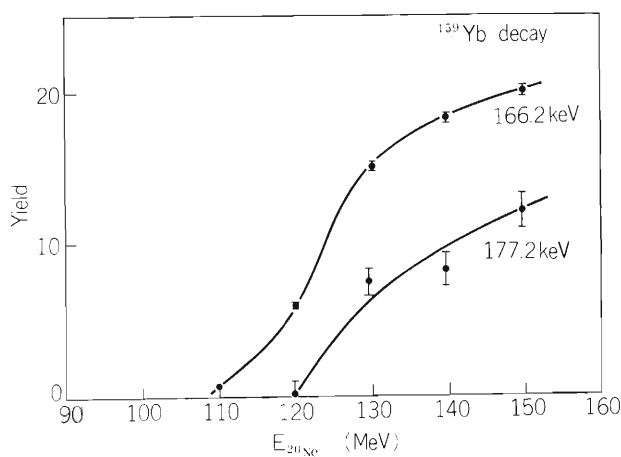


Fig. 3. Relative yield curve of  $^{159}\text{Yb}$ .

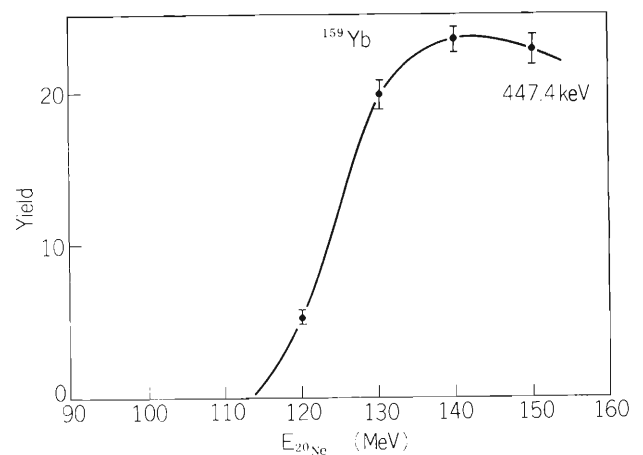


Fig. 4. Excitation function of  $^{159}\text{Yb}$  taken with 447.4 keV prompt  $\gamma$ -ray.

## References

- 1) A. Hashizume, T. Katou, Y. Tendow, and H. Kumagai: IPCR Cyclotron Progr. Rep., 12, 74 (1978).
- 2) I. Adam, G. Beyer, M. Gonusek, K. Gromov, K. Zibert, U. Kalinnikov, A. Liatuszynskii, S. Strusny, and M. Yakhim: Izv. Akad. Nauk SSSR, Ser. Fiz., 38, 1572 (1974).
- 3) I. Skokev: *ibid.*, 42, 777 (1978).
- 4) D. Sarantites, J. Barker, M. Halbert, D. Hensley, R. Dayras, E. Eichler, N. Johnson, and S. Gronemeyer: Phys. Rev., C14, 2138 (1976).
- 5) K. Gromov, M. Honusek, I. Penev, H. Siebert, J. Zuber, A. Latuszynski, A. Potempa, and K. Zuber: Acta Phys. Polo., B8, 317 (1977).
- 6) F. de Boer, M. Cardoso, P. Goudsmit, P. Koldewijn, J. Konijin, and B. Meijer: CERN 70-30, 2, 937 (1970).

5-3. In-Beam  $\alpha$ -,  $\gamma$ -Spectroscopic Study on  $^{214}\text{Rn}$ 

Y. Gono, K. Hiruta, T. Nomura, M. Ishihara,  
H. Utsunomiya, T. Sugitate, and K. Ieki

The ground state  $\alpha$ -decay has for a long time been studied to obtain informations on nuclear masses as well as on the characteristics of the levels. The recent development of the heavy ion accelerators has made this kind of experiments more important for the study of the nuclei which locate far from the  $\beta$ -stability line. Several years ago, Nomura et al. performed the pioneer work on the  $\alpha$ -decay from the short lived isomer in  $^{216}\text{Ra}$  applying the in-beam spectroscopic techniques.<sup>1)</sup> Recently Lieder et al.<sup>2)</sup> reported on the  $\alpha$ -decay from the  $8^+$  isomer in  $^{212}\text{Po}$  using a  $\Delta E - E$  counter telescope to identify the reaction channel  $^{207}\text{Bi}(\alpha, p)^{212}\text{Po}$ .

In this experiment, the latter technique was applied to the heavy ion induced reaction. The nucleus  $^{214}\text{Rn}$  could be easily reached by specifying a reaction channel of  $^{208}\text{Pb}(^{12}\text{C}, \alpha xn)^{216-x}\text{Rn}$ .

An enriched target  $^{208}\text{Pb}$  of about  $1 \text{ mg/cm}^2$  was irradiated with 79 MeV  $^{12}\text{C}$  beam from the IPCR cyclotron. The emitted charged particles were detected by a  $\Delta E - E$  counter telescope which consists of two  $450 \text{ mm}^2$  annular Si surface barrier detectors of  $50 \mu\text{m}$  and  $2000 \mu\text{m}$  thickness. A  $100 \mu\text{m}$  Al-foil was placed in front of them to stop the scattered beam. Those were set at about 40 mm from the target. Another Si surface barrier detector of  $200 \text{ mm}^2$  and  $1000 \mu\text{m}$  thickness was set at  $150^\circ$  and 50 mm apart from the target to detect the discrete  $\alpha$ -lines from the product nuclei. The  $\gamma$ -rays were also measured with a  $70 \text{ cm}^3$  Ge(Li) detector at  $90^\circ$  in coincidence with the charged particles which were detected by the counter telescope.

The discrete  $\alpha$ -lines observed in this work are listed in Table 1. The  $\alpha$ -ray energies of 10.48 and 10.66 MeV are higher than those of the ground state  $\alpha$ -decay in this mass region. Hence they must be the  $\alpha$ -decay from the excited states. They are assigned to the  $\alpha$ -decay from the ( $6^+$ ) and ( $8^+$ ) states in  $^{214}\text{Rn}$  to the  $0^+$  ground state in  $^{210}\text{Po}$  based on the following facts: (i) Those lines were observed in coincidence with the continuum  $\alpha$ -particles. (ii) The  $\alpha$ -particle

Table 1. Energies and intensities of the discrete  $\alpha$ -lines observed in the  $^{12}\text{C} + ^{208}\text{Pb}$  reaction. ( $E = 79 \text{ MeV}$ )

Reaction channel	Product nucleus	$E_\alpha$	$I_\alpha$ (in the total projection spectrum)
$8\text{Be}$	$^{212}\text{Po}$	8.798	46
$\alpha 2n$	$^{214}\text{Rn}$	9.037	100 (100) <sup>a)</sup>
$p 4n$	$^{215}\text{Fr}$	9.345	23
$\alpha 2n$	$^{214}\text{Rn}$	10.48	4.7 (2.2) <sup>a)</sup>
$\alpha 2n$	$^{214}\text{Rn}$	10.66	4.6 (4.3) <sup>a)</sup>

a) Intensities in the continuum energy  $\alpha$  particle gated discrete  $\alpha$ -particle spectrum.

emission channel in this reaction is dominated by the  $^{208}\text{Pb}(^{12}\text{C}, \alpha 2n)^{214}\text{Rn}$  channel since the total continuum  $\alpha$ -particle energy spectrum was well reproduced in shape by the spectrum observed in coincidence with the 9.037 MeV  $\alpha$ -line which had been known as the  $0^+_{\text{grd}}(^{214}\text{Rn}) \rightarrow 0^+_{\text{grd}}(^{210}\text{Po})$  transition. (iii) Furthermore those energies of the two  $\alpha$ -lines fit well to those transition energies which were obtained after the construction of the level scheme of  $^{214}\text{Rn}$  using the  $\gamma$ -rays data. The level scheme of  $^{214}\text{Rn}$  could be constructed taking the  $\gamma$ -rays which appeared prominently in the spectrum in coincidence with the continuum  $\alpha$ -particles and is shown in Fig. 1. Level schemes of  $^{212}\text{Po}$ (Ref. 2) and  $^{216}\text{Ra}$ (Ref. 1) were also referred in its construction.

The half-life of the  $(8^+)$  state in  $^{214}\text{Rn}$  was deduced to be 7 ns using the time spectra between these  $\gamma$ -rays and the continuum  $\alpha$ -particles.

Preliminary analysis was performed to obtain the reduced  $\alpha$ -decay width  $\gamma_{\alpha}^2$  for the  $\alpha$ -transition from the  $(8^+)$  state in  $^{214}\text{Rn}$ . The penetrability factor was calculated after

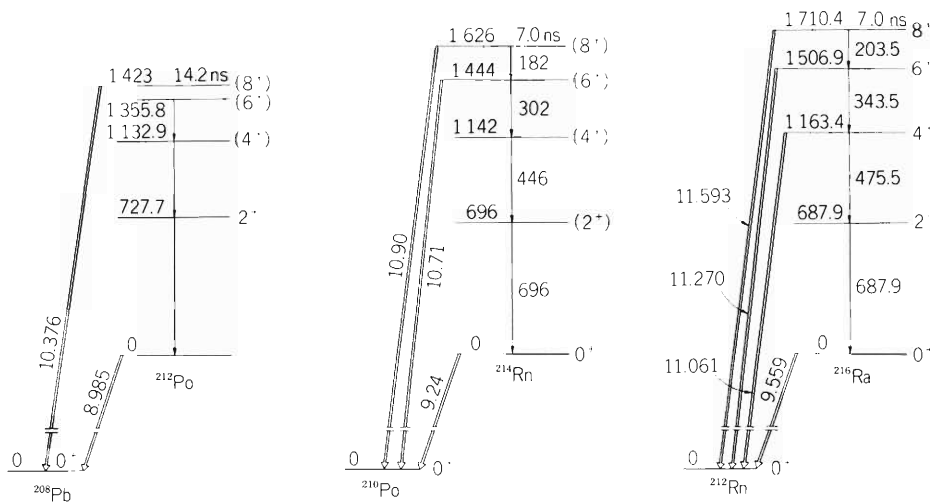


Fig. 1. Level schemes of  $N = 128$  isotones  $^{212}\text{Po}$ (Ref. 2),  $^{214}\text{Rn}$ , and  $^{216}\text{Ra}$  (Ref. 1). Levels and the  $\alpha$ -decays from the excited states in  $^{214}\text{Rn}$  are resulted from the present work. The  $\alpha$ -decay energies are given by  $Q_{\alpha}$ -values.

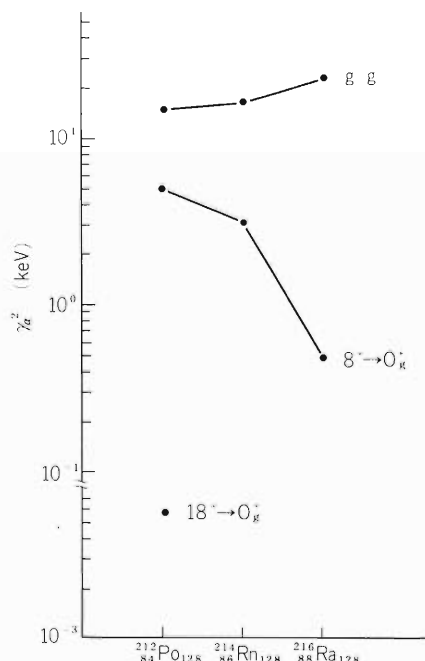


Fig. 2. The reduced  $\alpha$ -decay widths  $\gamma_{\alpha}^2$  for  $\alpha$ -transitions in  $N = 128$  isotones.

Rasmussen's paper.<sup>3)</sup> The present result is shown in Fig. 2 as well as those of the decays of  $8^+(^{216}\text{Ra})$ ,  $8^+(^{212}\text{Po})$  and the ground state  $\alpha$ -decays of these nuclei.

The reduced widths  $\gamma_\alpha^2$  of the  $8^+ \rightarrow 0^+$  transitions are smaller than those of the  $0^+_{\text{grd}} \rightarrow 0^+$  transitions for these nuclei.

The reduced widths  $\gamma_\alpha^2$  of the  $8^+ \rightarrow 0^+$  transitions decrease as the atomic number increases for these  $N = 128$  isotones in contrast to the increasing tendency of those of the  $0^+_{\text{grd}} \rightarrow 0^+_{\text{grd}}$  transitions in these nuclei.

#### References

- 1) T. Nomura, K. Hiruta, M. Yoshie, H. Ikezoe, T. Fukuda, and O. Hashimoto: *Phys. Lett.*, 58B, 273 (1975).
- 2) R. M. Lieder, J. P. Bibeletz, H. Beuscher, O. R. Haenni, M. Müller-Veggian, A. Neskakis, and C. Mayer-Böricke: *Phys. Rev. Lett.*, 41, 742 (1978).
- 3) J. O. Rasmussen: *Phys. Rev.*, 113, 1593 (1959).

## 6. ATOMIC AND SOLID-STATE PHYSICS

### 6-1. X-Rays Following Multiple Inner-Shell Ionization (4)

Y. Awaya, T. Katou, H. Kumagai, T. Tonuma,  
Y. Tendow, K. Izumo, T. Takahashi,  
A. Hashizume, and T. Hamada

The spectra of Mo, Ag, and Sn L X-rays induced by N-ions and He-ions were measured by using a Bragg crystal spectrometer.<sup>1)</sup> There are few reports on heavy-ion-excited L X-rays from heavy target atoms.<sup>2)-4)</sup>

A flat crystal of Ge(111) was used for Mo and Ag L X-rays and that of LiF(200) for Sn L X-rays. The incident energy of projectiles ranged from 4.8 MeV/amu to 8.2 MeV/amu. The detection of X-rays was made by using a side-window gas flow type proportional counter with a 1  $\mu\text{m}$  polypropylene window operated at atmospheric pressure using a mixture of 90 % argon and 10 % methane gases. The integrated beam current was kept constant at each angle and the spectrometer was controlled automatically. The thickness of target foils was about 1 mg/cm<sup>2</sup> for Ag and Sn and about 3 mg/cm<sup>2</sup> for Mo.

Some examples of L X-ray spectra are shown in Figs. 1 and 2. The arrows with the symbol  $L^m M^n \alpha$  show the positions of peaks with  $m$  L-shell and  $n$  M-shell vacancy configuration in the

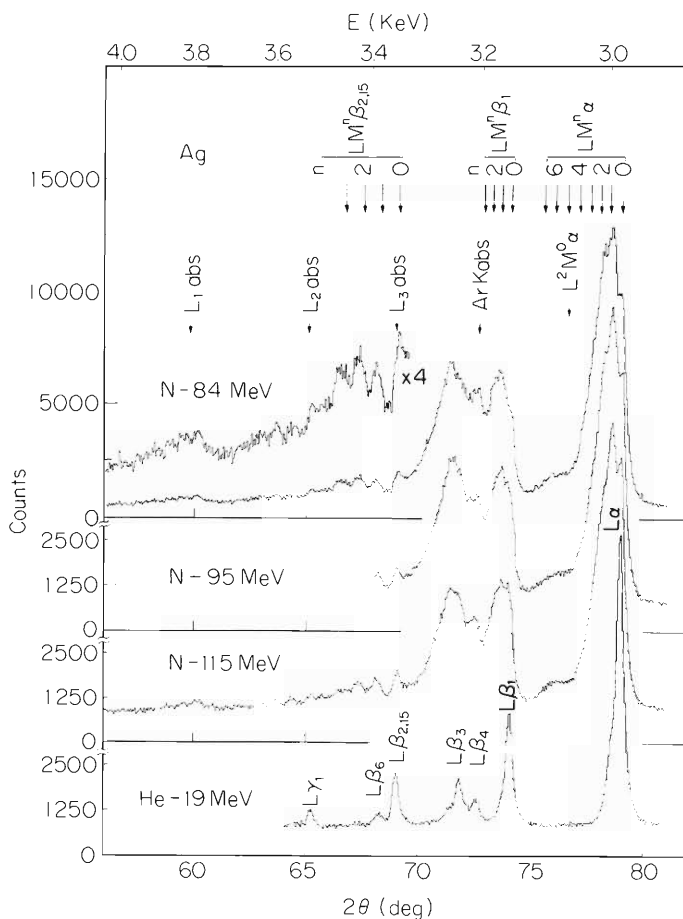


Fig. 1. Mo L X-ray spectra excited by N- and He-ions. The incident energies are shown in the figure.

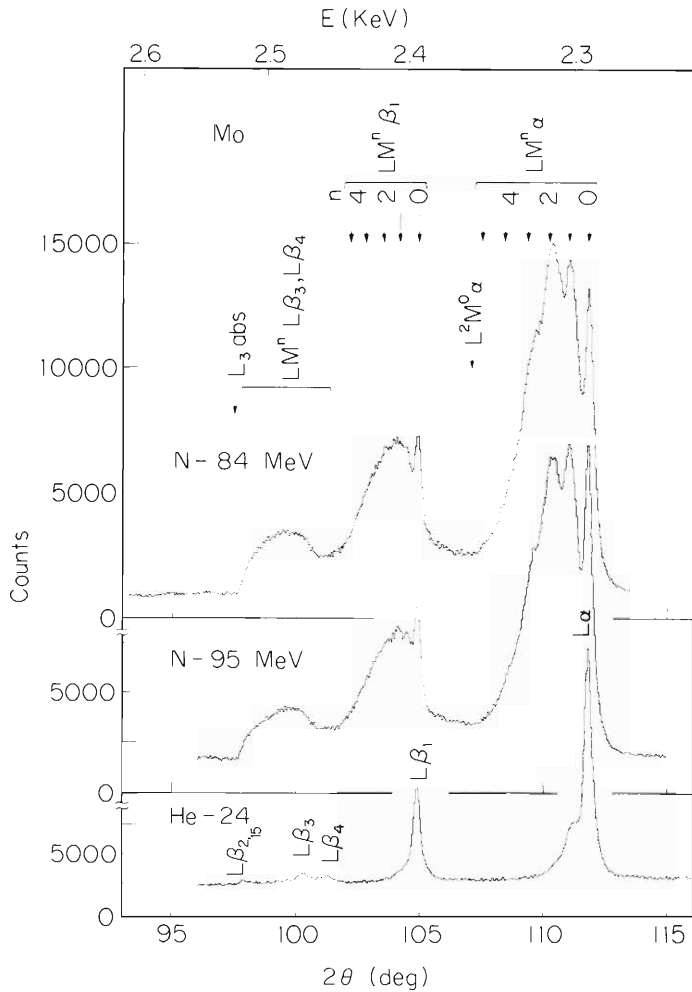


Fig. 2. Ag L X-ray spectra excited by N- and He-ions. The incident energies are shown in the figure.

initial state predicted by Hartree-Fock-Slater calculation.<sup>5)</sup> Symbols  $\alpha$  and  $\beta$  denote that the lines are the satellites of  $L\alpha$  and  $L\beta$  lines, respectively. In the L X-ray spectra of Ag, which are shown in Fig. 2, a broad unresolved peak corresponding to double L-shell electron vacancies is observed. This may be the first case in which the  $L^2$ -lines are observed clearly. This peak was observed for Sn also. The broadness of the peak is mainly due to the fact that there are three L sub-shells. Besides this combination of two L-shell electron vacancies, multiple M-shell electron vacancies contribute to this peak. The satellites of  $L\beta_{2,15}$  are also observed for Ag. Symbols  $L_{j\text{abs}}$  ( $j = 1, 2, 3$ ) denote the  $L_j$ -absorption edge and  $ArK_{\text{abs}}$  denotes the K-absorption edge of Ar gas used in the proportional counter.

The results of analysis of  $L\alpha$  satellite lines will be reported elsewhere in this volume.<sup>6)</sup>

## References

- 1) Y. Awaya, Y. Tendow, H. Kumagai, M. Akiba, T. Katou, and T. Hamada: IPCR Cyclotron Progr. Rep., 9, 79 (1975).  
H. Kumagai, Y. Awaya, Y. Tendow, T. Katou, and M. Akiba: Reports I.P.C.R., (in Japanese), 53, 153 (1977).
- 2) D. K. Olsen, C. F. Moore, and P. Richard: Phys. Rev. A, 7, 1244 (1973).
- 3) P. G. Burkhalter, A. R. Knudson, and D. J. Nagel: *ibid.*, p. 1936.

- 4) Y. Awaya, K. Katou, H. Kumagai, T. Tonuma, Y. Tendow, K. Izumo, T. Takahashi, A. Hashizume, M. Okano, T. Hamada, and S. Özkök: IPCR Cyclotron Progr. Rep., 12, 79 (1978).
- 5) F. Herman and S. Skillman: Atomic Structure Calculation (Prentice-Hall. Englewood Cliffs, N.J., 1963).
- 6) Y. Awaya, K. Izumo, T. Tonuma, T. Katou, Y. Tendow, H. Kumagai, T. Takahashi, A. Hashizume, and T. Hamada: IPCR Cyclotron Progr. Rep., 13, 76 (1979).

## 6-2. Systematics in Multiple Ionization

Y. Awaya, K. Izumo, T. Tonuma, T. Katou,  
Y. Tendow, H. Kumagai, T. Takahashi,  
A. Hashizume, and T. Hamada

It has been found that the ionization probabilities of L-shell and M-shell electrons in multiple ionization can be fitted to the theoretical universal curve by choosing an appropriate scaling factor. In this analysis, in addition to the previously obtained results in our experiments,<sup>1)-3)</sup> newly obtained data on the Mo, Ag, and Sn L X-rays<sup>4)</sup> and on the Kr K X-rays<sup>5)</sup> induced by N ions were included. The experimental conditions are summarized in Table 1, where the target elements, projectiles and their energies are listed.

Table 1. Summary of target elements, projectiles and energies.

X-rays	Target element	Projectile	Energy (MeV)
K	Al, Ti, Cr, Fe, Ni, Kr, Y	N	84
	Ti	N	66, 71, 84, 95, 108
		C	61, 72, 81
	Ar	N	66, 68, 70, 74, 78, 82 83.5, 86, 107, 110
		He, C, N, O	6 MeV/amu
L	Y	N	84
	Mo, Ag	N	84, 95, 115(Ag only)
	Sn	N	84, 115
	Y, Mo, Ag, Sn	He	24 or 19

The cross section of simultaneous  $m$  K-shell and  $n$  L-shell ionization,  $\sigma_{mK, nL}$ , has been obtained by extending the impact parameter formulation for the single ionization both through the BEA (binary encounter approximation) theory<sup>6)</sup> and the SCA (semi-classical approximation) theory.<sup>7)</sup> The expression becomes as follows when each electron shell is considered to be independent:

$$\sigma_{mK, nL} = \int 2\pi b \binom{2}{m} \left\{ P_K(b) \right\}^m \left\{ 1 - P_K(b) \right\}^{2-m} \binom{8}{n} \left\{ P_L(b) \right\}^n \left\{ 1 - P_L(b) \right\}^{8-n} db, \quad (1)$$

where  $P_K(b)$  and  $P_L(b)$  are the probabilities per electron for ionization of the K-shell and L-shell electrons, respectively, and  $b$  is the impact parameter. In this expression, the probability for ionizing L-electrons is assumed to be the same for all sub-shells. In the region where  $P_K(b)$  is not zero,  $P_L(b)$  is almost constant and can be replaced by  $P_L(0)$ . Then the cross section for single K-shell and  $n$  L-shell ionization is reduced to

$$\sigma_{1K, nL} = \binom{8}{n} \left\{ P_L(0) \right\}^n \left\{ 1 - P_L(0) \right\}^{8-n} \sigma_K, \quad (2)$$

where  $\sigma_K$  is the ionization cross section of K-electrons. Thus  $\sigma_{1K, nL}$  is approximately represented by the binomial distribution.

In the case of single L- and  $n$  M-shell ionization, the formula of the binomial distribution becomes

$$\sigma_{1L, nM} = \binom{18}{n} \left\{ P_M(0) \right\}^n \left\{ 1 - P_M(0) \right\}^{18-n} \sigma_L \quad (3)$$

Hereafter, the ionization probability,  $P_L(b)$  or  $P_M(b)$  will be replaced by  $P_n(b)$ , where  $n$  denotes the principal quantum number of electron shell under consideration.  $P_n(b)$  is approximated from the calculated ionization cross section of  $n$ -shell electrons,  $\sigma_n$ , of BEA<sup>6)</sup> as

$$\begin{aligned} P_n(b) &= \sigma_n / (N\pi R^2) = P_n & b \leq R, \\ &= 0 & b > R, \end{aligned} \quad (4)$$

by assuming proper range  $R$  for the impact parameter, where  $N$  is the number of electrons in the shell under consideration.

Experimentally, the  $P_L(=P_2)$  values are obtained by fitting the  $K\alpha$  X-ray data to the binomial distribution. Some of them were reported already, though the scaling factor different from the present one was adopted.<sup>1),2)</sup> The  $P_M(=P_3)$  values are also obtained by applying the same method to  $L\alpha$  satellites. We suppose this is the first case where the binomial distribution analysis has been applied to single L-shell and  $n$  M-shell ionization.

In this analysis, it was assumed that the fluorescence yield is the same for all satellite lines and that there is no outer-shell rearrangement prior to the decay of the K vacancy for K X-rays and that of the L vacancy for L X-rays. We estimated the fluorescence yield for each satellite configuration of Ti, Cr, and Ni K X-rays by using the calculated values of radiative transition probability and those of Auger transition probability.<sup>1)</sup> When we take the fluorescence yield into account, the  $P_L$  value becomes about 8% smaller for Ti and about 3% smaller for Ni. Since the estimated error for  $P_L$  or  $P_M$  values is between 10 to 15%, the change of the value by inclusion of the fluorescence yield is within the limit of error. The assumption as to the rearrangement was confirmed by the work made by Schmiedekamp et al.<sup>8)</sup>

The  $P_L$  and  $P_M$  values thus obtained are shown in Fig. 1 for various target elements and projectiles. The points giving  $P_L$  and those for  $P_M$  lie in different region separated by the dash-dotted line.  $V_i$  is the velocity of the projectile and  $V_n$  is the velocity of  $n$ -orbital electron. The broken line is drawn only to indicate the points of  $P_L$  obtained by 84 MeV N-ion bombardment.

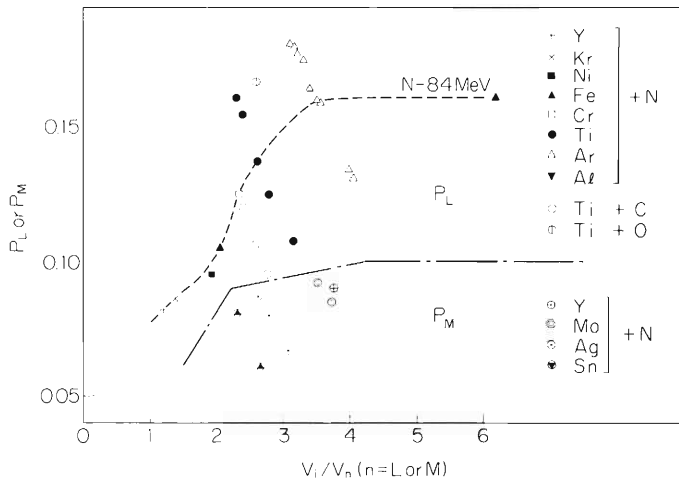


Fig. 1. Experimental  $P_L$  and  $P_M$  values vs. scaled velocity. Target elements and projectiles are shown in the figure.

We tried to find a universal law concerned with these values by use of a proper scaling factor. This scaling is derived from the formula given by McGuire and Richard<sup>6)</sup> on the basis of BEA. According to them,

$$\sigma_n = (NZ_1^2 \sigma_0 / u_n^2) G(V), \quad (5)$$

where  $Z_1$  is the atomic number of the projectile,  $\sigma_0 = \pi e^4$ ,  $u_n$  is the binding energy of the electrons in the  $n$ -orbit and  $G(V)$  is a universal function of scaled velocity,  $V = V_i/V_n$ . We adopted the Gerguoy-Vriens-

Garcia's  $G(V)$ . By assuming that  $R = \sqrt{2}a$  in Eqn. (4) and  $(Z_{\text{eff}}/n)^2 = u_n/Ry$ , where  $a = n^2 a_0/Z_{\text{eff}}$ ,  $a_0$  being Bohr radius,  $Z_{\text{eff}}$  being the effective nuclear charge for the  $n$ -orbit and  $Ry = 13.6$  eV, we can derive the relation of  $P_n$  to  $G(V)$  as

$$n^2 u_n P_n / Z_1^2 = kG(V). \quad (6)$$

The  $k$  is a constant which represents  $\sigma_0/(2\pi a_0^2 Ry)$ .

The result is shown in Fig. 2. We used the averaged binding energy over sub-shell. The calculated theoretical universal curve by BEA shown in the figure reproduces the experimental results fairly well. When we multiply the calculated value by a factor of 0.84, fit is better to the points for  $P_L$  values, and a very good fit is obtained for  $P_M$  values by multiplying by a factor of 1.25.

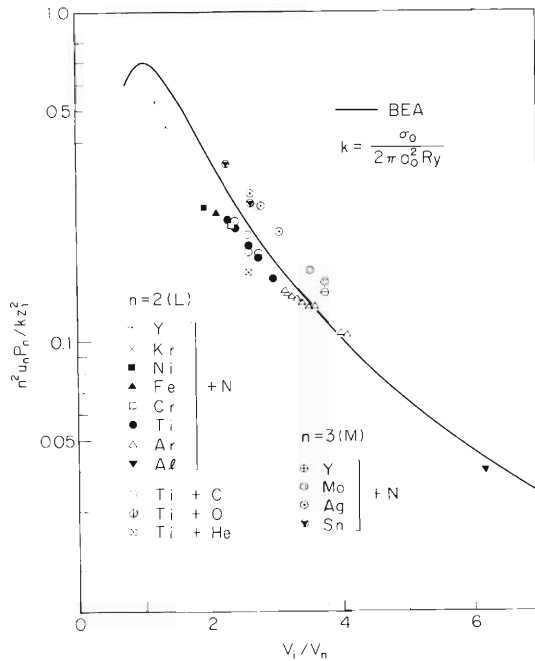


Fig. 2. Scaled  $P_L$  and  $P_M$ , and theoretical universal curve vs. scaled projectile velocity.

This may explain that the value of  $R$  used in the calculation is a little too small for L-shell and a little too large for M-shell. By the correction of  $R$  of about 10%, that is by taking  $R = 1.09 \times \sqrt{2}a$  for the L-shell and  $R = 0.9 \times \sqrt{2}a$  for the M-shell, we get the factors mentioned above. The difference in the correction factor between L-shell and M-shell will be reduced to the difference between the pattern of  $P(b)$  plotted against  $b$ . Since the value of  $n^2 u_n$  is proportional to  $Z_{\text{eff}}^2$ , the present scaling can also be represented by

$$Z_{\text{eff}}^2 P_n / Z_1^2 = K'G(V). \quad (7)$$

## References

- 1) Y. Awaya, K. Izumo, T. Hamada, M. Okano, A. Hashizume, T. Takahashi, Y. Tendow, H. Kumagai, T. Katou, and T. Tonuma: *IPCR Cyclotron Progr. Rep.*, 11, 93 (1977).
- 2) Y. Awaya, T. Katou, H. Kumagai, T. Tonuma, Y. Tendow, K. Izumo, T. Takahashi, A. Hashizume, M. Okano, T. Hamada, and S. Özkök: *ibid.*, 12, 79 (1978).
- 3) T. Tonuma, Y. Awaya, T. Kambara, H. Kumagai, I. Kohno, and S. Özkök: *Phys. Rev. A*, 20, 989 (1979).
- 4) Y. Awaya, T. Katou, H. Kumagai, T. Tonuma, Y. Tendow, K. Izumo, T. Takahashi, A. Hashizume, and T. Hamada: *IPCR Cyclotron Progr. Rep.*, 13, 73 (1979).
- 5) T. Tonuma, Y. Awaya, T. Kambara, H. Kumagai, I. Kohno, and M. Kase: *ibid.*, 13, 82 (1979).
- 6) J.H. McGuire and P. Richard: *Phys. Rev. A*, 8, 1374 (1973).
- 7) J.M. Hansteen and O.P. Mosebekk: *Phys. Rev. Lett.*, 29, 1361 (1973).
- 8) C. Schmiedekamp, B.L. Doyle, T. J. Gray, R.K. Gardner, K.A. Jamison, and P. Richard: *Phys. Rev. A*, 18, 1892 (1978).

### 6-3. Contribution of Electron Transfer to K-Shell Ionizations by $N^{7+}$ -Ion Bombardment

M. Kamiya, A. Kuwako, M. Sebata, K. Ishii,  
S. Morita, Y. Awaya, and T. Tonuma

Until now, the cross sections of electron-transfer from the K-shell of target atoms to the incident ions have been obtained from the difference of ionization cross sections between a fully-stripped ion and a low-charge state ion. But, in this method, a gas target<sup>1)</sup> or an extremely thin target<sup>2)</sup> must be used, and it involves experimental difficulty. Here we use a thin solid target and derive the electron-transfer cross section from the ratio of ionization cross sections for  $N^{7+}$ -ions and  $\alpha$ -particles assuming the validity of PWBA including Coulomb deflection, increased-binding and polarization effect<sup>3)</sup> (PWBA-CBP) at high energy where increased-binding and polarization effects cancel each other. Since few measurements of electron transfer have been carried out by heavy-ion bombardment at high energy, our aim is to measure the electron-transfer cross sections in this energy range in order to test the validity of existing theory.

5, 6, and 7 MeV/amu  $N^{4+}$ -ions and  $\alpha$ -particles were accelerated by the cyclotron.  $N^{7+}$ -ions were selected by a switching magnet after passing through  $150 \mu\text{g}/\text{cm}^2$  Al foil.  $10 - 30 \mu\text{g}/\text{cm}^2$  targets of  ${}_{20}\text{Ca}$ ,  ${}_{21}\text{Sc}$ ,  ${}_{22}\text{Ti}$ ,  ${}_{23}\text{V}$ ,  ${}_{24}\text{Cr}$ ,  ${}_{26}\text{Fe}$ , and  ${}_{28}\text{Ni}$  were prepared by vacuum evaporation onto about  $30 \mu\text{g}/\text{cm}^2$  Al backings. Before the heavy-ion-excitation,  $K\alpha$  and  $K\beta$  spectra were taken by fluorescence excitation and the drift of amplifier gain was frequently checked by using a  ${}^{57}\text{Co}$  X-ray source.

Since the target thickness was not measured yet, absolute cross sections for  $\alpha$ -particles were determined from interpolation of published ionization cross sections<sup>4)</sup> of Ca, Ti, Fe, Co, and Ni for 5, 6, and 7 MeV protons. The errors were estimated to be  $\sim 10\%$ . In the case of  $N^{7+}$ -ion bombardment corrections of fluorescence yield due to multiple ionization was made according to Larkins' method using L vacancy number determined from the energy shifts of  $K\alpha$  and  $K\beta$  lines.

Ionization cross sections for  $\alpha$  particle agree well with PWBA-CBP, while those for  $N^{7+}$ -ion exceed the theoretical values and the energy dependence is different from the theoretical prediction as is seen in Fig. 1. This discrepancy can be attributed to the electron transfer. In Fig. 2 the cross section ratios for  $N^{7+}$ -ions and  $\alpha$ -particles are shown. We define the cross section ratio as

$$R = \sigma_N / \sigma_\alpha ,$$

$$\sigma_N = \sigma_N^D + \sigma_N^C , \quad \sigma_\alpha = \sigma_\alpha^D + \sigma_\alpha^C \approx \sigma_\alpha^D ,$$

where  $\sigma_N$  and  $\sigma_\alpha$  are ionization cross sections for  $N^{7+}$ -ions and  $\alpha$ -particles, respectively, and D and C refer to direct ionization and electron transfer processes, respectively. Then we obtain

$$\sigma_N^C = (R_{\text{exp}} - R_{\text{PWBA-CBP}}) \cdot \sigma_\alpha .$$

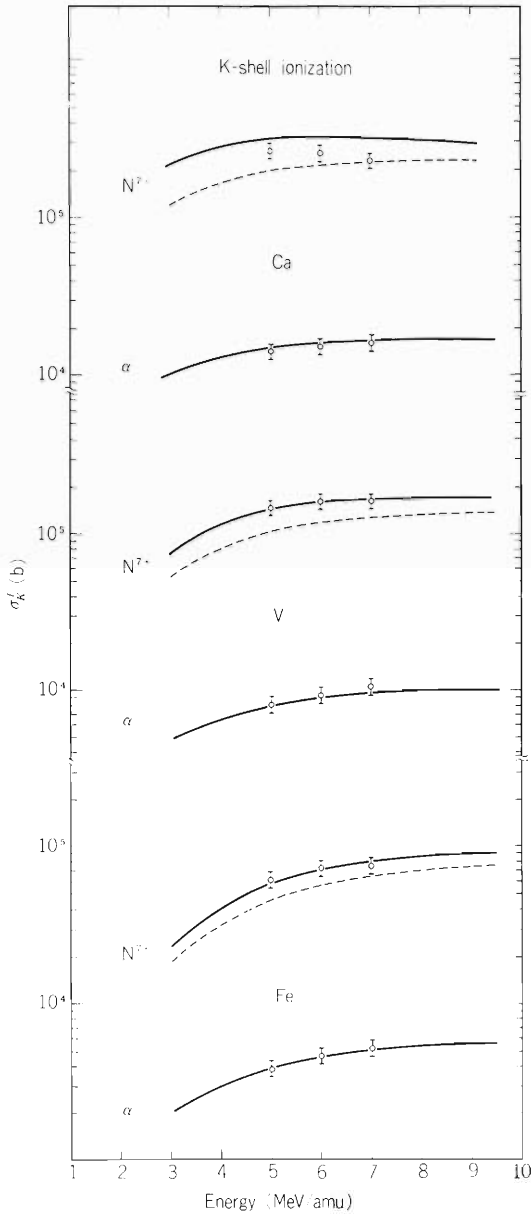


Fig. 1. K-shell ionization cross sections in  $N^{7+}$ -ion and  $\alpha$  particle bombardment of Ca, V, and Fe. The dashed lines show the PWBA-CBP calculation and the solid lines include, in addition, electron transfer process.

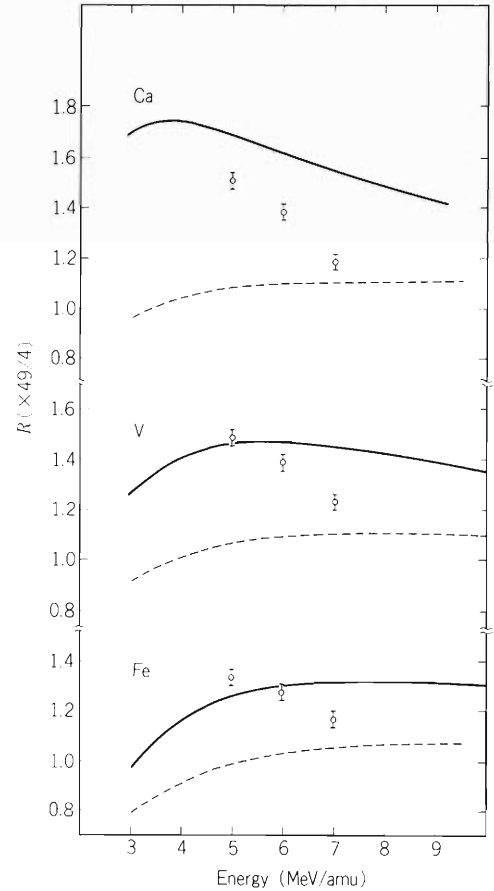


Fig. 2. The ratio of ionization cross section in  $N^{7+}$ -ion and  $\alpha$  particle bombardment of Ca, V, and Fe. The dashed lines show the PWBA-CBP calculation and the solid line includes, in addition, electron transfer process.

Figure 3 shows that the electron transfer cross section decreases much faster, as the incident energy increases, than the prediction from Brinkman-Kramers approximation including Coulomb deflection and increased binding energy effects developed by Lapicki and Losonsky.<sup>5)</sup> Though it is expected that two-center atomic expansion method is appropriate for the region  $V_i/V_k \approx 1$ , where  $V_i$  and  $V_k$  are velocity of the incident ion and target K-electron velocity, respectively, we cannot obtain the calculated results.

For  $N^{7+}$ -ions the ratio  $K\beta/K\alpha$  is 0.16 – 0.17 for all the elements investigated. The energy shift of  $K\alpha$  is constant, while that of  $K\beta$  gradually decreases as the incident energy increases

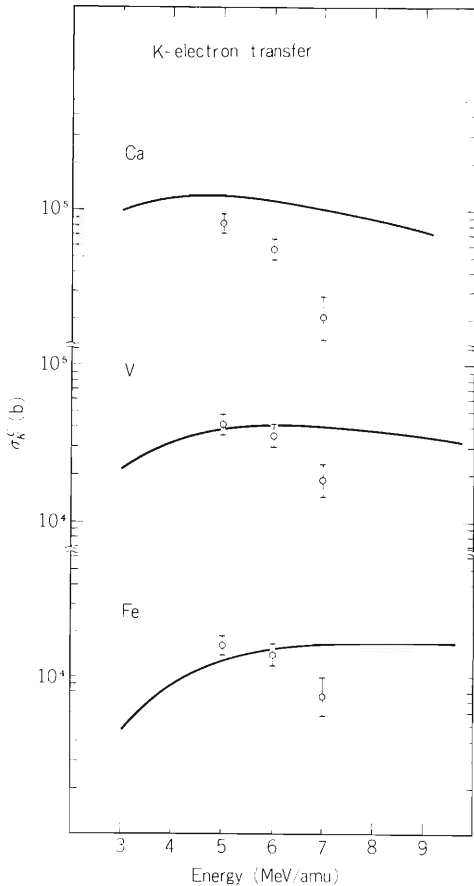


Fig. 3. Cross sections for electron transfer in  $N^{7+}$ -ion bombardment of Ca, V, and Fe. Solid lines show the theoretical values.

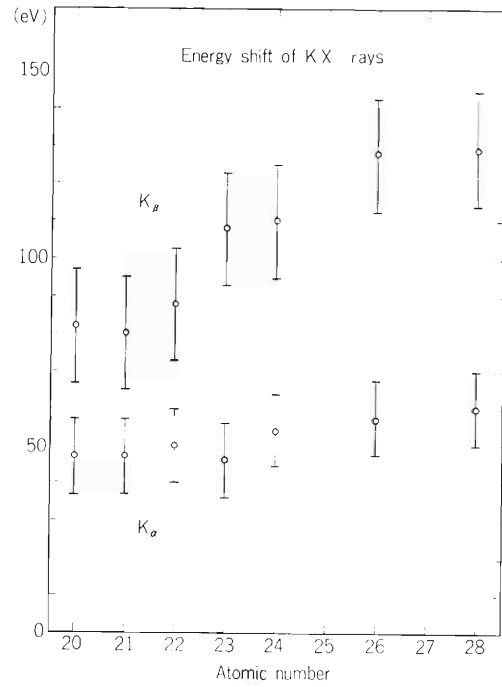


Fig. 4. Averaged energy shifts of  $K\alpha$  and  $K\beta$  lines in  $N^{7+}$ -ion bombardment.

according to the decrease in L-shell ionization probability for  $V_i/V_L > 1$ , where  $V_L$  is the L shell electron velocity averaged over subshells.  $K\alpha$  and  $K\beta$  energy shifts for  $N^{7+}$ -ions averaged over incident energy is shown in Fig. 4.

#### References

- 1) F. Hopkins, R. Brenn, A.R. Whittemore, N. Cue, V. Dutkiewicz, and R.P. Chaturvedi: Phys. Rev., A13, 74 (1976).
- 2) H. Tawara, P. Richard, T.J. Gray, J. Newcomb, K.A. Jamison, C. Schmiedekamp, and J.M. Hall: *ibid.*, A18, 1373 (1978).
- 3) G. Basbas, W. Brandt, and R. Laubert: *ibid.*, A17, 1655 (1978).
- 4) G.A. Bissinger, J.M. Joyce, E.J. Ludwig, W.S. McEver, and S.M. Shafroth: *ibid.*, A1, 841 (1970); R.B. Liebert, T. Zabel, D. Miljanic, H. Larson, V. Valkovic, and G.C. Phillips: *ibid.*, A8, 2336 (1973); R. Akselsson and T.B. Johansson: Z. Physik., 266, 245 (1974); F. Hopkins, R. Brenn, A.R. Whittemore, J. Karp, and S.K. Bhattacharjee: Phys. Rev., A11, 916 (1975).
- 5) G. Lapicki and W. Losonsky: Phys. Rev., A15, 896 (1977).

## 6-4. K X-Rays of Kr Measured with a Crystal Spectrometer

T. Tonuma, Y. Awaya, T. Kambara, H. Kumagai,  
M. Kase, and I. Kohno

The spectra of Kr K X-rays produced by ion collisions were measured with a crystal spectrometer equipped with a LiF(200) crystal and a scintillation counter.<sup>1)</sup> He- and N-ions with energies of 6 MeV/amu were used to bombard Kr gas contained in a gas cell.

Figure 1 shows the  $K\alpha$  and  $K\beta$  spectra obtained by measuring the second order reflection in the Bragg condition when the Kr gas pressure was 270 Torr. The  $K\alpha$  spectrum obtained by N-ion bombardment had an insufficient energy resolution but it was found that the spectrum had some satellites in contrast to that obtained by He-ion bombardment. The  $K\alpha$  spectrum obtained by N-ion bombardment was resolved by the least square fitting of the multiple Gaussian curves and the probability of single ionization for L-shell electrons  $P_L(0)$  was found to be about 0.08 for Kr.

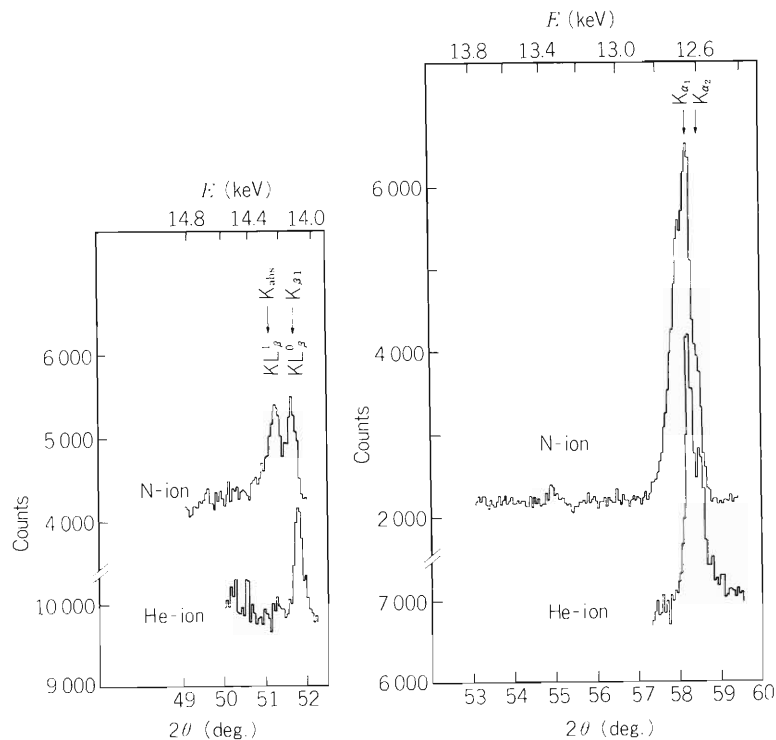


Fig. 1. Energy spectra of Kr K X-rays produced by 6 MeV/amu He- and N-ions.

In the  $K\beta$  spectrum obtained with N-ion bombardment,  $KL^0\beta$  and  $KL^1\beta$  peaks were observed. The energy of  $KL^0\beta$  line is about 38 eV higher than that of  $K\beta_1$  line induced by He-ion bombardment. The energy difference between  $KL^0\beta$  and  $KL^1\beta$  is about 90 eV, which agrees with the value obtained by extrapolating X-ray energy difference data of the solid targets under the 6 MeV/amu N-ion bombardment with respect to the target atomic number.<sup>1)</sup>

The  $KL^n\beta(n \geq 2)$  satellites were not observed because the energies of those satellites are above the absorption edge which is shown by the arrow denoted as  $K_{abs}$  in Fig. 1.

#### Reference

- 1) Y. Awaya, M. Akiba, T. Katou, H. Kumagai, Y. Tendow, K. Izumo, T. Takahashi, A. Hashizume, M. Okano, and T. Hamada: *Phys. Letters*, 61A, 111 (1977).

## 6-5. K X-Rays of Kr Measured with a Si(Li) Detector

T. Tonuma, Y. Awaya, T. Kambara,  
H. Kumagai, M. Kase, and I. Kohno

K X-rays of Kr produced by 6 MeV/amu He-, N-, and Ne-ion bombardment were measured with a Si(Li) detector as a function of Kr gas pressure.<sup>1)</sup> Figure 1 shows  $K\alpha$  and  $K\beta$  spectra of Kr obtained by He- and N-ion bombardment when the Kr gas pressure was 155 and 150 Torr, respectively.

Figure 2 shows the ratio of  $K\beta$  to  $K\alpha$  X-ray yields  $I_{K\beta}/I_{K\alpha}$  of Kr as a function of Kr gas pressure. The measured intensity ratio  $I_{K\beta}/I_{K\alpha}$  induced by He-ion bombardment is almost independent of gas pressure. On the other hand, the ratios for N- and Ne-ion bombardment decrease with increasing gas pressure and the decreasing rate of the ratio for Ne-ion is larger than that for N-ion bombardment. The gas pressure dependency of  $I_{K\beta}/I_{K\alpha}$  can be explained by the fact that  $K\beta$  X-ray spectra induced by heavy-ion bombardment have satellites  $KL^n\beta$  and the energies of some  $KL^n\beta$  ( $n \geq 2$ ) satellites are above the K-shell absorption edge. The self-absorption in the target gas makes  $K\beta$  X-ray yields decrease as described in the preceding paper.<sup>2)</sup>

$KL^n\beta$  X-rays are emitted by the transition of a M-shell electron to K shell when single K-shell and n L-shell electrons are ionized simultaneously by heavy ion-atom collisions. The decrease of

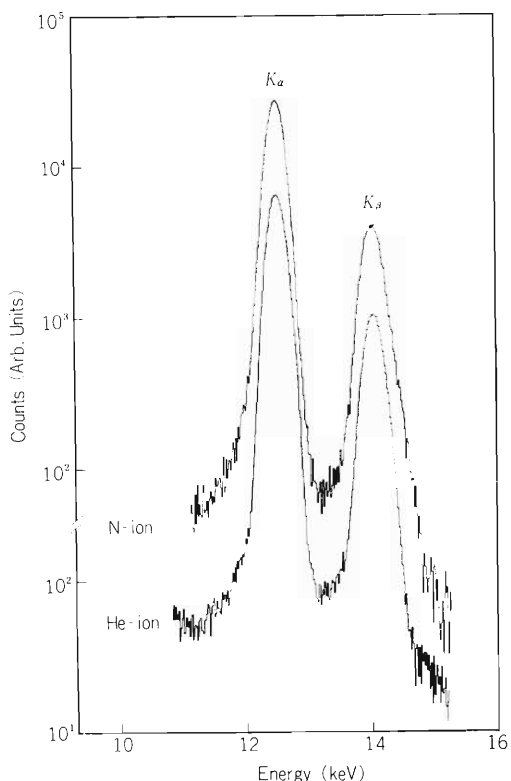


Fig. 1.  $K\alpha$  and  $K\beta$  spectra of Kr induced by 6 MeV/amu He- and N-ions.

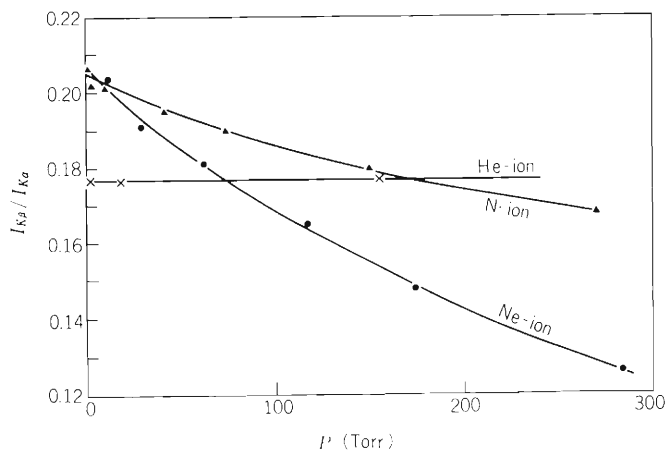


Fig. 2.  $I_{K\beta}/I_{K\alpha}$  ratios of Kr X-rays induced by 6 MeV/amu He-, N-, and Ne-ions as a function of Kr gas pressure. Solid lines are drawn to guide the eye.

the ratio  $I_{K\beta}/I_{K\alpha}$  with increasing gas pressure enables an estimation of the transition ratio of  $KL^n\beta$  ( $n \geq 2$ ) to total  $K\beta$  lines<sup>1)</sup> and, furthermore, a relative transition yield for each  $KL^n\beta$  line on the assumption that fluorescence yield for each  $KL^n\beta$  is constant and the vacancy distribution in the L shell is the binomial one. Figure 3 shows a relative transition yield of multiple ionization of Kr by He-, N-, and Ne-ion bombardment estimated by the present data. The values of parameter  $P_L(0)$  are 0, 0.15, and 0.24 for He-, N-, and Ne-ion bombardment, respectively.  $P_L(0)$  value for N-ion bombardment agrees with that obtained by a binomial fitting of  $K\beta$  spectrum which is measured with the crystal spectrometer as shown in Ref. 2. But this is about two times larger than that by the  $K\alpha$  spectrum and this difference will be a further problem to be studied.

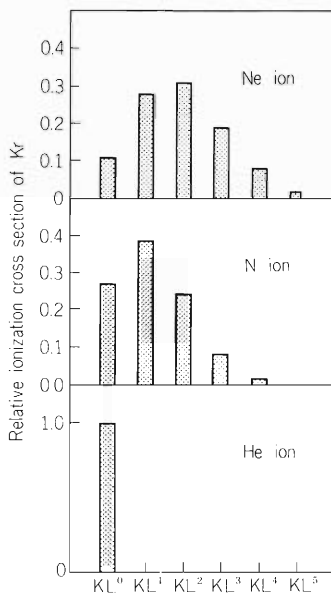


Fig. 3. Relative transition yield of Kr  $KL^n\beta$  line produced by 6 MeV/amu He-, N-, and Ne-ion bombardment.

The ratio of  $I_{K\beta}/I_{K\alpha}$ , in particular, for a solid target has been measured with a Si(Li) detector and the ratio difference between light- and heavy-ion bombardment has been studied.<sup>3)</sup> The ratios of  $I_{K\beta}/I_{K\alpha}$  for Kr obtained by He-, N-, and Ne-ion bombardment were  $0.177 \pm 0.001$ ,  $0.205 \pm 0.002$  and  $0.207 \pm 0.002$ , respectively, by an extrapolation to zero gas pressure without the self-absorption. The ratios did not need to be corrected by the detection efficiency which was almost constant in the Kr  $K\alpha$  and  $K\beta$  energy region. The cause of the ratio difference between He-ion and N- and Ne-ion bombardment is attributed to the multiple ionization.<sup>4)</sup>

It is found that the intensity ratio of  $K\alpha$  and  $K\beta$  X-ray yields without a self-absorption can be obtained by a change of a target thickness and by an extrapolation to zero thickness.

## References

- 1) T. Tonuma, Y. Awaya, T. Kambara, H. Kumagai, and I. Kohno: IPCR Cyclotron Progr. Rep., 12, 84 (1978).
- 2) T. Tonuma, Y. Awaya, T. Kambara, H. Kumagai, M. Kase, and I. Kohno: *ibid.*, 13, 82 (1979).
- 3) Y. Awaya, K. Izumo, T. Hamada, M. Okano, T. Takahashi, A. Hashizume, Y. Tendow, and T. Katou: *Phys. Rev.*, A13, 992 (1976); T. K. Li and R. L. Watson: *ibid.*, A9, 1574 (1974).
- 4) J. Tricomi, J. L. Duggan, F. D. McDaniel, P. D. Miller, R. P. Chaturvedi, R. M. Wheeler, J. Lin, K. A. Kuenhold, L. A. Rayburn, and S. J. Cipolla: *ibid.*, A15, 2269 (1977).

## 6-6. Vacancy Rearrangement in the M Shell Prior to X-Ray Emission

M. Uda, K. Maeda, H. Endo,  
Y. Sasa, and M. Kobayashi

Prior to a characteristic X-ray emission, the rearrangement of electron vacancies in the valence band may occur. Such a change is revealed in the X-ray satellite structure resulted from a multiply ionized state. A quantitative analysis of the satellite intensity distributions has been performed on F  $K\alpha$  spectra of several fluorides induced by p,  $\alpha$ ,  $C^{4+}$  and  $N^{4+}$

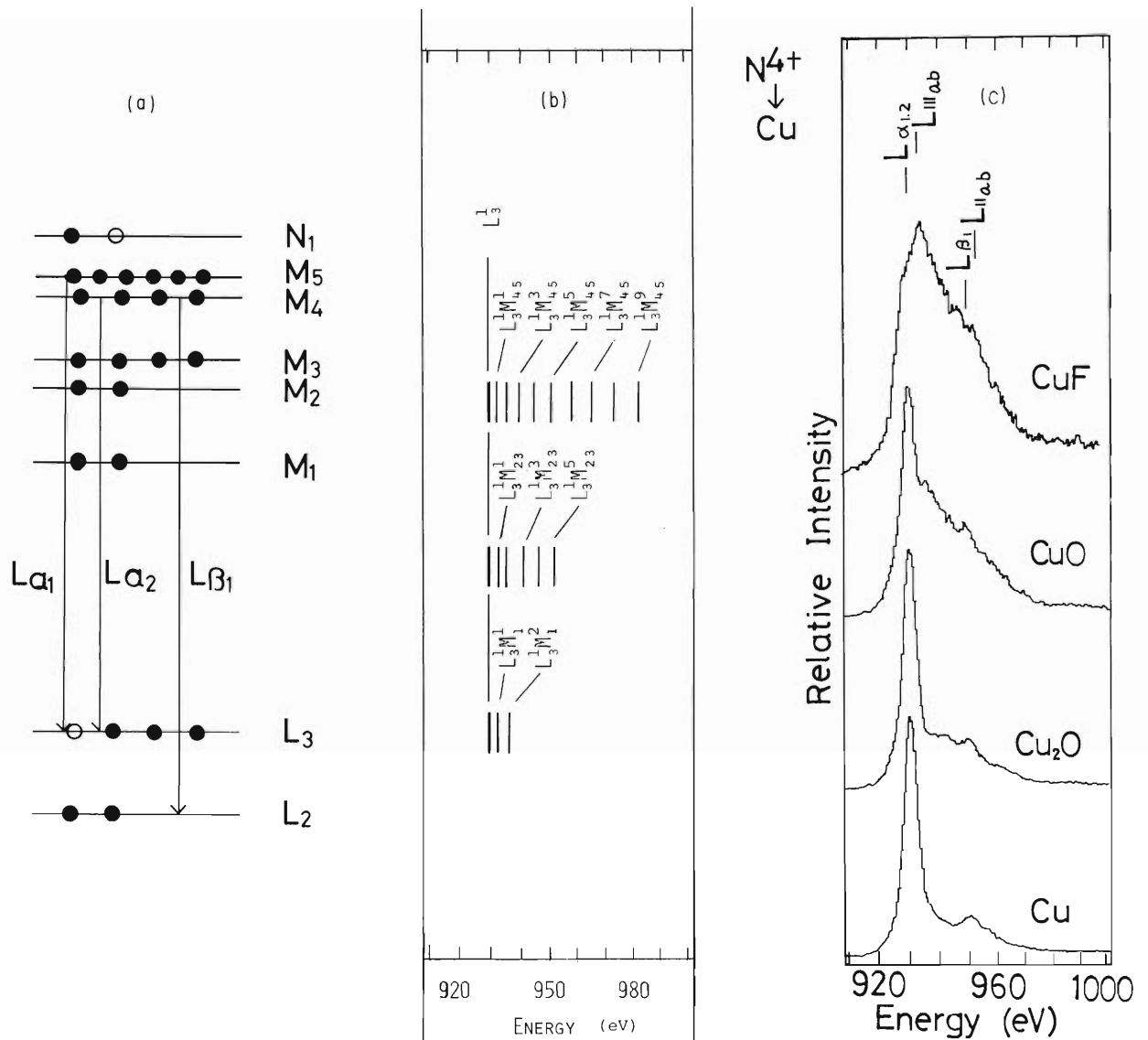


Fig. 1. Relationship between energy diagram and L X-ray emission (a), and calculated (b) and observed (c) L X-ray spectra of Cu. RAP(001) and the proportional counter were employed.

(6 MeV/amu).<sup>1)-3)</sup> The present study deals with L X-ray emission spectra emitted from Fe, Co, Ni, Cu, Zn and Ge, and their chemical compounds.

Target materials used here were in the form of thin films, thickness of which was in the range of 1 – 5 mg/cm<sup>2</sup>. 84 MeV N<sup>4+</sup> beam was generated by the cyclotron. Energy levels for multiply ionized states of the atoms under study were calculated by use of the Hartree-Fock-Slater method whose computer program was written by Herman-Skillman.<sup>4)</sup>

Figure 1(a) and 1(b) show the schematic energy levels and calculated L emission energies for Cu. L<sup>1</sup>M<sup>n</sup> denotes L $\alpha$  emission from Cu atom with one L and n M vacancies at the initial state. In Fig. 1(c) the observed L spectra from several Cu compounds are shown. Structures of high energy satellites of L $\alpha$  are quite different from one compound to the other. This is caused by the vacancy rearrangement of the M shell which is one of the component of the valence band. Prior to the X-ray emission, primary vacancies in the valence band are partially filled by the valence electrons of the surrounding atoms. The rate of the vacancy refilling is proportional to the covalency or the degree of overlapping of the electron wave functions of the compounds. Then the intensity of L<sup>1</sup>M<sup>n</sup> is high in the most ionic compound CuF<sub>2</sub> and low in the least ionic or the most covalent solid Cu.

Similar spectra were obtained from the other metals and their compounds used. Some representatives are shown in Figs. 2(a) and 2(b) for Zn and Ge, respectively.

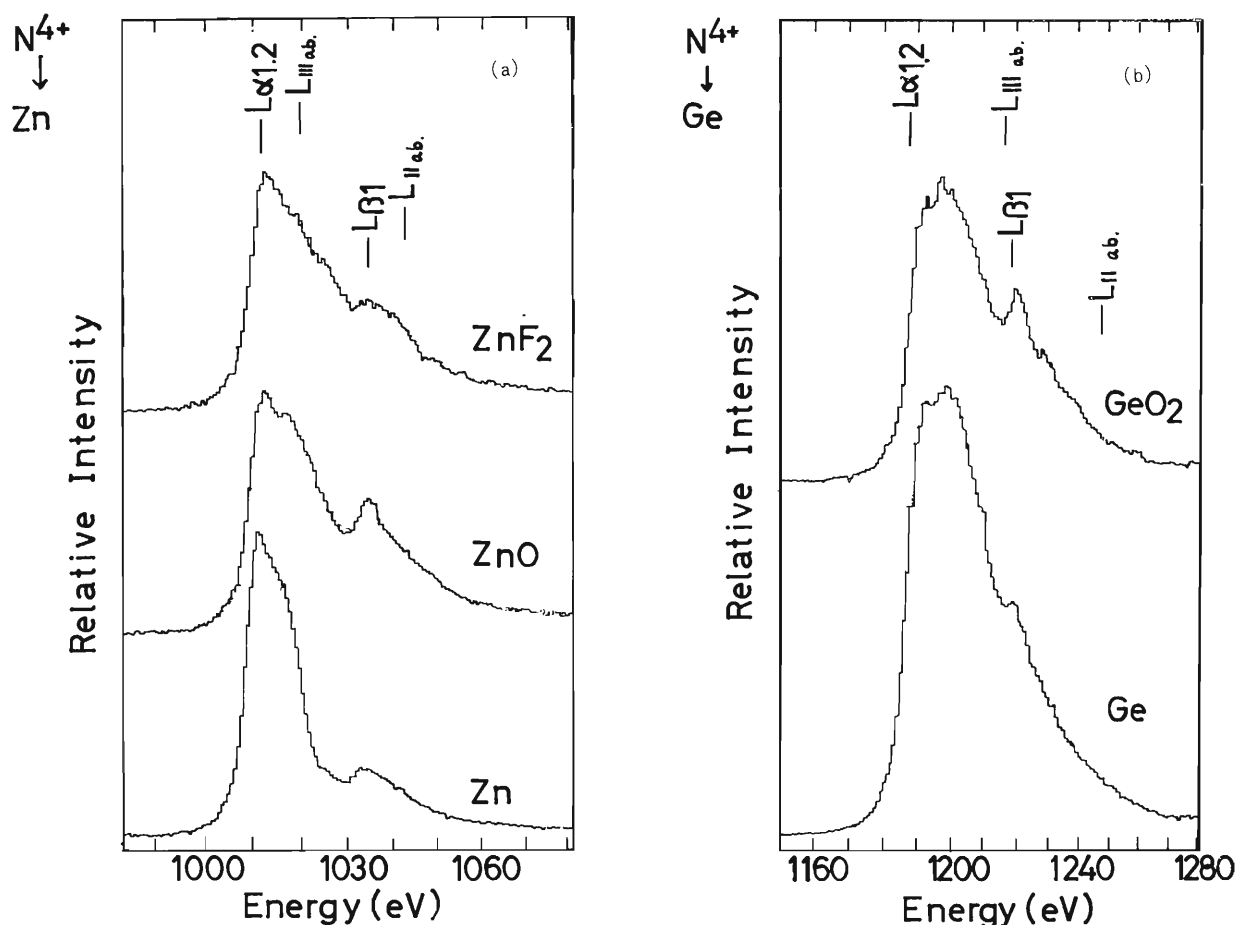


Fig. 2. L X-ray spectra of Zn (a) and Ge (b).

## References

- 1) M. Uda, H. Endo, K. Maeda, Y. Awaya, M. Kobayashi, Y. Sasa, H. Kumagai, and T. Tonuma: Phys. Rev. Lett., 42, 1257 (1979).
- 2) M. Uda, H. Endo, K. Maeda, M. Kobayashi, and Y. Sasa: IPCR Cyclotron Progr. Rep., 12, 88 (1978).
- 3) H. Endo, M. Uda, K. Maeda, M. Kobayashi, and Y. Sasa: *ibid.*, p. 90.
- 4) F. Herman and S. Skillman: "Atomic Structure Calculations", Prentice Hall Inc., Englewood Cliffs, New Jersey (1963).

## 6-7. Effects of Strain Rate on High Temperature Mechanical Properties of Helium-Injected Fe-Ni-Cr Austenitic Alloys

H. Shiraishi, H. Shinno, R. Watanabe,  
H. Kamitsubo, I. Kohno, and T. Shikata

Fe-Ni-Cr austenitic alloy is one of the candidates for first wall and blanket structural materials of a future fusion reactor. The ductility of this material decreases at high temperature due to the presence of helium produced by  $(n, \alpha)$  reactions. We previously reported the effects of various metallurgical conditions on the helium embrittlement of 316 stainless steel and Fe-Ni-Cr alloys.<sup>1)</sup> A knowledge of the mechanical properties under impact loading is important in the core design. In the present work, the effects of strain rate ranging from  $5 \times 10^{-4}$ /sec to  $5 \times 10^{-2}$ /sec on the mechanical properties at the test temperature of 923 K were investigated.

Table 1 shows the chemical composition of materials used and metallurgical treatments before helium injection. Sample 7506 is a solid-solution-strengthened alloy and sample 7510 is an alloy hardened by the precipitation of the intermetallic compound  $\text{Ni}_3(\text{Ti}, \text{Al})$ . Sample 7510B is aged so as to get maximum strength. Treatment conditions prior to the injection were

Table 1. Chemical composition of materials used  
and helium pre-injection treatments.

Sample No.	C	Ni	Cr	Mn	Si	Mo	Ti	Al	Pre-injection treatments
7506A	0.057	35.1	14.7	1.41	0.45	1.59	—	—	ST
7506B	"	"	"	"	"	"	—	—	ST + 5 % PS
7510A	0.063	35.6	14.9	0.94	0.51	1.71	1.79	0.24	20 % CR + AG
7510B	"	"	"	"	"	"	"	"	AG + 20 % CR

ST: solution-treated, 1323K, 30 min, PS: pre-strained, CR: cold rolled,  
AG: aged for 1000 h at 923 K

determined taking the following facts into account. The pre-straining of 5 % was very effective to suppress the helium embrittlement in 316 stainless steel.<sup>1)</sup> Also, 20 % cold work was applied to minimize the void swelling of 316 stainless steel. Specimens for tensile test were of a plate-like form. The dimension of their gauge section was 12 mm long, 4 mm wide, and 0.2 mm thick. Helium was injected into the specimens using the cyclotron. The tensile test was carried out in the vacuum of  $10^{-4}$  Pa using Instron type machine. The details of experimental procedures were reported elsewhere.<sup>2)</sup>

Figures 1 and 2 show the effect of strain rate on the ultimate strength of both alloys. The ultimate strength of the precipitation-hardened alloy was much higher than that of the solid-solution-strengthened alloy. Also, the ultimate strength increase caused by the increase

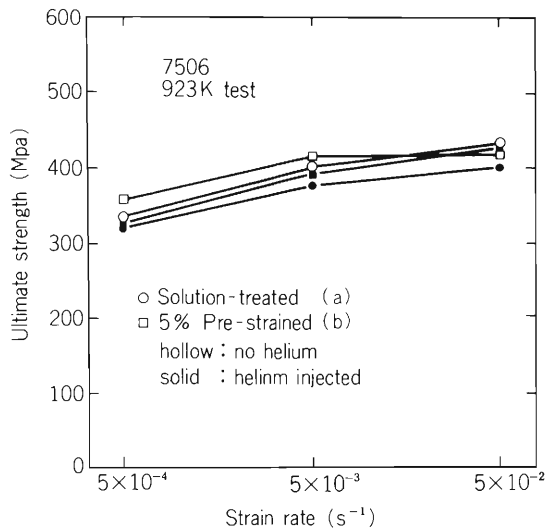


Fig. 1. Effect of strain rate on ultimate strength of helium injected 7506 alloy.

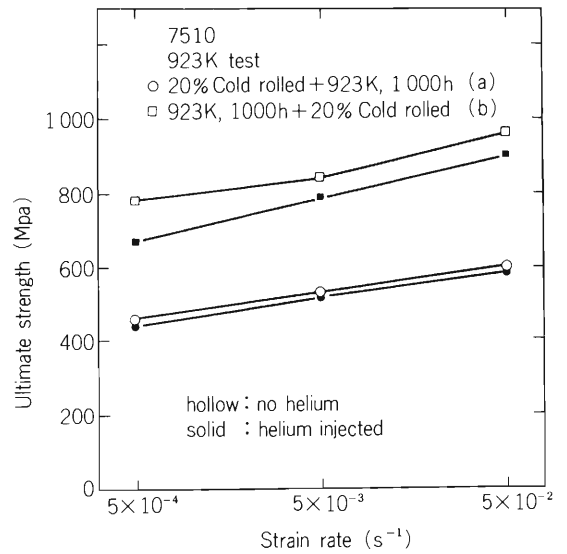


Fig. 2. Effect of strain rate on ultimate strength of helium injected 7510 alloy.

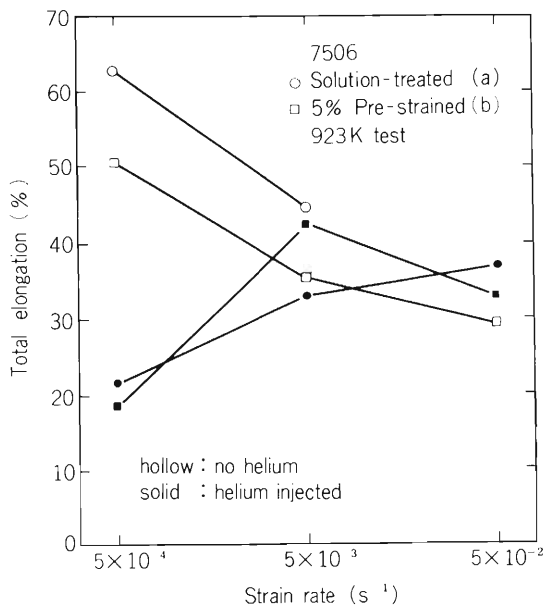


Fig. 3. Effect of strain rate on total elongation of helium injected 7506 alloy.

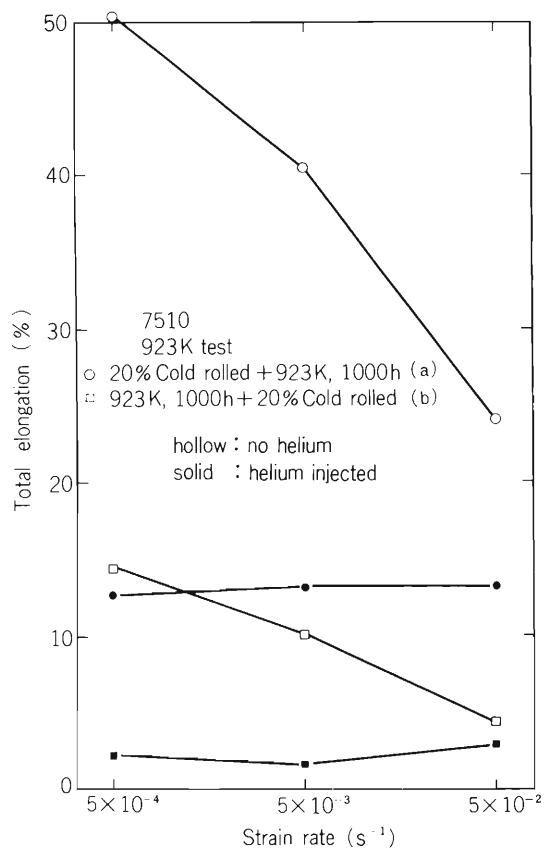


Fig. 4. Effect of strain rate on total elongation of helium injected 7510 alloy.

of strain rate was higher for the former than for the latter. Helium injection reduced the strength of both alloys.

Figures 3 and 4 show the effect of strain rate on the total elongation. With the increase of the strain rate of the order of two, the total elongation of the materials without helium injection decreased by factor of two. On the contrary, the total elongation of the solid solution type alloy bombarded with helium increased with the increase of the strain rate. The effect of helium disappeared at the strain rate between  $5 \times 10^{-3}/\text{sec}$  and  $5 \times 10^{-2}/\text{sec}$ . The similar observation was reported in the helium injected 316 stainless steel<sup>3)</sup> and in the neutron irradiated Incoloy 800 and Hasteloy X.<sup>4)</sup> In the case of the precipitation-hardened alloy, the recovery of the total elongation was not observed, but, from Table 2, we can see that the effect of helium is reduced with the increase of the strain rate.

Table 2. Helium embrittlement sensitivity defined as a ratio of the total elongation of the helium-injected material to that of the corresponding material without helium injection.

Sample	Strain rate ( $\text{sec}^{-1}$ )		
	$5 \times 10^{-4}$	$5 \times 10^{-3}$	$5 \times 10^{-2}$
7510A	0.29	0.33	0.55
7510B	0.17	0.17	0.68

#### References

- 1) H. Shinno, H. Shiraishi, R. Watanabe, H. Kamitsubo, I. Kohno, and T. Shikata: IPCR Cyclotron Progr. Rep., 11, 114 (1977); *ibid.*, 12, 96 (1978).
- 2) R. Watanabe, H. Shiraishi, H. Shinno, H. Kamitsubo, I. Kohno, and T. Shikata: *ibid.*, 10, 104 (1976).
- 3) K. Matsumoto, T. Kataoka, M. Terasawa, M. Shimada, S. Nakahigashi, H. Sakairi, and E. Yagi: J. Nucl. Mater., 67, 97 (1977).
- 4) H. Böhm and K-D. Closs: Radiation Effects in Breeder Reactor Structural Materials, June (1977), Scottsdale, Arizona, U. S. A., p. 347.

## 6-8. Lattice Location of Sn Atoms Implanted into Al

A. Koyama and H. Sakairi

By a channeling experiment on dilute aluminum alloys which were irradiated at 40 – 70 K, Swanson et al. showed that mixed split interstitials are formed by the combination of substitutional impurities, Ag, Mn, and Zn, with Al self interstitials produced by the irradiation.<sup>1)</sup> We were interested in Ni atoms implanted into Al, because Ni has very small solubility in Al. The result of the experiment, which was reported in the last issue, was that Ni atoms also produce mixed split interstitials, which are stable at room temperature in contrast to those of the above three elements studied by Swanson et al.<sup>2)</sup>

This year we investigated implanted Sn atoms in Al instead of the dilutely alloyed Sn atoms which were studied by Swanson et al. In the experiment Swanson et al. showed a strange feature of Sn interstitials such that they are not produced directly by the irradiation at 40 – 70 K but appear only after an annealing at 220 – 240 K. This feature is strongly in contrast with that observed for interstitials of Ag, Mn, and Zn which annihilate by the annealing. Swanson et al. did not identify the configuration of the Sn interstitials, but only showed that they are not the  $\langle 100 \rangle$  mixed split interstitials.

The channeling effect of 4.8 MeV protons accelerated by the cyclotron was investigated with the angular scan through  $\langle 100 \rangle$  and  $\langle 110 \rangle$  axes of Al single crystals. The beam was collimated to have a divergence less than  $0.025^\circ$ . The backscattered protons were detected by a surface-barrier solid state detector placed at a scattering angle of  $150^\circ$  with an acceptance angle of about  $9^\circ$ . Aluminum single crystals were chemically polished and annealed in vacuum at  $550^\circ\text{C}$  for 7 h. The implantation of 150 KeV Sn atoms was carried out at room temperature with a dose of  $1 \times 10^{16}$  ions/cm<sup>2</sup>. The target was maintained at room temperature during the experiment.

Figure 1 (a) shows the normalized backscattering yields from Sn and Al atoms as a function of angle  $\theta$  between the incident beam direction and the  $\langle 110 \rangle$  axis direction. Figure 1 (b) shows the results for the  $\langle 100 \rangle$  axis. It can be seen that there are a quadruple peak and a triple peak in the  $\langle 110 \rangle$  and the  $\langle 100 \rangle$  spectra for Sn atoms, respectively.

These peaks may not be explained by only one type of the interstitial configuration. The interstitial configurations conceivable in fcc metals are as follows, one is a mixed interstitial which is split along  $\langle 100 \rangle$  direction, and the others are those in which the impurity atoms are located at tetrahedral and octahedral interstitial sites. None of them can explain the occurrence of side peaks of the  $\langle 100 \rangle$  spectrum. The mixed split interstitial along  $\langle 110 \rangle$  direction, which is not yet found in fcc metals, can, however, lead to their occurrence. It is therefore expected that these spectra are explained by considering the coexistence of some of the configurations mentioned above.

A quantitative analysis of the structure of the backscattering yields from Sn atoms and the investigation of the fine structure of Al-dips are now in progress.

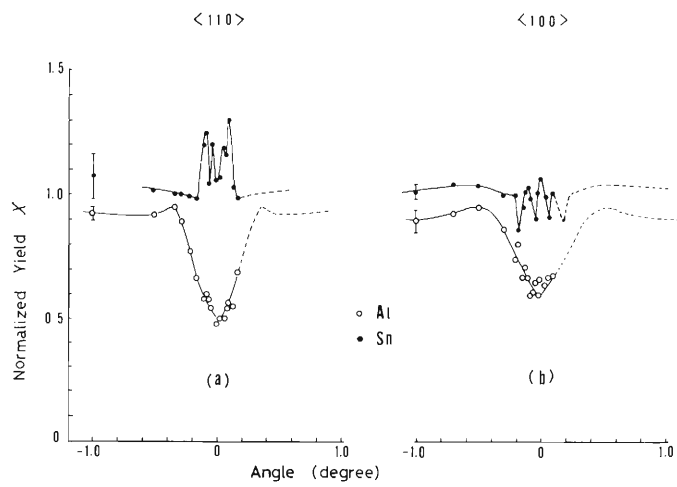


Fig. 1. Normalized backscattering yield from Sn and Al atoms as a function of the angle  $\theta$  between the incident beam direction and the  $\langle 110 \rangle$  axial direction (a), and the  $\langle 100 \rangle$  axial direction (b).

#### References

- 1) M. L. Swanson and F. Maury: *Canad. J. Phys.*, 53, 1117 (1975).
- 2) E. Yagi, A. Koyama, H. Sakairi, and R. R. Hasiguti: *IPCR Cyclotron Progr. Rep.*, 12, 99 (1978).

## 6-9. Secondary Electron Emission from Metals by High-Speed Proton Bombardments

A. Koyama, T. Shikata, and H. Sakairi

In the last issue we described the experimental apparatus to measure the secondary electron emission coefficient (SEEC) of the vacuum evaporated clean surfaces.<sup>1)</sup> This year, SEECs of Al, Cu, Ag, and Au were measured under high speed proton bombardment.

The target materials of 99.99 % purity were vacuum evaporated on the mechanically polished iron substrates at a pressure of about  $3 \times 10^{-7}$  Torr, and *in-situ* measurements were made at  $1 \sim 2 \times 10^{-8}$  Torr. As the time necessary for one data run was less than 10 minutes, the exposure of the fresh surface to the residual gas was less than  $2 \times 10^{-7}$  Torr·minutes. For such a slight exposure to oxygen or water vapor, the decrease of the work function of Al is known to be negligibly small.<sup>2)</sup> The incident energy of protons from the cyclotron was 4 to 16 MeV. The intensity of the beam current was about  $1 \text{ nA/mm}^2$ .

Figure 1 shows the incident energy dependence of SEECs for the four materials. The emission coefficient,  $\gamma$ , increases with the effective electron density, to be excited with the proton, of the target. The dotted line is taken from the experimental result for Al by Aarset et al. In their experiment the target surface was not prepared inside the vacuum system.<sup>3)</sup> By extrapolating the curve for Al obtained in the present experiment to the lower energy region near 2 MeV, it can be seen that the value of  $\gamma$  obtained by them is twice as large as that obtained by us.

Figure 2 shows the relation between  $\gamma/S_e$  and  $E_p$ .  $S_e$  is the electronic stopping power for

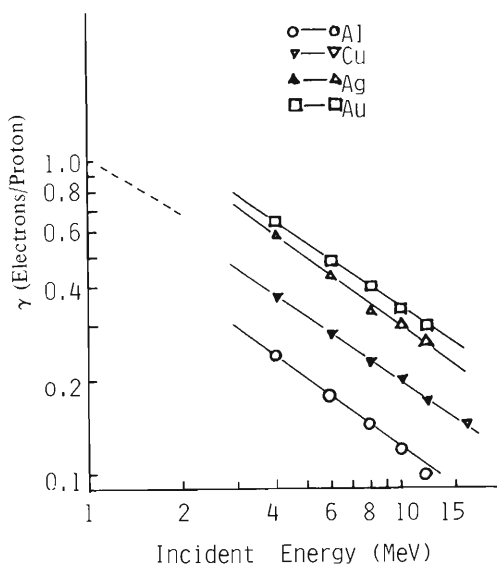


Fig. 1. Energy dependence of the the secondary electron emission coefficient.

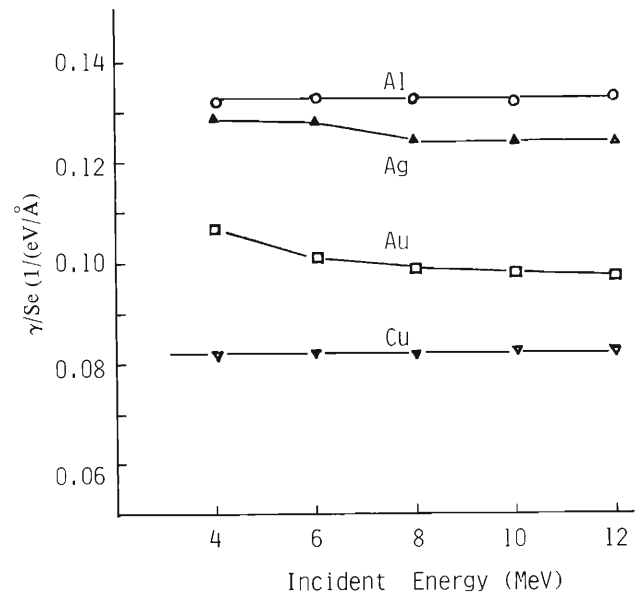


Fig. 2. Energy dependence of the ratio of the secondary electron emission coefficient to the electronic stopping power.

protons ( $\text{eV}/\text{\AA}$ ) and  $E_p$  is the proton incident energy (MeV). The values of  $S_e$  were taken from the table given by Northcliffe and Schilling.<sup>4)</sup> It can be seen that the proportionality between  $\gamma$  and  $S_e$  holds good within the limits of the experimental error ( $\pm 4\%$ ). The same proportionality as this was also found in the much lower energy region from 10 to 50 keV, by Baragiola et al. who produced clean surfaces by *in-situ* vacuum evaporation in ultra high vacuum.<sup>5)</sup>

The values of  $\gamma/S_e$  were listed in Table 1. The values presented by Baragiola et al. are almost equal to those obtained in the present experiment for all the four materials. However, the values of  $\gamma/S_e$  of Al obtained from the data by Aarset et al. is twice as large as the data from the other two experiments, although that of Au is almost equal to those from the other two experiments. It will be due to the fact that the Al target used by Aarset et al. was not free from surface contamination.

Table 1. Ratio of the secondary electron emission coefficient to the electronic stopping power,  $\gamma/S_e$ .

Target	$\gamma/S_e$ ( $\ell/(\text{eV}/\text{\AA})$ )	Energy	Authors	
Al	{	0.13	4 ~ 10 MeV	present
		0.22	0.7 ~ 2 MeV	Aarset et al.
		0.11	2 ~ 50 keV	Baragiola et al.
Cu	{	0.082	4 ~ 10 MeV	present
		0.08	2 ~ 50 keV	Baragiola et al.
Ag	{	0.126	4 ~ 10 MeV	present
		0.13	2 ~ 50 keV	Baragiola et al.
Au	{	0.10	4 ~ 10 MeV	present
		0.085	0.7 ~ 2 MeV	Aarset et al.
		0.12	2 ~ 50 keV	Baragiola et al.

Figure 3 shows the value of  $\gamma$  for Al calculated as  $0.13 \times (S_e(L) + S_e(\text{cond.}))$ , following the observed relation that  $\gamma = 0.13S_e$ . The values  $S_e(L)$  and  $S_e(\text{cond.})$  are the energy losses per unit length due to the ionization of L-shell electrons and the excitation of conduction electrons which are given rise to by incident protons, respectively. The value of  $S_e(L)$  was calculated by using the L-shell ionization cross section given by Manson.<sup>6)</sup> On the other hand, that of  $S_e(\text{cond.})$  was evaluated from the equation given by Neufeld and Ritchie.<sup>7)</sup> The calculated value of  $\gamma$  amounts to 84 % of the experimental one. We can conclude from this figure that in the case of Al the ionized electrons from L-shell constitute a major part of the primarily excited secondary electrons (PESE), and also that those excited from the conduction band constitute a minor one.

A more detailed calculation was done by considering the transport and the emission process of the inner secondary electrons. In order to describe the transport process we took account of the excitation of L-shell electrons and the plasmon, and the individual excitation in the conduction band, by inner secondaries with enough energy. With respect to the emission process it was assumed that the inner secondary electrons must have normal velocities larger than  $\sqrt{\frac{e}{m}(E_F + \phi)}$  to overcome the surface barrier. Here,  $m$ ,  $E_F$ , and  $\phi$  are the electron mass, the Fermi energy and

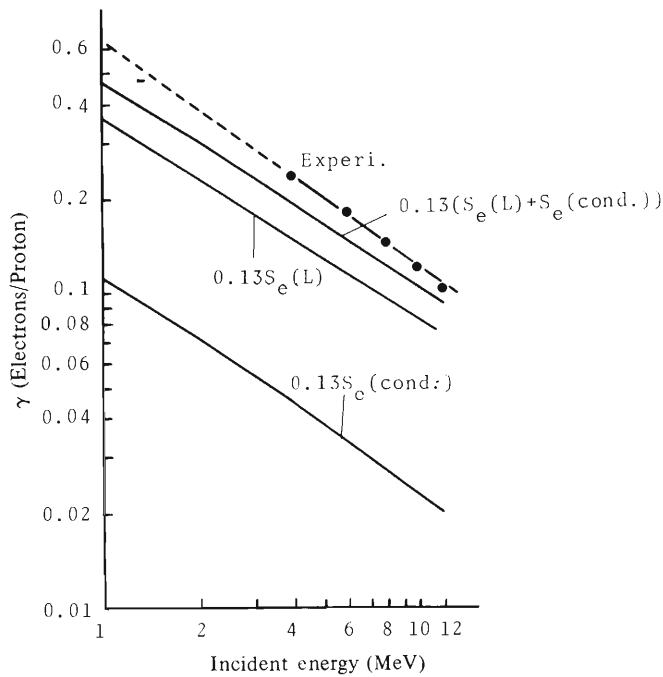


Fig. 3. Comparison of the semi-theoretical value of the secondary electron emission coefficient for Al with the experimental one. See the text for the definitions of  $S_e(L)$   $S_e(\text{cond.})$ .

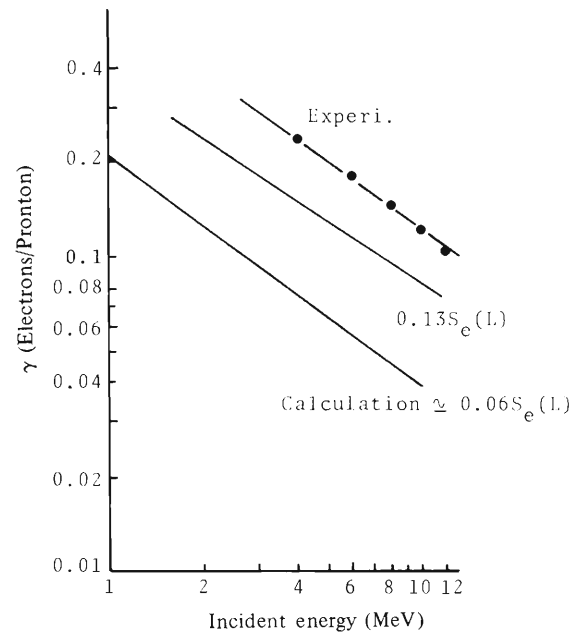


Fig. 4. Comparison of the calculated value of the secondary electron emission coefficient for Al with the experimental one. The semi-theoretical curve expressing  $0.13S_e(L)$  given in Fig. 3 is also included. See the text for the definition of  $S_e(L)$ .

the work function of Al, respectively. Figure 4 shows the result of the calculation of SEEC due to PESE from only L-shell. The calculated value is nearly equal to  $0.06 \times S_e(L)$  and is only one half of  $0.13 \times S_e(L)$  which is expected from the experiment. A further theoretical investigation is being continued.

## References

- 1) A. Koyama, T. Shikata, and H. Sakairi: IPCR Cyclotron Progr. Rep., 12, 94 (1978).
- 2) E. E. Huber, Jr. and C. T. Kirk, Jr.: Surface Science, 5, 447 (1966).
- 3) B. Aarset, R. W. Cloud, and J. G. Trump: J. Appl. Phys., 25, 1359 (1954).
- 4) L. C. Northcliffe and R. F. Schilling: Nuclear Data Tables, A7, 233 (1970).
- 5) R. A. Baragiola, E. V. Alouse, and A. O. Florio: Phys. Rev., B19, 121 (1979).
- 6) S. T. Manson: *ibid.*, A6, 1013 (1972).
- 7) J. Neufeld and R. H. Ritchie: *ibid.*, 98, 1632 (1955).

## 6-10. Angular Correlation of Positron Annihilation Radiation and Compton Profiles in Magnesium

N. Shiotani, T. Okada, N. Sakai, H. Sekizawa, and S. Wakoh

The electron momentum distribution in magnesium was studied by the angular correlation measurements and the  $\gamma$ -ray Compton profile measurements. At the same time the theoretical electron momentum distribution was calculated by the APW method.

### 1) Angular correlation of annihilation radiation

Angular correlation of annihilation radiations in magnesium single crystals was measured along three crystallographic directions, namely  $\Gamma A$ ,  $\Gamma K$ , and  $\Gamma M$ , using a parallel slit system. The angular resolution of the system was measured to be 0.80 mrad. The crystals were kept at room temperature in vacuum. The observed angular correlation along  $\Gamma A$  direction is shown in Fig. 1 together with the theoretical one convoluted with the experimental angular resolution. Both curves are normalized to the same area. There is a noticeable disagreement between the theory and the experiment. This disagreement is similar to those found in aluminum,<sup>1)</sup> vanadium group,<sup>2)</sup> chromium group<sup>3)</sup> and in other metals. The observed crystalline anisotropy of the angular correlations is illustrated in Fig. 2 together with the corresponding theoretical one. The

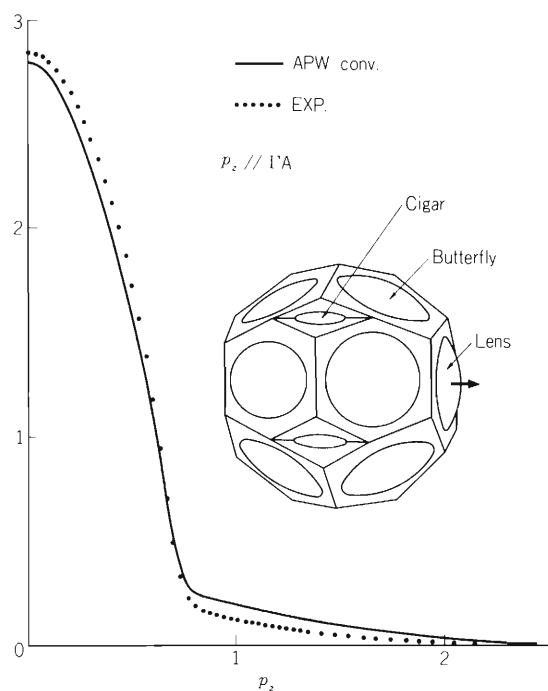


Fig. 1. The experimental and theoretical angular correlations in Mg along the  $\Gamma A$  direction.

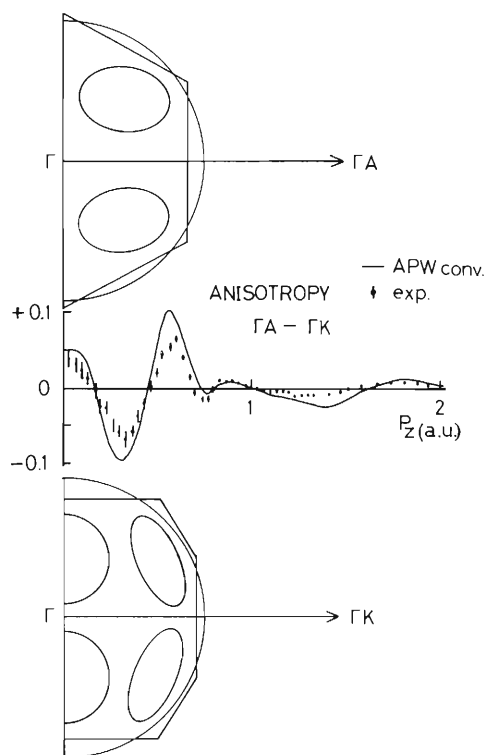


Fig. 2. The anisotropy of the angular correlations. The schematic diagrams illustrate the side views of the large zone and the Fermi surface with the butterflies.

origin of this anisotropy is that, due to the band gap across the  $(10\bar{1}1)$  zone face, the “butterflies”, one of the Fermi surfaces in the third zone and centered at L as shown in the inset of Fig. 1, are smaller than those of the free electron model. This observation is consistent with the results of other Fermi surface measurements such as the magnetoacoustic effect reported by Ketterson and Stark.<sup>4)</sup>

2) Compton profile

The  $\gamma$ -ray Compton profiles were measured using 59.54 keV ( $^{241}\text{Am}$ )  $\gamma$ -rays. The magnesium crystals of 2mm thickness were the same ones as used for the angular correlation measurements. During the measurements the specimens were kept at room temperature in vacuum. The  $\Gamma\text{A}$  Compton profile, corrected for the background, the sample absorption, the detector efficiency, the Compton cross section and the “long tail”, is shown in Fig. 3, together with the theoretical profiles: one not convoluted and one convoluted with the experimental resolution of 0.66 a.u.

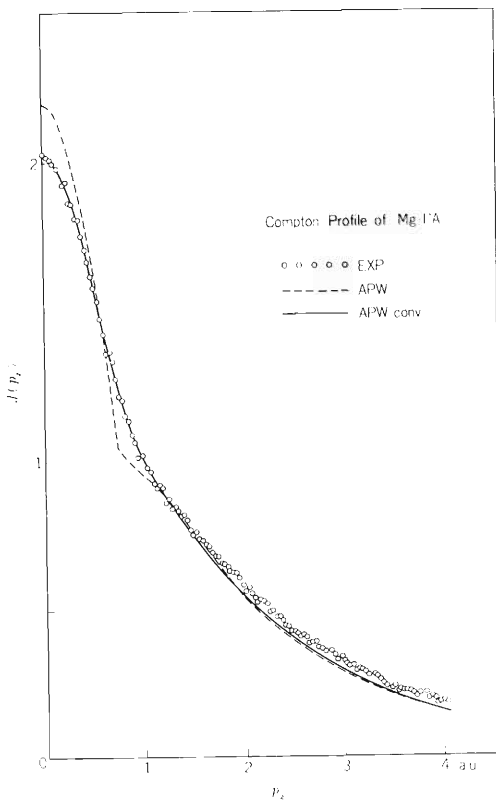


Fig. 3. The  $\gamma$ -ray Compton profile of Mg.

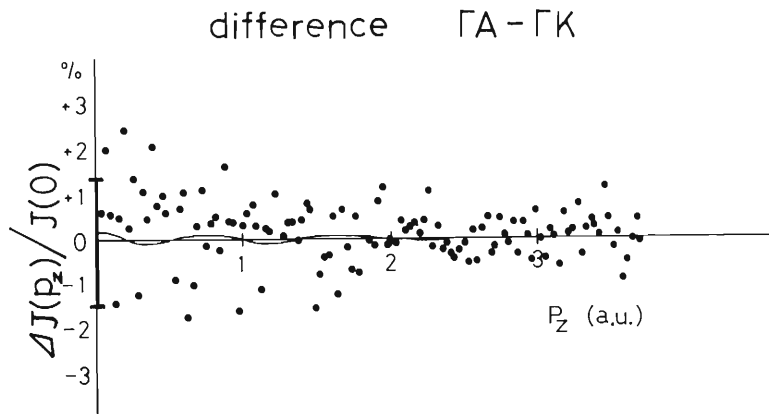


Fig. 4. The anisotropy of the Compton profile of Mg.

The agreement between the experiment and the theory is very good. However a slight disagreement is found in the higher momentum region. The multiple scattering effect may cause this discrepancy. Weiss<sup>5)</sup> reported a large crystalline anisotropy of the Compton profile in magnesium. Our experimental and theoretical results do not agree with Weiss's results. In Fig. 4 the experimental and the theoretical anisotropies are shown. The theoretical anisotropy, convoluted with the experimental resolution, is undetectably small. This is consistent with the experimental result.

#### References

- 1) T. Okada, H. Sekizawa, and N. Shiotani: J. Phys. Soc. Japan, 41, 836 (1976).
- 2) N. Shiotani, T. Okada, T. Mizoguchi, and H. Sekizawa: *ibid.*, 38, 423 (1975);  
S. Wakoh, Y. Kubo, and J. Yamashita: *ibid.*, p.416.
- 3) N. Shiotani, T. Okada, H. Sekizawa, S. Wakoh, and Y. Kubo: *ibid.*, 43, 1229 (1977).
- 4) J. B. Ketterson and P. W. Stark: Phys. Rev., 156, 748 (1967).
- 5) R. J. Weiss: Phil. Mag., 24, 1477 (1971).

6-11. Mössbauer Study of  $^{119}\text{Sn}$  in Chromium and Manganese Dioxides

T. Okada and H. Sekizawa

$^{119}\text{Sn}$  Mössbauer studies of the supertransferred hyperfine magnetic field  $H_{\text{hf}}$  in magnetic oxides such as  $\text{MnFe}_2\text{O}_4$ ,  $\text{CaMnO}_3$ ,  $\text{NiFe}_2\text{O}_4$  and  $\text{VO}_2$  have been made to investigate the mechanisms of the spin transfer in weakly covalent materials. We report new results on  $H_{\text{hf}}$  at  $^{119}\text{Sn}$  in the system  $\text{Cr}_{1-x}\text{Mn}_x\text{O}_2$  ( $0 \leq x \leq 1$ ) with the rutile structure.

Since  $\text{CrO}_2$  is known to be ferromagnetic with the simplest spin structure, Mössbauer measurements of  $H_{\text{hf}}$  in Sn-doped  $\text{CrO}_2$  give us a valuable clue to the origins of  $H_{\text{hf}}$ . The magnetic properties of the system  $\text{Cr}_{1-x}\text{Mn}_x\text{O}_2$  have been measured by several authors. The present samples were prepared by thermal reaction of the powdered mixture of  $\text{CrO}_3$ ,  $\text{MnO}_2$  and  $\text{SnCl}_2$  (85 % enriched with  $^{119}\text{Sn}$ ) at  $420 - 550^\circ\text{C}$  under an oxygen pressure of  $150 \text{ kg/cm}^2$ . Each sample contains 0.1 – 0.5 at % of Sn ions.

The Mössbauer spectrum of  $^{119}\text{Sn}$  in  $\text{CrO}_2$  at 80K is shown in Fig. 1. The spectrum consists of well resolved six lines due to  $^{119}\text{Sn}$  in  $\text{CrO}_2$  (as drawn with the solid lines) and others. The latter are assigned to  $^{119}\text{Sn}$  in  $\text{SnO}_2$  and  $\text{Cr}_2\text{O}_3$ . The sign of  $H_{\text{hf}}$  is determined by applying an external longitudinal magnetic field of 35 kOe. The obtained values of  $H_{\text{hf}}$ , the isomer shift IS relative to  $\text{CaSnO}_3$ , the magnetic moment  $\sigma_0$  and the Curie temperature  $T_c$  are listed in Table 1. As can be seen, the value of IS in  $\text{Cr}_{1-x}\text{Mn}_x\text{O}_2$  decreases with the Mn content  $x$ ; in  $\text{CrO}_2$  the IS is  $+0.18 \text{ mm/sec}$  and nearly zero in  $\text{MnO}_2$ . This result shows that the Sn ions are in tetravalent state, and somewhat more covalent in  $\text{CrO}_2$  compared with very ionic ones in  $\text{MnO}_2$ . The observed electric quadrupole splitting is negligibly small.

The observed value of  $H_{\text{hf}}$  at  $^{119}\text{Sn}$  in  $\text{CrO}_2$  ( $+380 \text{ kOe}$ ) is positive and very large compared with the values in other magnetically ordered oxides, for instance,  $250 \text{ kOe}$  in  $\text{NiFe}_2\text{O}_4$ . In general, the mechanisms giving rise to  $H_{\text{hf}}$  in various magnetic oxides have much similarity to

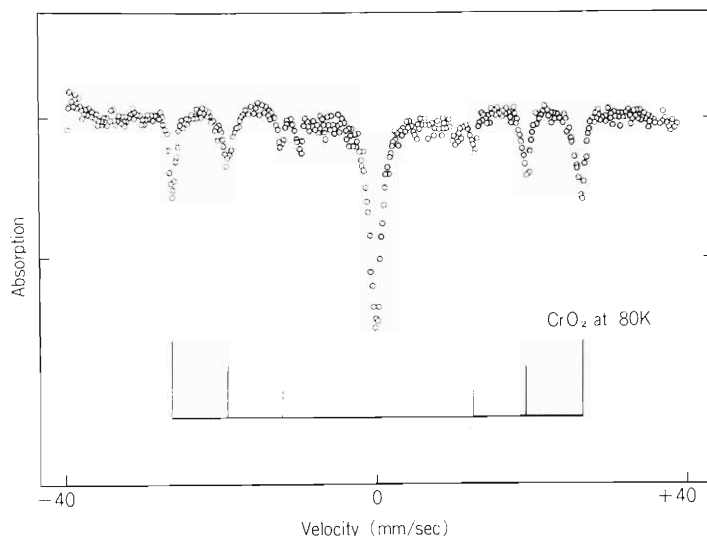


Fig. 1. Mössbauer spectrum of  $^{119}\text{Sn}$  in  $\text{CrO}_2$  containing 0.1 at % of Sn at 80K.

Table 1. Hyperfine field ( $H_{\text{hf}}$ ) and isomer shift (IS) at 5K at  $^{119}\text{Sn}$  in  $\text{Cr}_{1-x}\text{Mn}_x\text{O}_2$ , the magnetic moment  $\sigma_0\mu_{\text{B}}$  at 0K and the Curie temperature  $T_{\text{C}}$ .

x	$H_{\text{hf}}$ kOe	IS mm/sec	$\sigma_0\mu_{\text{B}}$	$T_{\text{C}}$
0	+380	+0.18	1.83	392
0.25	250	+0.14	1.32	384
0.50	120	+0.07	0.60	380
1.0	50	0.0	—	$T_{\text{N}}=90$

those for the superexchange interaction between the magnetic ions. In  $\text{CrO}_2$ , the superexchange between the unit cell corner and the body-center  $\text{Cr}^{4+}$  ions via oxygen ion is thought to be the dominant interaction for the ferromagnetism. Therefore, we examined various paths of spin transfer from the chromium ion at the body-center to the Sn ion at the corner via the oxygen ion. However, we found that these paths could give negative  $H_{\text{hf}}$  only.

We can understand the mechanism qualitatively as follows. The spin transfer to the Sn ion at the corner comes directly from the Cr ions at the neighbouring corners of the unit cell. We take the coordinate system for the nearly octahedral site for Cr ion at the corner as shown in Fig. 2. The nearly degenerate three  $d_e$  states would split into two states, the lower  $d_{yz}$ ,  $d_{zx}$  states and the slightly higher  $d_{xy}$  state, and the former states are occupied by the two  $d$ -electrons of  $\text{Cr}^{4+}$  with parallel spins. Fairly strong mixing is expected between the empty  $d_{xy}$  and the  $5s$  of  $\text{Sn}^{4+}$  because of the relatively short distance between the cations and the loose packing of the oxygen ions. The mixing of the empty LCAO  $d_{xy}+\lambda 5s$  of the relatively low energy excited state with the occupied  $d_{yz}$  and  $d_{zx}$  of the ground state results in the spin transfer giving rise to the observed large positive  $H_{\text{hf}}$  at  $^{119}\text{Sn}$  in  $\text{CrO}_2$ .

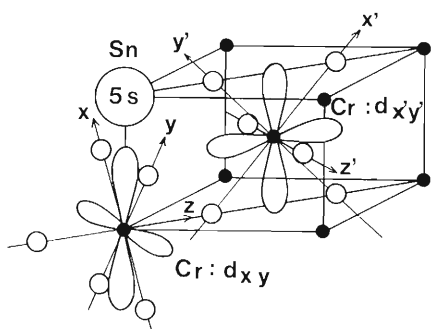


Fig. 2. The empty orbitals of the Cr ions and the Sn ion in the rutile structure.

An alternative band model mechanism is also able to account for the  $H_{\text{hf}}$  correctly. The  $d_e$  orbitals of Cr ions make up a narrow band which is split by the ferromagnetic exchange interaction. In this model, the  $d_{xy}$  orbital is partly occupied by ferromagnetic electrons which can easily be transferred to the Sn  $5s$  orbital giving rise to the observed large positive  $H_{\text{hf}}$  at the  $^{119}\text{Sn}$  nucleus.

## 7. RADIOCHEMISTRY AND NUCLEAR CHEMISTRY

### 7-1. Charged-Particle Activation Analyses of Oxygen in $\text{GaAs}_{1-x}\text{P}_x$

T. Nozaki, Y. Terai, F. Yajima,  
M. Toyoda, and T. Tsukazaki

Oxygen in  $\text{GaAs}_{1-x}\text{P}_x$  layers on GaP plates was analyzed by charged particle activation analysis. The sample was prepared by Mitsubishi Monsanto Chemical Industry Ltd. for use as light-emitting diode, and their oxygen content is suspected to have some important effect on its luminescence character. The oxygen was activated to  $^{18}\text{F}$  by the  $^{16}\text{O}(^3\text{He}, \text{p})^{18}\text{F}$  reaction, and the  $^{18}\text{F}$  was separated and its activity was measured. Since the  $^3\text{He}$  bombardment of the matrix gives various radio-nuclides of arsenic, bromine, etc., a chemical process should first be established for the separation of  $^{18}\text{F}$  completely free from them. A combination of the scavenging with  $\text{Zn}(\text{OH})_2$ , the distillation of  $\text{H}_2\text{SiF}_6$  and the precipitation of  $\text{LiF}$  proved to give a suitable separation.

The sample with about  $1.5 \text{ cm} \times 1.5 \text{ cm}$  dimension and about  $100 \mu\text{m}$   $\text{GaAs}_{1-x}\text{P}_x$  layer thickness was covered with a thin aluminium foil and set on a water-cooled target holder. It was bombarded with a  $^3\text{He}$  beam of 11 MeV energy at the layer surface and about  $1 \mu\text{A}$  flux for 20 to 40 min. This energy was selected from excitation function for the  $^{16}\text{O}(^3\text{He}, \text{p})^{18}\text{F}$  reaction, the sample layer thickness and the range-energy curve for  $^3\text{He}$  particles. The sample surface with  $5 \text{ mg/cm}^2$  thickness was then etched off in aqua regia with the aid of ultra-sonic waves. The sample after the surface contamination removal was put into a polyethylene bottle containing aqua regia (30 ml) and carrier HF (2 mol/l, 2 ml). After most part of air in the bottle was rapidly squeezed out, the bottle was stoppered and placed on an ultra-sonic wave generator. Within 15 min the  $\text{GaAs}_{1-x}\text{P}_x$  layer was dissolved together with some part of the GaP plate.

The solution was diluted with water (150 ml), and  $\text{Zn}(\text{NO}_3)_2$  (20% soln, 5 ml) was added to it. It was then neutralized with NaOH, and the precipitate thus formed was removed by centrifugation. Fluorine in the solution was then precipitated as  $\text{CaF}_2$  together with  $\text{CaCO}_3$  by the usual method, and the coprecipitate was filtered on a glass filter paper and washed with hot water. The precipitate together with the filter paper was added to  $\text{HClO}_4$  (60%, 150 ml), and the fluorine was steam-distilled at 140 to 150°C as  $\text{H}_2\text{SiF}_6$ . The distillate (200 to 300 ml) was received in a LiOH solution and treated with LiCl (2 mol/l soln, 100 ml) and ethanol (200 ml) to give LiF precipitate, which was collected by filtration and washed with 50% ethanol containing LiCl.

Annihilation radiation from the LiF was measured with a NaI(Tl) scintillation detector connected to a single channel analyzer, and the decay was followed. The decay curve agreed well with that of  $^{18}\text{F}$ . Also, the absence of any  $\gamma$ -ray other than annihilation radiation was ascertained by a Ge(Li) detector. For the measurement of carrier recovery, the LiF was dissolved

in dil. HCl and fluorine quantity in an aliquot volume of the solution was determined by the lanthanum titration in the presence of a fluoride-sensitive electrode. As for the activation standard, a silica plate covered with an aluminium foil thicker by  $5 \text{ mg/cm}^2$  than the foil used in the sample bombardment was bombarded with a lower flux and for a shorter time.

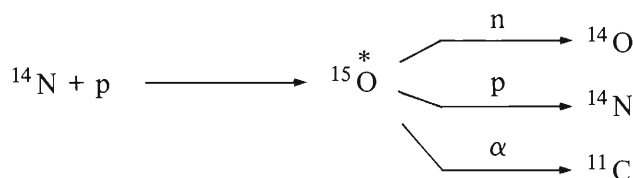
Down to about 20 ppb of oxygen in  $\text{GaAs}_{1-x}\text{P}_x$  was proved to be determined by this technique. Various oxygen concentrations were found on the present samples, ranging from 60 ppb to about 100 ppm. Some correlations can be observed of the oxygen concentration with the production condition of the sample as well as with its luminescence characteristics. This study is still under way to make the correlations clearer.

## 7-2. Yield of Low-Z Radionuclides in Charged - Particle Reactions

T. Nozaki and M. Iwamoto

Several low-Z elements are abundant in nature and play roles vitally important especially in the biosphere. Various low-Z radioisotopes are shown to be very useful in fundamental and applied life sciences including nuclear medicine. The excitation function, however, cannot be predicted with confidence from any theory for reactions of low-Z nuclides. It is, therefore, regarded as worth while collecting reliably measured excitation functions for low-Z reactions and arrange them systematically into a chart which gives the yield of individual radio-nuclide in relatively simple reactions of the compound nucleus mechanism.

In order to make such a chart, the branching ratio should be obtained for p-, n-, and  $\alpha$ -emission from a compound nucleus. We have assumed that relative branching ratio for a given compound nucleus can be approximated by (1) the mean cross section over energy range between  $E_{th} + 2$  MeV and  $E_{th} + 8$  MeV when the compound nucleus is of  $Z \leq 9$  or (2) the maximum cross section in the excitation function when it is of  $Z > 9$ . For example, the mean cross sections for the following reactions are obtained to be about 7 mb and 110 mb for the formation of  $^{14}\text{O}$  and  $^{11}\text{C}$ , respectively, from the measured excitation functions:<sup>1)</sup>



With further approximation that the cross section of compound nucleus formation is  $60 A^{2/3}$  mb, the mean formation cross section of  $^{14}\text{N}$  in the above reaction is given to be about 230 mb. Hence, the branching ratios for n-, p-, and  $\alpha$ -emission from  $^{15}\text{O}$  are obtained to be 2 %, 67 %, and 31 %, respectively.

Since no enough variety of excitation functions has yet been measured reliably, we set up the following formulas to complement the insufficiency:

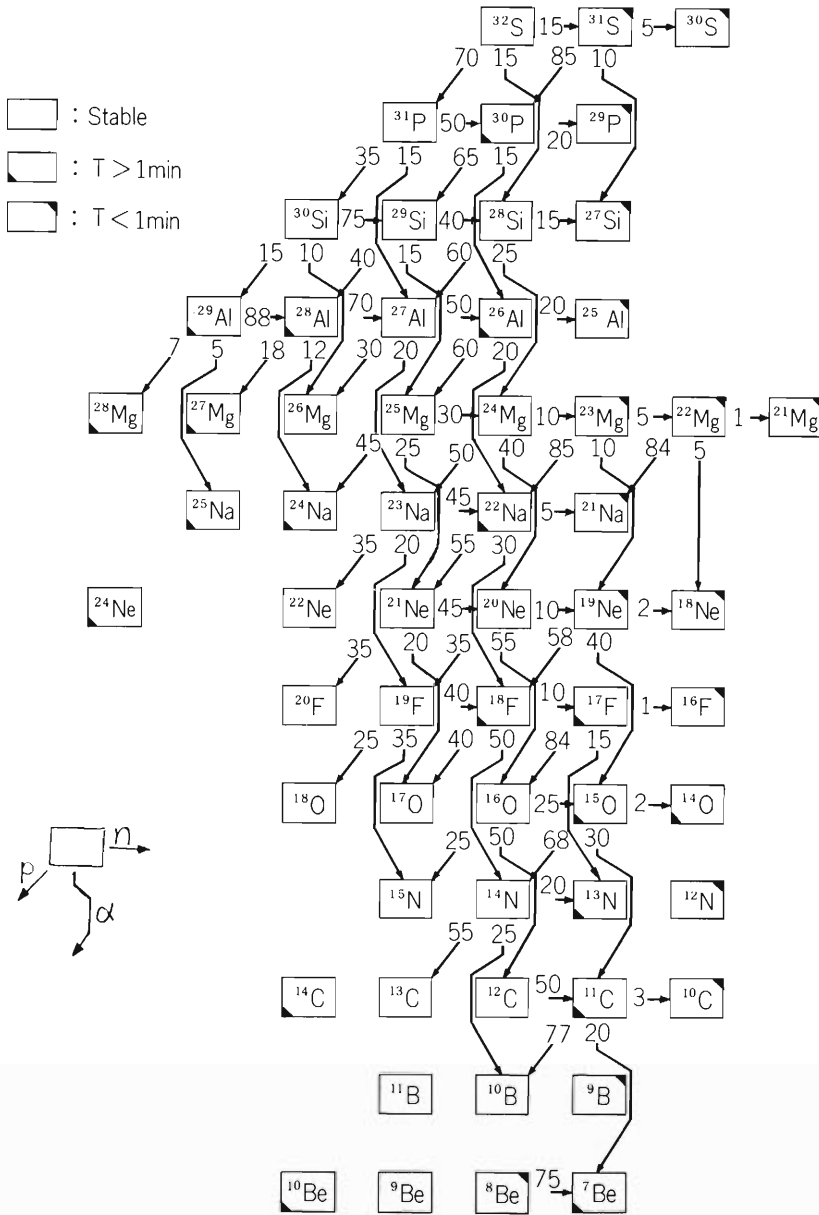
$$w_n + w_p + w_\alpha = 100 (\%)$$

$$w_j = 2^{(S_j/2 + \delta - B)} ,$$

where  $w_j$  is the relative branching ratio for the emission of particle  $j$ ,  $S_j$  is its separation energy in MeV,  $\delta$  is the even-odd term, and  $B$  is for the Coulomb barrier correction. For even-even, odd-A and odd-odd product nuclei  $\delta$  is taken to be -1, 0, and +1, respectively, with the exception of  $^{16}\text{O}$  where  $\delta = -2$  was adopted. For proton emission,  $B$  is taken to be 0 for a compound nucleus with  $Z < 14$  and 1 for  $14 \leq Z \leq 16$ ; for  $\alpha$ -particle emission,  $B = 0, 1, \text{ and } 2$  were adopted for

$Z < 9$ ,  $9 \leq Z \leq 14$ , and  $14 \leq Z \leq 16$ , respectively. These formulas give fairly correct values for the formation of  $^{18}\text{F}$  and  $^{30}\text{P}$  by various reactions but a value smaller by about 35 % for  $^{11}\text{C}$ .

Branching ratios which seem to be the most probable at present have been assembled to make a chart for compound nuclei with  $Z = 6$  (carbon) to  $Z = 16$  (sulphur). The chart is shown below. This chart inevitably involves many small errors and incorrectness, which should be corrected in future. The branching ratio is thought to vary with the excitation energy of the compound nucleus, and this also provides a future problem.



Reference

- 1) T. Nozaki, T. Karasawa, M. Iwamoto, Y. Terai, and M. Okano: IPCR Cyclotron Progr. Rep., 12, 106 (1978).

7-3. Recoil Range of  $^{18}\text{F}$  Formed by Various Reactions

T. Nozaki, M. Iwamoto, K. Usami,  
K. Mukai, and A. Hiraiwa

The distribution of forward recoil range of  $^{18}\text{F}$  was measured for the following formation reactions: (1)  $^{16}\text{O}(^3\text{He}, \text{p})^{18}\text{F}$ , (2)  $^{16}\text{O}(\alpha, \text{pn})^{18}\text{F}$ , and (3)  $^{20}\text{Ne}(^3\text{He}, \alpha\text{p})^{18}\text{F}$ . The excitation functions for these reactions are already known.<sup>1)</sup> The incident energies for Reactions 1, 2, and 3 were selected to be 8, 35, and 20 MeV, respectively, which are the energies to give the maximum cross sections. For Reaction 1, the measurement was also undertaken for 14 MeV incident energy.

The technique of thin stacked foil recoil catcher cannot be adopted in the present study, because oxygen on the foil surface interferes seriously. We used a semiconductor silicon wafer of a known surface area as the recoil catcher, because of the following reasons: (1) its surface can be made mirror-flat, (2) its surface oxygen quantity is known,<sup>2)</sup> (3) a NaOH solution is known to be suitable as its etching solution, and the silicon concentration in the solution can be determined conveniently by colorimetry, (4) its high purity can be guaranteed, and (5) silicon gives no notable activity other than  $^{30}\text{P}$  (2.5 min half-life) in the present bombardments. The target-catcher systems used are shown in Fig. 1. A  $\text{SiO}_2$  film with 50 or 100 nm thickness was prepared on a silicon wafer as the oxygen target. A set of a special design was prepared for the neon target-catcher system, in which neon from a cylinder was slowly streamed between two silicon wafers of 0.3 mm aperture. The initial energy of  $^3\text{He}$ - or  $\alpha$ -particles was so adjusted as to be degraded to the value given above at the layer of  $\text{SiO}_2$  or neon.

The target-catcher system was bombarded with about  $1 \mu\text{A}$  beam for 10 to 15 min. The catcher wafer was then etched with 15 ml of 5 % NaOH solution heated to about  $50^\circ\text{C}$  in a small polyethylene bottle. The etching duration was changed from 1 to 8 min according to the thickness to be removed. The etching was repeated 10 to 15 times in a new bottle for each time. The annihilation radiation from the bottle was then measured with a scintillation detector

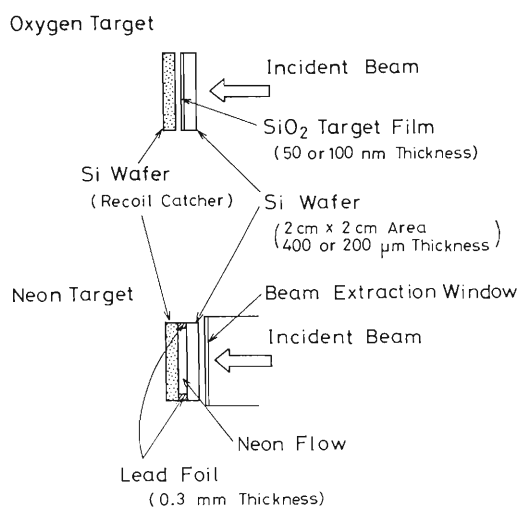


Fig. 1. Target assembly.

connected to a single channel analyzer, and the decay was followed. After more than 2 h from the bombardment, the decay curve showed good agreement with that of  $^{18}\text{F}$ . Silicon content of the solution in each bottle was determined by the silico-12-molybdate colorimetry. The distribution of the recoil range was thus obtained as a histogramme.

The reproducibility of the result is exemplified by Fig. 2, in which two results in six measurements for Reaction 2 are given. Other two results lie between them, and the rest two are outside of them. The etching uniformity was checked by electron microscopes. No etching pits but some pyramids were found in the bombarded domain after the etching, but their heights did not exceed  $1\ \mu\text{m}$ . Thus, this etching was proved to be satisfactory. Mechanical grinding was also tried, but gave poorer results.

The distribution curves thus obtained for the forward recoil range of  $^{18}\text{F}$  is shown in Figs. 3 and 4. The maximum and minimum recoil energy of  $^{18}\text{F}$  can be calculated for each reaction together with its most probable recoil energy, provided that the reaction proceeds via the

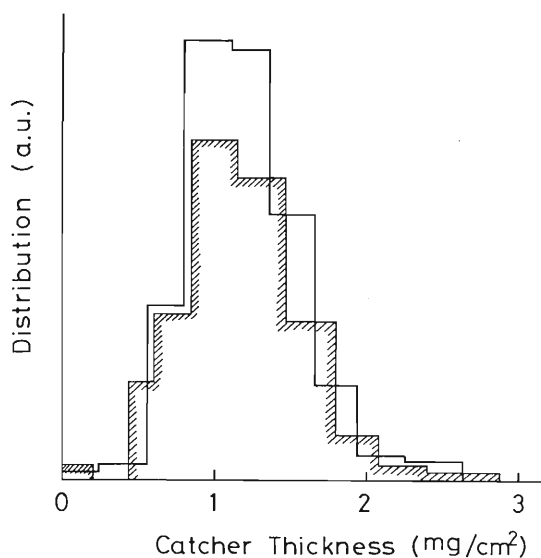


Fig. 2. Reproducibility of the result.

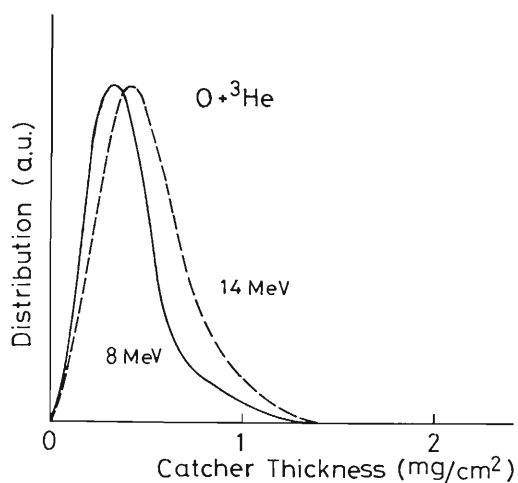


Fig. 3. Distribution of forward recoil range.

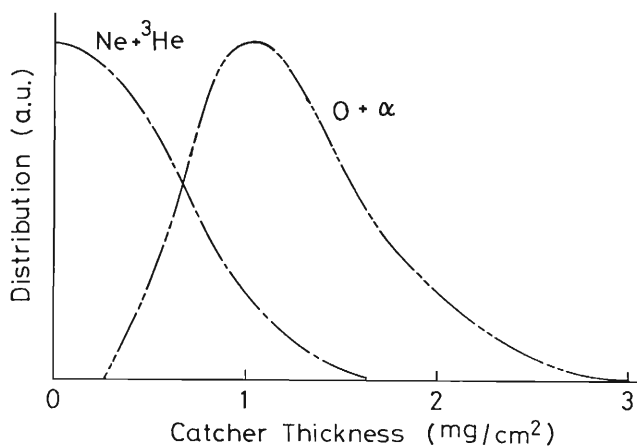


Fig. 4. Distribution of forward recoil range.

compound nucleus. These values of recoil energy are shown in Table 1 together with the experimental results of recoil range. It is clearly demonstrated in Fig. 4 that the direct process is the predominant mechanism for the  $^{20}\text{Ne}(^3\text{He}, \alpha\text{p})^{18}\text{F}$  reaction. These results offer information important in the charged particle activation analysis of oxygen as well as in the design of gas targets for  $^{18}\text{F}$  production. Similar measurements are under way for the  $^{18}\text{O}(\text{p}, \text{n})^{18}\text{F}$ ,  $^{20}\text{Ne}(\text{d}, \alpha)^{18}\text{F}$ , and  $^{19}\text{F}(^3\text{He}, \alpha)^{18}\text{F}$  reactions.

Table 1. Forward recoil energy and forward recoil range (in Si) of  $^{18}\text{F}$ .

Formation reaction	Incident energy (MeV)	Forward recoil energy (MeV)			Forward recoil range (mg/cm <sup>2</sup> in Si)	
		Max.	Min.	Highest distribn.	Highest distribn.	80 % Stop
$^{16}\text{O}(^3\text{He}, \text{p})^{18}\text{F}$	8	3.15	0.17	1.20	0.3	0.45
	14	5.29	0.35	2.09	0.4	0.65
$^{16}\text{O}(\alpha, \text{pn})^{18}\text{F}$	35	10.59	3.12	6.30	1.1	1.5
$^{16}\text{O}(\alpha, \text{d})^{18}\text{F}$		12.89	2.04			
$^{20}\text{Ne}(^3\text{He}, \alpha\text{p})^{18}\text{F}$	20	8.91	-0.02	2.04	≤0.2	0.8

#### References

- 1) T. Nozaki, M. Iwamoto, and T. Ido: Intern. J. appl. Radiat. Isotopes, 25, 393 (1974).
- 2) T. Nozaki, M. Iwamoto, K. Usami, K. Mukai, and A. Hiraiwa: IPCR Cyclotron Progr. Rep., 12, 111 (1978).

#### 7-4. $^{119}\text{Sn}$ -Mössbauer Emission Study on Se and SnSe Doped with $^{119\text{m}}\text{Te}$

S. Ambe and F. Ambe

Mössbauer emission spectroscopy is useful in determining the chemical state of defect atoms produced by nuclear decays and reactions. We have studied the chemical state of  $^{119}\text{Sn}$  arising from the EC decay series of  $^{119\text{m}}\text{Te} \rightarrow ^{119}\text{Sb} \rightarrow ^{119}\text{Sn}$  in compounds of Sb and Te. This year a new series of experiments has been started. In this, matrices which contain neither Sb nor Te as a macro component are to be studied by doping technique. Here the emission spectra of metallic Se and SnSe doped with carrier-free  $^{119\text{m}}\text{Te}$  are reported. The results are discussed in comparison with those reported previously for Te metal and SnTe labelled with  $^{119\text{m}}\text{Te}$ .<sup>1),2)</sup>

Metallic Se doped with  $^{119\text{m}}\text{Te}$  was prepared by the following radiochemical procedure. A tin plate containing  $^{119\text{m}}\text{Te}$  formed by irradiation with 40 MeV  $\alpha$ -particles from the cyclotron was dissolved in a mixture of HCl and  $\text{HNO}_3$ . After evaporation, the residue was dissolved in dil. HCl containing Se(IV). Carrier-free  $^{119\text{m}}\text{Te}$  was coprecipitated with Se metal by reduction with  $\text{Na}_2\text{SO}_3$  and  $\text{N}_2\text{H}_4 \cdot 2\text{HCl}$ . The Se( $^{119\text{m}}\text{Te}$ ) was purified by sublimation and was fused at  $260^\circ\text{C}$  under an Ar stream. The Se metal obtained was in the hexagonal form which is isomorphous with Te metal.  $^{120}\text{SnSe}$  doped with  $^{119\text{m}}\text{Te}$  was prepared by fusion of a stoichiometric mixture of  $^{120}\text{Sn}$  and Se( $^{119\text{m}}\text{Te}$ ) metals at  $920^\circ\text{C}$  under Ar. Mössbauer emission spectra of the samples were measured against a  $\text{BaSnO}_3$  absorber at 78 K, after a radioactive equilibrium had been attained between  $^{119\text{m}}\text{Te}$  and  $^{119}\text{Sb}$ .

In Se metal containing a small amount of Te, the Te atoms are reported to replace Se atoms in the lattice.<sup>3)</sup> Therefore, carrier-free  $^{119\text{m}}\text{Te}$  occupies evidently the lattice position of Se in the Se( $^{119\text{m}}\text{Te}$ ) sample. The observed emission spectrum of Se( $^{119\text{m}}\text{Te}$ ) is shown in Fig. 1 with that of Te( $^{119\text{m}}\text{Te}$ ) for comparison. Least squares fitting of the experimental points with Lorentzians assuming a singlet and a doublet resulted in lines with the isomer shifts of 1.8 and 3.2 mm/sec. The former line is ascribed to  $^{119}\text{Sn(IV)}$  and the latter to  $^{119}\text{Sn(II)}$  coordinated with selenium on the basis of the Mössbauer parameters obtained in absorption experiments.<sup>4)-6)</sup> On the other hand, no  $^{119}\text{Sn}$  in the tetravalent state was found in the less electronegative Te matrix.<sup>1)</sup>

In  $^{120}\text{SnSe}$ ,  $^{119\text{m}}\text{Te}$  atoms are considered to be in the Se site. The emission spectrum of  $^{120}\text{SnSe}(^{119\text{m}}\text{Te})$  [Fig. 2(a)] was decomposed into two components with isomer shifts of 1.3 and 3.09 mm/sec, which are also assigned to  $^{119}\text{Sn(IV)}$  and  $^{119}\text{Sn(II)}$  surrounded by selenium ions. The result obtained suggests that most  $^{119}\text{Sn}$  atoms and accordingly most  $^{119}\text{Sb}$  atoms have been stabilized in the Sn site. (The position of  $^{119}\text{Sn}$  determined from the isomer shifts represents at the same time the position of  $^{119}\text{Sb}$  in the lattice, since the recoil energy accompanying the EC decay of  $^{119}\text{Sb}$  is much smaller than the displacement energy.<sup>1), 2)</sup> The result on  $^{120}\text{SnSe}(^{119\text{m}}\text{Te})$  presents a striking contrast to the case of  $^{120}\text{SnTe}(^{119\text{m}}\text{Te})$  [Fig. 2(b)], in which  $^{119}\text{Sb}$  atoms were distributed both in Sn and Te sites.<sup>2)</sup> Since the electronegativity of Sb lies almost in the middle of Sn and Te,  $^{119}\text{Sb}$  can be stabilized both in the Sn and Te sites of SnTe as cationic and anionic defects respectively. The  $^{119}\text{Sb}$  atoms, however, are considered to have been preferentially stabilized in

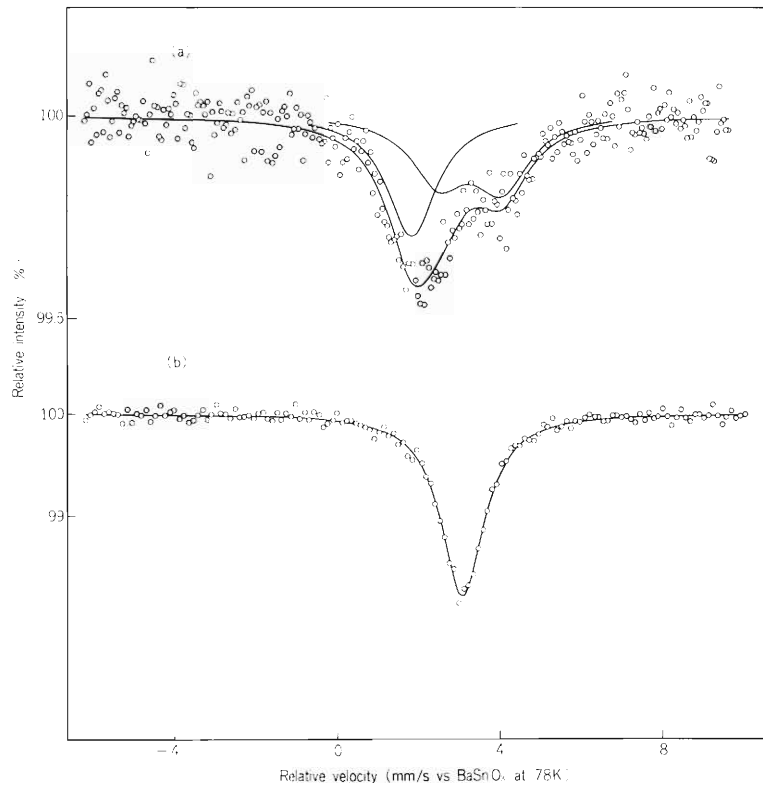


Fig. 1.  $^{119}\text{Sn}$ -Mössbauer emission spectrum of (a)  $\text{Se}(^{119\text{m}}\text{Te})$  and (b)  $\text{Te}(^{119\text{m}}\text{Te})$ .

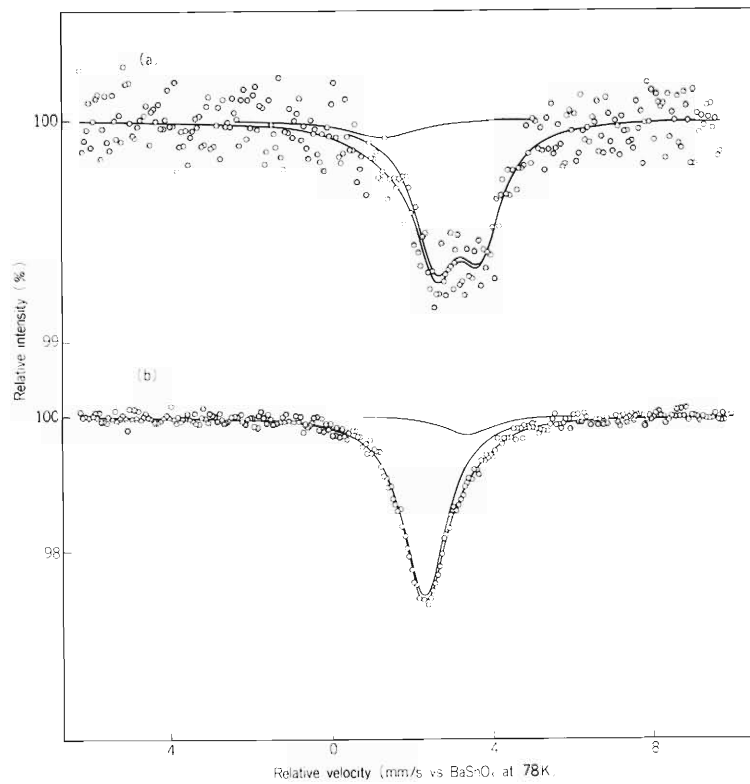


Fig. 2.  $^{119}\text{Sn}$ -Mössbauer emission spectrum of (a)  $^{120}\text{SnSe}(^{119\text{m}}\text{Te})$  and (b)  $^{120}\text{SnTe}(^{119\text{m}}\text{Te})$ .

Sn site of SnSe as cationic defects, because the electronegativity of Sb lies much closer to that of Sn than to that of Se.

It is also interesting to note that defect  $^{119}\text{Sn}$  atoms were found both in divalent and tetravalent states after the EC decays of  $^{119\text{m}}\text{Te}$  in Se and SnSe. This indicates that selenium anions can stabilize defect  $^{119}\text{Sn}$  in the tetravalent state, though less electronegative tellurium can not.

#### References

- 1) F. Ambe, S. Ambe, H. Shoji, and N. Saito: *J. Chem. Phys.*, 60, 3773 (1974).
- 2) F. Ambe and S. Ambe: *J. Physique*, 37, C6-923 (1976).
- 3) C. H. W. Jones and M. Mauguin: *J. Chem. Phys.*, 67, 1587 (1977).
- 4) V. Fano and I. Ortalli: *ibid.*, 61, 5017 (1974).
- 5) L. N. Vasil'ev: *Izv. Akad. Nauk. SSSR. Neorg. Mater.*, 13, 1752 (1977).
- 6) P. P. Seregin, M. A. Sagatov, F. S. Nasredinov, and L. N. Vasil'ev: *Fiz. Tverd. Tela*, 15, 1928 (1973) [*Sov. Phys. Solid State*, 15, 1291 (1973)].

## 7-5. Chemical States of Defect Tin Atoms in InSb and In<sub>2</sub>Te<sub>3</sub> by Mössbauer Emission Spectroscopy

F. Ambe and S. Ambe

The chemical state of dilute impurity atoms in compound semiconductors is not fully explored yet in spite of their importance in determining electrical properties of the matrices. Although measurements of macroscopic parameters such as conductivity, Hall coefficient etc. give information on such impurities,<sup>1)</sup> direct determination of their lattice position and electronic state requires spectroscopic methods with high sensitivity. The <sup>119</sup>Sn Mössbauer emission spectroscopy developed in our laboratory<sup>2)-4)</sup> is expected to give useful information on the chemical state of impurity tin atoms in compound semiconductors. In this period <sup>119</sup>Sn atoms in InSb and In<sub>2</sub>Te<sub>3</sub> were studied.

<sup>119</sup>Sb and <sup>119m</sup>Te were produced by bombarding a tin plate with 14 MeV protons or 40 MeV  $\alpha$ -particles from the cyclotron. The radiochemical procedures to prepare Sb and Te metals labelled or doped with the source nuclides have been reported elsewhere.<sup>2), 5)</sup> The sources were prepared by fusing stoichiometric mixtures of indium and the labelled or doped metals under Ar. <sup>119</sup>Sn Mössbauer emission spectra of the sources were measured against a BaSnO<sub>3</sub> absorber at 78K as described previously.<sup>3), 4)</sup>

Indium antimonide labelled with <sup>119</sup>Sb (In<sup>119</sup>Sb) gave a single emission line with the isomer shift of  $1.94 \pm 0.03$  mm/sec relative to BaSnO<sub>3</sub> as shown in Fig. 1. The line is attributed to <sup>119</sup>Sn occupying the Sb site in the zinc blende-type cubic lattice of InSb, since the EC decay of <sup>119</sup>Sb to <sup>119</sup>Sn causes no atomic displacement.<sup>2)</sup> The isomer shift shows that the <sup>119</sup>Sn atoms coordinated by four In atoms are in a covalent Sn<sup>IV</sup> state and the s-electron density at their nuclei is only slightly smaller than that of <sup>119</sup>Sn in the diamond-type  $\alpha$ -tin.

In the InSb source doped with carrier-free <sup>119m</sup>Te (InSb (<sup>119m</sup>Te)) the <sup>119m</sup>Te atoms are considered to be in the Sb site of the matrix, since the electronegativity of Te is larger than that of Sb. The emission spectrum of the source was decomposed into two Lorentzian lines with the

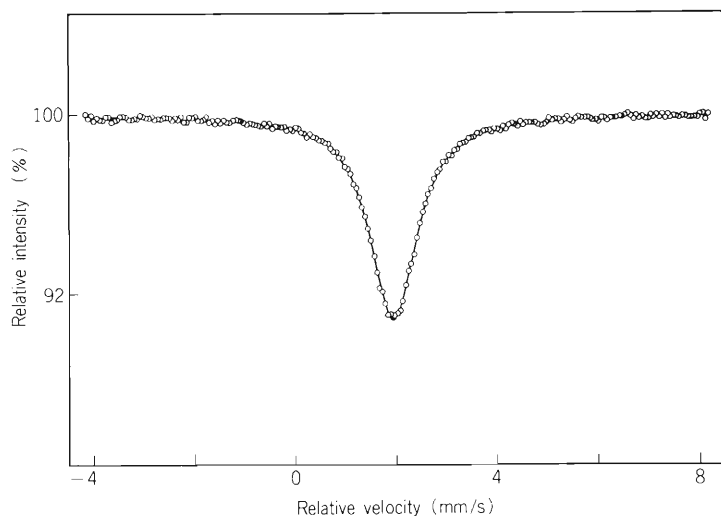


Fig. 1. <sup>119</sup>Sn-Mössbauer emission spectrum of In<sup>119</sup>Sb against BaSnO<sub>3</sub> at 78 K.

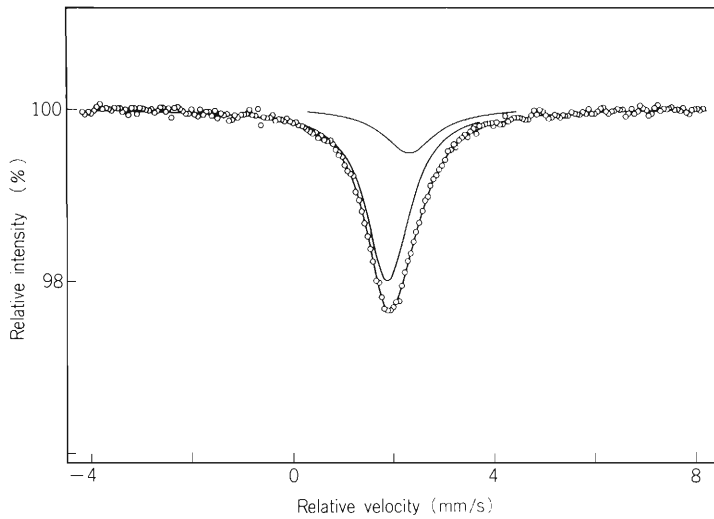


Fig. 2.  $^{119}\text{Sn}$ -Mössbauer emission spectrum of  $\text{InSb}(^{119\text{m}}\text{Te})$  against  $\text{BaSnO}_3$  at 78 K.

isomer shifts of  $1.88 \pm 0.05$  and  $2.3 \pm 0.1$  mm/sec (Fig. 2). The former line is attributed to  $^{119}\text{Sn}$  remaining in the Sb site from its similarity in isomer shift with the emission line of  $\text{In}^{119}\text{Sb}$  described above. The latter line with an isomer shift typical of  $^{119}\text{Sn}$  (II) surrounded by Sb atoms<sup>4)</sup> is ascribed to  $^{119}\text{Sn}$  arising from  $^{119}\text{Sb}$  which had been transferred to the In site as a result of the EC decay of  $^{119\text{m}}\text{Te}$ .

$\text{In}_2\text{Te}_3$  has a zinc blende-type structure, in which 1/3 of the In site is vacant. As shown in Fig. 3, the  $\text{In}_2^{119\text{m}}\text{Te}_3$  gave an emission spectrum composed of a doublet (isomer shift  $1.6 \pm 0.3$  mm/sec, quadrupole splitting  $1.5 \pm 0.3$  mm/sec) and a broad singlet (isomer shift  $3.21 \pm 0.05$  mm/sec). The doublet is considered to be due to  $^{119}\text{Sn}$  in the Te site on the basis of both the isomer shift and the quadrupole splitting: The low isomer shift suggests electropositive ligands rather than tellurium atoms, and a quadrupole splitting is in fact expected for  $^{119}\text{Sn}$  in the Te site because of the vacancies in the In site. The singlet is attributed to  $^{119}\text{Sn}$  (II) in the In site, since the isomer shift lies in the region for  $^{119}\text{Sn}$  coordinated by Te atoms.<sup>4)</sup>

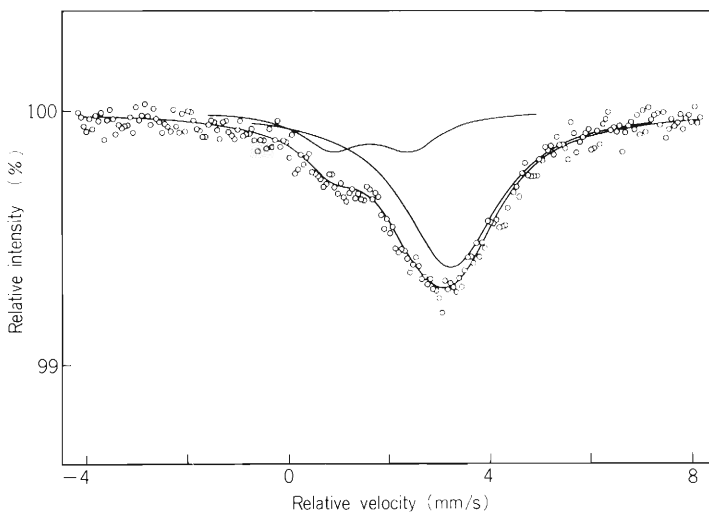


Fig. 3.  $^{119}\text{Sn}$ -Mössbauer emission spectrum of  $\text{In}_2^{119\text{m}}\text{Te}_3$  against  $\text{BaSnO}_3$  at 78 K.

The  $^{119}\text{Sn}$  Mössbauer emission spectroscopy using  $^{119}\text{Sb}$  and  $^{119\text{m}}\text{Te}$  as the source nuclides has thus been shown to enable determination of the electronic state of defect  $^{119}\text{Sn}$  in definite lattice sites of  $\text{InSb}$  and  $\text{In}_2\text{Te}_3$ . The results can be further utilized to determine the lattice position of  $^{119}\text{Sn}$  atoms incorporated into the matrices by diffusion or by ion implantation from their Mössbauer absorption spectra.

Similar investigations on other semiconductors are in progress.

#### References

- 1) C. Hilsum and A. C. Rose-Innes: *Semiconducting III-V Compounds*, (Pergamon Press 1961) p. 68.
- 2) F. Ambe, S. Ambe, H. Shoji, and N. Saito: *J. Chem. Phys.*, 60, 3773 (1974).
- 3) F. Ambe and S. Ambe: *Chem. Phys. Lett.*, 39, 294 (1976).
- 4) F. Ambe and S. Ambe: *J. Physique*, 37, C6-923 (1976).
- 5) The preceding report of this volume.

## 7-6. Exchange Reaction of Seleno-Compound with Elemental Selenium

K. Ogawa,\* K. Taki, and T. Nozaki

As reported previously,<sup>1)</sup>  $^{75}\text{Se}$ - or  $^{73}\text{Se}$ -2-selenouracil is obtained by the exchange reaction of the selenium atom of 2-selenouracil with elemental selenium-75 or selenium-73. In order to decide the optimum condition for the exchange reaction, several experiments were performed using elemental selenium-75. The elemental selenium-75 was prepared by the reduction of  $^{75}\text{Se-H}_2\text{SeO}_3$  to red selenium with hydrazine and extracted into carbon disulfide. The exchange reaction is caused by heating the above selenium solution with 2-selenouracil in a sealed tube. The solution should be well degassed to prevent the oxidation of elemental selenium and 2-selenouracil.

$^{75}\text{Se}$ -2-Selenouracil produced in the reaction mixture was separated by the previous method<sup>1)</sup> and its radioactivity was determined by paper chromatography using a mixture of n-butanol, acetic acid and water (2:1:1).

2-Selenouracil is soluble in pyridine but insoluble in carbon disulfide, while elemental selenium is soluble in pyridine and much more soluble in carbon disulfide. Therefore, the exchange reaction was affected by the composition of the reaction mixture and also by the reaction temperature. The activity yield of  $^{75}\text{Se}$ -2-selenouracil as a function of the mixture ratio of the two solvents is shown in Fig. 1, and the yield of  $^{75}\text{Se}$ -2-selenouracil against the reaction temperature is shown in Fig. 2. From the above results, the practical exchange reaction is

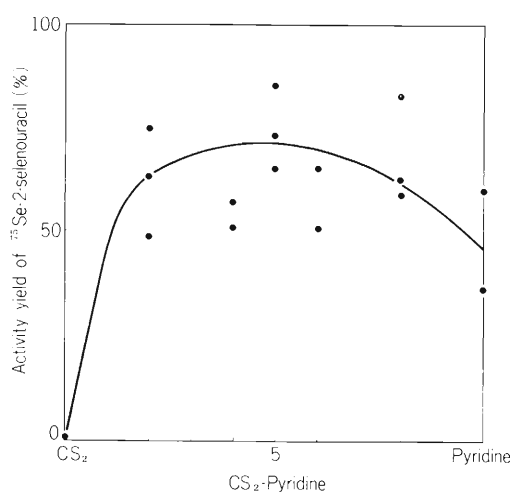


Fig. 1. Activity yield of  $^{75}\text{Se}$ -2-selenouracil as a function of mixing ratio of  $\text{CS}_2$  and pyridine. 2-Selenouracil, 1 mg; Elemental selenium-75, 4.9  $\mu\text{g}$  (1  $\mu\text{Ci}$ ); Solvent (various ratio), 2 ml; Reaction time, 10 h; Reaction temp., 110°C.

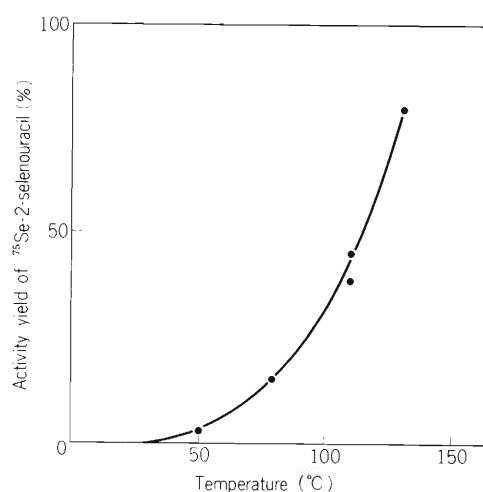


Fig. 2. Activity yield of  $^{75}\text{Se}$ -2-selenouracil as a function of reaction temperature. 2-Selenouracil, 1 mg; Elemental selenium-75, 4.9  $\mu\text{g}$  (1 mCi); Solvent,  $\text{CS}_2$ : Pyridine (1:1) 2 ml; Reaction time, 3 h.

\* Faculty of Hygienic Science, Kitasato University.

recommended to be carried out in the mixture of pyridine and carbon disulfide (1:1) at 130°C.

Figure 3 shows both the specific activity and total activity of  $^{75}\text{Se}$ -2-selenouracil for the various amount of 2-selenouracil. It seems that the exchange reaction of a small amount of elemental selenium with a much larger amount of 2-selenouracil is of first order with respect to the concentration of the latter. Hence, the use of a large amount of 2-selenouracil gives a faster exchange but with lowering of the specific activity of product selenouracil. It is necessary to add 2-selenouracil  $2 \times 10^2$  times as much as elemental selenium in order to introduce about 70 % selenium activity under the given experimental condition.

The solid line in Fig. 4 shows the activity yield in the exchange reaction of 1 mg 2-selenouracil and 4.9  $\mu\text{g}$  elemental selenium-75 in 2 ml of the mixture of pyridine and carbon disulfide (1:1) at 130°C. When  $^{73}\text{Se}$  is used instead of  $^{75}\text{Se}$ , the activity yield of  $^{73}\text{Se}$ -2-selenouracil can be given by the dotted line in Fig. 4. Because of 7.1 h half life of  $^{73}\text{Se}$ , the activity yield can give the maximum value at a reaction time of about 1-2 h.

Actually, 1.3 mCi of  $^{73}\text{Se}$ -2-selenouracil was prepared by the above method in 1 h from 5 mCi of elemental selenium-73 produced by the nuclear reaction  $^{75}\text{As}(p, 3n)^{73}\text{Se}$ .

In general, the exchange reaction is applicable to other selenium compounds having selenocarbonyl group.  $^{75}\text{Se}$ -2-Selenothymine and  $^{75}\text{Se}$ -6-selenopurine were also obtained from 2-selenothymine and 6-selenopurine.

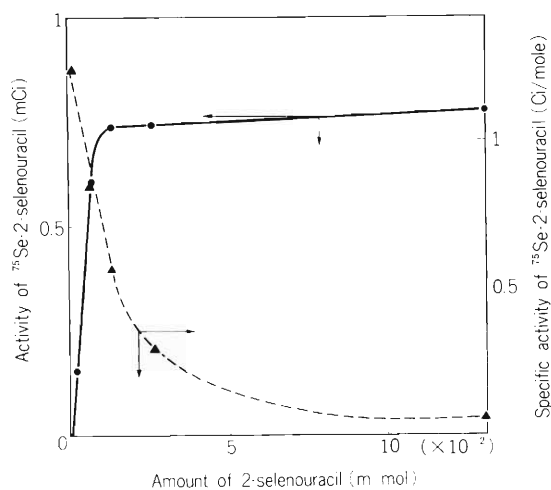


Fig. 3. Activity (—●—) and specific activity (---▲---) of  $^{75}\text{Se}$ -2-selenouracil as a function of the amount of 2-selenouracil. Elemental selenium-75, 4.9  $\mu\text{g}$  ( $6.2 \times 10^{-5}$  m mol), 1  $\mu\text{Ci}$ ; Solvent,  $\text{CS}_2$ : Pyridine (1:1) 2 ml; Reaction time, 10h; Reaction temp., 110°C.

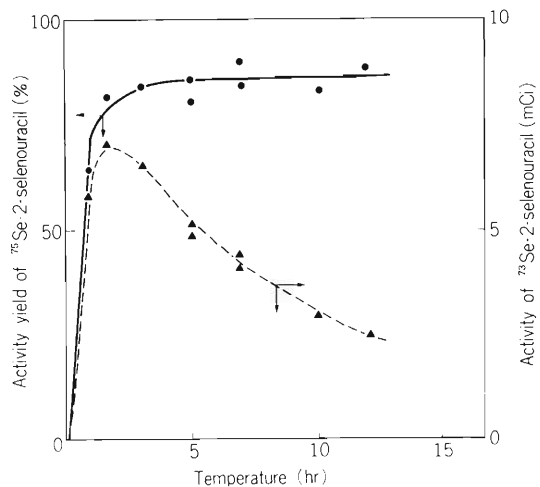


Fig. 4. Activity yield of  $^{75}\text{Se}$ -2-selenouracil (—●—) and activity of  $^{73}\text{Se}$ -2-selenouracil (---▲---) as a function of reaction time. 2-Selenouracil, 1 mg; Elemental selenium-75, 4.9  $\mu\text{g}$  (1  $\mu\text{Ci}$ ); Solvent,  $\text{CS}_2$ : Pyridine (1:1) 2 ml; Reaction temp., 130°C.

## Reference

- 1) K. Ogawa, K. Taki, and T. Nozaki: IPCR Cyclotron Progr. Rep., 12, 116 (1978).

## 8. RADIATION CHEMISTRY AND RADIATION BIOLOGY

### 8-1. Measurement of the Decay of the Emission from $\sigma$ -Excitons Produced in a KBr Crystal by Heavy-Ion Irradiation

K. Kimura and M. Imamura

We have continued measurement of the fast decay of the emission from  $\sigma$ -excitons in a KBr single crystal produced by heavy ion-irradiation, using the apparatus reported in the preceding report.<sup>1)</sup> The apparatus is capable of recording time-dependent spectra in the nanosecond range.

One of the striking features found from heavy-ion irradiation experiments is the enhancement of the  $\sigma$ -emission intensity, i.e., a large ratio of  $\sigma$ -emission to  $\pi$ -emission intensity compared to that observed in electron irradiation.<sup>2)</sup>

Extensive studies have been focused on the mechanism giving such a large  $I_{\sigma}/I_{\pi}$  ratio in heavy-ion irradiation. The results led to the conclusion that the  $\sigma$ - and  $\pi$ -excitons are produced in a ratio different from that in electron irradiation. Free excitons, which are regarded as precursors of the  $\sigma$ - and  $\pi$ -excitons, are created in the heavy-ion tracks so densely that they will inevitably experience collisions with each other. On the other hand, almost all free excitons created by low-LET radiations undergo intersystem crossing without collision to form  $\sigma$ - and  $\pi$ -exciton. No experimental evidence has been obtained for the preferential formation of  $\sigma$ -excitons by collision, however. Further studies will be made on this essential point.

#### References

- 1) K. Kimura and M. Imamura: IPCR Cyclotron Progr. Rep., 12, 118 (1978).
- 2) K. Kimura and M. Imamura: Phys. Lett., 67A, 159 (1978).

## 8-2. New Apparatus for Cyclotron-Beam Irradiation of Biological Samples

F. Yatagai and A. Matsuyama

Beams of helium-, carbon-, nitrogen-, and oxygen-ions accelerated by the cyclotron have been employed for biological experiments. The biological irradiation system, which has been used so far, is summarized as follows. The ion beam passed through collimators, slits, and a scattering foil for dosimetry, and emerged horizontally into air from an aluminum vacuum window. After traversing an air gap, most of the beam reached the filter on which the samples to be irradiated were spread in a thin layer. As the size of the beam spot (2 mm square) is smaller than the area of the filter (8 or 24 mm in diameter), the filter was moved in the plane perpendicular to the beam axis to be uniformly irradiated.<sup>1)</sup> Solid state detectors and a Faraday cup were used for the determination of particle fluence according to the method of Kochanny et al.<sup>2)</sup>

Various effects of high-LET radiations on biological materials, such as bacterial cells and phages, have been investigated by using this irradiation system. For radiosensitive materials such as mammalian cells for which a low-dose irradiation is required, a mechanical chopper was attached to this irradiation system to decrease the beam intensity.<sup>3)</sup> However, in such a case, an accurate dosimetry and a uniform irradiation could not be obtained easily. A new apparatus was, therefore, constructed to irradiate various biological materials using the beam elastically scattered

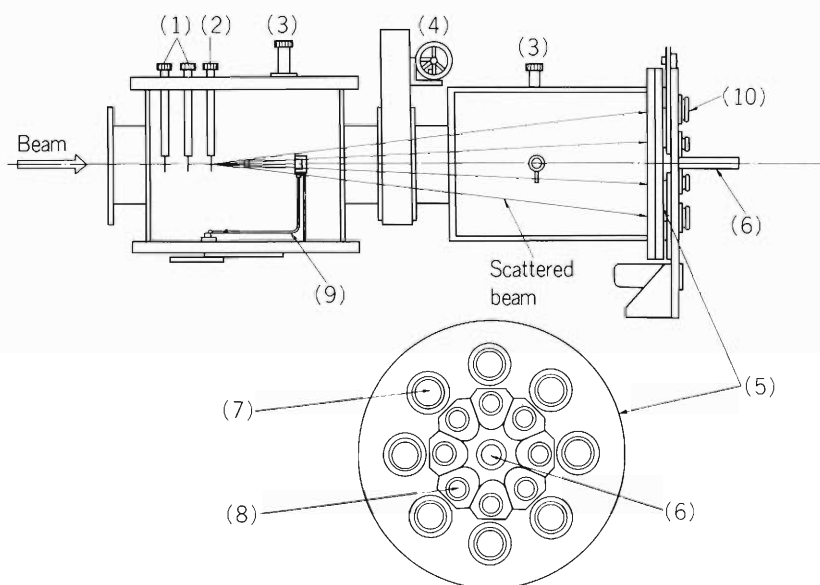


Fig. 1. Scheme of new apparatus for biological irradiations.

- (1) Slit (2) Scattering foil (3) Vacuum gauge (4) Gate valve (5) End of vacuum chamber (6) Faraday cup (7) Vacuum windows for low-dose irradiations (8) Vacuum windows for high-dose irradiations (9) Arm to suspend a solid state detector (10) Sample holders.

at some angle by the scattering foil. As shown in Fig. 1, the end of vacuum chamber, which is at a distance of 800 mm from the scattering foil, has two sets of vacuum windows on different circles. The radii of two circles are 38 and 83 mm corresponding to the scattering angle of  $2^{\circ}45'$  and  $6^{\circ}00'$ , respectively. The radius of each of the windows located on the  $2^{\circ}45'$  circle is 10 mm and that located on the  $6^{\circ}00'$  circle is 25 mm. The former is made smaller because the relative intensity decreases rapidly at small angles with the increase of the scattering angle. There are two kinds of sample holders for the two sizes of the windows, and the sample mounted on the holder faces the window and is made to rotate to ensure uniform irradiation. The radiosensitive samples mentioned above can be irradiated at lower dose-rate by the ion beam passing through the larger windows ( $\theta = 6^{\circ}00'$ ). Such positions and sizes of windows were determined from both the preliminary results on dose distributions obtained with photographic paper and theoretical calculations based on the Rutherford scattering law.

Although this new apparatus has many advantages over the previous one, further improvements to get better dosimetry and uniform-irradiation are in progress.

#### References

- 1) F. Yatagai, T. Takahashi, Y. Kitajima, and A. Matsuyama: *J. Radiat. Res.*, 15, 90 (1974).
- 2) G. L. Kochanny, Jr., A. Timnick, C. J. Hochanadel, and C. D. Goodman: *Radiat. Res.*, 19, 462 (1963).
- 3) Y. Yamawaki, F. Yatagai, I. Kaneko, K. Sakamoto, S. Okada, and A. Matsuyama: *IPCR Cyclotron Progr. Rep.*, 10, 117 (1976).

## 8-3. Inactivation of Ribonuclease A in Solution by Cyclotron Beams

Y. Hattori, F. Yatagai, and A. Matsuyama

In connection with the development of a new biological irradiation device, the vessel for the irradiation of enzyme solution has been improved in this period. As the range in water of heavy ion beams accelerated by the cyclotron is about  $200\mu\text{m}$ , we are forced to irradiate sample solution in a vessel with a window of thin foil or film through which the ion beams are shot into the solution. In the previous experiments<sup>1), 2)</sup> we used a glass vessel with a flange to which aluminum foil of  $20\mu\text{m}$  thickness was fixed with a screw cap, and the sample solution therein was agitated by a magnetic stirrer during the irradiation. Recently we have been aware that fluctuations in the experimental results were largely attributable to the vessel which was apt to form bubbles in the sample solution by the agitation because of its shape and consequently to lead to error in the dose estimation. In order to improve this fault a new type vessel was tested. It is a cuvette for spectrophotometer modified by making a window of Mylar film of  $10\mu\text{m}$  thickness by pasting the film with adhesive agent to a hole ( $10\text{ mm} \times 10\text{ mm}$ ) made on one side of the cuvette. The sample solution is irradiated with ion beams through the film under agitation by a magnetic stirrer. This irradiation vessel has proved to give more reproducible results than before.

Using the new type vessel, dilute solution of ribonuclease (RNase) A was irradiated by N-ions focusing attention to the stability of remaining enzymic activity after irradiation. The result obtained up to date suggests that the RNase solution irradiated with N-ion beam would be more unstable when kept in the refrigerator than unirradiated control. The experiment is to be continued.

## References

- 1) Y. Hattori, F. Yatagai, and A. Matsuyama: IPCR Cyclotron Progr. Rep., 11, 130 (1977).
- 2) F. Yatagai, S. Kitayama, Y. Hattori, and A. Matsuyama: *ibid.*, 12, 123 (1978).

## 8-4. Studies on Mutation Induction in Microorganisms by Cyclotron Beams

A. Matsuyama, F. Yatagai, A. A. Baradjanegara,\*  
K. Sone,\*\* and H. Matsuura\*\*

### 1. Irradiation of *E. coli*

Mutation induction in *E. coli* by  $\alpha$ -particles, C- and N-ions accelerated in the cyclotron was studied with its two strains, WP2 (try<sup>-</sup>) and Sd-4 (TC). The reverse mutation from tryptophan requirement in WP2 (try<sup>-</sup>) and from streptomycin dependence in Sd4 (TC) was induced by these heavy charged particles with different behaviours in the two strains. With strain WP2, the reverse mutation frequency increased exponentially with increasing radiation doses<sup>1)</sup> (Table 1). At doses giving the same lethal effect, the mutational effect of both  $\alpha$ -particles and heavy ions was greater than that of <sup>60</sup>Co  $\gamma$ -rays. On the other hand, in the case of strain Sd-4, the effect of N-ions on mutation induction was smaller than that of <sup>60</sup>Co  $\gamma$ -rays, although the effect of  $\alpha$ -particles was somewhat greater than the  $\gamma$ -ray effect (Table 2).

Table 1. Mutation induction in *E. coli* WP2.

Type of radiation	Beam energy (MeV/amu)	Total LET (keV/ $\mu$ m)	Lethality <sup>a)</sup> (A)	Mutation induction <sup>b)</sup> (B)	Ratio (B/A)
<sup>60</sup> Co $\gamma$ -rays		(~0.4)	0.088	0.079	0.90
			0.112	0.089	0.80
$\alpha$ -particles	{ 5.5	29.1	0.110	0.115	1.05
	{ 2.9	49.2	0.179	0.235	1.31
C-ions	{ 4.8	290	0.055	0.053	0.97
	{ 4.1	330	0.019	0.022	1.18
	{ 2.4	468	0.038	0.053	1.41
N-ions	4.8	392	0.042	0.050	1.20

a) Decrease in surviving fraction in log/krad.

b) Increase in revertants/10<sup>8</sup> survivors in log/krad.

\* Bandung Reactor Center, National Atomic Energy Agency, Indonesia.

\*\* Kaken Chemical Co., Ltd.

Table 2. Mutation induction in *E. coli* Sd-4.

Type of radiation	Beam energy (MeV/amu)	Total LET (keV/μm)	Revertants/10 <sup>8</sup> survivors				
			For D <sub>30</sub>		For D <sub>10</sub>		
			EA	CF	EA	CF	
<sup>60</sup> Co γ-rays		(~0.4)	300	—	590	—	
α-particles	{	4.8	33.3	315	—	640	—
		4.7	33.7	430	350	—	—
N-ions	{	4.9	375	101	—	192	—
		4.8	390	155	150	228	182
		4.8	390	—	118	—	240
		4.8	390	190	170	298	215
		4.8	390	110	110	198	170

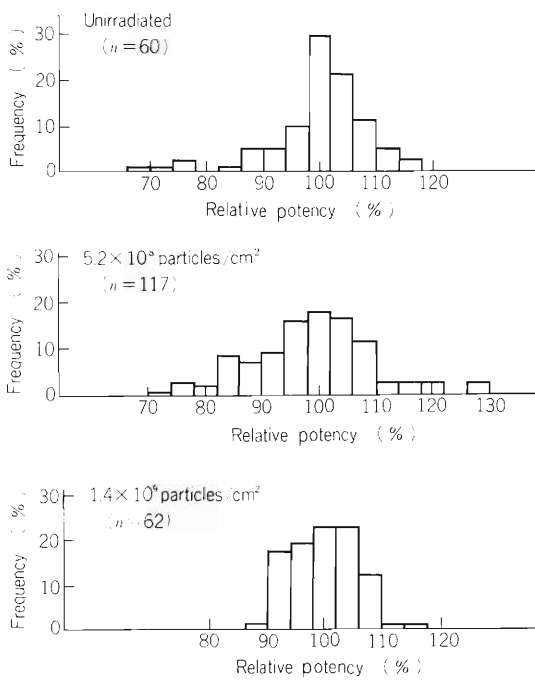


Fig. 1. Survival curve of *Streptomyces griseochromogenes* spores for N-ions (4.96 MeV/amu).

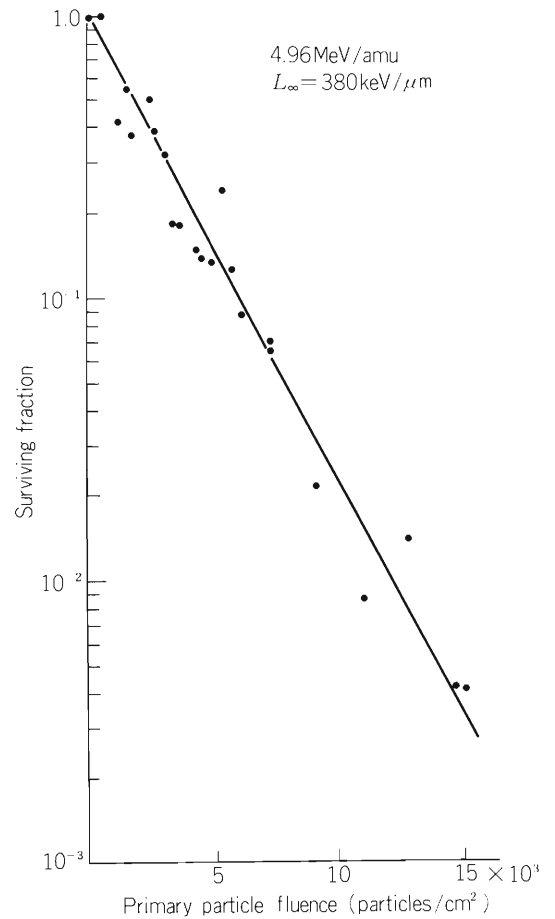


Fig. 2. Effects of N-ions (4.96 MeV/amu) on the frequency distribution pattern of blasticidin S production by *S. griseochromogenes*.

## 2. Irradiation of Streptomyces spores

In the previous experiments on mutation induction by heavy ions using  $\phi$ X 174 phage infected into host cells of E. coli, mutation induction in phage was observed only with UV-preirradiated host cells.<sup>2)</sup> Following this finding, mutagenic effects of cyclotron beams on the frequency pattern of blasticidin-S production by Streptomyces griseochromogenes were determined. Spores of this strain suspended in sterile distilled water were irradiated by  $\alpha$ -particles and N-ions without any pre- and post-treatments (Fig. 1) and subjected to the determination of the frequency distribution pattern of relative potency with survivors at different doses. Tentative results indicate that the potency distribution pattern in spreading out toward both higher and lower sides after irradiation (Fig. 2). This trend was most remarkable at doses giving 1 – 10 % survival and the variance in the relative potency distribution appeared to become smaller at doses exceeding this level.

## References

- 1) A. A. Baradjanegara, F. Yatagai, F. Kaneko, and A. Matsuyama: J. Radiat. Res., 20, 60 (1979).
- 2) F. Yatagai, S. Kitayama, Y. Hattori, and A. Matsuyama: IPCR Cyclotron Progr. Rep., 12, 123 (1978).

## 9. RADIATION MONITORING

### 9-1. Routine Monitoring

K. Igarashi, I. Usuba, S. Fujita, and I. Sakamoto

Results of routine radiation monitoring carried out on the cyclotron from April 1978 to March 1979 are described.

No remarkable change in leakage radiation and residual activities was observed during this period. Some aspects of the leakage radiation are described in the following report.

#### (1) Surface and air contamination

The surface contamination has been kept below  $10^{-6}$   $\mu\text{Ci}/\text{cm}^2$  on the floor of cyclotron room and the underground passage, and below  $10^{-7}$   $\mu\text{Ci}/\text{cm}^2$  in the experimental areas, hot laboratory and chemical laboratories. The contamination was wiped off twice a year, and immediately after this decontamination, the contamination on the floor of cyclotron room and the underground passage had been reduced to a value below  $10^{-7}$   $\mu\text{Ci}/\text{cm}^2$ .

When the accelerating chamber was opened, slight contamination of the air in the cyclotron room was observed. The value of radioactivity concentration (beta-gamma) was  $10^{-12}$   $\mu\text{Ci}/\text{cm}^3$ .

#### (2) Drainage

The radioactive concentration of the drain water from the cyclotron building was found to be of the order of  $10^{-6}$  –  $10^{-7}$   $\mu\text{Ci}/\text{cm}^3$ . The total quantity of activities in the aqueous effluents in

Table 1. Annual exposure dose received by the cyclotron workers from April 1978 to March 1979.

Workers	Dose undetectable	Number of persons			Collective dose (man-mrem)
		10-100 (mrem)	101-300 (mrem)	>300 (mrem)	
Operators	1	3	2	1	890
Nuclear physicists	13	3		1	500
Accelerator physicists	6	2			20
Physicists in other fields	12	4			130
Nuclear chemists	4	8	3		990
Radiation chemists	4				
Biological chemists	8				
Health physicists	1	1			10
				Total	2540

Average annual dose per person: 33.0 mrem

Maximum individual annual dose: 420 mrem

this period was about 53.5  $\mu\text{Ci}$ , and the radioactive nuclides found by the gamma-ray spectrometry were mainly  $^{65}\text{Zn}$ ,  $^{57}\text{Co}$ ,  $^{58}\text{Co}$ , and,  $^{60}\text{Co}$ .

### (3) Personnel monitoring

The external exposure dose to personnel was measured with gamma-ray and neutron film badges. The dose received during the present period by all the cyclotron workers is shown in Table 1. The collective gamma-ray dose to all workers was 2540 man-mrem, while those owing to thermal and fast neutron exposures were too small to be detected.

The collective dose to the cyclotron workers is about five-sevenths of the value in the preceding period. In this period the dose to the cyclotron operators was 890 man-mrem, which was 35.0 % of the dose of cyclotron workers, and the maximum individual annual dose was 420 mrem.

## 9-2. Leakage-Radiation Measurement at the Underground Passage

I. Sakamoto

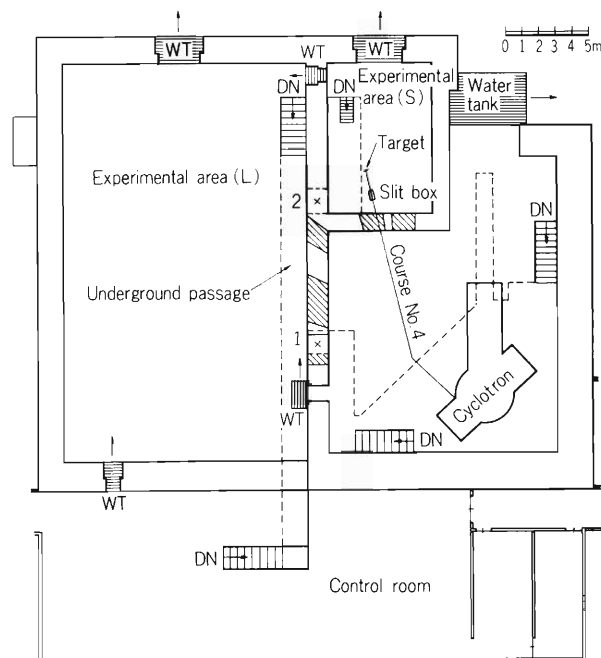
Leakage radiation during operation of the cyclotron at the underground passage of the cyclotron building was measured. Leakage dose received from April 1978 to March 1979 by gamma-ray and neutron film badges which were left at the underground passage, is shown in Table 1. No machine time was allotted for deuteron acceleration in this period.

Among dose values at the point No. 1 measured every month, the maximum dose of 360 mrem was observed in November. In this case, the values of gamma dose and thermal neutron dose were 290 mrem and 70 mrem, respectively.

Table 1. Leakage radiation dose (in mrem) at the underground passage from April 1978 to March 1979.

Radiation	Point of observation*	
	1	2
gamma-ray (mrem)	1540	520
thermal neutron (mrem)	470	140
fast neutron (mrem)	30	180
total (mrem)	2040	840

\* See the figure shown below.



The fast neutron dose of 180 mrem was observed at the point No. 2 in February 1979, but it was not observed in other months in this period. As a result of the investigation, it was concluded that the fast neutron dose was due to the 22 MeV  $\alpha$ -particle bombardment on a brass slit at about 100 nA in case of irradiation experiment in the beam course No. 4. The slit will be replaced by the one made of material which yields much less neutrons by alpha bombardment.

## 10. HEAVY ION LINEAR ACCELERATOR PROJECT

### 10-1. Status of the Constructional Work

M. Odera

The constructional work of the linac which was started in 1975 by a contract with a factory to build the first resonator and has been pursued with many debates, troubles, contracts followed by contracts with a number of firms is nearing completion.

The six resonators, the main vacuum system and the environmental radiation monitoring system were installed last year. They have been operated for a year and some defects such as vacuum leaks or circuit failures which developed under various conditions were repaired and improved. Meanwhile, high power test of the proto-type amplifier, coupled with the first resonator was successfully carried out in January 1979. The multipactoring phenomenon in the cavity was overcome within two hours after starting excitation of the cavity. A few days later, an accelerating voltage of 80 % of design value was obtained across the drift tube gaps. Incorporating the experience obtained in that test operation, the final details of the amplifier design were fixed, and an order was given to a factory to construct the remaining amplifiers. Installation of those amplifiers began in March and was completed at the end of August 1979. Figure 1 shows the main parts of the accelerator system in the vault.

Beam acceleration test was started in July. Firstly, alignment of the injector beam line and then those of the drift tubes was examined using DC beam having a small emittance value. Ions used were singly or doubly-charged nitrogen, neon and argon. Acceleration simulation by the first cavity was made in the variable frequency mode. Frequency change was found not cumbersome at least in the range below 30 MHz used in the test operation. Drift of resonant frequency of the cavity was not excessive and could be easily compensated manually. Fast response of the feed back loops for the phase and amplitude stabilization seems not required. Since, wiring and conditioning of the control system is still underway in the accelerator vault, the acceleration test can not be very complete. However, performance of the power amplifier has been found improving day by day and the maximum accelerating voltage has exceeded the design value in a week after the test has begun. Stability of the amplifier against vacuum sparking also improved by time, showing the effect of the surface condition of the vacuum vessel on the operation of the amplifiers coupled with cavities.

Installation of the cooling system was finished in June. Though most of the system was installed already in March, the Freon circulation system for cooling of the drift tubes was not completed until that month.

The polyethylen insulators used for measurements of the proto-type buncher characteristics were replaced with the ceramic insulators so that insulation can withstand power test under vacuum. The length of the coaxial stem was shortened in order that the range of the resonant frequencies desired can be covered in spite of increase of the dielectric constant of the insulators. The low power characteristics were remeasured and were found in good agreement with those expected.



Fig. 1. The resonators and amplifiers in the accelerator vault, July 1979.

The beam bunch signal pick-up probes and beam profile monitors are being tested in the beam line together with the slits system. Those beam diagnostic elements use solely welded-bellows for introduction of mechanical motion into vacuum.

Installation and wiring of the control system are somewhat behind the schedule and will be finished in the fall 1979. The delay is partly caused by the delay to fix detailed specifications of control sequences, which in turn are tightly related with the operation scheme of the ratio-frequency amplifiers. Since the parallel operation of the six power amplifiers is still in the testing stage, the final operation scheme will not be fixed for a while. Therefore, acceleration test will be made tentatively by the local manual control. In view of the improvement observed in the amplifier performance, the local operation mode does not seem difficult to carry out.

Figure 2 shows the plan view of the linac facility. The control and counting areas are united in a single room in order to keep close contact between experimenters and accelerator operators. Quick access to the irradiation rooms and the accelerator vault from this room is possible because the rooms are on the same floor level except the biological experimental room which is situated 3.7 m under ground. Beams will be bent downward vertically into that room.

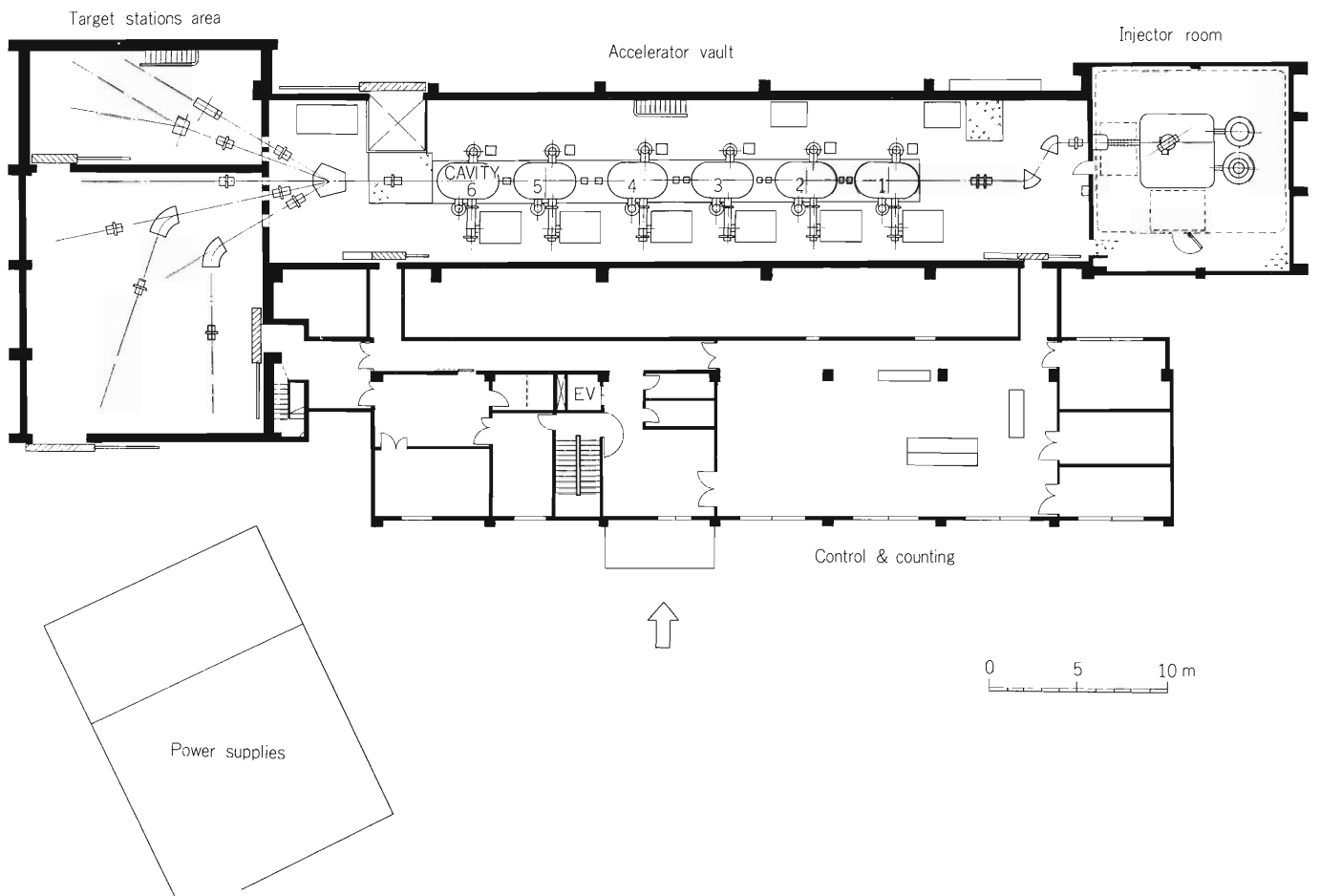


Fig. 2. Plan drawing of the linac facility.

## 10-2. Vacuum System

Y. Miyazawa

The vacuum system of the accelerator can be divided into three blocks: that for the injector, six cavities and the beam lines in the experimental area. This report is confined to the description of the vacuum equipment for the six cavities.

Each tank of the cavities has a volume of 11000  $\ell$  and a surface area exposed to vacuum of approximately 120  $\text{m}^2$ . Forty two percent of the exposed surface is made of stainless steel and the rest is mostly of copper. Organic seals occupy 0.3 % of the exposed surface. Each tank is connected to the next tank by a beam line of approximately 1.6 m which contains various magnetic and diagnostic elements. This part of the vacuum system presents relatively large surface area compared to volume. Figure 1 shows how the turbo-molecular pumps are connected to the tank. Conductance through the rf-compensator is 13000  $\ell/\text{sec}$  for air. Each tank is provided with two turbo-molecular pumps having pumping speed of 5000 and 2400  $\ell/\text{sec}$ . Total pumping speed through the rf-compensators is 4000  $\ell/\text{sec}$  for air when the two pumps are used in parallel.

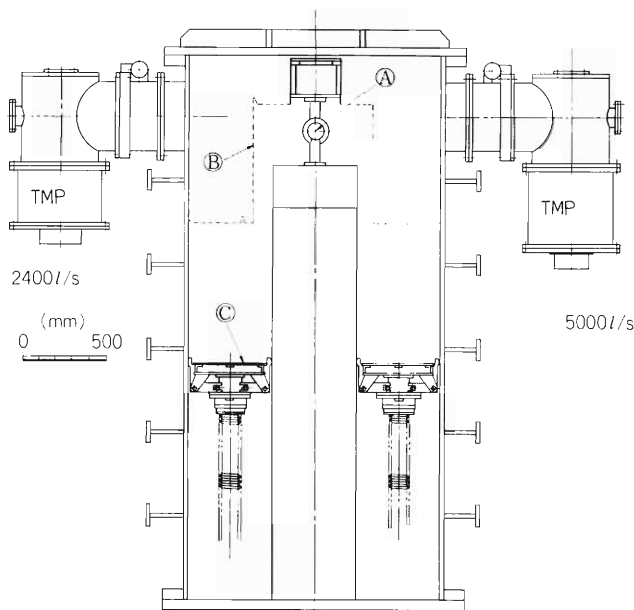


Fig. 1. Cross section of a cavity and positions of the large capacity turbo-molecular pumps.

A: Beam axis. B: rf compensators and pumping holes. C: Shorting device.

Figure 2 shows a schematic diagram of the vacuum system. A roots pump (300  $\text{M}^3/\text{h}$ ) and a rotary pump (342  $\ell/\text{min}$ ) are used as backing pumps for the two turbo-molecular pumps. The European vacuum ISO type NW 63 pipes are used to provide the beam path between the tanks. Roughing of the tanks from atmospheric pressure down to 0.5 Torr is accomplished by a 2500  $\text{M}^3/\text{h}$  roots pump and a 6500  $\ell/\text{min}$  rotary pump located on the lower floor of the accelerator vault. A typical time for the tanks to reach 0.5 Torr is 7 min. When the pressure in tank reaches 0.5 Torr, a pressure switch (Pirani gauge) closes a valve (VR-) leading to the tank to prevent backstreaming of oil vapour from the mechanical pump. If the tank is dry and vacuum tight, it will reach the



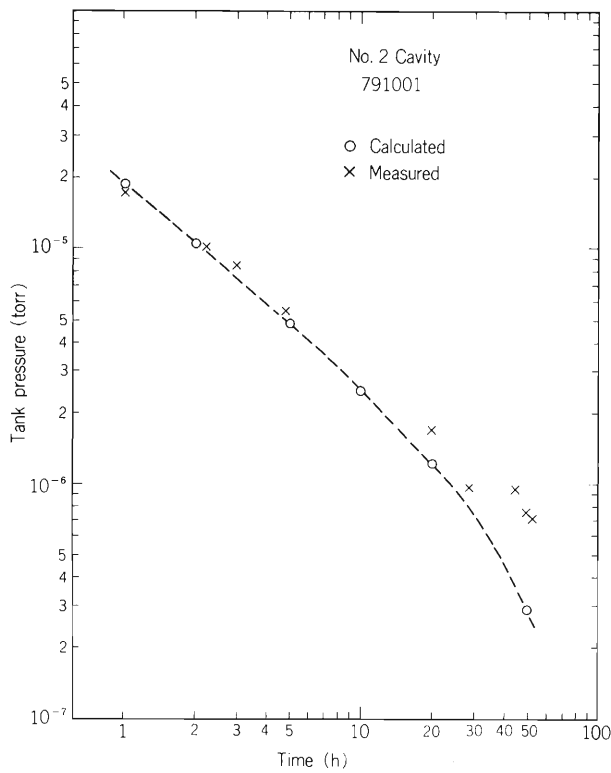


Fig. 3. Typical pumping down characteristics of a tank.

Table 1. Outgassing rate as a function of pumping down time.

Torr. $\ell/\text{sec} \cdot \text{cm}^2$	hour					
	1	2	5	10	20	50
$q_{\text{Cu}}$	$4 \times 10^{-5}$	$2.2 \times 10^{-5}$	$8.8 \times 10^{-6}$	$4 \times 10^{-6}$	$2 \times 10^{-6}$	$5.5 \times 10^{-7}$
$q_{\text{g}}$	$7 \times 10^{-3}$	$4.5 \times 10^{-3}$	$2.5 \times 10^{-3}$	$1.5 \times 10^{-3}$	$7 \times 10^{-4}$	$1.3 \times 10^{-4}$

$q_{\text{Cu}}$ : rate of outgassing of copper.

$q_{\text{g}}$ : rate of outgassing of organic seals.

T. Kambara, M. Odera, and S. Takeda

The Installation of the control system is now in progress with some delay from schedule.

In the linac vault, four data stations have been installed and the wiring between them and magnet power supplies has been almost completed. Figure 1 is the photograph of one of the data stations (right) and the power supplies for the drift tube quadrupole magnets of the cavities 1 to 3. The data station has an intelligent interface HP2240A/2241A (two boxes at the bottom) and signal conditioner modules (contained in five boxes above the interface). The intelligent interface has a microcomputer which talks with a control computer via a GPIB and a serial link, and provides input/output functions to control and monitor linac devices. The signal conditioner modules are used for signal conversion and electrical isolation between the interface and linac devices. Five types of signal conditioners are used: 1) Analog input with amplification and isolation, 2) analog output (10 bit resolution) with isolation, 3) analog output (14 bit resolution) with isolation, 4) digital input from floating contact with optical isolation and 5) digital output by contact with optical isolation. The signal conditioner modules have been manufactured, tested and installed by the contractor.

In the control room, monitoring panels for cooling and vacuum systems, a graphic panel to show the status of the whole linac system, and a control console have been set. The wiring for the monitoring panels and the graphic panel have been completed.

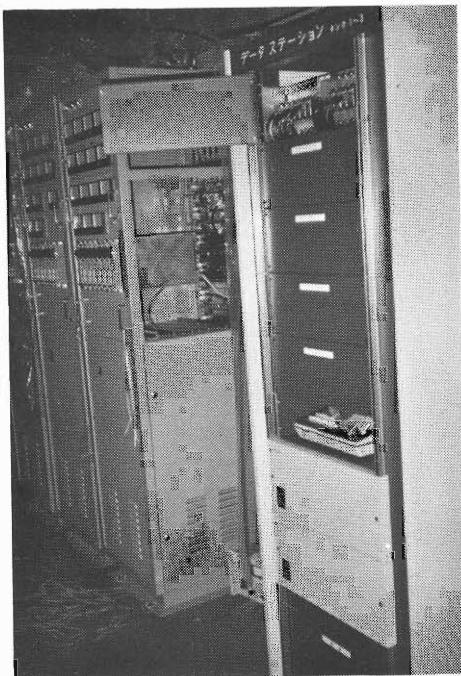


Fig. 1. A data station in the linac vault (right) and magnet power supplies.



Fig. 2. Control console (right) and monitoring panels and graphic panel on them (left).

Figure 2 is a photograph of the monitoring panels, the graphic panel and the control console. Two CRT's (HP2645A and HP2648A) which are connected to the control computer are installed in the console to be used for the control of the linac.

The control computer system (HP system 1000) has been changed a little from that reported previously.<sup>1)</sup> The operating system was upgraded from RTE-III to RTE-IV, and a CRT terminal (HP2621P) was added for exclusive use as the system console. An I/O extender was also added to allow future extension of the system. The graphic panel mentioned above is controlled by a micro-computer which talks with the computer with a high speed interface. In future we will have another micro-computer for a control panel in the control console, interfaced to the computer, where we can control the linac with more familiar devices (knobs, pushbuttons, switches etc.) rather than alphanumeric keyboards of the CRT's. A block diagram of the resultant system is shown in Fig. 3.

Figure 4 is the layout of devices in the control room and in the computer room which is air-conditioned separately.

The main part of the computer system has been installed and the software development is underway in cooperation with the contractor.

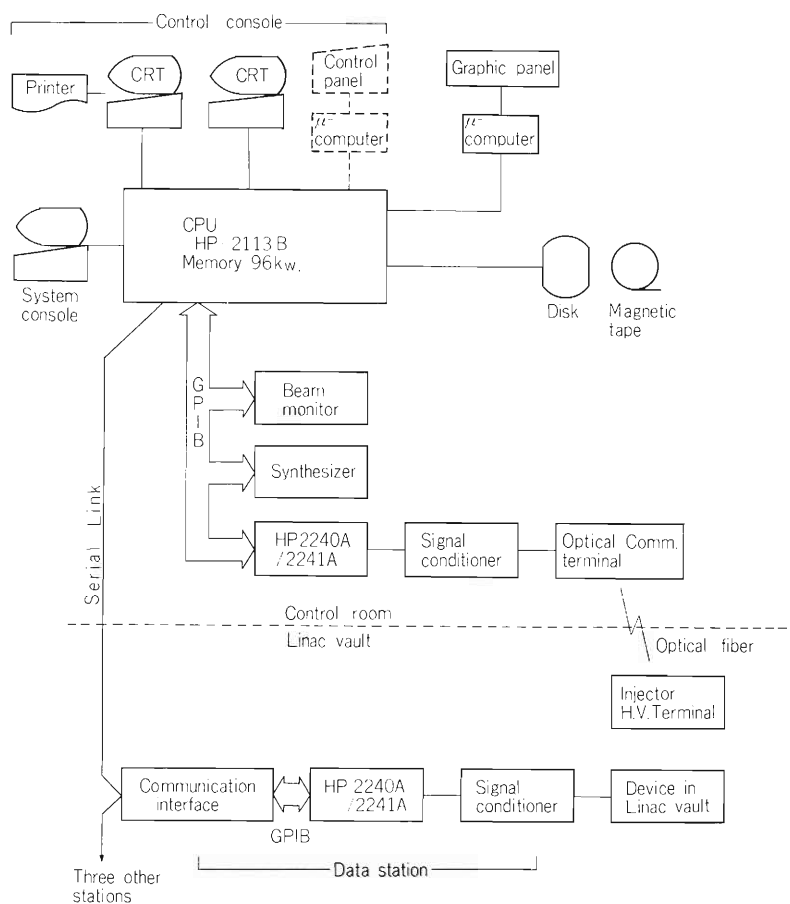


Fig. 3. Block diagram of the computer system.

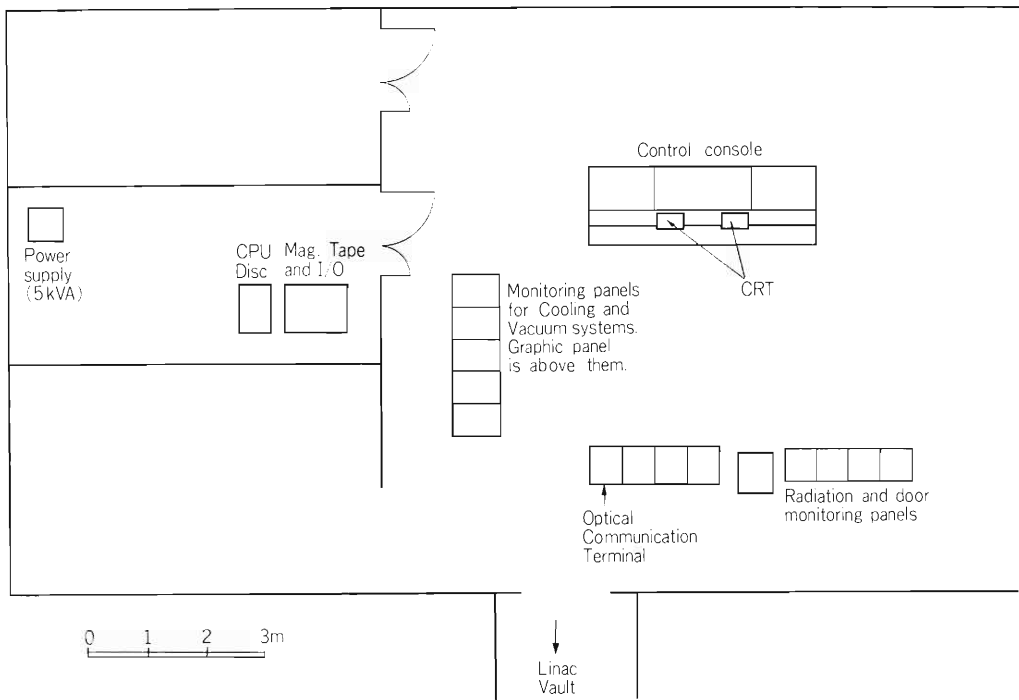


Fig. 4. Layout of devices in the control room and the computer room.

#### Reference

- 1) T. Kambara, M. Odera, and S. Takeda: IPCR Cyclotron Progr. Rep., 12, 131 (1978).

## 10-4. Installation of the Cooling System

T. Inoue

Figure 1 is the diagram of the cooling system. The system consists of the part for the injector and drift tube, and the main part. The former block was installed last year on the underground floor of the accelerator vault and has been in operation since. It supplies high resistivity deionized water to cool the instrument on the high voltage terminal of the injector. It

Table 1. Specifications of the cooling system.

Symbols	Apparatus	Specifications	Power (kW)	Weight (kg)
CT-1	Cooling tower	50 freezing-ton	1.5	515
CT-2	Cooling tower	500 freezing-ton	11	6300
CR-1	Chilling unit	127000 kcal/h	37	1150
P-1	Freon pump	500 $\ell$ /min 5 kg/cm <sup>2</sup>	15	170
P-2	Injection deionizer water pump	100 $\ell$ /min 9.5 kg/cm <sup>2</sup>	11	283
P-3	Auxiliary pump	30 $\ell$ /min 5 kg/cm <sup>2</sup>	3.7	144
P-4	Deionizer pump	10 $\ell$ /min 2 kg/cm <sup>2</sup>	1.5	85
P-5	Power amplifier deionizer water pump	1500 $\ell$ /min 9 kg/cm <sup>2</sup>	45	450
P-6	Deionizer pump	150 $\ell$ /min 2 kg/cm <sup>2</sup>	1.5	90
P-7	Resonator cooling pump	3500 $\ell$ /min 6.5 kg/cm <sup>2</sup>	55	610
P-8a	Vacuum system	150 $\ell$ /min 4 kg/cm <sup>2</sup>	3.7	105
P-8b	Cooling pump			
P-9	Cooling tower pump	600 $\ell$ /min 2 kg/cm <sup>2</sup>	3.7	86
P-10	Chilled water pump	430 $\ell$ /min 2.7 kg/cm <sup>2</sup>	3.7	53
P-11	Cooling tower pump	6400 $\ell$ /min 3 kg/cm <sup>2</sup>	55	905
T-1	Freon reservoir	1000 $\ell$ Stainless	—	2850
T-2	Deionizer water reservoir	400 $\ell$ Stainless	—	700
T-3	Deionizer water reservoir	2500 $\ell$ Stainless	—	3300
T-4	Ordinary water reservoir	500 $\ell$ Steel. Anticorrosion coated	—	800
T-5	Expansion tank	100 $\ell$ Steel. Anticorrosion coated	—	220
HEX-1	Heat Exchanger	78000 kcal/h	—	970
HEX-2	Heat Exchanger	49000 kcal/h	—	690
HEX-3	Heat Exchanger	75000 kcal/h	—	2350
HEX-4	Heat Exchanger	11500 kcal/h	—	2670
FW-1	Deionizer	10 $\ell$ /min $5 \times 10^6 \Omega$ -cm	—	
FW-2	Deionizer	18 $\ell$ /min $\times 8$ unit $5 \times 10^6 \Omega$ -cm	—	70 $\times$ 8

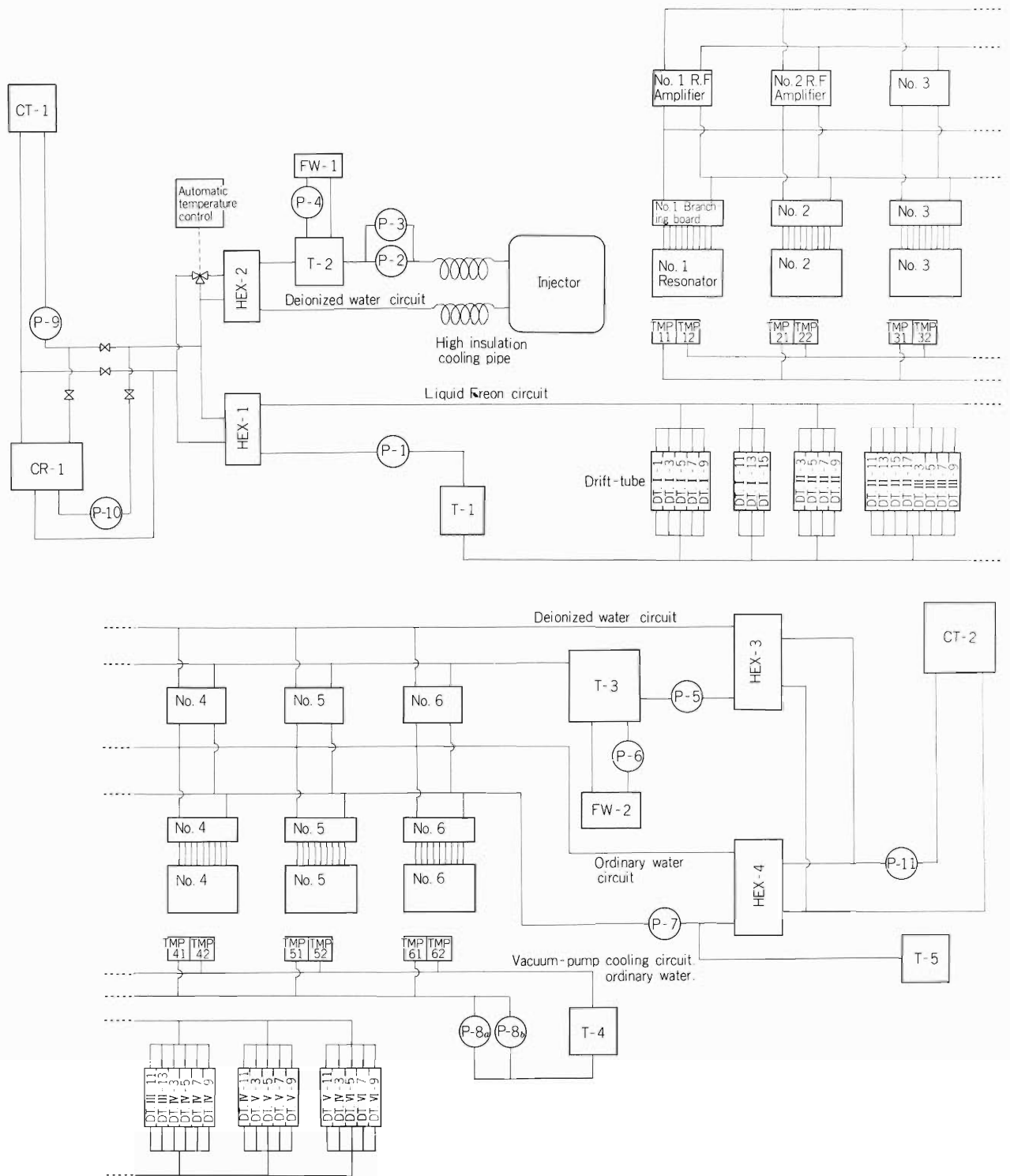


Fig. 1. Cooling system diagram. For meanings of symbols, see Table 1.

also contains a circulation system of liquid Freon and a chilling unit. It was built in advance of the main part of the whole system to provide coolant for test operation of the proto-type power amplifiers and the injector. Installation of the main part was begun from the fall last year when the building for the experimental area was completed. A room was provided in this area for the main system. Therefore, the pumps and the heat exchangers of the injector and drift tube block and the main part are located at the different parts of the accelerator building.

The main part has two circuits of ordinary water for cooling the resonators and the vacuum pumps, and one deionized water circuit for the power tubes. Table 1 shows the specifications of the whole system.

### 10-5. Insulating Pipe and Column Structure for Supply of Coolant to the High Voltage Terminal

T. Inoue

The maximum power dissipation of the instruments such as the ion sources or magnets on the high voltage terminal can be as high as 50 kW. In order to remove such a quantity of heat generated at the terminal, cooling by liquid coolant is preferable to forced air cooling. Coolant other than water, for instance Freon 113, was a candidate because of its superior insulation capability. However, when heat capacity, viscosity and density were taken into account, water was considered to be the best medium as coolant.

Therefore, we decided to use long tubes made of Nylon to supply high resistivity deionized water. Figure 1 shows a photograph of the structure designed to support the tubes. It is made of polyvinyl chloride and two identical units were fabricated. Each contain two 50 m tubes having 25.4 mm inner diameter. When the specific resistivity of water is 2 Megohm-cm, total leakage current shall be less than 1 mA at the terminal voltage of 500 kV. The supporting structure was constructed using adhesives and use of metals such as pipe connection fittings were made carefully to minimize local high field. No trouble has occurred for more than six months of usage and leakage current is less than 1 mA at 500 kV as expected.

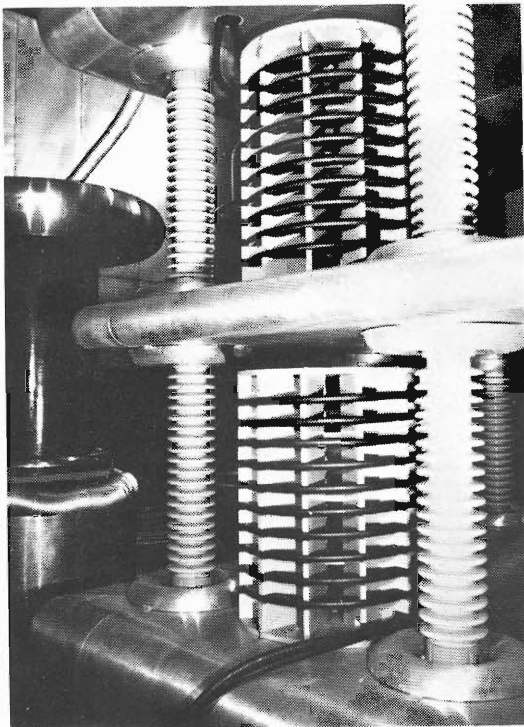


Fig. 1. Nylon tube supporting structure.

## 10-6. Plate Power Supplies for the Exciter Amplifiers of the IPCR Heavy-Ion Linear Accelerator

Y. Chiba

The IPCR heavy ion linear accelerator consists of six resonators of variable frequency type, having a tuning range from 17 to 45 MHz.<sup>1)</sup> Each resonator is excited through a respective high power r.f. amplifier using a tetrode, RCA 4648, as the final stage.

Three sets of plate power supply are provided for the final stages. Each feeds two amplifiers in parallel and is capable of supplying the maximum r.f. output (at 45 MHz) with plate efficiency of 60 % and power margin of  $\sim 7$  %. Their output powers and voltages are listed in Table 1 together with the maximum r.f. voltage at accelerating gaps of each resonator. Figure 1 shows the block diagram of no. 3 power supply. Two others have similar constitution.

The output voltage is adjustable by a step of  $\sim 2$  kV in off power state by a remotely controlled tap changer on the primary windings of transformer. For initial curing of a new tube, the tap changer also provides lower output voltages by delta-star conversion in the primary connection.

The rectifier is an oil convection cooled silicon diode stack; its series elements are equalized by parallel resistors and capacitors.

Table 1. r.f. voltages and dissipations of linac resonators and  
output powers of plate power supplies.

Resonator No.	# 1	# 2	# 3	# 4	# 5	# 6
Max. peak r.f. voltage(kV) at accelerating gaps	180	200	230	250	280	300
Required r.f. power(kW) at 45 MHz for the max. gap voltage	108	133	176	208	261	300
Plate power supply no.	# 1		# 2		# 3	
Rated output power(kW)	440		690		1000	
Max. output voltage(kV)	14		14		16	

The ripple voltage at the rated full load is  $\sim 3$  % peak to peak. The voltage drop from non load to the rated full load is  $\sim 12$  %.

For protection of the 4648, an ignitron crowbar circuit is employed. A rush current caused by sparking in a vacuum tube is detected by a small shunt resistor and triggers a SCR pulser; then the ignitron is fired by the pulser and shorts the output of power supply about  $2 \mu\text{s}$  after the

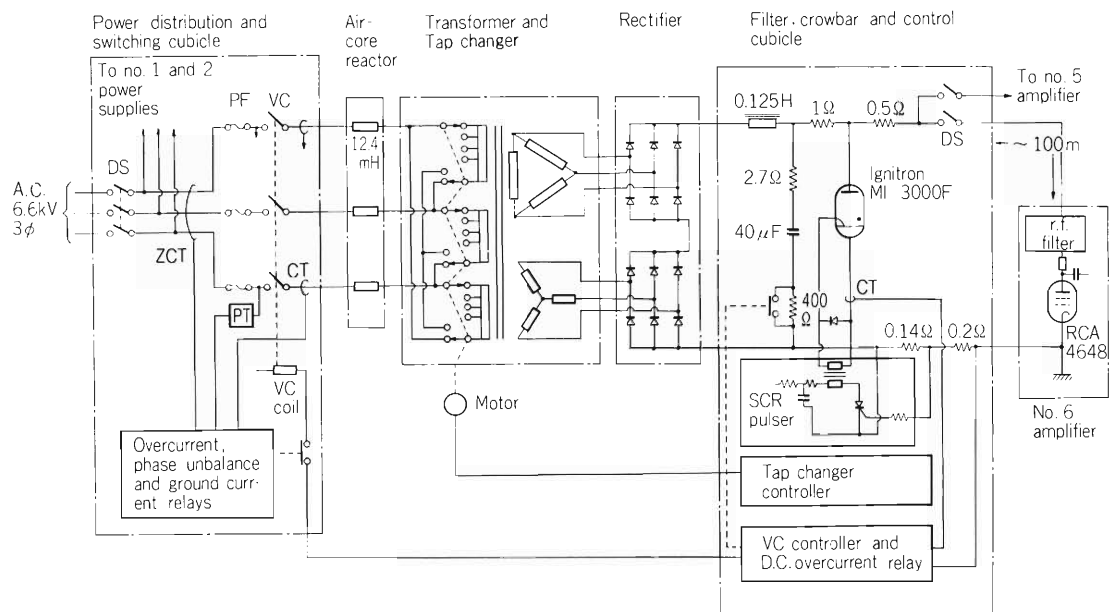


Fig. 1. Block diagram of plate power supply No. 3.

DS: disconnecting switch      PT: potential transformer  
 PF: power fuse                      CT: current transformer  
 VC: vacuum contactor              ZCT: zero phase CT

outbreak of the rush current. Following the crowbar operation, a vacuum contactor takes 40 ms to open the primary 6.6 kV lines. Surge currents on those lines during this period are limited to  $\sim 7$  times as large as the rated full load current by leakage inductances of the transformer and external series air-core reactors.

The system is protected by overcurrent relays in both a.c. and d.c. sides, a phase unbalance relay, ground current relay and power fuses in a.c. side.

The whole system is accommodated in  $12 \times 13 \text{ m}^2$  area in the power supply building neighbouring the accelerator building.

These power supply systems were manufactured by Nihon-Kosuhu Co., Ltd. according to the basic plan of IPCR. The installation was finished at July 1979.

## Reference

- 1) M. Odera: IPCR Cyclotron Progr. Rep., 7, 140 (1973).

## 10-7. Initial Operation of the Proto-Type Power Amplifier Coupled with the First Cavity

Y. Chiba

The radio-frequency system for generation of the accelerating voltages specified by beam dynamics,<sup>1)</sup> is composed of six high power amplifier chains coupled to each cavity separately. The maximum power consumption in each cavity is indicated in Table 1 of the report on the plate power supply.<sup>2)</sup> Except for the difference in the output power specifications, the components and structure of the amplifiers are perfectly the same. A proto-type amplifier was built and its characteristics were investigated to set final design of the amplifiers. Figure 1 shows schematically the diagram of the proto-type amplifier. A frequency synthesizer supplies low level signals of around 10 mW to the six amplifier chains. Each chain has an amplitude and phase controller as the first stage and a solid state wide band amplifier having 100 W capacity as the second stage. Then a vacuum tube amplifier amplifies the signal to 2 kW and excites the last stage power tube. Both stages are grounded cathode tuned amplifiers using tetrodes. Both stages are grounded cathode tuned amplifiers using tetrodes.

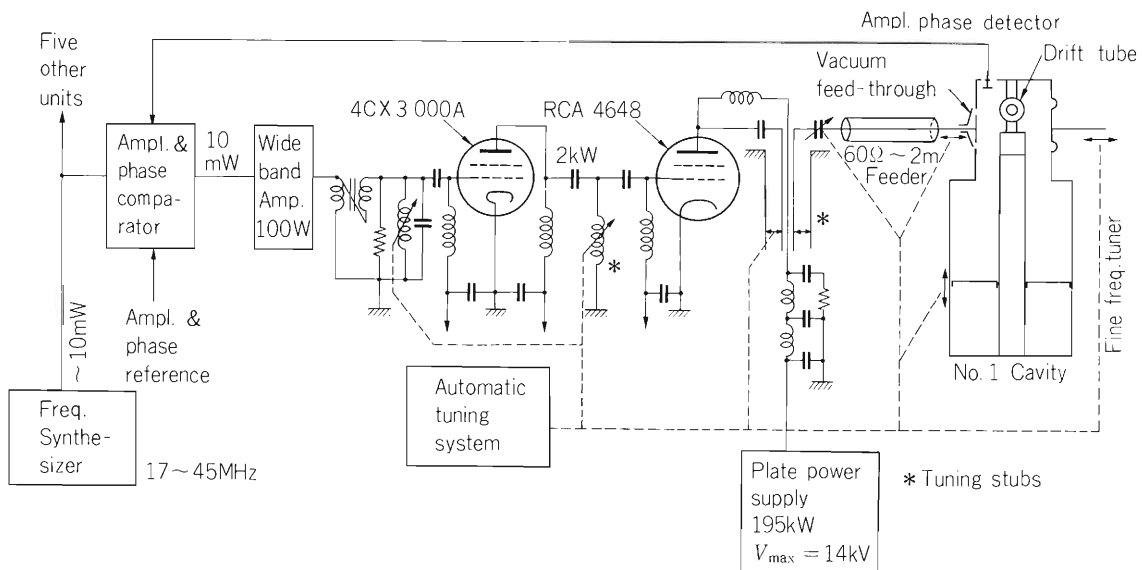


Fig. 1. Radio-frequency power amplifier diagram.

Test of the amplifier with a water-cooled resistance as a dummy load was done in autumn 1978. Then it was coupled with the first cavity via a power feeder. The mode of coupling is capacitive. Impedance matching between the cavity and the feeder is made by changing the insertion depth of the capacitance disk into the cavity; it forms the front end of center conductor of the feeder. The impedance seen from the plate of the output power tube is adjustable by a variable capacitor placed at the entrance to the feeder.

Excitation test of the cavity was started on Jan. 12, 1979. The multipactoring phenomenon characterised by glow discharge and very small power drain to the cavity from the amplifier

persisted for two hours. In the meantime, the vacuum pressure in the cavity improved gradually except occasional sudden increases of pressure caused by sparking. In order to get through the multipactoring region we applied sharply rising signal to the control grid of the power tube so that a sufficiently large voltage develops across drift tube gaps before the phenomenon grows. Once a large voltage is generated, condition for the secondary electron multiplying phenomenon disappears. However, if the gap voltage is allowed to grow further it soon will become larger than the voltage holding limit of the gap and sparking will begin. We found it possible to overcome this difficulty by use of a frequency slightly detuned from resonance. Of course the method would not have been necessary if the voltage stabilization scheme by feed back of the cavity signal to the first stage of the amplifier was available. However, the feed back loop was not completed at that time.

Frequency used for the first operation was 20 MHz. Later, excitations of the cavity upto 30 MHz were realized without difficulty. Accelerating voltage, 80 % of the design value at 20 MHz was obtained within a few days after the test operation was started. Voltage holding test at other frequencies was postponed because of lack of time. The temporary wiring and plumbing made for the test run around the amplifier system had to be rebuilt into the final ones and the work started from Jan. 20th.

Operation above 30 MHz was found a little unstable probably because of insufficient performance of the screen grid by-pass condensers at high frequencies. Their improvements are under investigation. Other modification of the amplifier structure or components was found almost unnecessary. However, for the sake of operational simplicity, the output power capacity of the wide band amplifier was increased to 250 W and the tetrode 4CX3000A was replaced with a grounded grid triode 3CX3000A7, so that no tuning is necessary up to this stage. This configuration was planned at first but it took years for the factory to manufacture a solid state wide band amplifier of 250 W capacity and we had to use tentatively the circuit shown in Fig. 1. Incorporating those modifications final design of the amplifiers and the power feeders was determined and orders were given to the factories to fabricate remaining parts. Those were carried in, assembled and coupled with the cavities before November 1979. Tuning of each RF system is in progress.

## References

- 1) T. Tonuma, F. Yoshida, and M. Odera: Reports I.P.C.R., (in Japanese), 51, 53 (1975).
- 2) Y. Chiba: IPCR Cyclotron Progr. Rep., 13, 141 (1979).

## 10-8. Current Load of the Injector High-Voltage Generator without Beam Acceleration

M. Hemmi

Current load of the injector high voltage generator was measured before carrying out the beam acceleration test. Figure 1 is the schematic diagram of the injector system. Table 1 gives various parameters at the time of measurement. Current drain from the high voltage generator as a function of voltage is shown in Fig. 2. Total load is 1.2 mA at 500 kV. After subtracting known contributions from the resistances attached between the terminal and the ground, 0.7 mA remained. It is the current drain, of which origin we are most interested in. Since resistance of water in the coolant supply structure<sup>1)</sup> is roughly 1000 M $\Omega$ , 0.5 mA flows through deionized

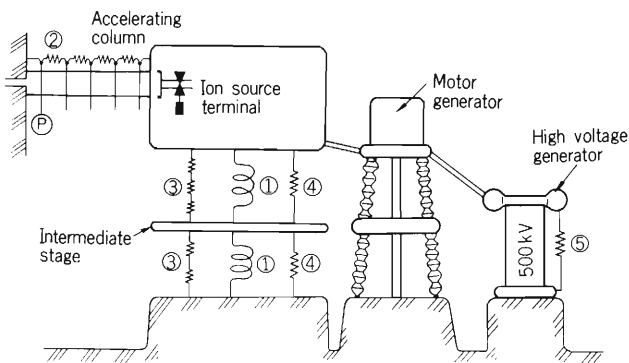


Fig. 1. Schematic diagram of the injector showing parts which contribute to current load.

- 1) Pipes to supply cooling water to the terminal, 2) Divider chain of accelerating column, 5000 M $\Omega$ . 3) Divider chain for light signal guiding cable cover, 4400 M $\Omega$ .
- 4) Divider chain to give half of the terminal potential to the intermediate stage, 3340 M $\Omega$ ,
- 5) Precision resistance for feed back stabilization of the high voltage, 3000 M $\Omega$ .

Table 1. Values of parameters at the time of the load current measurement.

Ambient temperature:	23° C
Relative humidity:	50 %
Pressure in the accelerating column:	$5.2 \times 10^{-7}$ Torr
Specific resistivity of cooling water:	4M $\Omega$ -cm
Resistances of various voltage dividers:	
Accelerating column:	5000 M $\Omega$
Fiber optic cable container:	4400 M $\Omega$
Divider to supply voltage to the intermediate stage of the high voltage terminal and the motor generator:	3340 M $\Omega$
Precision resistance network for stabilization of the high voltage:	3000 M $\Omega$

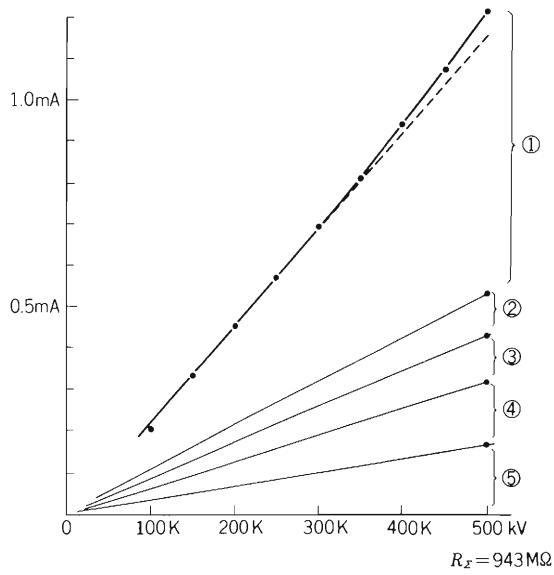


Fig. 2. Current drain as a function of the terminal voltage. Some deviation from linear relation is seen. Calculated contributions of various resistances are also indicated.

water. The remaining 0.2 mA may be the leakage current over the surface of the insulators or the current lost by Corona discharge. The deviation from linearity seen in the high voltage region might be attributed to the occurrence of discharge.

#### Reference

- 1) T. Inoue: IPCR Cyclotron Progr. Rep., 13, 137 (1979).

## 10-9. Performance Test of Injector System

M. Kase, M. Hemmi, and S. Nakajima

Figure 1 shows schematically the system of the injector and low energy extension. The qualities of nitrogen-ion beam from the injector were examined for the test of performance of the injector system.

For producing the nitrogen ions the axially extracting PIG ion source<sup>1)</sup> was used because of its comparatively good beam emittance and easy handling. The ion-extracting voltage,  $V_{ext}$ , of the ion source was fixed to 10 kV in the test.

The beam profiles were observed at position A shown in Fig. 1 using a wire probe. Variations of the beam width with the injector voltage,  $V_{inj}$ , are shown in Fig. 2. As seen from the figure,

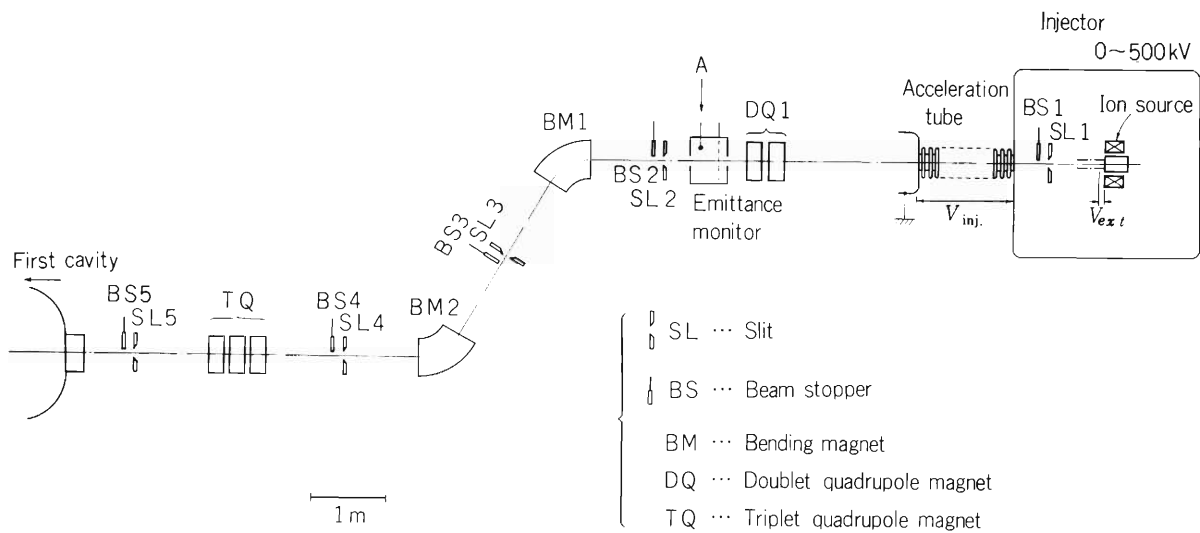


Fig. 1. Schematic view of the system of injector and low energy extension.

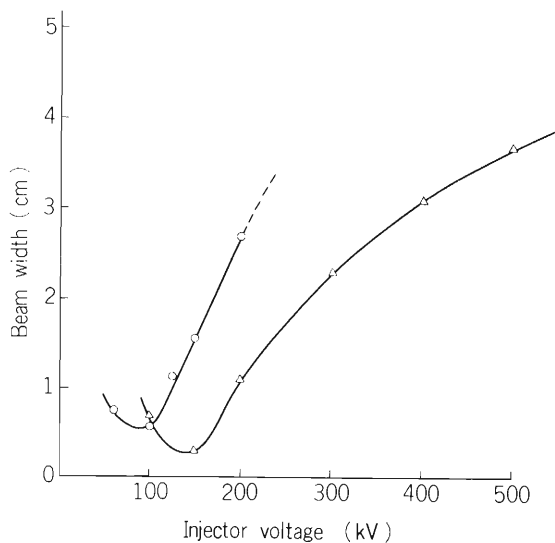


Fig. 2. Variations of beam width with  $V_{inj}$  without magnetic fields in DQ1. ○ is for the case when the electric fields of the acceleration tube is constant; △ is when the electric field of the first two sections of the acceleration tube is half that of the other 23 sections.

the tendency of beam broadening with  $V_{inj}$  can be reduced by lowering the electric field of the first two sections of the acceleration tube. The beam emittances were also measured at the same position with emittance monitor<sup>2)</sup> and the results for  $V_{inj} = 300$  kV and 500 kV are shown in Fig. 3 (a) and (b), respectively. The beam currents after being analysed through the first bending magnet BM1 were measured by the beam stopper BS3. The results were  $0.9 \mu\text{A}$  for  $\text{N}_2^+$  beam and  $5 \mu\text{A}$  for  $\text{N}_2^+$  beam with the best adjustment of magnetic fields of the doublet quadrupole magnet DQ1 and BM1. The component of the molecular ion beam is large mainly because the arc power of the ion source is small. We confirmed that these beams could be transported to BS5 at the entrance to the first cavity without appreciable beam losses.

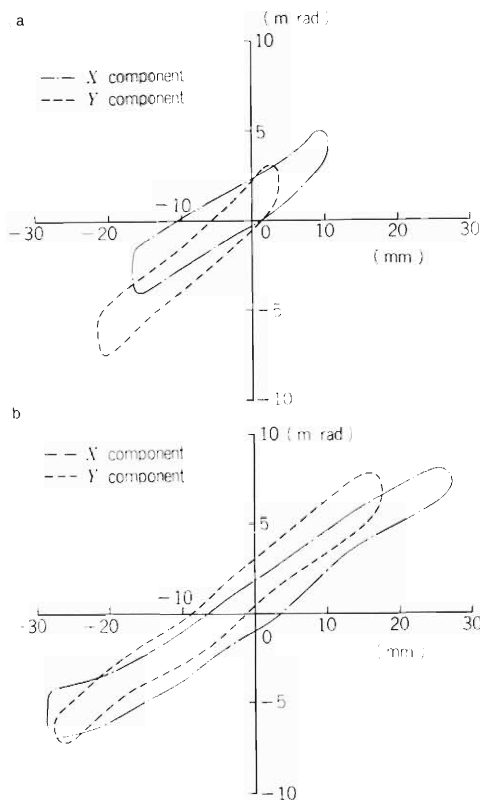


Fig. 3. Beam emittances, (a) for  $V_{inj} = 200$  kV and (b) for 500 kV. These data were obtained without magnetic fields in DQ1.

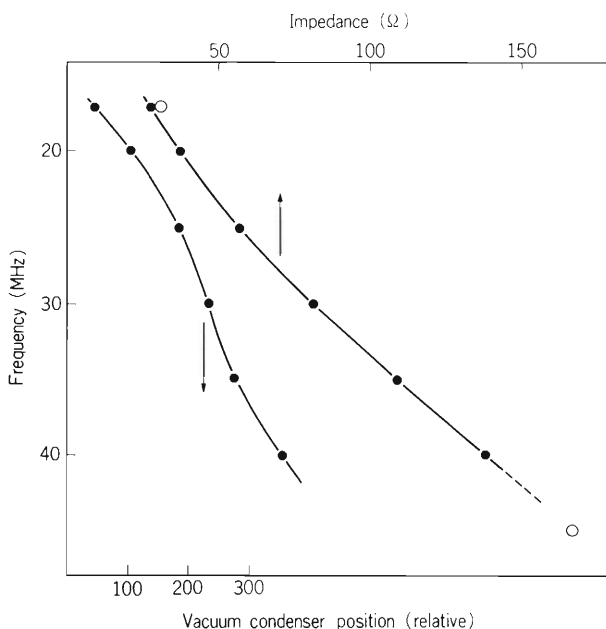
## References

- 1) S. Nakajima: IPCR Cyclotron Progr. Rep., 12, 141 (1978).
- 2) J. Schimizu and M. Odera: *ibid.*, p. 133.

## 10-10. Beam Buncher Characteristics

M. Yanokura and M. Odera

The proto-type buncher reported previously<sup>1)</sup> was modified for practical use and its characteristics were examined. The vacuum sealing insulators made of polyethylene at the drift tube gaps were replaced with high frequency ceramic insulators made of alumina. The length of the coaxial stem was shortened to get desired resonant frequency, in spite of the increase of capacity by change of the dielectric constant of the insulators at the gaps. Position of the radio-frequency power coupler was determined taking into account the decrease of Q-values. In order to simplify operation, the usual scheme of changing coupling strength according to frequency was not adopted. Instead, a wide band power amplifier is provided which can supply necessary power irrespective of change of input impedance at the coupling point. The amplifier can function under occurrence of some power reflection from the buncher cavity. Since the shunt impedance of the cavity at low frequency is lower than that at high frequency, coupling point near the shorting end of the coaxial stem was chosen to give smaller SWR at lower frequency than at higher frequency. A water cooling circuit for the center conductor and a blower for forced air cooling of the insulators and the variable vacuum condenser were added for power testing. Figure 1 shows the input impedance. Closed circles show measured values and open circles calculated ones. The agreement is excellent. A wide band amplifier having 1 kW capacity is used as an exciter. Test under vacuum showed the occurrence of multipactoring phenomenon, but it could be easily overcome. The reason is probably the use of the insulators which limits the exposure of resonator surface in the vacuum to only a small portion of the drift tube where voltage develops rapidly. Fast rise of voltage across the electrode gaps is known to be effective to suppress the multipactoring process. Figure 2 is the buncher in the injection line, at 3 m upstream of the first cavity.



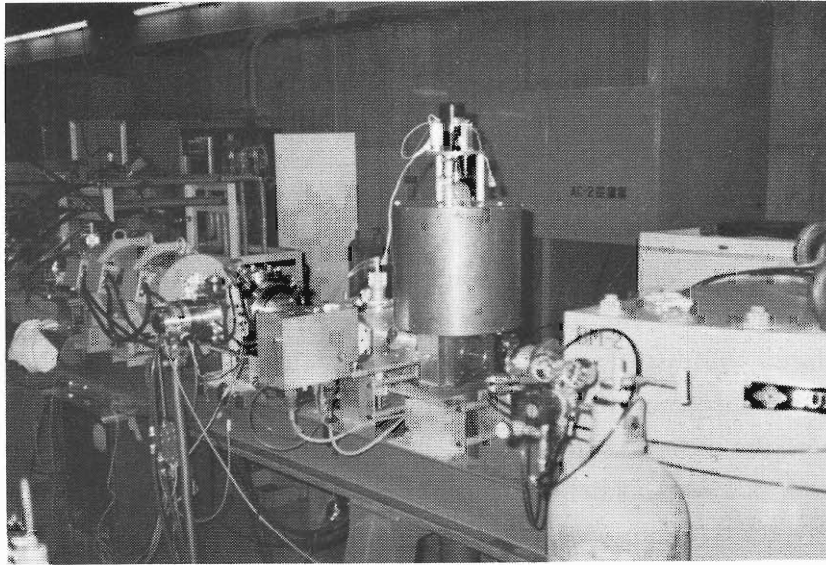


Fig. 2. A photograph of the buncher in the injection beam line, 3 m upstream of the first cavity.

#### Reference

- 1) M. Odera, I. Takeshita, and F. Yoshida: *IPCR Cyclotron Progr. Rep.*, 11, 145 (1977).

10-11. Design of a Magnet for the Side-Extraction PIG-Type Ion Source<sup>3)</sup>

Y. Miyazawa, M. Yanokura, M. Hemmi, F. Yoshida,  
M. Kase, and M. Odera

The axial extraction PIG ion source reported previously<sup>1)</sup> is being used for initial acceleration test of the linac system.<sup>2)</sup> With its small emittance of the extracted beam and simplicity of operation, it is a convenient tool for testing purposes. However, it can not yield multiply charged ions. In order to produce ion of a large charge to mass ratio for heavy elements, we have planned to use a side-extraction indirectly heated cathode PIG source with which we have some experiences.<sup>3)</sup> A new magnet for the ion source was designed, fabricated and installed in July 1979.

For proper operation of the source to produce enough quantity of the multiply charged ions of heavy elements, the height of the anode chimney in which the arc plasma is formed by discharge must be long enough than a certain length. The pole gap of the magnet ought to be large in order to be able to accept such an ion source. We chose 15 cm for the gap length. The large gap makes the fringing field extend far out of the edge of the magnet, and also requires a large excitation current to get the necessary field. Since the power available on the high voltage terminal on which the magnet is to be installed is limited, some compromise must be made among the maximum field strength, mass to charge ratio, trajectory curvature and extractor voltage. Figure 1 shows region of parameter values chosen. Then by using a hard edge approximation, a rough survey of the orbit properties such as horizontal and vertical focusing length was made by changing rotation angles of the beam up to the effective field boundary and angles of exit. Nearly parallel beam in both the horizontal and vertical directions is desirable to get a good focus at the entrance of the accelerating column by use of an einzel lens. Figure 2 shows two examples of such surveys. A number of configurations were chosen from such parameter search, and the trajectories were calculated for each case taking into account the extended fringing field. The field distributions were calculated using a program "MAGNET".<sup>4)</sup> A combination of the rotation angle of 120 degree and exit angle of 30 degree was judged to give trajectories nearly parallel horizontally and vertically. Since field patterns given by "MAGNET" code is for poles

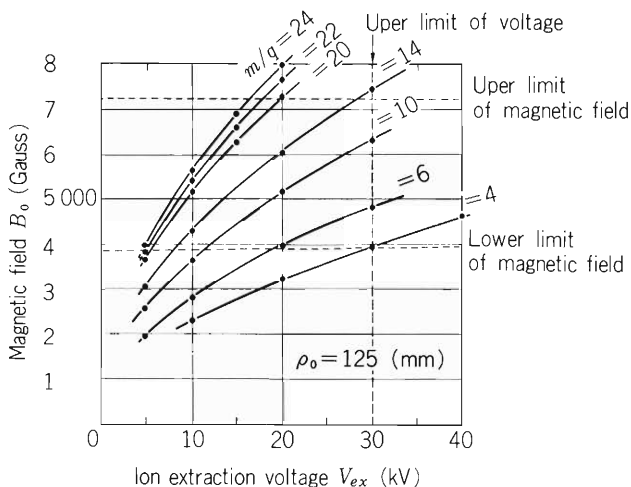


Fig. 1. Diagram showing range of parameters intended for the side-extraction PIG source.

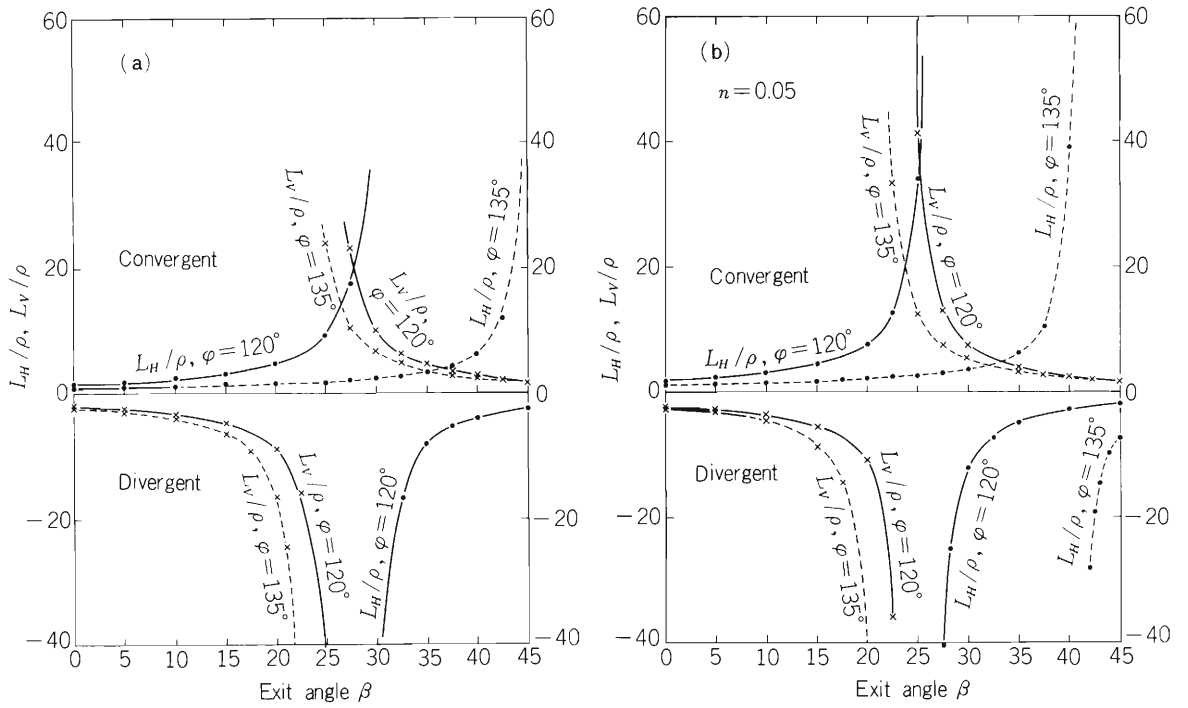


Fig. 2. Two examples from parameter searches under the hard edge approximation for orbit calculation: a) field is uniform within boundary, b) outward falling gradient with field index of 0.05 along the trajectory.  $\varphi$ , rotation angle;  $\beta$ , exit angle;  $L_H$  and  $L_V$  are horizontal and vertical focusing length measured from the effective boundary.  $\rho$  is the radius of curvature of beam in the field.

infinitely long perpendicular to the plane in which the distribution is calculated, the trajectories obtained for such field are not necessarily coincident with the real ones. For the pole face shape chosen, the effect of finiteness of the magnet is a slight outward fall of the field for substantial portion of the orbit. As seen in Fig. 2 the existence of such field gradient makes beam less convergent horizontally and less divergent vertically.

Therefore, the field of real magnet was measured. The relative distribution was found constant with the change of exciting currents. Then, the numerical calculation of the orbit using measured distributions was carried out to accurately determine correct position and configuration of the ion source in the high voltage terminal. The magnet was installed in the terminal using the results of the calculation. Table 1 shows specifications of the magnet and Fig. 3 is the plan drawing of the magnet and the vacuum chamber. Figure 4 shows the horizontal trajectory calculated.

Table 1. Specifications of Magnet.

Pole gap	150 mm
Pole area	200×280 mm <sup>2</sup>
Maximum field	7200 gauss
Maximum current	150 A
Total Amp. turns	1.2×10 <sup>5</sup> AT
Total weight	3000 kg

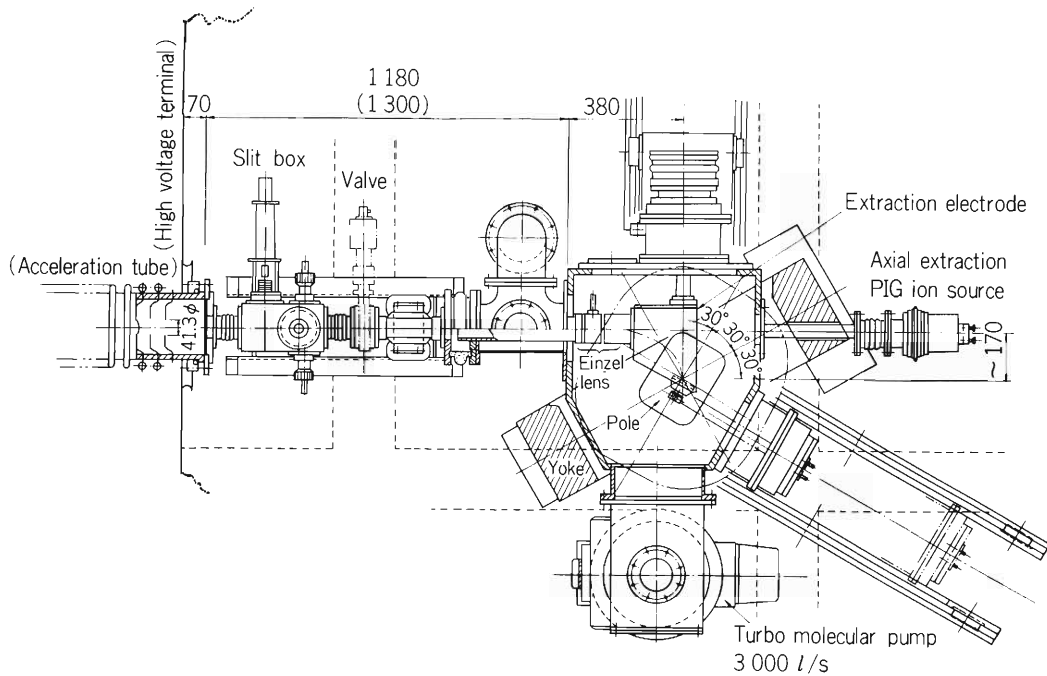


Fig. 3. Plan drawing of the magnet and the vacuum chamber.

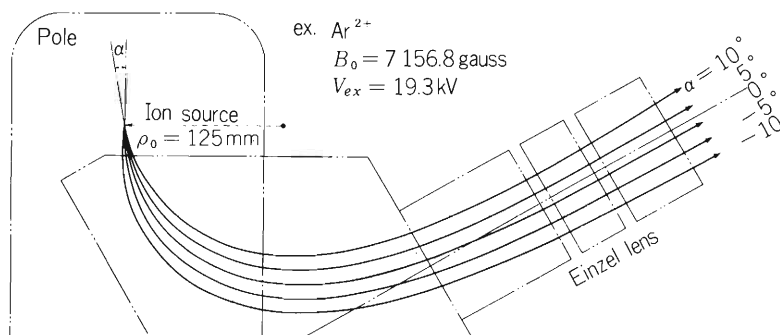


Fig. 4. Calculated beam trajectory in the measured field of the magnet manufactured.

The results of this calculation show that beam extracted with spreading angle of  $\pm 10^\circ$  becomes a nearly parallel beam at the exit of einzel lens and well focused beam can be injected into the center of the acceleration tube.

#### References

- 1) S. Nakajima: IPCR Cyclotron Progr. Rep., 12, 141 (1978).
- 2) M. Kase, M. Hemmi, and S. Nakajima: *ibid.*, 13, 147 (1979).
- 3) I. Kohno: *ibid.*, 1, 13 (1967).
- 4) Ch. Iselin: CERN Computer Program Library T 600.

## 10-12. Performance of the Quadrupole Magnets of the Beam Transport System

M. Hemmi and F. Yoshida

Characteristics of one of the quadrupole magnets fabricated using the tape-coil technology as components of the beam transport system<sup>1)</sup> was measured. Table 1 shows its specifications. Main difference from the quadrupole magnets of the drift tubes<sup>2)</sup> is its coil cooling method which uses metal disks having coolant channels embedded within and pressed tight to get close contact with the end surfaces of the coils. There are thin insulating layers between the disks and the coil. The insulation consists of thermo-conductive epoxy resin layers painted and polymerized on the disks and layers of thermoconductive grease which usually is used for heat sink of high power transistors. Since heat transfer across insulator layers is not efficient when compared with the direct flood cooling technique applied to the drift tube magnets, care was taken to keep the thickness of the layers as thin as possible. Temperature difference across the layers was calculated for the best (epoxy 100  $\mu\text{m}$ , grease 200  $\mu\text{m}$ ) and the worst (epoxy 100  $\mu\text{m}$ , grease 500  $\mu\text{m}$ ) cases as was made previously.<sup>2)</sup>

Table 1. Design specifications of the quadrupole magnet.

Maximum lens strength in normal operation	60 kG
Distance between poles	63.5 mm $\begin{matrix} + 0.1 \\ - 0 \end{matrix}$
Axial length (mechanical)	360 mm
Type of coil	Tape coil wound from 0.8 mm copper sheets
Number of turns	65
Cooling method	Conduction cooling by the water cooled plates attached at each end of the coil
Power consumption	950 W max. for each coil

Figure 1 is the excitation curve for the field gradient. Upper limit of the current determined by the temperature rise of the insulator is above the design value and a sufficient margin of safety has been realized for normal operation. Change of temperature on the surface of the innermost turn of the coil at the center along the axial length was measured by a resistance thermometer and is shown in Fig. 2. The result is satisfactorily nearer to the curve calculated for the best case than to that of the worst case. The theoretical curves were calculated assuming radial heat flow across the interlaced layers of the copper and insulator as well as axial flow within copper sheets.<sup>3)</sup>

Effective axial length deduced from the fringing field is 38.5 cm. The field gradient of 1.56 kG/cm at normal operation multiplied with this effective length gives the design lens strength of 60 kG mentioned in Table 1. Position of the field boundary which is apart from the pole edge by about 20 % of the aperture does not move for change of the field strength shown in Fig. 1.

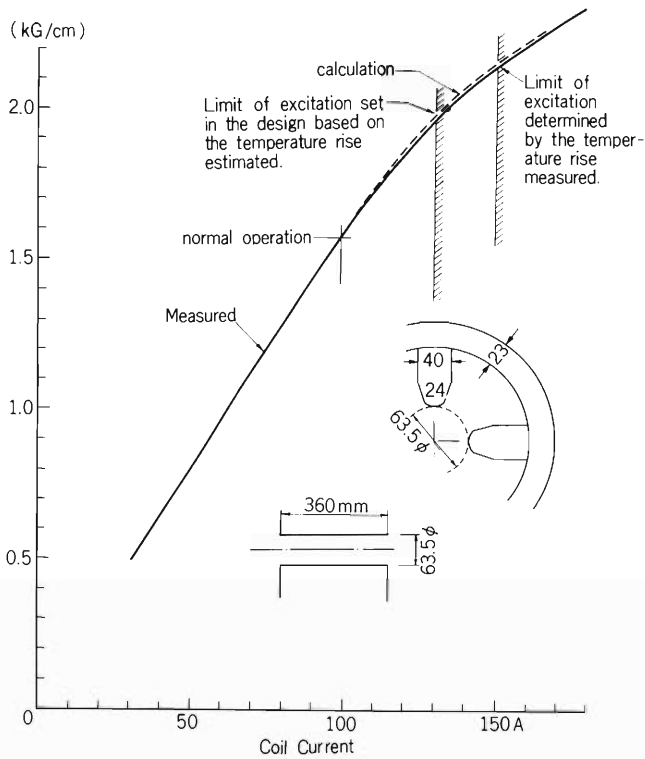


Fig. 1. Field gradient as a function of coil current. Number of turns per pole is 65.

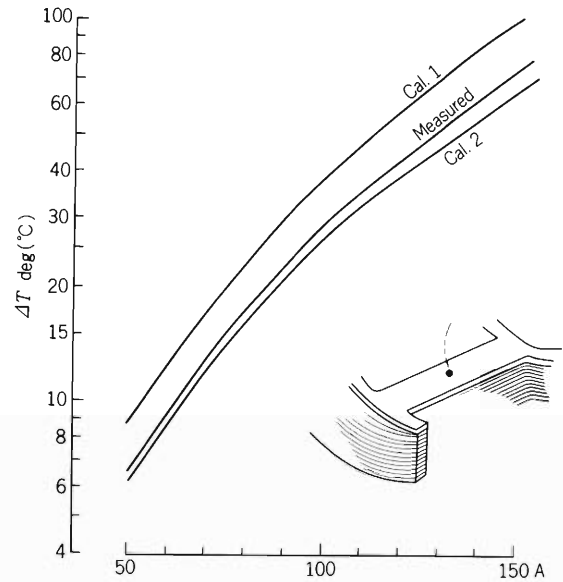


Fig. 2. Temperature rise of the coil at the center of the innermost turn as a function of current. Cal. 1 is that calculated for the case where the thickness of the insulation filler between end surface of the tape coil and the cooling plate is maximum and Cal. 2 is that calculated for the most favorable case. See, Ref. 3.

Deviations from the quadrupole symmetry of the field were measured by a Hall probe. The sextupole ( $n = 3$ ) component at the radial distance of 80 % of the aperture was 5 % of the main field. Other significant higher harmonics was that of  $n = 5$  and was around 1 %. Those percentages also remained constant against change of field gradient shown in Fig. 1.

## References

- 1) M. Hemmi, Y. Miyazawa, M. Odera, and F. Yoshida: IPCR Cyclotron Progr. Rep., 12, 138 (1978).
- 2) Y. Miyazawa, T. Inoue, M. Hemmi, Y. Chiba, F. Yoshida, and M. Odera: *ibid.*, 10, 130 (1976); Y. Miyazawa, T. Inoue, and M. Odera: *ibid.*, 9, 113 (1975).
- 3) M. Hemmi and F. Yoshida: *ibid.*, 10, 145 (1976).

## 11. LIST OF PUBLICATIONS

1. Machine development and accelerator physics
2. Nuclear physics and nuclear instrumentation
  - 1) A. Neskakis, R. M. Lieder, H. Beuscher, Y. Gono, D. R. Haenni, M. Muller-Veggian, and C. Mayer-Boricke: "Observation of Rotation-Aligned Band in the Odd-Odd Nuclei  $^{190, 192, 194}\text{Au}$ ", Phys. Lett., 80B, 194 (1979).
  - 2) H. Amakawa, S. Yamaji, A. Mori, and K. Yazaki: "Adiabatic Treatment of Elastic Deuteron-Nucleus Scattering", Phys. Lett., 82B, 13 (1979).
  - 3) H. Amakawa and K. Yazaki: "Adiabatic Treatment of Deuteron Breakup on a Nucleus", Phys. Lett., 87B, 159 (1979).
  - 4) T. Nomura, H. Utsunomiya, T. Inamura, T. Motobayashi, and T. Sugitate: "Energy Relaxation during the Fusion Process Probed by Preequilibrium  $\alpha$  Emission in Heavy-Ion Reactions", J. Phys. Soc. Japan, 46, 335 (1979).
  - 5) N. Kishida and H. Ohnuma: "Exact Finite-Range DWBA and Adiabatic-Deuteron-Breakup Calculations Including the Deuteron D-state for the  $^{58}\text{Ni}(p, d)^{57}\text{Ni}$  Reaction at 52 MeV", J. Phys. Soc. Japan, 46, 1375 (1979).
  - 6) M. Muller-Veggian, H. Beuscher, R. M. Lieder, Y. Gono, D. R. Haenni, A. Neskakis, and C. Mayer-Boricke: " $10^+$  Isomers Observed in Even-Even 78 Neutron Nuclei", Z. Physik, A290, 43 (1979).
  - 7) K. Sato, S. Yamaji, K. Harada, and S. Yoshida: "A Numerical Analysis of the Heavy-Ion Reaction Based on the Linear Response Theory", Z. Physik, A290, 149 (1979).
  - 8) Y. Gono, R. M. Lieder, M. Muller-Veggian, A. Neskakis, and C. Mayer-Boricke: "In-Beam  $\gamma$ -Ray Study of  $^{189, 191, 193}\text{Au}$ ", Nucl. Phys., A327, 269 (1979).
  - 9) H. Amakawa and K. -I. Kubo: "Analyzing Power of Two-Step ( $\vec{p}, t$ ) Reaction Leading to the Unnatural-Parity State", Phys. Rev., C19, 2403 (1979).
  - 10) T. Tamura, T. Udagawa, K. E. Wood, and H. Amakawa: "Exact Finite Range DWBA Form Factor for Heavy-Ion Induced Nuclear Reactions", Comput. Phys. Commun., 18, 163 (1979).
  - 11) S. Yamaji: "Analysis of Heavy-Ion Reactions Based on the Linear Response Theory", Sci. Papers I.P.C.R., 73, 19 (1979).
  - 12) J. Fujita and M. Ichimura: "Mesonic Effects in Photonuclear Sum Rules", Meson in Nuclei, (eds. M. Rho and D.H. Wilkinson), North-Holland Pub. Co., Amsterdam, 2, 627 (1979).
3. Atomic and solid-state physics
  - 1) N. Shiotani, T. Okada, H. Sekizawa, A. Nakamoto, H. Murakami, and K. Mori: "A Two Dimensional Position Sensitive  $\gamma$  Ray Detector for Angular Correlation Measurements", Proc. 5th Intern. Conf. Positron Annihilation, The Japan Institute of Metals, Sendai, p.267 (1979).
  - 2) N. Shiotani, T. Okada, N. Sakai, H. Sekizawa, and S. Wakoh: "Angular Correlation of Positron Annihilation Radiation and Compton Profiles in Magnesium", Proc. 5th

- Intern. Conf. Positron Annihilation, The Japan Institute of Metals, Sendai, p.669 (1979).
- 3) K. Hinode, S. Tanigawa, M. Doyama, K. Shiraishi, and N. Shiotani: "Positron Lifetime Study of Gas Bubbles", Proc. 5th Intern. Conf. Positron Annihilation, The Japan Institute of Metals, Sendai, p.733 (1979).
  - 4) N. Owada, H. Kumakura, K. Hinode, S. Tanigawa, M. Doyama, S. Okuda, and N. Shiotani: "The Annealing Study of  $^3\text{He}$  and Neutron Irradiated Platinum by means of Positron Annihilation", Proc. 5th Intern. Conf. Positron Annihilation, The Japan Institute of Metals, Sendai, p.775 (1979).
  - 5) S. Tanigawa, K. Hinode, R. Nagai, M. Doyama, and N. Shiotani: "Effect of Doping and Thermal Vacancies on Positron Annihilation in Semiconductors", J. Appl. Phys., 18, 81 (1979).
  - 6) M. Uda, H. Endo, K. Maeda, Y. Awaya, M. Kobayashi, Y. Sasa, H. Kumagai, and T. Tonuma: "Bonding Effect on F  $K\alpha$  Satellite Structure Produced by 84 MeV  $\text{N}^{4+}$ ", Phys. Rev. Lett., 42, 1257 (1979).
  - 7) T. Tonuma, Y. Awaya, T. Kambara, H. Kumagai, I. Kohno, and S. Özkök: "Argon  $K\alpha$  X-ray Satellites Produced by Impact of Nitrogen Ions in the 4.7 – 7.8 MeV/amu Energy Range", Phys. Rev., A20, 989 (1979).
  - 8) T. Takahashi, Y. Awaya, T. Tonuma, H. Kumagai, K. Izumo, A. Hashizume, S. Uchiyama, and A. Hitachi: "Energy Straggling of C and He Ions in Metal Foils", Nucl. Instr. Meth., 166, 587 (1979).
  - 9) Y. Awaya, K. Izumo, T. Katou, H. Kumagai, T. Tonuma, Y. Tendow, T. Takahashi, A. Hashizume, and T. Hamada: "The L X-rays Following Multiple Inner-Shell Ionization", Atomic Collision Research in Japan Progress Report, 5, 81 (1979).
4. Radiochemistry, radiation chemistry and radiation biology
- 1) F. Yatagai, S. Kitayama, and A. Matsuyama: "Inactivation of Phage  $\phi\text{X} 174$  by Accelerated Ions. Enhanced  $\delta$ -ray Effect by Air Layer in Front of the Samples", Radiat. Res., 77, 250 (1979).
  - 2) T. Nozaki, M. Iwamoto, and Y. Itoh: "Production of  $^{77}\text{Br}$  by Various Nuclear Reactions", Int. J. appl. Radiat. Isotopes, 30, 79 (1979).
  - 3) T. Nozaki, Y. Itoh, and K. Ogawa: "Yield of  $^{73}\text{Se}$  for Various Reactions and Its Chemical Processing", Int. J. appl. Radiat. Isotopes, 30, 595 (1979).
  - 4) T. Nozaki, M. Iwamoto, K. Usami, K. Mukai, and A. Hiraiwa: "Helium-3 Activation Analysis of Oxygen in Silicon Nitride Films on Silicon Wafers", J. Radioanal. Chem., 52, 449 (1979).

(Papers presented at meetings)

1. Machine development and accelerator physics

- 1) N. Nakanishi, N. Iida, S. Motonaga, T. Wada, and F. Yoshida: "Orbit Calculation I in IPCR SSC", Ann. Meeting of Phys. Soc. of Japan, Osaka, Apr. (1979).
- 2) M. Odera, Y. Chiba, M. Hemmi, Y. Miyazawa, T. Tonuma, T. Kambara, T. Inoue, M. Kase, M. Yanokura, E. Ikezawa, and F. Yoshida: "Status of the Riken Linear

Accelerator”, Autumn Meeting of Phys. Soc. of Japan, Kochi, Oct. (1979).

- 3) N. Nakanishi, N. Iida, F. Yoshida, and H. Kamitsubo: “Orbit Calculation II in IPCR SSC”, Autumn Divisional Meeting of Phys. Soc. of Japan, Kochi, Oct. (1979).
- 4) Y. Yano, T. Wada, F. Yoshida, and H. Kamitsubo: “Design of Injection System for RIKEN SSC 3”, Ann. Meeting of Phys. Soc. of Japan, Kochi, Oct. (1979).
- 5) T. Wada, Y. Yano, F. Yoshida, H. Takebe, H. Kamitsubo, S. Motonaga, and K. Ogiwara: “Design of Injection System for RIKEN SSC 2”, Ann. Meeting of Phys. Soc. of Japan, Kochi, Oct. (1979).

## 2. Nuclear physics and nuclear instrumentation

- 1) A. Ichimura and M. Ichimura: “Coulomb-Nuclear Interference Phenomena and the Quadrupole Moment of  $^{18}\text{O}$ ”, Ann. Meeting of Phys. Soc. of Japan, Osaka, Apr. (1979).
- 2) H. Amakawa, S. Yamaji, A. Mori, and K. Yazaki: “Adiabatic Treatment of Elastic Deuteron-Nucleus Scattering”, Ann. Meeting of Phys. Soc. of Japan, Osaka, Apr. (1979).
- 3) H. Amakawa and K. Yazaki: “Adiabatic Treatment of Deuteron Breakup on Nucleus”, Ann. Meeting of Phys. Soc. of Japan, Osaka, Apr. (1979).
- 4) A. Hashizume, T. Katou, Y. Tendow, and H. Kumagai: “High Spin Status Excited with  $^{144}\text{Nd} + ^{20}\text{Ne}$  Reaction”, Spring Divisional Meeting of Phys. Soc. of Japan, Osaka, Apr. (1979).
- 5) H. Amakawa, S. Yamaji, A. Mori, and K. Yazaki: “Validity of the Adiabatic Treatment of Deuteron-Nucleus Scattering”, Ann. Meeting of Phys. Soc. of Japan, Kochi, Oct. (1979).
- 6) T. Sugitate, T. Nomura, M. Ishihara, and H. Utsunomiya: “Correlations between Heavy Ions and Alpha Particles in the  $^{27}\text{Al} + ^{14}\text{N}$  Reaction at 95 MeV”, Ann. Meeting of Phys. Soc. of Japan, Kochi, Oct. (1979).
- 7) M. Yanokura, I. Kohno, Y. Nagame, and H. Nakahara: “Fission-like Events of  $^{14}\text{N} + ^{58}\text{Ni}$  System”, Ann. Meeting of Phys. Soc. of Japan, Kochi, Oct. (1979).
- 8) H. Utsunomiya, T. Nomura, M. Ishihara, T. Sugitate, K. Ieki, and Y. Gono: “Relaxation Phenomenon of Angular Momentum in Heavy-ion Reactions”, Ann. Meeting of Phys. Soc. of Japan, Kochi, Oct. (1979).
- 9) T. Kubo, N. Kishida, H. Ohnuma, T. Hasegawa, N. Ueda, T. Fujisawa, T. Wada, K. Iwatani, and T. Suehiro: “ $(\vec{d}, p)$  and  $(\vec{p}, d)$  Reaction of  $\ell_n = 0$  and the Spin-orbit Terms of Distorting Potentials”, Autumn Divisional Meeting of Phys. Soc. of Japan, Kochi, Oct. (1979).
- 10) N. Kishida, J. Kasagi, T. Kubo, T. Murakami, Y. Kamatani, H. Ohnuma, and M. Yasue: “Measurement of Particle- $\gamma$  Angular Correlations for the  $^{58}\text{Ni}(p, d)^{57}\text{Ni}$  Reaction at  $E_p = 30$  MeV”, Autumn Divisional Meeting of Phys. Soc. of Japan, Kochi, Oct. (1979).
- 11) A. Ichimura and M. Ichimura: “Coulomb-Nuclear Interference Phenomena in Inelastic Scatterings of  $^{18}\text{O}$ ”, Autumn Divisional Meeting of Phys. Soc. of Japan, Kochi, Oct. (1979).
- 12) Y. Gono, K. Hiruta, T. Nomura, M. Ishihara, H. Utsunomiya, T. Sugitate, and K. Ieki: “In-Beam  $\alpha$ -,  $\gamma$ -Spectroscopy on Heavy Nuclei”, Ann. Meeting of Phys. Soc. of Japan, Kochi, Oct. (1979).

- 13) M. Yanokura, I. Kohno, Y. Nagame, and H. Nakahara: "Isotopic Dependence of 115 MeV Nitrogen Induced Reaction", Discussion Meeting of Radiochem., Osaka, Oct. (1979).

3. Atomic and solid-state physics

- 1) Y. Awaya, T. Hamada, T. Takahashi, K. Izumo, Y. Tendow, T. Katou, T. Tonuma, and T. Doke: "Deviation from  $Z^2$  – Dependence of Heavy-Ion-Induced Inner-Shell Ionization Cross Section", Symp. on Atoms and Molecules, as a Part of the Special Project Research 'Heavy Ion Science', Tokyo, Feb. (1979).
- 2) Y. Awaya and T. Tonuma: "Measurements of X-rays Following the Inner-Shell Ionization", Symp. on the Production of Excited Atoms and the Interaction, Tokyo, Feb. (1979).
- 3) H. Shiraishi, H. Shinno, R. Watanabe, H. Kamitsubo, I. Kohno, and T. Shikata, "Helium Embrittlement of High Ni Austenitic Alloys", Ann. Meeting of Atomic Energy Soc. of Japan, Osaka, March (1979).
- 4) M. Uda, H. Endo, K. Maeda, M. Kobayashi, and Y. Sasa: "Bonding Effect of F  $K\alpha$  Spectra on their Intensity Distributions", Ann. Meeting of Phys. Soc. of Japan, Osaka, March (1979).
- 5) H. Endo, M. Uda, K. Maeda, M. Kobayashi, and Y. Sasa: " $Z_2$  Dependence of L Shell Vacancy Rearrangement Process", Ann. Meeting of Phys. Soc. of Japan, Osaka, March (1979).
- 6) M. Uda, Y. Terasaka, H. Endo, and Y. Sasa: "Bonding Effect on X-rays Induced by Low Energy Ions", Ann. Meeting of Phys. Soc. of Japan, Matsuyama, Sept. (1979).
- 7) M. Uda, K. Maeda, Y. Sasa, M. Kobayashi, Y. Terasaka, and K. Fuwa: "Chemical Effect on Ion Induced L X-ray Spectra", Ann. Meeting of Phys. Soc. of Japan, Matsuyama, Sept. (1979).
- 8) T. Tonuma, Y. Awaya, T. Kambara, H. Kumagai, I. Kohno, and S. Özkök: "Argon  $K\alpha$  X-ray Satellites by Impact of Nitrogen Ion in the 4.7 – 7.8 MeV/amu Energy Range", XIth Intern. Conf. on the Physics of Electronic and Atomic Collisions, Kyoto, Aug. (1979).
- 9) Y. Awaya: "Systematics of Multiple Ionization in Heavy Ion Collision" (Invited talk), XIth Intern. Conf. on the Physics of Electronic and Atomic Collisions, Kyoto, Aug. (1979).
- 10) M. Uda, H. Endo, K. Maeda, Y. Sasa, and M. Kobayashi: "Chemical Effects through Electron Rearrangement Prior to X-ray Emission", XIth Intern. Conf. on the Physics of Electronic and Atomic Collisions, Kyoto, Aug. (1979).
- 11) H. Endo, M. Uda, Y. Sasa, Y. Terasaka, K. Maeda, and M. Kobayashi: "Search for Bonding Effects on REC and MO X-rays", XIth Intern. Conf. on the Physics of Electronic and Atomic Collisions, Kyoto, Aug. (1979).
- 12) M. Kamiya, A. Kuwako, M. Sebata, K. Ishii, S. Morita, Y. Awaya, and T. Tonuma: "Contribution of Electron Transfer to K-Shell Ionization by  $N^{7+}$ -Ion Bombardment", VIth Intern. Seminar on Ion-Atom Collisions, Tokai, Sept. (1979).
- 13) M. Kamiya, A. Kuwako, M. Sebata, K. Ishii, S. Morita, Y. Awaya, and T. Tonuma: "Contribution of Electron Transfer to K-Shell Ionizations by  $N^{7+}$ -Ion Bombardment", VIth Intern. Seminar on Ion-Atom Collisions, Tokai, Sept. (1979).

- 14) A. Koyama, T. Shikata, and H. Sakairi: "Measurements of Secondary Electron Emission Coefficients from Metals under Fast Proton Bombardments", The 40th Science Lecture Meeting of Japan Society of Applied Physics, Sapporo, Oct. (1979).

4. Radiochemistry, radiation chemistry and radiation biology

- 1) K. Ogawa, K. Taki, and T. Nozaki: "Labeling of 2-Selenouracil by Exchange Reaction with Elementary  $^{73}\text{Se}$ ", ACS/CSJ Chemical Cong., Honolulu, Hawaii, Apr. (1979).
- 2) F. Yatagai, S. Kitayama, and A. Matsuyama: "Induced Mutagenesis in Phage  $\phi\text{X 174}$  Irradiated by Various Types of Radiation", 6th Intern. Cong. of Radiation Research, Tokyo, May (1979).
- 3) T. Takahashi, F. Yatagai, and A. Matsuyama: "Possible Long-Range Effect in the Inactivation of Bacterial Cells by Heavy Ions", 6th Intern. Cong. of Radiation Research, Tokyo, May (1979).
- 4) K. Kimura, T. Fujisawa, and M. Imamura: "Measurement of Fast Emission Decay of Heavy Ion-Irradiated Single Crystals: Nanosecond Time-Resolved  $\sigma$ -Emission Spectra of KBr", 6th Intern. Cong. of Radiation Research, Tokyo, May (1979).
- 5) F. Yatagai, T. Takahashi, and A. Matsuyama: "Effect of Heavy Ions on Bacterial Spores", Spore Radiobiology Meeting, Tokyo, May (1979).
- 6) T. Nozaki and M. Iwamoto: "Comparison of Yields of Light Nucleus by Charged Particle Reactions", Discussion Meeting on Radiochem., Osaka, Oct. (1979).
- 7) T. Nozaki, M. Iwamoto, K. Usami, K. Mukai, and A. Hiraiwa: "Recoil Range of  $^{18}\text{F}$  Formed by Various Reactions", Discussion Meeting on Radiochem., Osaka, Oct. (1979).
- 8) S. Ambe and F. Ambe: "A  $^{119}\text{Sn}$ -Mössbauer Emission Study on Se and SnSe Doped with  $^{119\text{m}}\text{Te}$  and  $^{119}\text{Sb}$ ", Discussion Meeting on Radiochem., Osaka, Oct. (1979).
- 9) F. Ambe and S. Ambe: " $^{119}\text{Sn}$ -Mössbauer Emission Spectra of III-V and II-VI Semiconductors and Related Compounds", Discussion Meeting on Radiochem., Osaka, Oct. (1979).
- 10) F. Yatagai, S. Kitayama, T. Takahashi, and A. Matsuyama: "W-Reactivation and W=Mutation in Phage  $\phi\text{X 174}$ ", 22th Ann. Meeting of Japan Radiation Research Soc., Osaka, Nov. (1979).
- 11) F. Yatagai and A. Matsuyama: "A New Apparatus for Cyclotron-Beam Irradiation of Biological Samples", 22th Ann. Meeting of Japan Radiation Research Soc., Osaka, Nov. (1979).

5. Heavy ion linear accelerator

- 1) T. Kambara and M. Odera: "Control System for the IPCR Linac", Ann. Meeting of Phys. Soc. of Japan, Osaka, Apr. (1979).
- 2) M. Odera, Y. Chiba, and T. Kambara: "Status of the Variable Frequency Heavy Ion Linac, RILAC", 1979 Linear Accelerator Conf., Montauk, Sept. (1979).

## 12. LIST OF PERSONNEL

## Members of the Board

DOE Toshihiko	土手敏彦 (Chairman)	HAMADA Tatsuji	浜田達二
KAMITSUBO Hiromichi	上坪宏道	KOHNO Isao	河野功
NAKANE Ryohei	中根良平	NOZAKI Tadashi	野崎正
ODERA Masatoshi	小寺正俊		

## Users Committee

HAMADA Tatsuji	浜田達二 (Chairman)	IMAMURA Masashi	今村昌
KAMITSUBO Hiromichi	上坪宏道	KOHNO Isao	河野功
MATSUYAMA Akira	松山晃	MORI Kazuo	森一夫
NOZAKI Tadashi	野崎正	ODERA Masatoshi	小寺正俊
SAKAIRI Hideo	坂入英雄	SEKIZAWA Hisashi	関沢尚

## Operation and Machine Maintenance Group

FUJITA Shin	藤田新	IKEGAMI Kumio	池上九三男
KAGEYAMA Tadashi	影山正	KOHARA Shigeo	小原重夫
KOHNO Isao	河野功	OGIWARA Kiyoshi	荻原清
TAKEBE Hideki	武部英樹		

## Scientific and Engineering Personnel

## Cyclotron Laboratory

AMAKAWA Hirotaka	天川博隆	FUJISAWA Takashi	藤沢高志
FUJITA Jiro	藤田二郎	INAMURA Takashi	稲村卓
ISHIHARA Masayasu	石原正泰	KAMITSUBO Hiromichi	上坪宏道
KARASAWA Takashi	唐沢孝	KOHMOTO Susumu	河本進
KOHNO Isao	河野功	KUMAGAI Noritaka	熊谷教孝
MOTONAGA Shoshichi	元永昭七	NAKAJIMA Shunji	中島諄二
NAKANISHI Noriyoshi	中西紀喜	NOMURA Toru	野村亨
SHIKATA Takashi	四方隆史	WADA Takeshi	和田雄
YAMAJI Shuhei	山路修平	YANO Yasushige	矢野安重

## (Visitors)

HATTORI Toshiaki 服部俊章 (Inst. Nucl. Study, Univ. of Tokyo)  
 HAYAKAWA Shunichiro 早川俊一郎 (Dept. Phys., Waseda Univ.)  
 HIRUTA Kotaro 蛭田幸太郎 (Dept. Phys., Tokyo Gakugei Univ.)  
 ICHIMURA Munetake 市村宗武 (Inst. Phys., College General Education, Univ. of Tokyo)  
 KAMMURI Tetsuo 冠哲夫 (Dept. Phys., Osaka Univ.)  
 KUBO Kenichi 久保謙一 (Dept. Phys., Tokyo Metropolitan Univ.)  
 NAGATANI Kunio 永谷邦夫 (Texas A and M Univ.)  
 NAKAHARA Hiromichi 中原弘道 (Dept. Chem., Tokyo Metropolitan Univ.)  
 NATOWITZ J.B. (Texas A and M Univ.)  
 NODA Akira 野田章 (Inst. Nucl. Study, Univ. of Tokyo)  
 OHNUMA Hajime 大沼甫 (Dept. Phys., Tokyo Inst. Technol.)

SHINNO Hitoshi 新野 仁 (Nat. Res. Inst. for Metals)  
 SHIRAISHI Haruki 白石春樹 (Nat. Res. Inst. for Metals)  
 TAKEMASA Tadashi 武政尹上 (Dept. Phys., Saga Univ.)

## (Students)

IEKI Kazuo 家城和夫 (Dept. Phys., Kyoto Univ.)  
 KISHIDA Norio 岸田則生 (Dept. Phys., Tokyo Inst. Technol.)  
 KOJIMA Toshiyuki 小島敏行 (Dept. Phys., Rikkyo Univ.)  
 NAGAME Yuichiro 永日論一郎 (Dept. Chem., Tokyo Metropolitan Univ.)  
 NAKAMURA Kyoko 中村京子 (Dept. Phys., Chuo Univ.)  
 NORO Tetsuo 野呂哲夫 (Dept. Phys., Kyoto Univ.)  
 OBANA Yoshiki 小花芳樹 (Dept. Phys., Chuo Univ.)  
 SATO Kenichi 佐藤憲一 (Dept. Phys., Tohoku Univ.)  
 SHIMODA Tadashi 下田正 (Dept. Phys., Kyoto Univ.)  
 SUGITATE Toru 杉立徹 (Dept. Phys., Tokyo Inst. Technol.)  
 TOBA Yoshiyuki 外羽吉幸 (Dept. Phys., Kyoto Univ.)  
 UTSUNOMIYA Hiroaki 宇都宮弘章 (Dept. Phys., Kyoto Univ.)

## Linac Laboratory

CHIBA Yoshiaki 千葉好明	CHIBA Toshiya 千葉利哉
HEMMI Masatake 逸見政武	IKEZAWA Eiji 池沢英二
INOUE Toshihiko 井上敏彦	KAMBARA Tadashi 神原正
KASE Masayuki 加瀬昌之	MIYAZAWA Yoshitoshi 宮沢佳敏
ODERA Masatoshi 小寺正俊	SCHIMIZU Jun 清水純
SHIMAMURA Akira 島村 晃	TONUMA Tadao 戸沼正雄
YANOKURA Minoru 矢野倉 実	YOKOYAMA Ichiro 横山一郎
YOSHIDA Fusako 吉田房子	

## (Visitors)

DOKE Tadayoshi 道家忠義 (Sci. and Eng. Res. Laboratory, Waseda Univ.)  
 EJIRI Hiroyasu 江尻宏泰 (Dept. Phys., Osaka Univ.)  
 FUKUZAWA Fumio 福沢文雄 (Dept. Nucl. Eng., Kyoto Univ.)  
 HARADA Kichinosuke 原田吉之助 (Japan Atomic Energy Res. Inst.)  
 HISATAKE Kazuo 久武和夫 (Tokyo Inst. Technol.)  
 ISHII Keishi 石井慶之 (Dept. Nucl. Eng., Kyoto Univ.)  
 ITO Noriaki 伊藤憲昭 (Dept. Crystalline Materials, Nagoya Univ.)  
 KAWAI Nanao 河合七雄 (Osaka Univ.)  
 MASUDA Kozo 升田公三 (Tsukuba Univ.)  
 MATSUI Masao 松井正夫 (Nagaoka Sci. and Tech. Univ.)  
 MORITA Susumu 森田 石 (Dept. Phys., Tohoku Univ.)  
 OHNO Shinichi 大野新一 (Japan Atomic Energy Res. Inst.)  
 OZAWA Kunio 小沢国夫 (Japan Atomic Energy Res. Inst.)  
 SAKISAKA Masakatsu 向坂正勝 (Dept. Nucl. Eng., Kyoto Univ.)  
 SATO Shin 佐藤 伸 (Tokyo Inst. Technol.)  
 TAKEDA Shigeru 竹田 繁 (Nat. Lab. High Energy Phys.)  
 TAWARA Hiroyuki 俵 博之 (Dept. Nucl. Eng., Kyushu Univ.)  
 TSURUBUCHI Seiji 鶴淵誠二 (Dept. Phys., Osaka Univ.)  
 WATANABE Ryoji 渡辺亮治 (National Res. Inst. for Metals)  
 YOSHIZAWA Yasukazu 吉沢康和 (Dept. Phys., Hiroshima Univ.)

## Radiation Laboratory

AWAYA Yohko	粟屋容子	HAMADA Tatsuji	浜田達二
HASHIZUME Akira	橋爪 朗	IZUMO Koichi	出雲光一
KATOU Takeo	加藤武雄	KONNO Satoshi	金野 智
KUMAGAI Hidekazu	熊谷秀和	OKANO Masaharu	岡野真治
TAKAHASHI Tan	高橋 旦	TENDOW Yoshihiko	天道芳彦

## (Visitors)

DOKE Tadayoshi	道家忠義	(Sci. and Eng. Res. Lab., Waseda Univ.)
FUJIOKA Manabu	藤岡 学	(Dept. Phys., Tohoku Univ.)
HAYASHIBE Shogo	林部昭吾	(Dept. Phys., Tohoku Univ.)
ISHII Keizo	石井慶造	(Cyclotron, Tohoku Univ.)
MORITA Susumu	森田 右	(Dept. Phys., Tohoku Univ.)
NAGAHARA Teruaki	永原照明	(Inst. Atomic Energy, Rikkyo Univ.)
TAWARA Hiroyuki	俵 博之	(Dept. Nucl. Eng., Kyushu Univ.)

## (Students)

KAMIYA Masami	神谷正己	(Dept. Phys., Tohoku Univ.)
KINEBUCHI Yoshiaki	杵淵義昭	(Dept. Phys., Tohoku Univ.)
KUWAKO Akira	桑子 彰	(Dept. Phys., Tohoku Univ.)

## Metal Physics Laboratory

FUKUSHIMA Hiroshi	福島 博	KOYAMA Akio	小山昭雄
SAKAIRI Hideo	坂入英雄	SHIOTANI Nobuhiro	塩谷亘弘
YAGI Eiichi	八木栄一		

## Magnetic Materials Laboratory

ASAI Kichizo	浅井吉蔵	OKADA Takuya	岡田卓也
SAKAI Nobuhiko	坂井信彦	SEKIZAWA Hisashi	関沢 尚

## (Visitor)

MIZOGUCHI Tadashi	溝口 正	(Dept. Phys., Gakushuin Univ.)
-------------------	------	--------------------------------

## Solid State Chemistry Laboratory

ENDO Hiroshi	遠藤 寛	KOBAYASHI Masayoshi	小林雅義
MAEDA Kuniko	前田邦子	SASA Yoshihiko	佐々嘉彦
UDA Masayuki	宇田応之		

## Radiochemistry Laboratory

AMBE Fumitoshi	安部文敏	AMBE Shizuko	安部静子
ARATANI Michi	荒谷美智	ITO Yoshiko	伊東芳子
IWAMOTO Masako	岩本正子	NOZAKI Tadashi	野崎 正
TERAI Yoshiro	寺井善郎		

## (Visitors)

HIRAIWA Atsushi	平岩 篤	(Central Res. Lab., Hitachi Electric Co.)
MUKAI Kiichiro	向 喜一郎	(Central Res. Lab., Hitachi Electric Co.)

TAKI Ko 滝 幸 (Dept. of Hygen., Kitazato Univ.)  
 TOYODA Minoru 豊田 稔 (Central Res. Lab., Mitsubishi Chemical Ind.)  
 TSUKAZAKI Toshimasa 塚崎 敏正 (Central Res. Lab., Mitsubishi Chemical Ind.)  
 USAMI Katsuhisa 宇佐美勝久 (Central Res. Lab., Hitachi Electric Co.)  
 YAJIMA Fumikazu 矢島 文和 (Central Res. Lab., Mitsubishi Chemical Ind.)

## Radiation Chemistry Laboratory

IMAMURA Masashi 今村 昌

KIMURA Kazuie 木村 一 宇

## Radiobiology Laboratory

HATTORI Yukihiro 服部 行彦  
 KITAYAMA Shigeru 北山 滋  
 YATAGAI Fumio 谷田 貝文夫

KANEKO Ichiro 金子 一 郎  
 MATSUYAMA Akira 松山 晃

## Safety Control Affairs Office

HAMADA Tatsuji 浜田 達二  
 KOYAMA Masashi 小山 政史  
 USUBA Isao 薄葉 勲

IGARASHI Kazui 五十嵐 一 成  
 SAKAMOTO Ichiro 坂本 一 郎

## 13. LIST OF OUTSIDE USERS AND THEIR THEMES

(Jan. – Dec. 1979)

- |  |   |
|--|---|
| 1) M. Shimada and M. Iimura<br>“Cyclotron Irradiation for Study of<br>Fast Breeder Reactor Material Embrittlement”   | Toshiba R & D Center  |
| 2) A. Hishinuma, T. Furuta, K. Fukai, and<br>T. Otomo<br>“Helium Implantation Effect on Creep<br>Rupture Properties of Modified 316 Stainless<br>Steel for Fast Reactor Material”  | Japan Atomic Energy Research Inst.  |
| 3) K. Suganuma and S. Yajima*<br>“Development of Ferritic Stainless Steel for<br>Atomic Reactor”   | Research Inst. for Iron, Steel and Other<br>Metals, Tohoku Univ.<br>*Irradiation Research Lab., in JMTR |
| 4) R. Nagura, H. Ono, Y. Narimatsu, and<br>T. Hishiyama<br>“Calibration of Space Environment Monitor<br>Carried on GMS-2 with Protons”   | Space Development Div., Nippon Electric<br>Co., Ltd.  |
| 5) H. Nakahara, Y. Nakamura, H. Kudo,<br>K. Muramatsu, and Y. Murakami<br>“Production of $^{57,58}\text{Co}$ , $^{113}$ , $^{119\text{m}}\text{Sn}$ , $^{111}\text{In}$ ,<br>$^{196}\text{Au}$ , $^{207}\text{Bi}$ , and $^{210}\text{Po}$ ” | Faculty of Science, Tokyo Metropolitan<br>Univ.   |
| 6) Y. Homma<br>“Production of $^{61}\text{Cu}$ and $^{77}\text{Br}$ ”  | Kyoritsu College of Pharmacy  |
| 7) F. Yajima<br>“Production of $^{18}\text{F}$ ”   | Mitsubishi Chemical Industries Ltd.   |
| 8) K. Yuita<br>“Production of $^{43}\text{K}$ ”  | National Inst. of Agricultural Sciences   |



## AUTHOR INDEX

- AMAKAWA Hirotaka 天川博隆 21
- AMBE Fumitoshi 安部文敏 109, 112
- AMBE Shizuko 安部静子 109, 112
- AWAYA Yohko 粟屋容子 73, 76, 79, 82, 84
- BARADJANEGARA A. A. 121
- CHIBA Yoshiaki 千葉好明 141, 143, 149
- ENDO Hiroshi 遠藤寛 86
- FRÖHLICH H. 51
- FUJISAWA Takashi 藤沢高志 10, 27, 30
- FUJITA Jiro 藤田二郎 4
- FUJITA Shin 藤田新 2, 124
- FUKUDA Tomokazu 福田共和 48, 56
- GONO Yasuyuki 郷農靖之 45, 59, 62, 65, 70
- HAMADA Tatsuji 浜田達三 73, 76
- HASEGAWA Takeo 長谷川武夫 27, 30
- HASHIZUME Akira 橋爪朗 65, 67, 73, 76
- HATANAKA Kichiji 畑中吉治 27
- HATTORI Yukihiro 服部行彦 120
- HEMMI Masatake 逸見政武 145, 147, 151, 154
- HIRAIWA Atsushi 平岩篤 106
- HIRUTA Kotaro 蛭田幸太郎 70
- ICHIMURA Atsushi 市村淳 36
- ICHIMURA Munetake 市村宗武 36
- IEKI Kazuo 家城和夫 45, 59, 62, 70
- IGARASHI Kazui 五十嵐一茂 124
- IKEGAMI Kumio 池上九三男 2, 15, 17
- IMAMURA Masashi 今村昌 117
- INAMURA Takashi 稲村卓 45
- INOUE Toshihiko 井上敏彦 137, 140
- ISHIHARA Masayasu 石原正泰 45, 48, 51, 56, 59, 62, 70
- ISHII Keizo 石井慶造 79
- IWAMOTO Masako 岩本正子 104, 106
- IWATANI Kazuo 岩谷和夫 30
- IZUMO Koichi 出雲光一 73, 76
- KAGEYAMA Tadashi 影山正 2, 17
- KAMATANI Yukio 釜谷幸男 33
- KAMBARA Tadashi 神原正 82, 84, 134
- KAMITSUBO Hiromichi 上坪宏道 7, 27, 48, 51, 56, 89
- KAMIYA Masami 神谷正巳 79
- KAMMURI Tetsuo 冠哲夫 39
- KARASAWA Takashi 唐沢孝 20
- KASAGI Jirhota 笠木治郎太 33
- KASE Masayuki 加瀬昌之 82, 84, 147, 149, 151
- KATOU Takeo 加藤武雄 65, 67, 73, 76
- KIMURA Kazuie 木村一字 117
- KISHIDA Norio 岸田則生 30, 33
- KOBAYASHI Masayoshi 小林雅義 86
- KOHARA Shigeo 小原重夫 2

- KOHNO Isao 河野 功 2, 15, 17, 24, 54, 82, 84, 89
- KOYAMA Akio 小山昭雄 92, 94
- KUBO Toshiyuki 久保敏幸 30, 33
- KUDO Hisaaki 工藤久昭 24
- KUMAGAI Hidekazu 熊谷秀和 65, 67, 73, 76, 82, 84
- KUWAKO Akira 桑子 彰 79
- MAEDA Kuniko 前田邦子 86
- MATSUOKA Kazuo 松岡和夫 39
- MATSUURA Hideo 松浦秀雄 121
- MATSUYAMA Akira 松山 晃 118, 120, 121
- MIURA Iwao 三浦 岩 48, 56
- MIYANO Kazumasa 宮野和政 24
- MIYAZAWA Yoshitoshi 宮沢佳敏 131, 151
- MORITA Susumu 森田 右 79
- MOTONAGA Shoshichi 元永昭七 4, 7, 12
- MUKAI Kiichiro 向喜一郎 106
- MURAKAMI Tatsurho 村上竜郎 33
- MURAMATSU Hisakazu 村松久和 24
- NAGAME Yuichiro 永目諭一郎 54
- NAGATANI Kunio 永谷邦夫 51
- NAKAHARA Hiromichi 中原弘道 24, 54
- NAKAJIMA Shunji 中島諄二 147
- NAKAMURA Masanobu 中村正信 27
- NAKANISHI Noriyoshi 中西紀喜 12
- NOMURA Toru 野村 亨 45, 59, 62, 70
- NOZAKI Tadashi 野崎 正 20, 102, 104, 106, 115
- ODERA Masatoshi 小寺正俊 128, 134, 149, 151
- OGATA Hiroshi 小方 寛 48, 56
- OGAWA Koji 小川幸次 115
- OGIWARA Kiyoshi 荻原 清 2, 4, 10
- OHNUMA Hajime 大沼 甫 30, 33
- OKADA Takuya 岡田卓也 97, 100
- SAKAI Nobuhiko 坂井信彦 97
- SAKAIRI Hideo 坂入英雄 92, 94
- SAKAMOTO Ichiro 坂本一郎 124, 126
- SANO Mitsuo 佐野光男 39
- SASA Yoshihiko 佐々嘉彦 86
- SEBATA Masao 瀬端正男 79
- SEKIGUCHI Masayuki 関口雅行 27
- SEKIZAWA Hisashi 関沢 尚 97, 100
- SHIKATA Takashi 四方隆史 89, 94
- SHIMODA Tadashi 下田 正 51
- SHINNO Hitoshi 新野 仁 89
- SHIOTANI Nobuhiro 塩谷亘弘 97
- SHIRAISHI Haruki 白石春樹 89
- SOGA Fuminori 曾我文宣 27
- SONE Kohei 曾根公平 121
- SUEHIRO Teruo 末広輝男 30
- SUGITATE Toru 杉立 徹 45, 59, 62, 70
- TAKAHASHI Tan 高橋 旦 73, 76

- TAKEBE Hideki 武部英樹 2, 4, 10
- TAKEDA Shigeru 竹田繁 134
- TAKI Ko 滝幸 115
- TAMURA Taro 田村太郎 51
- TANAKA Masayoshi 田中正義 48, 56
- TANAKA Teruaki 田中照明 27
- TENDOW Yoshihiko 天道芳彦 65, 67, 73, 76
- TERAI Yoshiro 寺井善郎 102
- TOBA Yoshiyuki 外羽吉幸 27
- TONUMA Tadao 戸沼正雄 73, 76, 79, 82, 84, 149
- TOYODA Minoru 豊田稔 102
- TSUKAZAKI Toshimasa 塚崎敏正 102
- UDA Masayuki 宇田応之 86
- UDAGAWA Takeshi 宇田川猛 51
- UEDA Nozomu 上田望 27, 30
- USAMI Katsuhisa 宇佐美勝久 106
- USUBA Isao 薄葉勲 124
- UTSUNOMIYA Hiroaki 宇都宮弘章 45, 59, 62, 70
- WADA Takeshi 和田雄 4, 7, 27, 30
- WAKOH Shinya 和光信也 97
- WATANABE Ryoji 渡辺亮治 89
- YAJIMA Fumikazu 矢島文和 102
- YAMAJI Shuhei 山路修平 42
- YANO Yasushige 矢野安重 7
- YANOKURA Minoru 矢野介実 24, 54, 149, 149, 151
- YASUE Masaharu 安江正治 27, 33
- YATAGAI Fumio 谷田具文夫 118, 120, 121
- YAZAKI Koichi 矢崎紘一 21
- YOSHIDA Fusako 吉田房子 10, 151, 154

# IPCR Cyclotron Progress Report

理化学研究所サイクロトン年次報告 第13巻(1979)

印刷 昭和55年(1980)3月25日

発行 昭和55年(1980)3月30日

発行者 理化学研究所

代表者 福井伸二

〒351 埼玉県和光市広沢2番1号

電話(0484)62-1111

編集者 理化学研究所加速器利用者委員会

印刷所 丸星印刷株式会社

〒130 東京都墨田区亀沢1丁目3番3号

定価 3,000円

理化学研究所

埼玉県 和光市 広沢